Synthesis of functional polymers within a protein cage for encapsulation and delivery of biomacromolecules and the development of composite hybrid membranes for water evaporation applications

Inauguraldissertation

zur Erlangung der Würde eines Doktors der Philosophie
vorgelegt der
Philosophisch-Naturwissenschaftlichen Fakultät
der Universität Basel

von

Martin Rother
aus Freiburg im Breisgau, Deutschland

Freiburg im Breisgau, 2016

UNI
BASEL

Genehmigt von der Philosophisch-Naturwissenschaftlichen Fakultät

auf Antrag von

Prof. Dr. Wolfgang P. Meier

(Universität Basel)

Fakultätsverantwortlicher / Dissertationsleiter

Prof. Dr. Nico Bruns

(Adolphe Merkle Institut, Université Fribourg)

Co-Dissertationsleiter

und

Prof. Dr. Marcus Textor

(ETH Zürich)

Korrefferent

Basel, den 8. Dezember 2015

Prof. Dr. Jörg Schibler

Dekan

Abstract

In this thesis two projects were conducted that had the incorporation of synthetic polymers in common albeit at different scales, the nano and the macro scale.

In the nanoscale project functional polymers were synthesized from initiators bound to the interior of a protein cage, the thermosome. The thermosome has pores that are large enough for biomacromolecules like nucleic acids or proteins to enter and leave the cavity. The synthesized cationic polymers within the thermosome acted as anchors through electrostatic interaction and prevented anionic macromolecules from diffusing out of the cage. Delivery experiments of biomacromolecules into mammalian cells were conducted with the thermosome-polymer conjugates. SiRNA and fluorescent proteins were delivered into cells and the results highlight the potential of the conjugates for therapeutic drug delivery. Moreover, the entrapped molecules were protected from degradation by the local biological environment and the cage structure of the thermosome shielded cells from positive charges, which are otherwise cytotoxic.

In the macroscale project a thin water vapor permeable membrane was equipped with synthetic polymers forming amphiphilic conetworks. The thin climate membranes are widely used in apparel or medical applications. Their drawback is that when punctured they cannot close this puncture autonomously. Therefore, the thin membrane was equipped with an amphiphilic conetwork in order to add self-closing properties while, in addition, being capable to let water vapor pass the membrane. The self-sealing properties increased with the thickness of the amphiphilic conetwork layer.

In the two projects, the addition of synthetic polymers allowed generation of new functionalities in nano transporters and they provided improvement of the properties of synthetic membrane.

Content

Abstract I
Content II
List of Figures IV
List of Tables VIII
Abbreviations IX

1 INTRODUCTION 1

1.1 AIMS AND MOTIVATIONS FOR THE THESIS 1
1.2 STRUCTURE OF THE THESIS 2
1.3 AN INTRODUCTION TO PREPERATION METHODS FOR PROTEIN-POLYMER CONJUGATE SYNTHESIS 3
1.3.1 PROTEIN-POLYMER CONJUGATES, THEIR PROPERTIES AND THEIR APPLICATIONS 3
1.3.2 METHODS OF PROTEIN-POLYMER SYNTHESIS 4
1.3.3 FUNCTIONALIZATION OF AMINO ACIDS 6
1.3.4 CONTROLLED RADICAL POLYMERIZATION METHODS USED FOR FOR PROTEIN-POLYMER SYNTHESIS BY A GRAFTING-FROM APPROACH 8
1.4 PROTEIN CAGES AND SYNTHETIC POLYMERS: A FRUITFUL SYMBIOSIS FOR BIONANOTECHNOLOGY 11
1.4.1 INTRODUCTION 11
1.4.2 STRUCTURE AND PROPERTIES OF PROTEIN CAGES 15
1.4.3 PROTEIN CAGES WITH A POLYMER CORONA: POLYMERS BOUND TO THE OUTSIDE OF PROTEIN CAGES 24
1.4.4 POLYMER CAGES AS FUNCTIONAL ADDITIVES IN POLYMERIC MATERIALS 34
1.4.5 PROTEIN CAGES ADSORBED TO POLYMER SURFACES 40
1.4.6 PROTEIN CAGES THAT ENCAPSULATE POLYMERS 41
1.4.7 CONCLUSION AND OUTLOOK 65

2 RESEARCH PROJECTS 69

2.1 SYNTHESIS OF FUNCTIONAL POLYMERS WITHIN A CHAPERONIN FOR ENCAPSULATION AND RELEASE OF BIOMACROMOLECULES 69
2.1.1 INTRODUCTION 69
2.1.2 RESULTS AND DISCUSSION 73
2.1.3 CONCLUSION 108

2.1.4 EXPERIMENTAL SECTION 109

2.2 SELF-SEALING AND PUNCTURE RESISTANT BREATHABLE MEMBRANES FOR WATER EVAPORATION APPLICATIONS 125

2.2.1 INTRODUCTION 125

2.2.2 RESULTS AND DISCUSSION 127

2.2.3 CONCLUSIONS 136

2.2.4 EXPERIMENTAL SECTION 136

3 GENERAL CONCLUSIONS AND OUTLOOKS 145

4 BIBLIOGRAPHY 150

ACKNOWLEDGMENTS 173

CURICULUM VITAE 175

List of Figures

Figure 1.1.1. The three most common ways to synthesize protein-polymer conjugates . 5
Figure 1.1.2. Common functionalization strategies of lysines and cysteines in proteins. 7
Figure 1.1.3. Examples of nitrogen-containing ligands used in ATRP. 9
Figure 1.1.4. Schematic respresentation of the ATRP-equilibrium. 10
Figure 1.1.5. ARGET ATRP equilibrium. 10
Figure 1.2.1. The symbiosis of protein cages with synthetic polymers creates many opportunities for nanobiotechnology. 15
Figure 1.2.2. Structures of protein cages and viruses found in nature. 23
Figure 1.2.3. Polymerization on the exterior of bacteriophage Qβ bacteriophage and the characterization of the conjugates. 28
Figure 1.2.4. Different strategies of polymer attachment to Qβ bacteriophage. 30
Figure 1.2.5. Schematic depiction of vaults that were modified with the thermoresponsive polymer PNIPAAm and TEM images showing the reversible aggregation of vault–PNIPAAm conjugates. 31
Figure 1.2.6. Schematic view of Adv–ABP–polymer conjugate. 33
Figure 1.2.7. Modification of ferritin resulted in liquid proteins. 34
Figure 1.2.8. Integration of a protein cage that encapsulated fluorescent proteins into a polymer matrix yields materials with self-reporting functionality. 36
Figure 1.2.9. The integration of ferritin into PAMPS fibers. 38
Figure 1.2.10. CCMV size modulation using PSS with different molecular weights. 44
Figure 1.2.11. The concentration of NaCl in the presence of an anionic polymer can influence the morphology of CCMV VLPs. 45
Figure 1.2.12. Self-assembly of CCMV-PEG using PSS. 46
Figure 1.2.13. Schematic representation of VLP formation using Ru phthalocyanine dendrimers. 47
Figure 1.2.14. Integration of a polymer into a vault protein cage. 48

Figure 1.2.15. Step-wise grafting-from approach within Hsp. 50
Figure 1.2.16. Schematic representation of the co-ordination polymers created by modifying a branched polymer network with phenanthroline within Hsp G41C. 51
Figure 1.2.17. Synthesis and labelling of $P22_{S39C}$–xAEMA. 54
Figure 1.2.18. P22–xAEMA as catalyst for photoreductions. 57
Figure 1.2.19. Synthesis of polymers in the cavity of Qβ bacteriophage. 59
Figure 1.2.20. THS-PAMAM as transporter for siRNA into cells. 61
Figure 1.2.21. Apoferritin as nanoreactor for the polymerization of phenylacetylenes. 63
Figure 1.2.22. Polymer synthesis in the cavity of THS. 65
Figure 2.1.1. Chemical structures 72
Figure 2.1.2. Structure of THS, polymerization within the cavity of THS, and use of the protein-polymer conjugate to bind and deliver biomacromolecules. 73
Figure 2.1.3. THS protein cage stability tests to find out at which polymerization conditions the cage remains intact. 75
Figure 2.1.4. Determination of available cysteines in THS and THS-Br by coupling of Alexa488 maleimide to Cys and fluorescence correlation spectroscopy (FCS). 80
Figure 2.1.5. Matrix-assisted laser desorption ionization mass spectroscopy (MALDI-ToF MS) THS and THS-poly(DMAEMA). 82
Figure 2.1.6. SDS-PAGE of THS-poly(DMAEMA) and BSA-poly(DMAEMA) conjugates. 85
Figure 2.1.7. Spectroscopic and gel electrophoretic characterization of THS and THS-conjugates. 87
Figure 2.1.8. Transmission electron microscopy images (TEM) of empty THS protein cages. 88
Figure 2.1.9. Transmission electron microscopy images (TEM) of THS-pDMAEMA3 protein cages. 89
Figure 2.1.10. Transmission electron microscopy images of THS-pDMAEMA-co-RhBMA protein cages. 90
Figure 2.1.11. Dynamic light scattering and transmission electron microscopy of THS and THS-polymer conjugates. 91
Figure 2.1.12. Characterization of the polymer that was used in this study and its binding capacity to siRNA. 92
Figure 2.1.13. The presence of polymers and their chain lenght is crucial for siRNA binding. 94

Figure 2.1.14. The cage structure of THS-pDMAEMA prevented aggregate formation when complexed with siRNA. 95
Figure 2.1.15. Transmission electron microscopy (TEM) image of THS-pDMAEMA3 protein cages that were incubated with siRNA. 96
Figure 2.1.16. THS-pDAMEAM3 can protect siRNA from degradation by RNAse II. 97
Figure 2.1.17. Toxicity data of THS-polymer conjugates and pDMAEMA. 98
Figure 2.1.18. Cellular uptake of THS-pDMAEMA-co-pRhBMA into U87 cells after 24h. 100
Figure 2.1.19. Agarose gels of THS-pDMAEMA-co-RhBMA with eYFP (a) and TurboGFP (b) to evaluate complex formation. 101
Figure 2.1.20. Fluorescence-activated cell sorting (FACS) of the THS-pDMAEMA-co-RhBMA/eYFP complex uptaken by U87 cells. 103
Figure 2.1.21. Cellular uptake of TurboGFP is promoted by THS-pDMAEMA-co-pRhBMA conjugates. 105
Figure 2.1.22. Delivery of siRNA into U87 cells by THS-pDMAEMA 107
Figure 2.1.23. Kalibration curve and equation for molecular weight calculation in SDS-PAGE. 115
Figure 2.2.1. ATR-FT-IR spectra of APCN/PEE composite membrane with a composition of PHEA:PDMS 90:10 (w/w). 128
Figure 2.2.2. SEM and AFM characterization of the APCN/PEE composite. 129
Figure 2.2.3. Mechanical properties of dry membranes. 130
Figure 2.2.4. SEM image of a puncture in a dry APCN/PEE composite membrane (side cut). 132
Figure 2.2.5. Self-sealing of APCN/PEE composite membranes with a composition of PHEA:PDMS 90:10 (w/w). 133
Figure 2.2.6. Leaking rates of 170 µm thick APCN/PEE composite membranes with different compositions and of unmodified PEE at water pressures between 0.02 bar and 0.04 bar. 134
Figure 2.2.7. Water evaporation and cooling due to evaporative heat loss in APCN/PEE-based, water-filled laminates. 135
Figure 2.2.8. Fabrication process of APCN/PEE composite membranes. 138
Figure 2.2.9. Inside view of the prechamber of the cryo preparation unit Gatan Alto 2500 with a

swollen and frozen APCN/PEE sample that was fixed on a cylindrical sample holder. 141

Figure 2.2.6. Schematic depiction of experimental setup for self-sealing experiments. 143

List of Tables

Table 2.1.1. Influence of different parameters (Cu (I) / Cu (II) in presence/absence of HMTETA and presence/absence of Na-ascorbate (NaAsc) on the structure of THS subunits. 76

Table 2.1.2. Influence of different parameters (Cu(I) /Cu (II) and TPMA as ligand) on the structure of THS. Investigation if the type of ligand changes THS structure 77

Table 2.1.3. Comparison of the ligands HMTETA and TPMA at different conditions and their influence on the THS cage structure. 78

Table 2.1.4. THS-polymer and BSA-polymer conjugates of this study. 81

Table 2.1.5. Experimental conditions for THS-pDMAEMA, THS-pDAMEMA-co-RhBMA and BSA-pDMAEMA 114

Table 2.1.6. Molar ratios between THS-pDAMEMA-co-RhBMA and eYFP 120

Table 2.1.7. Molar ratios between THS-pDMAEMA-co-RhBMA and TurboGFP 120

Table 2.2.1. Quantity of reagents used for APCNs with the size of 16.3 x 10.3 cm and a thickness of 200 µm 138

Abbreviations

Adv	Adenovirus
AHA	Azidohomoalanine
AFM	Atomic force microscopy
AIBN	Azobisisobutyrylnitrile
APCN	Amphiphilic polymer conetwork
APD	Avalanche photodiode
ATP	Adenosine triphosphate
ATRP	Atom transfer radical polymerization
ARGET ATRP	Activators regenerated by electron transfer atom transfer radical polymerization
AUC	Area under the curve
BBMV	Broad bean mottle virus
BMV	Brome mosaic virus
BN-PAGE	Basic native polyacrylamide gel electrophoresis
BSA	Bovine serum albumin
BSA-Br	Bovine serum albumin ATRP macroinitiator
CPM	Counts per molecule
CPMV	Cowpea mosaic virus
CCMV	Cowpea chlorotic mottle virus
CLSM	Confocal laser scanning microscopy
CNT	Carbon nanotube
CuBr	Copper(I)bromine
$CuBr_2$	Copper(II)bromine
Cys	Cysteine
D	Diffusion coefficient
DLS	Dynamic light scattering
DMAEMA	2-Dimethyamino ethyl methacrylate
DMIAAm	2-(Dimethyl maleinimido)-*N*-ethyl-acrylamide
DMSO	Dimethylsulfoxide
DMEM	Dulbecco's modified eagle medium
DOTA	1,4,7,10-tetraazacyclododecane-1,4,7,10-tetraacetic acid
DTPA	Diethylenetriamine pentaacetic acid
DTT	Dithiothreitol
Dox	Doxorubicin
(ds)DNA	(Double-stranded) desoxyribonucleic acid
eCFP	Enhanced cyan fluorescent protein
EDC	*N*-(3-dimethylaminopropyl)-*N*-ethylcarbodiimide hydrochloride
EDTA	Ethylenediaminetetraacetic acid
eYFP	Enhanced yellow fluorescence protein
EX	Expanded P22 capsid
FACS	Fluorescence-activated cell sorting
FITC	Fluorescein isothiocyanate
FP	Fluorescence protein
FRET	Fluorescence resonance energy transfer
FLIM	Fluorescence lifetime imaging

FMN	Flavin mononucleotide
GAPDH	Glyceraldehyde-3-phosphate dehydrogenase
GFP	Green fluorescence protein
HEA	Hydroxyethyl acrylate
HMTETA	1,1,4,7,10,10-Hexamethyltriethylenetetramine
Hsp	Heat-shock protein
ICP–OES	Inductively coupled plasma optical emission spectrometry
LCST	Lower critical solution temperature
MALDI-ToF MS	Matrix-assisted laser desorption/ionization time-of-flight mass spectrometry
MA-PDMS-MA	α,ω-Dimethacrylate-terminated poly(dimethylsiloxane)
Me_6TREN	Tris[2-(dimethylamino)ethyl]amine
MHPH	3-Maleimido-6-hydraziniumpyridine hydrochloride
MPC	Methacyryloyloxyethyl phosphorylcholine
MPC	Methacryloyloxyethyl phosphorylcholine
MPS-PPV	Poly(2-methoxy-5-propyloxy sulfonate phenylene vinylene)
MRI	Magnetic resonance imaging
MTFB	Maleimido trioxa-6-formyl benzamide
MWCO	Molecular weight cut-off
NaAsc	Sodium ascorbate
NADH	Nicotinamide adenine dinucleotide
NEAA	Non-essential amino acid
NHS	*N*-hydroxysuccinimidyl
OEGMA	Oligoethylene glycol methacrylate
OLED	Organic light-emitting diode
opti-MEM	optimized Minimum Essential Medium
P2VP-*b*-PEO	Poly(2-vinylpyridine)-*block*-poly(ethylene oxide) block copolymer
pAAm	Poly(acrylamide)
PAMAM	Poly(amidoamine)
PAMPS	Poly(2-acrylamino-2-methyl-1-propane sulfonic acid)
PBS	Phosphate buffered saline
PCL	Poly(ε -caprolactone)
PDTD	Poly(desaminotyrosyl tyrosine dodecyl ester carbonate)
PDMS	Poly(dimethylsiloxane)
PEE	Poly(ether ester)
PEG-g-PEI	Poly(ethylene glycol)-grafted polyethyleneimine
PHEA	Poly(2-hydroxyethyl acrylate)
PHEA-l-PDMS	Poly(2-hydroxyethyl acrylate) linked to Poly(dimethylsiloxane)
PEI	Polyethyleneimine
PET	Polyethylene terephthalate
pI	Isoelectric point
PMMA	Poly(methyl methacrylate)
PNIPAAm	Poly(*N*-isopropylacrylamide)
POX	Poly(2-alkyl-2-oxazolines)
PTFE	Polytetrafluorethylene
PS-*b*-PEO	Polystyrene-*block*-poly(ethylene oxide)

PS-*b*-PMMA	Polystyrene-*block*-poly(methyl methacrylate) block copolymer
PSD	Particle size distribution
p-SCN-Bn-DTPA-Gd	2-(4-isothiocyanatobenzyl)-diethylenetriamine pentaacetic acid gadolinium
PSS	Poly(styrene sulfonate)
PVA	Poly(vinyl alcohol)
RAFT	Reversible addition-fragmentation chain transfer
RF	Radio frequancy
R_H	Hydrodynamic radii
RhBMA	Methacryloxyethyl thiocarbamoyl rhodamine B
RNAi	RNA interference
PET–CT	Positron emission tomography–computed tomography
RNA	Ribonucleic acid
SAXS	Small-angle X-ray scattering
SDS-PAGE	Sodium dodecyl sulphate polyacrylamide gel electrophoresis
SEC	Size exclusion chromatography
SEM	Scanning electron microscopy
S-HyNic	Succinimidyl-6-hydrazino-nicotinamide
siRNA	Small interfering ribonucleic acid
TBS	Tris-buffered saline
TBST	Tris-buffered saline with Tween 20
τ_D	Diffusion time
TEDETA	*N*,*N*,*N*′,*N*′-tetraethyldiethylenetriamine
TEM	Transmission electron microscopy
TEMED	Tetramethylethylenediamine
THF	Tetrahydrofuran
THS	Thermosome from the archaea *Thermoplasma acidophilum*
THS-Br	Thermosome ATRP macroinitiator
Tf	Transferrin
TMS	Trimethylsilyl
TMSOEA	2-(Trimethylsilyloxy)ethyl acrylate
TMSPMA	3-(Trimethoxysilyl)propyl methacrylate
TPMA	Tris(2-pyridylmethyl)amine
PEG	Polyethyleneglycol
TMV	Tobacco mosaic virus
UV/Vis	Ultraviolet-visible
VP	Vault-particle
VLP	Virus-like particle
WB	Wiffle-ball morphology of the P22 capsid

Chapter 1

1 Introduction

1.1 Aims and motivations for the thesis

The work for this dissertation is based on two separate projects. The first and main project is to synthesize polymers within a protein cage, the thermosome, to obtain protein cage-polymer conjugates with the ability to deliver therapeutic biomacromolecules into cells. Protein cages show a high uniformity when compared with synthetic nanocapsules and a high stability. The thermosome has, in contrast to other protein cages, pores that allow the encapsulation of macromolecules like proteins or DNA/RNA. Inspired by other researchers working in the field of protein-polymer conjugates and viral capsids, our motivation was to prepare tailor-made polymers within the interior of the thermosome. Those polymers should act as anchors for biomacromolecules that reversibly bind the cargo into the cavity and have fluorescent labels that allow tracking the cell uptake of the protein-polymer conjugate. To this end, ATRP initiators had to be covalently bound to specific sites on the inside wall of a mutated thermosome variant. Then, functional homo and copolymers had to be synthesized within the cavity of the thermosome by ATRP. A methacrylate with a tertiary amine group in the side chain was selected to yield a polymer that is cationic at physiological pH, and a fluorescent methacrylate was selected as comonomer to yield fluorescently labeled polymers. Another aim of polymer synthesis within the cavity was to obtain polymers that do not protrude from the cavity, as this can lead to cell toxicity. Moreover, the idea was to create protein-cage polymer conjugate that could protect the cargo (e.g. siRNA) from degradation by enzymes and do not form aggregates in the presence of it. With the developed thermosome-polymer conjugates cell uptake and toxicity studies had to be conducted as well as binding studies with biomacromolecules. In addition, delivery experiments of biomacromolecules (e.g. siRNA, fluorescence proteins) should be performed to

show the possibility of the protein cage-polymer conjugate as delivery platform for therapeutic cargo.

The second project was a joined project between the University of Applied Sciences Northwestern Switzerland (FHNW) and the company Unico swiss tex GmbH. Unicoswiss tex does not have an own research facility, therefore a NanoArgovia-project was established with the motivation to improve an already existing product of this company. The product is a medical cooling laminate based on a polyethylene terephthalate fabric sandwiched between two thin semi-permeable membranes. Water is filled into this laminate and evaporates through the breathable and water proof membranes. The water evaporation reduced the temperature in the vicinity of the laminate, and can therefore be used to cool the skin of patients. The drawback of such thin membranes is that they become easily damaged and punctured, which makes the cooling laminate leaky. Our motivation was to implement self-sealing properties into the membranes so that small defects of the membrane are autonomously closed by the material. The aim was to coat the membranes with a layer of polymer network that swells upon contact with water and that can close defects by this swelling. In addition, the material should not hamper the evaporation of water through the membrane and should be able to close defects when overpressures are applied.

1.2 Structure of the thesis

The main focus of this thesis is protein cage-polymer conjugates. For this reason, in chapter 1, an introduction to the preparation methods of protein-polymer conjugates is given and afterwards the topic of protein cages with synthetic polymers is reviewed. The research results and experimental works of the two projects that were conducted for this dissertation are presented in chapter 2. A general conclusion of the research projects with a brief reflection of the experimental work and an outlook for further developments is given in chapter 3.

1.3 An introduction to preperation methods for protein-polymer conjugate synthesis

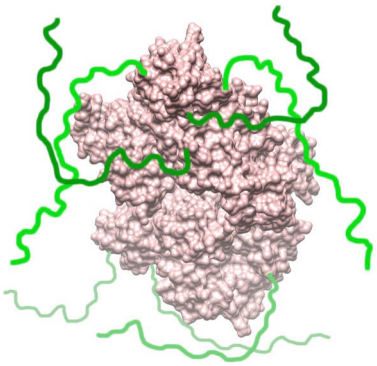

In this chapter, the different preparation methods of protein-polymer conjugates and their applications are described. Polymers can either be attached to proteins or they can be synthesized from the protein. Moreover, functional groups for polymer attachment to a protein, possible modifications for selective attachment andpolymerization methods for conjugate synthesis in aqueous solutions are shown.

1.3.1 Protein-polymer conjugates, their properties and their applications

Protein-polymer conjugates also termed bioconjugates are hybrid materials in which one or more synthetic polymers are covalently bound to a protein.[1,2] The idea behind this boundary is to profit from the advantages of each compound, while reducing the drawbacks.[1-3] Thus, creating a synergy between proteins and polymers is of scientific interest. Attaching polymers to a therapeutic protein can increase its circulation-lifetime in the body; decrease its immunogenicity and enzymatic degradation, and increase their bioavailability.[4-7] Moreover, polymers can stabilize a protein at lower pH or higher temperatures[8,9] increase their shelf-life[9] and increase[10] or regulate the activity of catalyst-proteins, so called enzymes.[10,11] In multimeric enzyme complexes, polymers can stabilize their structure and the stability is often a drawback of enzymes if intended to be used in large scale biocatalytic applications.[12] Most proteins denaturate due to disruption of molecular interactions in pure organic solvents or in mixtures in which the organic solvent is over 50 %. With attached polymers to the proteins, these proteins can be stabilized and remain dissolved in the organic solvent.[13,14] Recent advancements in protein-polymer conjugate synthesis involve polymers that are responsive to external stimuli (e.g. pH, light, temperature) so called smart polymer bioconjugates.[15] Such conjugates react upon influence of external stimuli and have properties like changed thermo and pH-precipitation for bioseperation and thermo- and light-responsiveness for biosensing applications.[15] On

the one hand, synthetic polymers support proteins in many ways. On the other hand, proteins were also used to improve and support polymers. In drug delivery applications for example, proteins were attached to polymers and promoted the cellular uptake of the polymers and polymer-bound drugs and improved the circulation of polymeric nanocarriers.[16-18]

1.3.2 Methods of protein-polymer synthesis

In protein-polymer synthesis, the control over the molecular weight of the polymer plays an important role, because the length of the polymers can significantly alter the properties of a protein-polymer conjugate (e.g. circulation time, enzyme activity, disruption of protein-receptor interactions).[5,10,19] Therefore polymerization techniques are applied that enable the synthesis of polymers with a low molecular weight distribution. [20-24]

Protein-polymer conjugates can be synthesized in various ways. The synthesis can be achieved either by a grafting-to, a grafting-through or a grafting-from approach (Figure 1.1.1a-c). In a grafting-to approach, the polymer chains are attached to the protein. In this case, polymers can be synthesized at optimized conditions (e.g. type of organic solvent, temperature or type of controlled polymerization (anionic,[20] cationic,[21] radical[22-24] amongst others[25-27]) and after synthesis and purification, synthetic polymers are attached to the protein (Figure 1.1.1a). The polymer has to have a functional group that can bind to an amino acid of the protein to form a stable conjugate. Besides the advantage of an optimized synthesis of the polymer, the grafting-to method also has disadvanages.[28] Attaching a macromolecule to another macromolecule mostly leads to low yields of the product due to lower reactivity, which is connected with steric hindrance.[15,28] Another drawback is the purification of the protein-polymer conjugate from the unreacted macromolecules (protein and polymer).[28]

The grafting-through approach is another method of bioconjugate synthesis (Figure 1.1.1b).[15] In this method, proteins having a polymerizable group (e.g. vinyl, acrylic or methacrylic) are embedded in a chain with a carbon backbone. This is in contrast to the grafting-to and grafting-from approach, where proteins are not incorporated into the polymer chain. In order to avoid low polymerization efficancy due to steric

hindrance with larger proteins, comomoners are added for better polymerization control.[15]

The grafting-from approach starts with the attachment of polymerization initiators to reactive amino acids of the proteins (Figure 1.1.2a-g).[15,28,29] From those initiators polymers are grown by the interconnection of monomers. The advantage of the grafting-from strategy is that after the polymerization reaction, separation of the products from the reactants is easier than in the grafting-to strategy. Reason for this is, that only small molecules (Catalysts, reducing agents and monomers) have to be separated from a high molecular weight product. Moreover, the product yield is higher because the conjugation reaction occurs between small molecules and the protein and thus steric hindrance is lower than for the grafting-to approach.[28]

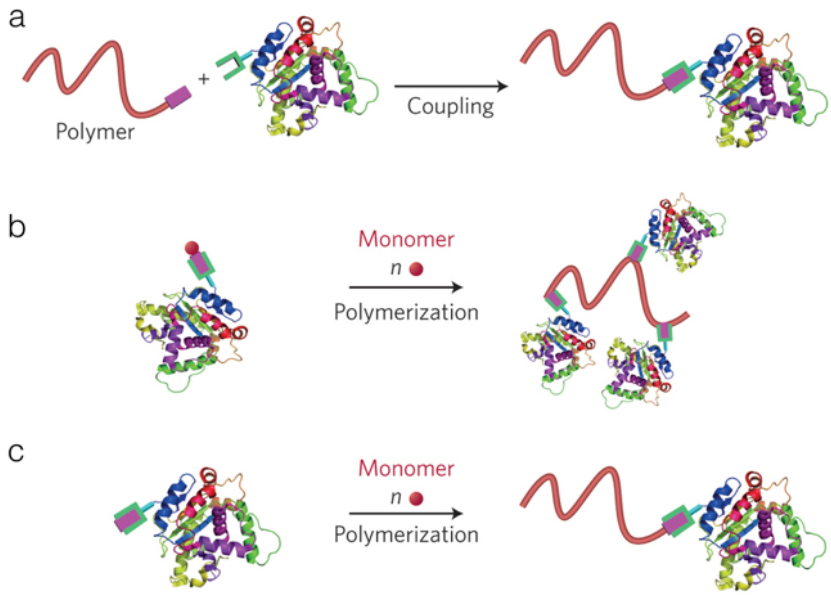

Figure 1.1.1. The three most common ways to synthesize protein-polymer conjugates. (a) "Grafting-to" synthesis: The polymer is synthesized separately and then attached to the protein by interaction of functional groups. (b) "Grafting-through" method: In this method, proteins, which contain a polymerizable group, are polymerized with other monomers. In this case, the proteins are embedded in the backbone of the polymer chain. (c) "Grafting-from" synthesis: Polymers are synthesized from a protein-coupled radical initiator or chain-transfer agent. The polymers grow from the protein. Adapted with permission from [15]. Copyright 2014 Nature Publishing Group.

1.3.3 Functionalization of amino acids

The most common amino acids used for direct attachment of polymers or polymerization initiators to proteins are lysines and cysteines (Figure 1.1.2).[15] Conjugation of lysines yields an amide bond between the protein and the attached polymer or initiator (Figure 1.1.2a-c).[15] Typical reagents for attachment of molecules to lysines have following functional groups incorporated: N-succimidyl ester (Figure 1.1.2a), pentafluorphenyl activated ester (Figure 1.1.2b) or a carboxylic acid (Figure 1.1.2c). The conjugation of functional molecules to cysteines results in disulphide bonds or thioether connections, depending on the reactive group of the conjugation partner.[15] Molecules can be attached to cysteines by a thiol-disulfide exchange with orthopyridyl disulphide, which results in the formation of a disulphide bond between the protein and the attached molecule (Figure 1.1.2d).[15,28] Thioether formation between protein and synthetic polymers or polymerization initiators was achieved by reaction of cysteines with molecules bearing a vinyl (Figure 1.1.2e),[15] maleimide (Figure 1.1.2f)[15,28,29] or vinyl sulphone functional group.[15]

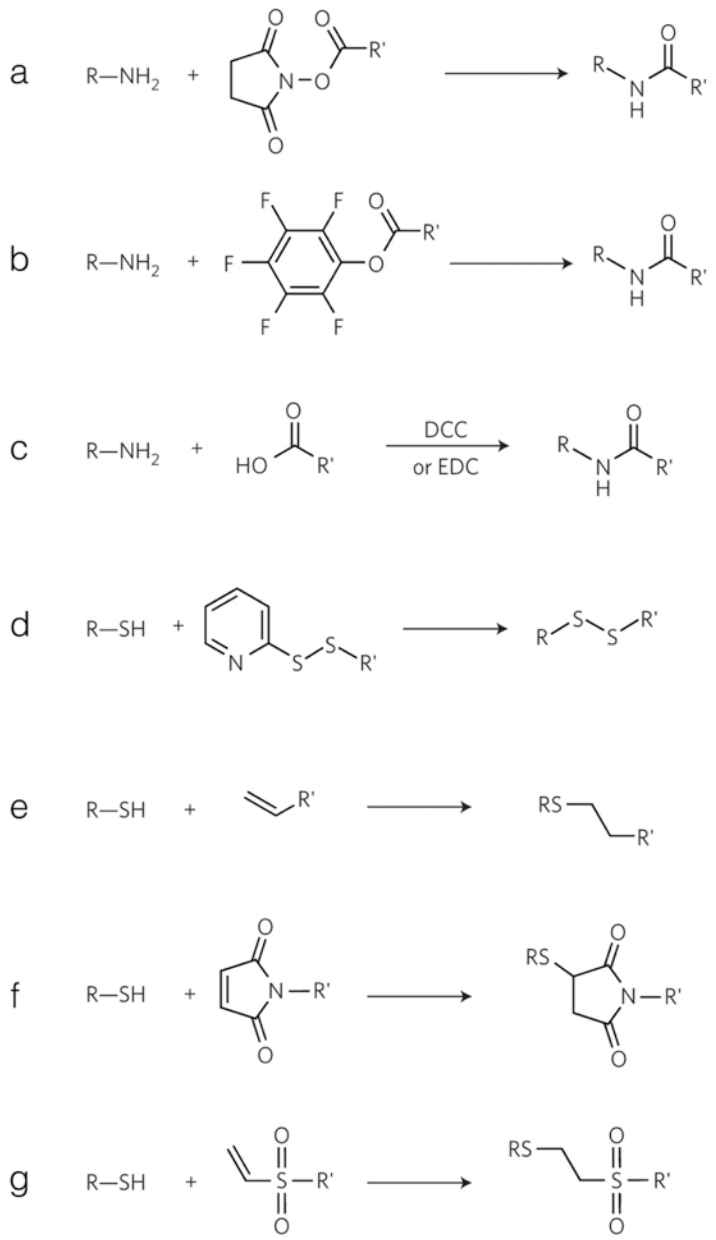

Figure 1.1.2. Common functionalization strategies of lysines and cysteines in proteins. For lysines (a) N-succimidyl esters, (b) pentafluorphenyl activated ester or (c) carboxylic acid in combination with 1-ethyl-3-(3`dimethylaminopropyl) corbodiimide (EDC) for amidation in water. Conjugation to cysteines is typically conducted by the reaction with (d) pyridyl disulfides, (e) vinyls, (f) maleimides or (g) vinyl sulphones. Adapted with permission from [15]. Copyright © 2014 Nature Publishing Group.

For biomedical applications of protein-polymer conjugates, it is desirable to control the stoichiometry between protein and polymer chains and also the site of modification.[28] This control is very difficult to achieve when lysines are intended to be used for conjugation because they are ubiquitously present on proteins. Therefore, alternative site-selective modifications are desired.[28] One strategy for example is the selective introduction of cysteines or amino acids with alkyne groups for alkyne-azide ligation into proteins by genetic methods.[15,30] Another example is the selective

transamination of the primary amine at the N-Terminus by pydridoxal-5-phosphate due to a different pKa-value (7.6-8.0) compared to the primary amines of lysines (pKa 10-12).[6,28] In addition, molecules can be conjugated to prolines by the reaction with o-aminophenols[28] and the binding to other amino acids (e.g. thyrosine) was also conducted.[6,15,28,29,31]

1.3.4 Controlled radical polymerization methods used for for protein-polymer synthesis by a grafting-from approach

There are known issues of proteins in organic solvents like possible denaturation. Thus, grafting-from syntheses have to be performed either in buffered solutions, pure water or in water with the addition of an organic co-solvent (e.g. methanol, THF or DMSO). There are three common ways of conducting controlled polymerization reactions, either anionic polymerization[20], cationic polymerization[21] or radical polymerization.[22,32,33] Anionic or cationic polymerization can not be applied in aqueous solutions due to the reaction of water with either carbanions or carbcations, which results in a termination of the polymerization reaction.[21,34] In addition, the polymerization initiators are inactivated by the reaction with water[21,34] Thus, radical polymerization methods were applied for the synthesis of protein-polymer conjugates, because of the compatibility with aqueous solutions.[15,29,35-38] Controlled radical polymerization is a method used for synthesis of polymers with low polydispersity. The principle behind this technique is that it uses radicals instead of cationic[21] or anionic[20] charges to activate unsaturated double bonds in molecules (vinyls, acrylates and methacrylates) allowing their interconnection and constant growth into polymers. The two most common controlled, also named reversible-deactivation, radical polymerization methods, which were applied for bioconjugate synthesis are atom transfer radical polymerization (ATRP)[32,39] and reversible addition-fragmentation chain-transfer (RAFT) polymerization.[40] ATRP is a radical polymerization technique that uses a transition metal complex in its lower oxidation state as catalyst in combination with an alkyl halide (R-X, wheras X = Cl, Br, I) to generate radicals in a controlled way.[22] The halides are can be bound bound to primary, secondary or tertiary carbon atoms, which influences the reactivity and a radical stabilizing group (e.g. ester, benzyl, cyanide).[39]

The ligands that form the transition metal complex together with metals (e.g. Cu,[41] Fe,[41] Ru,[42]Ni[43]) usually contain nitrogen as ligating atom (Figure 1.1.3).[44]

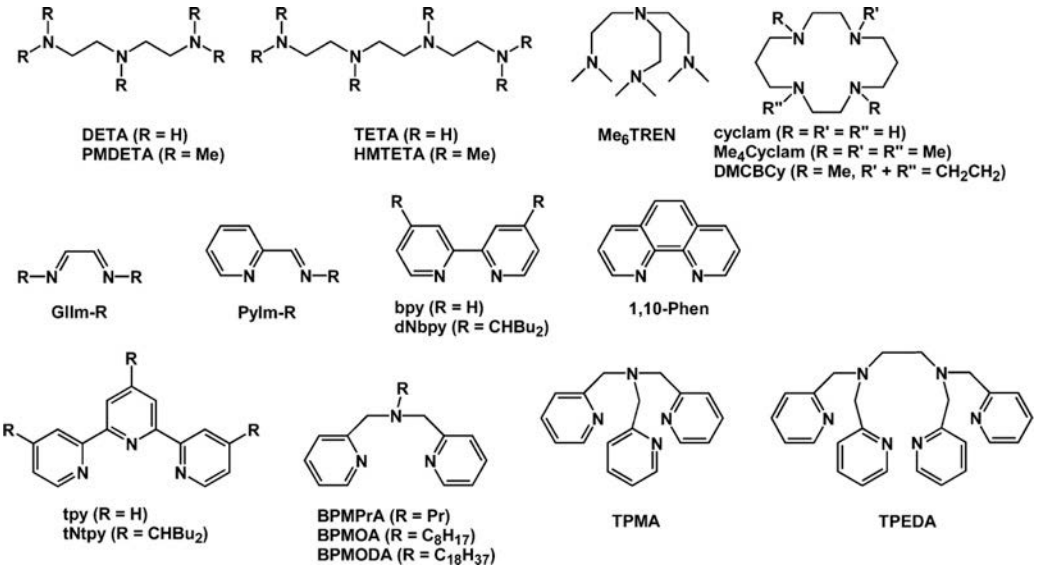

Figure 1.1.3. Examples of nitrogen-containing ligands used in ATRP. Adapted with permission from[44]. Copyright © 2007 American Chemical Society.

In ATRP the control over the molecular weight of the polymers relies on an equilibrium between propagating radicals (Figure 1.1.4, right side) and a dormant species (Figure 1.1.4, left side). The dormant species is the alkylhalide/polymer-X (R-X/ P_n-X). It reacts with the transition metal complexes in their lower oxidation state (Mt^m/L) with an activation rate constant (k_{act}). In this reaction, a halogen transfer from the dormant species to the lower oxidation state transition metal complex (Mt^m/L with e.g. Cu^I) occurs. This transfer causes the creation of a radical on the alkyl halide/polymer, while in parallel, the transition metal complex is transformed into its higher oxidation state (X-Mt^{m+1}/L e.g. Cu^{II}) due to the binding of the halide. The generated radical reacts with meth(acrylate) monomers in the solution, which results in constant polymer growth. The halogen transfer is a chemical equilibrium and thus reversible with a corresponding k_{deact}. The halide is transferred back to the radical species and this back transfer interrupts the polymerization process, until the dormant species/the polymer-halide is activated again by the transition metal complex.[22] The equilibrium is influenced by many factors (e.g. metal-binding capability of the ligand, reactivity of the initiator and their concentrations as well as the choice of solvent)[22,39]

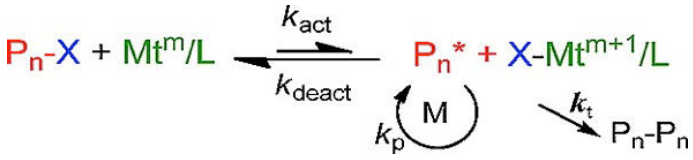

Figure 1.1.4. Schematic representation of the ATRP equilibrium. Adapted with permission from[22]. Copyright © 2012 American Chemical Society.

In classical ATRP copper-catalyts are usually applied and the drawback is that usually larger (e.g. equimolar) amounts of copper are used for the reaction. High amounts of copper (several mM to M) can cause toxic reactions.[45] In order to reduce the amount of copper in the synthesis of polymers and therefore make the procedure more environmentally friendly, a polymerization method was developed that uses low amounts (ppb) of copper. This method is called activators regenerated by electron transfer atom transfer radical polymerization (ARGET ATRP).[46] In ARGET ATRP, a reducing agent is added to the reaction mixture (e.g. sodium ascorbate, ascorbic acid, tin(II)ethylhexanoate, glucose) (Figure 1.1.5).[22] The reducing agent reduces the higher oxidation state catalyst, which is more stable in aqueous solution and creates the active lower oxidation state catalyst.[22]

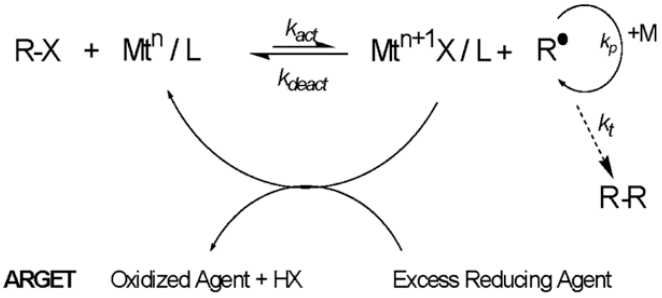

Figure 1.1.5. ARGET ATRP equilibrium. Adapted with permission from[22]. Copyright © 2012 American Chemical Society.

Reversible-addition fragmentation transfer (RAFT) polymerization[47] is another technique that is applied for protein-polymer conjugate synthesis.[48] Instead of a transition metal complex in combination with an alkyl halide like in ATRP, radical formation is initiated by a free radical polymerization initiator e.g. azobisisobutyrylnitrile (AIBN).[49] The control over molecular weight of the polymers and their dispersity ($Đ$) is achieved by the addition of a reversible-addition fragmentation transfer agent, which is typically based on trithiocarbonates, dithiocarbamates or dithioesters.[40,50]

In this thesis the focus was set on ARGET ATRP, due to difficulties with the synthesis of a RAFT-transfer agent that could be coupled with proteins. Moreover, in ARGET ATRP the copper amount in solution is lowered, which is beneficial for biological applications of the conjugates.

1.4 Protein cages and synthetic polymers: A fruitful symbiosis for bionanotechnology

This chapter will be submitted for publication as an invited review as: Rother M., Nussbaumer M. G., Renggli K., Bruns N., Protein cages and synthetic polymers: A fruitful symbiosis for bionanotechnology, Chem. Soc. Rev., **2016**

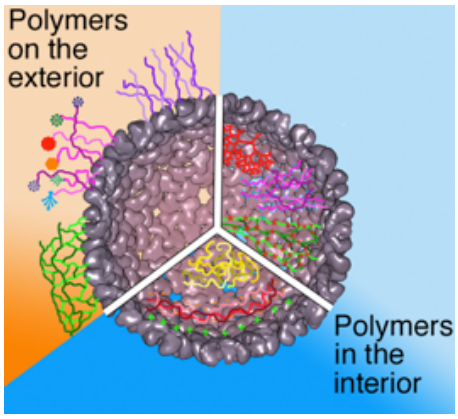

Protein cages have been investigated as e.g. templates for the synthesis of inorganic and organic nanoparticles, as transporter for biomedical applications or as nano reactors. In this chapter, the recent developments in the field of protein cages combined with synthetic polymers are reviewed. Polymers can be attached on the exterior to extend circulation time of the nano vehicles and decrease immunogenicity and, in addition, to promote cellular uptake. Polymers in the interior allow the implementation of higher densities of cargo for biomedical applications and they allow the modulation of cage structures that do not occur in nature. The interior of protein cages can be used as reaction vessel for polymer synthesis. Moreover, synthetic materials in which protein cages were integrated exhibit enhanced materials properties.

1.4.1 Introduction

Hollow nanoparticles play an important role in nanotechnology, materials science and in the biomedical field because they can be used as nanoscale reaction vessels,[51-59] as templates for the synthesis of nanostructured inorganic and organic materials[60-64] and as capsules for the delivery and controlled release of therapeutics.[53,65-67] Prominent examples for synthetic nanoscale objects are self-assembled block

copolymer vesicles,[55,67,68] lipid vesicles[69] or layer-by-layer polyelectrolyte capsules.[70] While there is no doubt about the tremendous potential of these systems, they have some limitations. It can be cumbersome to equip them with advanced functionalities, and it is not possible to modify their shell site-selectively with, e.g. targeting ligands or catalysts. Moreover, their wide size distribution can represent a problem for their use as templates or in drug delivery. Nature provides us with a rich toolbox of functional micro- and nanocompartments, e.g. organelles and lipid vesicles. Protein cages, such as the iron storage protein ferritin, viral capsids or chaperonins, are particularly interesting types of natural nanocompartments.[54,58,71-79] The term 'protein cage' describes a broad range of proteinaceous structures that share the common feature that protein subunits self-assemble into hollow nanoobjects with at least one cavity. These cavities are large enough to enclose e.g. inorganic nanoparticles, nucleic acids and other proteins. Each kind of protein cage is uniform in size. Protein cages are highly symmetric structures. Therefore, only a few different types of protein subunits, but many copies of these subunits are needed to form them. For example, ferritin is a hollow sphere with an outer diameter of approximately 12 nm and an inner diameter of 7–8 nm that consists of 24 copies of a protein.[77] The P22 bacteriophage capsid is 58 nm in diameter and assembled from 420 coat proteins.[78] The interior of protein cages is accessible through pores that are located in between protein subunits. These pores are well defined with respect to their size and polarity.[54] Moreover, some protein cages are dynamic structures that can be assembled and disassembled on demand in response to external stimuli,[78] or that undergo conformational changes that open or close pores.[54] A more detailed description of the structure and biological function of various protein cages is given in the first section of this review.

Protein cages are ideal building blocks for bionanotechnology because of their well-defined size and structure. Moreover, they are non-toxic, biodegradable and many exhibit chemical and thermal stability.[72,75,80,81]

Their pores and their intrinsic functionality make them attractive candidates for applications ranging from nanoreactors to materials synthesis and drug delivery.[54,58,72-74,76-78,82-96] Their most prominent application is the use of viral capsids as vectors for gene therapy.[97–98,99]

The unique feature of protein cages is, in comparison with synthetic nanocapsules or lipid-based compartments, that their subunits can be modified at precisely known

locations by genetic engineering[100] or by chemical means.[74,101-103] Structures of many protein cages have been resolved and are available in databases. Thus, it is possible to tune the properties of protein cages by modifying them on their outside surface, on their inside, i.e. on the surface that lines the cavity and at the interface between subunits.[13,72,104-106] Genetic engineering of protein cage subunits allows insertion of cysteines or non-native amino acids at a desired location in or on protein cages. As protein cages consist of many copies of the same protein subunits, one genetic modification will result in multiple copies of the modification distributed around the protein cage, their location defined by the symmetry of the structure. Such point mutations can act as specific attachment points for chemical conjugation[102] of, e.g. drugs, imaging agents, targeting moieties, (bio) catalysts, polymerization initiators and polymers.[61,75,105,107-120] Moreover, abundantly present amino acids such as lysine, can be chemically modified to introduce a high number of ligands.[72,74,101,121,122] The exterior of the protein cages represents an ideal surface for multivalent ligand display. It was e.g. modified with cell targeting and penetrating moieties such as the tripeptide RGD,[110,123] TAT peptide,[124] LyP-1 peptide,[125] EPCR-targeting peptide and PAR-1-activating peptides,[122] SP94 peptide,[126] folic acid,[107] hyaluronic acid,[127] biotin,[128] the trimeric decoration protein from bacteriophage L[129] and aptamers,[130] to enhance uptake of the protein cages into specific cell lines and, in addition, with nanoparticles[92,131,132] for nanomaterial synthesis. The interior surface offers the possibility to bind catalysts,[61,62,120,133] enzymes,[90,134-136] nanoparticles,[91,137-144] therapeutic cargo[107,110,112,145] and contrast agents[119,123,146-148] into the protein cage. Moreover, the interface between subunits can be modified to tune the stability of the protein cages,[106]or to change the permeability of the pores.[72] Compared with synthetic nanocapsules, protein cages offer many advantages. However, also some drawbacks have to be mentioned. If intended for use as a drug-delivery vehicle, they can be a source of immune reactions, because they are foreign proteins to the human body.[149-151] Moreover, bare protein cages might be rapidly cleared from circulation or neutralized by antibodies.[149,150,152] It is not surprising that such problems were addressed by attaching PEG chains to the outside of protein cages.[152-154] PEGylation is a proven method to hide protein therapeutics from the immune system and to increase their circulation time.[155] Thus, the combination of protein cage delivery agents with synthetic macromolecules is highly beneficial. Other combinations of protein cages and synthetic polymers have emerged in recent years, either to

circumvent intrinsic shortcomings of the protein structures or to obtain multifunctional hybrid systems that combine the best of two worlds, the possibility to synthesize tailor-made functional polymers with the intriguing structure and functionalities of protein cages. Thus, new concepts in bionanotechnology,[77,102,114,148,156-160] biomedical applications[74,75,77,81,101,104,111,113-115,153,161-165] or materials science[52,61,62,77,102,158,166-177] can be pursued. This review will summarize the emerging field of protein cage polymer hybrids. After an overview of the structure and function of several protein cages, it will cover the modification of the exterior surface of protein cages with polymers, embedding protein cages into polymeric materials, the adsorption of protein cages onto polymeric surfaces, the encapsulation of polymers into protein cages and the synthesis of polymers within protein cages (Figure 1.2.1). The reader will be introduced to the basic concepts, and potential fields of applications will be highlighted. The focus is set on the beneficial combination of protein cages and synthetic polymers. Reports on preparation methods of protein-polymer conjugates with either synthetic polymers or natural polymers (e.g. glycopolymers, peptides, poly(nucleic acids) and their applications have been nicely summarized elsewhere.[3,15,28,29,31,178-180]

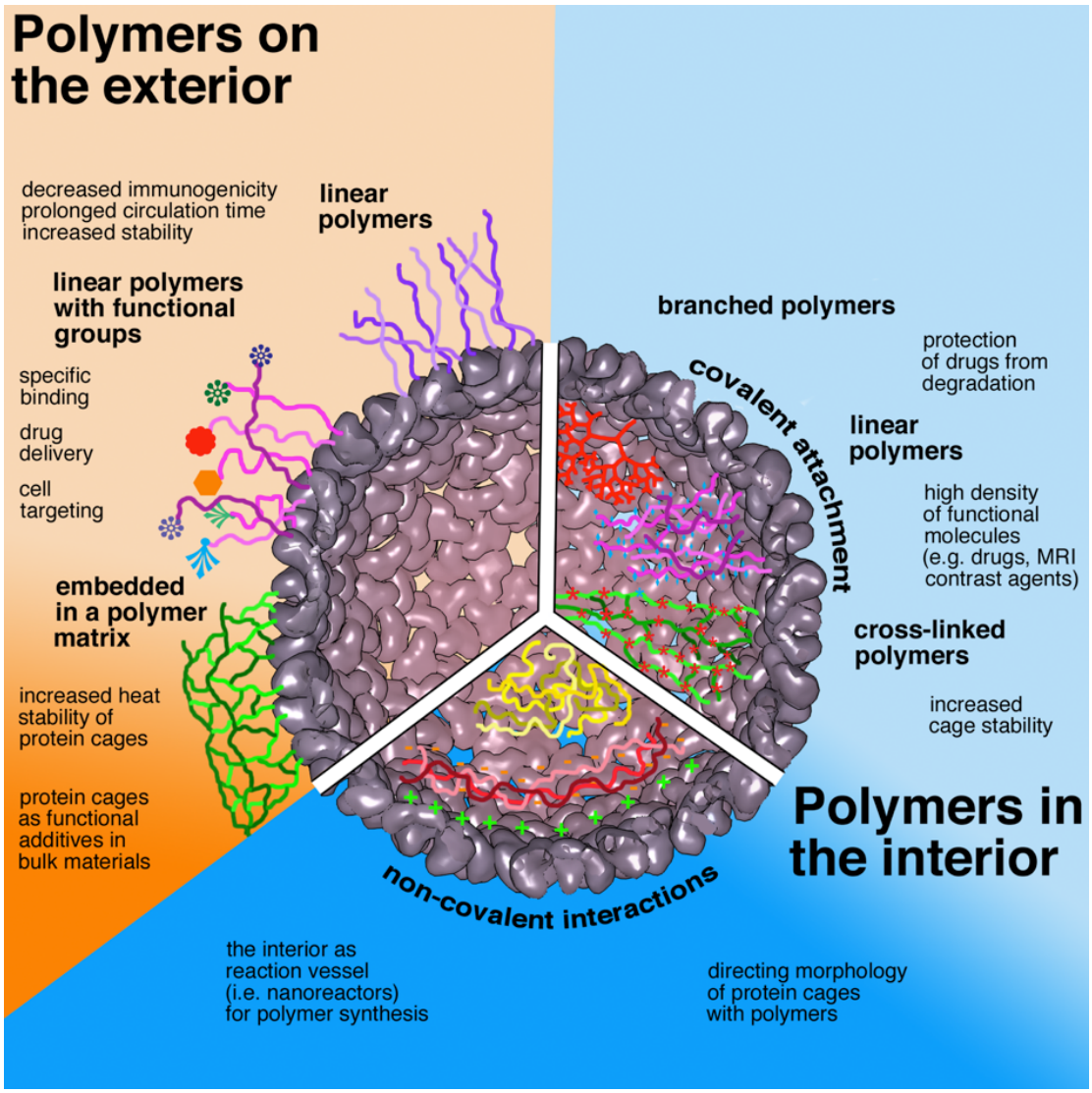

Figure 1.2.1. The symbiosis of protein cages with synthetic polymers creates many opportunities for nanobiotechnology. This scheme summarizes the main approaches to combine protein cages with polymers and highlights properties and applications of the resulting protein–polymer hybrids.

1.4.2 Structure and properties of protein cages

1.4.2.1 General aspects

Protein cages can be categorized into non-viral cages and virus-like particles (VLPs).[93,181,182] Examples of non-viral protein cages are ferritins,[183] vaults,[184] heat-shock proteins,[185,186] chaperonins,[187,188] lumazine synthase,[189] encapsulins[108,190,191] and bacterial microcompartments.[192-194] Most of these protein cages are roughly spherical in shape. Their size ranges from 9 nm for the spherical DNA-binding protein of starved cells (Dps)[72] to bacterial microcompartments with a diameter of 80–150 nm.[192-194] Viruses occur in various morphologies. For example the tobacco

mosaic virus (TMV)[195] and the M13 bacteriophage are rod-shaped viruses, while cowpea mosaic virus (CPMV),[196,197] cowpea chlorotic mottle virus (CCMV),[197,198] bacteriophage MS2[199,200] and adenovirus (Adv)[201-203] have icosahedral, i.e. quasi-spherical structures. Rod-shaped viruses have been extensively investigated as templates for inorganic and polymeric materials.[116,204-207] However, as they do not feature a large internal cavity, they are not protein cages in the sense of this review and therefore will not be covered in detail. Icosahedral viral capsids tend to be larger than non-viral protein cages. Their diameter ranges from approximately 14 nm to 880 nm.[78,105,208] Icosahedral viruses can be described with a symmetry triangulation number *T* due to their high symmetry. Caspar and Klug developed this concept of a specific number of protein repeating units that form regular viruses.[209,210] VLPs are derived from native viruses, but lack encapsulated viral DNA or RNA.[181] VLPs can have the same structure as the native viral capsids, but may also differ in morphology, size and number of subunits.

Most protein cages have static pores in their protein shell at the interface between subunits. These pores range in diameter from 0.4 nm for ferritin,[211] over approximately 3 nm for heat-shock proteins[212,213] to 10 nm for the P22 capsid in its wiffle-ball (WB) structure.[214] These pores connect the interior cavity of the proteins with the exterior environment. Small molecules (e.g. ions, water, organic molecules) can diffuse through them. Thus, the pores act as size-exclusion gates because molecules bigger than the pore size cannot enter the cavity.[133,215] As some pores carry electrostatic potentials or are lined by hydrophobic residues, they can also discriminate between molecules according to their polarity and charge.[62]

At first sight, protein cages are often perceived as static structures. However, many protein cages are dynamic in nature. Some VLPs (e.g. CCMV) reversibly increase in size in response to external stimuli, e.g. a change in pH or the presence of metal ions.[72,198,216,217] This process is caused by subunits moving along symmetry axes to larger radii and the concurrent cleavage and formation of contacts between subunits.[198] It is referred to as swelling as the VLP expands, although this term has a different meaning in material sciences. Swelling of protein cages causes their pores to widen, thus enabling a better mass transport across their shell. Some protein cages (e.g. CCMV, ferritin and thermosomes) can be disassembled into their subunits and reassembled into the full cage by pH changes.[218-225] This process can be exploited to encapsulate guests that are too large to fit through the pores in the wall of the cage.[220]

Chaperonins such as the GroEL–GroES complex, mammalian TRIC/CCT and archaeal thermoses have actively gated pores that open and close, using ATP as the energy source.[226-228] This active gating allows these protein cages temporarily to encapsulate guests such as unfolded proteins. Interestingly, the open–close cycle of chaperonins can be blocked and the proteins locked into a closed conformation by ATP derivatives that mimic the transition state of ATP hydrolysis.[229]

A great variety of protein cages exists and only a subset has been explored as functional nanoparticles for applications in nanotechnology, drug delivery and functional materials. For a comprehensive overview of protein cage structures, functions and applications, we would like to refer the reader to several excellent reviews published on this topic.[54,72,73,78] Here, we will describe those protein cages in detail that have been used in conjunction with polymers.

1.4.2.2 Non-viral protein cages

1.4.2.2.1 Ferritin

Ferritins are non-viral protein cages that are ubiquitous in animals, plants and bacteria (Figure 1.2.2b). Their natural function is the biomineralization of Fe^{2+} to $Fe_2O_3 \bullet H_2O$, i.e. to store iron in a bioavailable and safe form. They play an important role in iron level regulation and in protection against oxidants. Moreover, they promote recovery from oxidative stress and help an organism to fight diseases in which iron accumulates.[183] Mammalian ferritins consist of 24 protein subunits that form a spherical cage with an outer diameter of 12 nm and an inner diameter of 8 nm.[211,230] Along the threefold symmetry axes eight hourglass shaped channels with a diameter of 0.4 nm, a constriction diameter of 0.33 nm and a length of 1.5 nm connect the cavity with the outside, so that Fe^{2+} ions can enter and exit the protein cage. Moreover, six hydrophobic channels exist at the fourfold axes, which are also approximately 0.4 nm wide. Native ferritins encapsulate an iron(III) oxide nanoparticle that can be easily dissolved by appropriate reagents such as solutions containing $[S_2O_4]^{2-}$, a mixture of nicotinamide adenine dinucleotide (NADH) and flavin mononucleotide (FMN) or dithiothreitol (DTT).[183] The empty cage is called apoferritin (apo-Fr). Ferritin and apoferritin are robust nanoparticles, i.e. they withstand temperatures up to 85 °C,[231] pH ranges from 2.0–9.0 and exposure to 6 M guanidine at pH 7.[232] Moreover, ferritins are readily available by extraction from natural sources, by recombinant expression or through commercial suppliers. Thus,

they are popular protein cages and have been used in a variety of studies ranging from drug delivery to template nanoparticle synthesis and nanoreactors.[58,77]

1.4.2.2.2 Heat-shock proteins

Cells express heat-shock proteins (Hsps) at an increased level when they are stressed, e.g. at elevated temperatures (Figure 1.2.2a).[185,186] Many Hsps are chaperones, i.e. they help to refold (partially) unfolded proteins, or they stabilize newly formed proteins. Therefore, they play an important role in protecting cells from environmental or physiological stress. Some Hsps have a cage-like structure. For example, small heat-shock protein (sHsp) from *Methanococcus jannaishii* consists of 24 protein subunits that self-assemble into a hollow sphere.[233] It has a diameter of 12 nm and a cavity that is 6.5 nm in diameter.[212] Eight pores with a diameter of 3 nm along the threefold symmetry axes and six pores with a diameter of 1.7 nm along the fourfold axes make the interior of the protein cage accessible for small organic molecules.[118,160]

1.4.2.2.3 Chaperonins

Another subclass of chaperones are chaperonins (Figure 1.2.2d).[187,234] They are cylindrical protein complexes that feature so-called folding chambers. Non-native proteins refold within these cavities, while being protected from interactions with other unfolded proteins. Chaperonins are classified as group I and group II chaperonins according to their structure and origin. Group I chaperonins feature a detachable co-chaperonin as a lid that closes the cavity, whereas group II chaperonins have a proteinaceous lid build into their structure.[188,226-228,234] Type I chaperonins (e.g. GroEL–GroES complex from *Escherichia coli*) occur in bacterial cytosol, chloroplasts and mitochondria, and type II chaperonins are present in archaeal cytoplasm (e.g. thermosome from the archaea *Thermoplasma acidophilum* (THS)) or in eukaryotic cytosol (e.g. TRiC/CCT). THS is the only chaperonin that has been modified with polymers or used as a nanoreactor for polymerization. Two eight-membered rings with alternating α- and β-subunits and pseudo-eightfold symmetry stack to form a cylindrical particle, i.e. THS in its fully open conformation. The fully closed conformation resembles a sphere with a diameter of approximately 16 nm.[235] Each hemisphere encloses an ovoid cavity of approximately 5.4×8.6 nm^2 and a volume of approximately 130 nm^3. The cavities are large enough to host globular proteins with a molar mass of up to 5×10^4 g mol^{-1}.[235] In contrast to

most other protein cages, chaperonins have large pores that allow proteins,[234,235] synthetic macromolecules[61,163] and inorganic nanoparticles[139] to enter and exit the cavities. In the case of THS, this pore is approximately 8–10 nm wide and gated by helical pertusions of the subunits.[106,236,237] Under consumption of ATP, the subunits undergo concerted conformational changes that close and open this built-in lid.[227,238]

1.4.2.2.4 Vault particles

Vault particles (VPs) are ribonucleoprotein particles that occur in higher eukaryotes (Figure 1.2.2k).[239-241] The name of the particle describes its barrel-like architecture, which resembles a vault ceiling of a gothic cathedral. Their size is 41 nm in diameter and approximately 73 nm in length.[242] VPs are assembled from the major vault protein (MVP) with a mass of 1×10^5 g mol^{-1}, the 1.93×10^5 g mol^{-1} vault poly(ADP ribose) polymerase (VPARP), the 2.4×10^5 g mol^{-1} telomerase-associated protein 1 (TEP1) and RNA, resulting in an overall molar mass of about 1.3×10^7 g mol^{-1}.[241] The function of VPs is unclear, but some studies suggest that they are involved in the protection of cells from toxins.[242]

1.4.2.2.5 Pyruvate dehydrogenase complex

The eukaryotic pyruvate dehydrogenase is the largest multienzyme complex known (Figure 1.2.2c).[243] It converts pyruvate into acetyl-CoA and therefore links the glycolysis cycle with the tricarboxylic acid cycle. The complex consists of about 22 pyruvate dehydrogenases (E_1) and about six copies of dihydrolipoamide dehydrogenase (E_3) that form a shell around a 60-mer complex of dihydrolipoamide acetyltransferase (E_2). The E_2 core is 24 nm in diameter and has pentagonal dodecahedron morphology, i.e. 12 pentagons form a spherical hollow particle.[244] The cavity has a diameter of 12 nm. Small organic molecules can access its interior through 12 5.2 nm wide pores along the fivefold symmetry axes. The E_2 core is stable without the E_1 and E_3 proteins and can therefore be used as a protein nanocapsule.[245]

1.4.2.3 Virus-derived icosahedral protein cages

1.4.2.3.1 Adenovirus

The human adenovirus (Adv), discovered in 1953,[246] is a non-enveloped, double-stranded DNA (dsDNA) virus with a molar mass of 1.50×10^8 g mol^{-1} (Figure

1.2.2j). It measures about 95 nm from vertex to vertex.[202,247,248] The capsid is assembled into a pseudo $T = 25$ icosahedral symmetry by three main proteins (capsomers): 720 subunits that form 240 hexon trimers, 12 pentagon-shaped penton-base pentamers that are all centred on the vertices of the cage, and 12 fibre trimers, which are interconnected with the penton-base pentamers.[202,247,248] The cage is composed of 20 facets and each facet is assembled from 12 hexon trimers and one penton-base at each vertex.[247] Every penton-base has a central pore of 5 nm, which allows the insertion of the fibre shaft protein domain.[247] The fibre trimers are responsible for interaction of the virus with host cells.[247,248] They have a length of 9 nm.[247] In addition, four minor proteins (IIIa, VI, VIII and IX) are incorporated into the capsid.[202] The minor proteins form networks of interactions, which provide additional stabilization to the cage.[202,248] On each facet, a network of nine capsomers is formed and on each vertex there is a network of six capsomers.[202] The minor proteins keep them together.[202] Human Adv is non-oncogenic and is therefore used in gene and cancer therapy.[249-252]

1.4.2.3.2 Cowpea mosaic virus (CPMV)

CPMV is a member of the genus *Comovirus* in the virus family of *Comoviridae* (Figure 1.2.2e).[253] Two single-stranded RNA molecules are encapsulated in its cavity.[253] CPMV is a non-enveloped virus with a diameter of approximately 30 nm.[254] The capsid is composed of two different types of subunits, small subunits that are composed of the A-domain and large subunits that are formed from the B + C domains.[254] Those subunits form pentons (A-domain) and hexons (B + C domains) that assemble around the single-stranded RNA into an icosahedral cage with a pseudo $T = 3$ structure.[254] Channels of 2 nm in diameter enable the exchange of molecules from the exterior to the interior.[255] The empty capsid has a molar mass of 3.94×10^6 g mol^{-1}.[254] CPMV is a plant virus, therefore it has no biological hazard towards other organisms.[254] In addition, it is stable at various conditions. For example, the cage is stable for more than two weeks in a solution containing 20% DMSO. At 50% DMSO content, the half-life of the cage is still several hours.[254] This property allows the introduction of relatively hydrophobic molecules into the cage.

1.4.2.3.3 Brome mosaic virus (BMV)

BMV is very similar to cowpea chlorotic mottle virus (Figure 1.2.2f). The virus, which has a diameter of 28 nm and $T = 3$ symmetry, is composed of 180 identical

polypeptides with different conformations (A, B and C conformation subunits).[256] Pentameric capsomers are formed from the A subunits. The B and C subunits form hexameric capsomers.[256] Small pores of 0.5 nm in diameter are present in the pentamers and 0.6 nm in diameter in the hexamers.[256] The cage structure is mainly created by protein–nucleic acid interactions of the positively charged inner cavity of the capsid with the negative charges of the encapsulated single-stranded RNA.[256] Interactions between single capsid subunits are weak; therefore the RNA is necessary for the stability of the cage. At pH < 6.0 and in the presence of Mg^{2+} ions, the cage structure is in its native state.[256] If conditions are changed (e.g. the pH is increased to 7.0) structural transitions of the cage occur that can result in the complete disassembly of subunits and release of RNA.[256] Disassembled subunits can be assembled into different morphologies as well as empty icosahedral cage structures ($T = 1$ and $T = 3$) at defined conditions.[257]

1.4.2.3.4 Broad bean mottle virus (BBMV)

BBMV is an icosahedral RNA-virus composed of 180 protein subunits, which is composed of approximately 190 amino acids and has a molar mass of approximately 2×10^4 g mol^{-1}.[258,259] The subunits are arranged as pentamers and hexamers that form a $T = 3$ capsid structure.[258] The external diameter of BBMV is approximately 26 nm and a central pore of 10–12 nm is integrated in the capsid.[258,260]

1.4.2.3.5 Bacteriophage λ procapsid

The icosahedral bacteriophage λ procapsid is the head of the bacteriophage λ, which is missing its flexible, approximately 150 nm long, tail that is used for injection of viral dsDNA into the bacterial host (Figure 1.2.2h).[261] The capsid is composed of 405 capsid proteins that are arranged to capsomers, which form a virus with a triangulation number $T = 7$.[262] The immature procapsid has a diameter of approximately 54 nm with a shell thickness of approximately 7 nm.[263] The immature procapsid expands after dsDNA encapsulation in the capsid to the mature capsid.[263] The external diameter increases to approximately 63 nm and the shell thickness decreases to 4 nm.[263] In addition, the structure changes from a spherical shape to an icosahedral shape. As a result of DNA packaging, the inner pressure increases. A cement protein is implemented into the capsid structure to prevent the disassembly of the capsid caused by the internal pressure.[262] Pores of 1.5–2.0 nm in diameter are present on many of the mature capsomers.[261]

1.4.2.3.6 MS2

The MS2 bacteriophage is an icosahedral virus with encapsulated single-stranded RNA (Figure 1.2.2i).[199] It only infects *E. coli* bacteria.[199] The protein shell, with T = 3 symmetry, is composed of 180 polypeptide chains (A, B and C chains), which have a molar mass of approximately 1.37×10^4 g mol^{-1} and are arranged as 60 triangular monomer units.[199,200] The viral capsid has a diameter of approximately 28 nm[200] and its shell has a thickness of 4 nm.[199] Channels of 1.6 nm in diameter are distributed all over the capsid.[200] In contrast to many other icosahedral viruses, the stability of the capsid is not primarily based on protein–nucleic acid interactions.[199] The self-assembly mechanism is mainly controlled by dimer–dimer contacts of the polypeptide chains. Therefore, RNA is not necessary for coat protein assembly.[199]

1.4.2.3.7 Qβ bacteriophage

The Qβ bacteriophage is an icosahedral RNA bacteriophage with T = 3 quasi-symmetry that, like MS2, infects *E. coli* bacteria (Figure 1.2.2h).[264] It is approximately 25 nm in diameter. Like MS2, it is composed of capsid proteins with different conformations (A, B, C coat proteins).[264] The empty capsid has a molar mass of 2.7×10^6 g mol^{-1}. It is composed of 180 coat proteins that are arranged as 12 pentamers and 20 hexamers.[265] The viral capsid features pores of approximately 2.5 nm in diameter.[265] The capsid is formed by hydrophobic interactions between the subunits and, in addition, is stabilized via disulfide bonds between the subunits.[264] As in the case of MS2 bacteriophage, RNA is not necessary for capsid assembly.[265] Depending on the conditions, it is possible to form rod-like structures from the spherical Qβ bacteriophage.[266]

1.4.2.3.8 P22 capsid

P22 is a dsDNA phage that infects *Salmonella* bacteria (Figure 1.2.2l).[267] The mature virion is developed through several maturation processes. The metastable procapsid with an external diameter of 58 nm and a T = 7 triangulation number is the first form in the development process.[268,269] It is assembled from 420 copies of a coat protein (CP) with molar mass 4.66×10^4 g mol^{-1} and about 300 copies of a scaffolding protein (SP) with molar mass 3.36×10^4 g mol^{-1}.[269] The CPs are assembled to pentons and hexons.[269] The SP aids the CP in capsid formation. After DNA insertion into the capsule, the SPs are removed. Insertion of DNA leads to an expansion of the

cage structure to 64 nm and, in addition, the thickness of the capsid wall decreases. The hollow procapsid, i.e. the empty cage structure (ES), can be created by removing the SP with guanidine hydrochloride. Heating of the empty P22 procapsid shell to 65 °C expands the cage from 58 nm to 64 nm, forming the expanded capsid (EX).[214,269] The mature capsid possesses a portal that is composed of 12 protein copies.[270] The portal is used for DNA insertion into the capsid.[270] The narrowest part of this portal channel is 2.5 nm in diameter.[270] Moreover, because of the maturation process, small openings of approximately 2.0 nm[148] at the centre of the hexons occur.[148] Additional heating of the expanded structure to 75 °C releases 12 penton subunits, creating the P22 WB structure.[214,269] It has the same size as the expanded cage but with additional larger pores that have a diameter of 10 nm.[269]

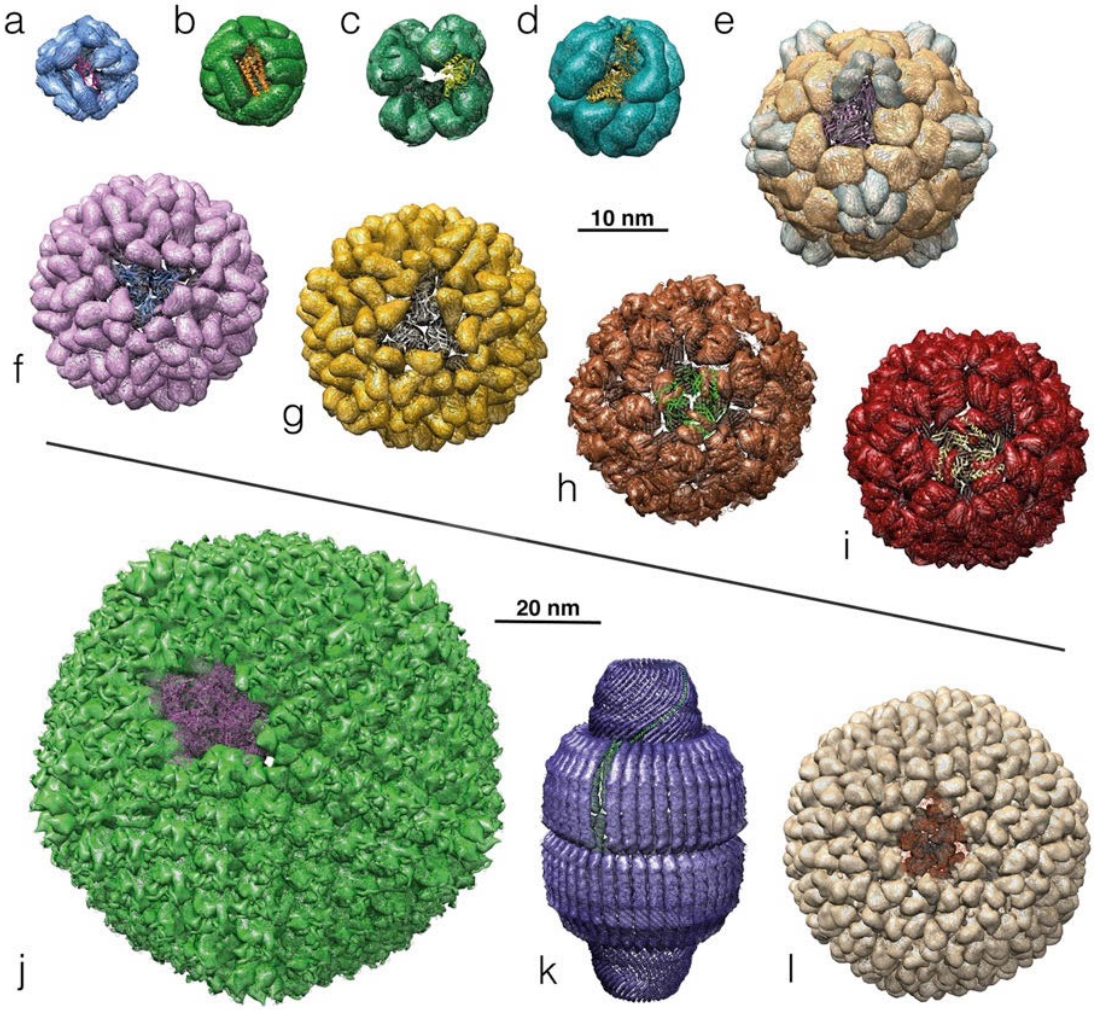

Figure 1.2.2. Structures of protein cages and viruses found in nature. (a) small heat-shock protein (HSP) (PDB: 1SHS),[213] (b) apoferritin (PDB: 1DAT)[211] (c) pyruvate dehydrogenase multienzyme complex (PDB: 1EAA),[271] (d) thermosome (THS) (PDB: 1A6D),[235] (e) cowpea mosaic virus (CPMV) (PDB: 1NY7),[255] (f) brome mosaic virus (BMV) (PDB: 1JS9),[256] (g) cowpea chlorotic mottle virus (CCMV) (PDB: 1CWP),[198] (h) bacteriophage lambda (rendering of similar bacteriophage Q beta PDB:

1QBE),[264] (i) bacteriophage MS2 (PDB: 2MS2),[200] (j) human adenovirus (Adv) (PDB: 1VSZ),[203] (k) vault particle (PDB: 4V60),[272] (l) bacteriophage P22 (PDB: 2XYY).[273] Structures were rendered using the Chimera program.[274]

1.4.2.4 Biodistribution of protein cages

Because many studies with protein cages aim to use them as nanosized drug-delivery systems, it is worthwhile to review briefly their fate in vivo. In a study by Young and co-workers,[149] the biodistribution of two protein cages, namely CCMV and Hsp, was analysed. Even though CCMV and Hsp differ in size (28 nm vs. 12 nm), in structure (icosahedral vs. octahedral) and in sequence, both protein cages showed a similar biodistribution in naïve and immunized mice. The reason could be their similar charge at neutral pH. Within one hour of intravenous injection, the protein cages were rapidly distributed and found in the majority of the organs. The protein cages translocated rapidly and easily through the tissues and extravasated from the circulatory system to the interstitial space, then further to the lymphatic system and eventually again into the vascular system. After 24 h, the majority of the protein cages were cleared from the mice, without any mortality. In contrast, similar studies with CPMV showed deposition of this protein cage in certain organs for up to 72 h.[275,276] CCMV and Hsp showed immunogenicity and induced IgG and IgM response. However, such side effects, which also occur with other therapeutic proteins, could be overcome with PEGylation or other shielding strategies (vide infra).[75] In general, protein cages are suggested as safe, non-toxic and biocompatible drug-delivery platforms.[149,150]

1.4.3 Protein cages with a polymer corona: Polymers bound to the outside of protein cages

Protein cages can be easily modified with polymers on their outside, as their surface is freely accessible for reagents from solution. Not surprisingly, conjugates of protein cages and polymers have been synthesized by many of the well-known methods to prepare protein–polymer conjugates,[15,29,277-281] such as the binding of preformed polymer chains to proteins via chemical linkers (grafting-to approach), the growing of polymer chains from protein-bound initiators (grafting-from approach), and the non-covalent binding of polymers to proteins, e.g. through multiple electrostatic interactions. Reasons to modify the exterior surface of protein cages with polymers

are to lower their immunogenicity and antigenicity, to increase the protein particles' circulation time in the body, to stabilize and protect protein cages against degradation by proteases and other degrading enzymes and to decrease protein–protein interactions.[155] Moreover, polymers can be used as flexible spacers to bind targeting molecules to the proteins to enhance the interaction of these targeting ligands with receptors on the surface of cells.[109,282-284] As polymers can be designed to feature multiple copies of functional groups along their structure, they can be used to bind a high number of contrast agents or drug molecules on the exterior of protein cages.[285]

PEGylation, i.e. the conjugation of poly(ethylene glycol) (PEG) to proteins and other (macro)molecules, is widely used to 'mask' nanoparticles, proteins and drugs from the immune system, thus effectively reducing their immunogenicity.[286,287] Moreover, the presence of PEG increases their hydrodynamic radius and therefore prolongs their circulation time. As PEG is biocompatible, non-toxic and FDI-approved, several PEGylated drugs have successfully been introduced to the market.[288-290] The scientific state-of-the-art of PEGylated nanomedicines was recently reviewed by Vllasaliu et al.[155]

Examples of protein cages that were PEGylated are CPMV,[153,154,291] CCMV,[292] the MS2 bacteriophage,[283,293] Adv,[152,164,294] ferritin[295,296] and the dodecahedral scaffold of E2 subunits from pyruvate dehydrogenase.[297] The chain length of PEG plays an important role in the effectiveness and behaviour of PEGylated protein cages. For example, modification of CPMV with PEG of a molar mass of 1×10^3 g mol^{-1} did not inhibit the uptake of the viral capsids into human colon adenocarcinoma cells, while PEG with 2×10^3 g mol^{-1} effectively prevented the capsid from interacting with these cells, possibly because the longer polymer shielded key interacting regions on the surface of the capsid or because the longer PEG created a sufficient hydration shell around the protein.[153] In addition to chain length, the number of polymer chains per protein subunit, i.e. the modification ratio, plays an important role in the interactions of PEGylated protein cages with cells and in the immune response they create in vivo. This was investigated by Nakagawa and co-workers using Adv.[164] They PEGylated Adv (PEG–Adv) with 5×10^3 g mol^{-1} PEG with various modification ratios (30%, 45% and 90%) and investigated their anti-Adv antibody and anti-tumour response. To this end, unmodified Adv and PEG–Adv were administered to rats. The level of anti-Adv immunoglobulins was determined. Immunoglobulin levels were similar when unmodified Adv and PEG–Adv with 30%

or 45% modification ratio were administered, while PEG–Adv with 90% modification ratio caused a significantly lower immune response. In addition, PEG–Adv with 90% PEGylation promoted expression of tumour necrosis factor-α and lowered the amount of metastatic colonies in the lung compared with unmodified Adv. In conclusion, a higher PEG density on Adv can reduce the number of antibodies against Adv and improve its efficacy against metastatic cancer.

PEGylated protein cages were also modified with targeting groups to promote specific binding and uptake into cells. PEG–Adv was additionally modified with protein subunits from enzymes,[282,298] monoclonal antibodies[294] or cancer-targeting peptide chains[284,299] for active targeting strategies. Transferrin-modified PEG chains were grafted to lysines on the exterior of bacteriophage λ procapsids (λ-PEG-Tf). The aim was to target transferrin receptors, which are overexpressed in some cancer cells.[109,300] The Tf modification resulted in an enhanced uptake of the capsid by cells expressing the Tf receptor.

Francis and co-workers explored the bacteriophage MS2 as a multifunctional drug-delivery platform.[283,293] They bound fluorescein into MS2 and grafted PEG to the outside of the capsid. By using PEG that carried biotin or a fluorescent coumarin at one chain end, PEGylated capsids were obtained that displayed small organic molecules as models of targeting ligands.[283] The fluorescently modified MS2 allows tracking of its cellular uptake in cell-based assays. To demonstrate the potential of MS2-PEG capsids as delivery agents in in vivo applications, MS2 was modified on its interior surface with DOTA chelators that were labelled with ^{64}Cu.[293] The protein was administered to mice. Its biodistribution was imaged by positron emission tomography–computed tomography (PET–CT) and measured by gamma counting of organs. PEGylated MS2 showed less cellular uptake into the spleen than bare MS2, but otherwise the biodistribution of the two types of capsids was similar.

In addition to the in vitro, ex vivo[153] and in vivo[301] advantages of PEGylated protein cages in biomedical applications, PEGylation can also be used to modulate the adsorption of protein cages on solid surfaces. PEGylation of ferritin reduced the adsorption of the protein onto silicon wafers and onto wafers that were modified with 3-aminopropyltrimethylsiloxane.[296] Moreover, the amount and chain length of PEG grafted onto ferritin influenced the adsorption behaviour of the protein cage.

Only a few research laboratories synthesize PEG in-house due to the difficult and dangerous handling of its monomer, ethylene oxide. Moreover, PEG cannot be synthesized in the presence of proteins because anionic polymerizations are not compatible with the functional groups of proteins. If ethylene glycol-based polymers with tailored properties need to be synthesized, it is more convenient to polymerize acrylates or methacrylates that have a PEG side chain. Wang and co-workers were the first to synthesize poly(oligoethylene glycol methacrylate) (poly(OEGMA)) by atom transfer radical polymerization (ATRP) from protein cage-bound initiators.[302] To this end, lysines on the exterior of apoferritin were chemoselectively modified with ATRP initiators via *N*-hydroxysuccinimidyl (NHS) ester conjugation. In a similar approach, reported by Hu et al., a NHS ester-functionalized ATRP initiator was attached to the exterior of ferritin and poly(OEGMA) chains were synthesized by a grafting-from approach with CuBr/bipyridine as catalyst.[159] In addition, conjugates of poly(methacyryloyloxyethyl phosphorylcholine) (poly(MPC)) and ferritin were prepared. Poly(MPC) is a zwitterionic polymer that is hydrophilic and biocompatible. As expected for a controlled radical polymerization, the length of the polymer chains on ferritin increased with an increasing monomer:initiator ratio [M:I]. Moreover, the diameter of the ferritin–polymer conjugates increased with a higher [M:I]. The diameter of native ferritin was measured as 12.9 ± 0.8 nm, while for ferritin–poly(OEGMA) with [M:I] = 100:1 the diameter was 18.9 ± 0.8 nm and for ferritin–poly(MPC) with the same [M:I] the diameter was 19.4 ± 1.2 nm. The polymers cover the surface of the protein cage, as shown by in vitro antibody recognition experiments. Both types of polymers reduced the amount of anti-ferritin antibodies that could bind to the protein nanoparticles by more than 80%. This is very important for drug-delivery applications, as the polymers would shield the ferritin from the immune system.

Poly(oligoethylene glycol methacrylate) was also synthesized on the exterior of the bacteriophage Qβ by Finn and co-workers (Figure 1.2.3).[285] The protein cage has 720 surface-accessible amine groups of which 180 ± 30 were modified with an azide-functionalized *N*-hydroxysuccinimide. Using click chemistry, a triglyme-based ATRP initiator with an alkyne end group was bound to the azides on the protein, followed by polymerization of OEGMA and OEGMA-N_3. The azide-functionalized monomer allowed further modification of the resulting polymer. The polymer coat increased the diameter of the VLP from 14 nm to approximately 24 nm. To show

potential applications of the protein–polymer conjugate, poly(OEGMA-N_3) on the VLP was modified by click chemistry with gadolinium chelating groups (Gd-DOTA). The resulting bacteriophage Q β –poly(OEGMA-Gd-DOTA) could be used as a magnetic resonance imaging (MRI) contrast agent. Its high loading capacity gave better contrast than established contrast agents. In addition, a doxorubicin (Dox) derivative that contained an alkyne group for click reactions and a hydrazine moiety for acidic cleavage was bound to Q β –poly(OEGMA-N_3) with the aim of using the hybrid particle as a pH-responsive anti-cancer drug. The Dox-carrying protein–polymer conjugate had a similar cytotoxicity on HeLa cells to free Dox, which proves its anti-cancer activity. Further studies could explore the VLP–polymer conjugate for imaging applications and targeted drug delivery.

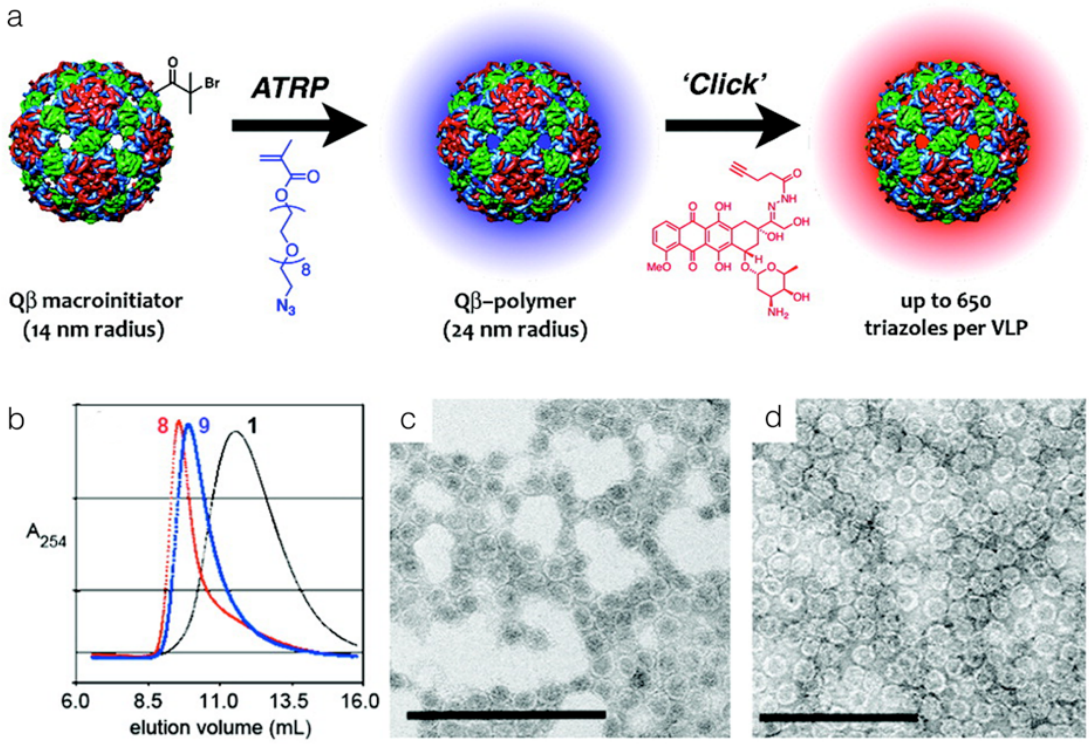

Figure 1.2.3. Polymerization on the exterior of bacteriophage Qβ bacteriophage and the characterization of the conjugates. (a) Schematic view of grafting-from ATRP on the exterior of bacteriophage Qβ and post-attachment of doxorubicin onto the polymer chains. Characterization of conjugates: (b) Size exclusion chromatographs of Qβ VLP (1), Qβ VLP with poly(OEGMA) (8) and Qβ VLP with poly(OEGMA-N_3) (9). (c) and (d) Transmission electron micrographs of (8) and (9). Scale bar is 200 nm. Adapted with permission from [285]. Copyright © 2011 American Chemical Society

While PEGylation with PEG or with poly(OEGMA) remains the most popular method to modify proteins and protein cages with polymers on their outside, it has some disadvantages.[155] PEGylated particles sometimes experience lower uptake by targeted cells.[303,304] In addition, recent studies indicate that the immune system can recognize PEG, as evidenced by the discovery of anti-PEG antibodies.[305] This can result in an enhanced clearance of PEGylated particles and raises concerns about their immunogenicity.[306] Moreover, chemical modifications are mostly restricted to the chain ends of PEG due to the nature of its polymerization. To overcome these drawbacks of PEGylation, other polymers have been bound to the exterior surface of protein cages. Poly(2-alkyl-2-oxazolines) (POX) are considered to be good alternatives to PEG.[307] The properties of poly(2-alkyl-2-oxazolines) make them suitable for biomedical applications.[308,309] They can be synthesized in a well-defined manner by living cationic polymerizations, their chemical composition and properties can be easily adjusted during synthesis, e.g. by selecting the hydrophilic 2-methyl-2-oxazoline or the less polar 2-ethyl-2-oxazoline. Moreover, copolymerizations with functionalized oxazolines can introduce functional groups into the polymer. Finn and co-workers bound poly(2-alkyl-2-oxazolines) on the surface of the bacteriophage Qβ by single-point attachment, and via multiple points, using copper-catalysed azide–alkyne cycloaddition click chemistry (Figure 1.2.4a).[310] For single-point attachment, propargyl-poly(2-methyl-2-oxazoline) or propargyl-poly(2-ethyl-2-oxazoline) were synthesized that featured a single alkyne at the chain terminus. For multiple-point attachments, copolymers of 2-methyl-2-oxazoline or 2-ethyl-2-oxazoline, and 2-(pent-4-ynyl)-2-oxazoline were prepared. The polymers were furthermore end-functionalized with an amine group to attach targeting molecules or fluorescent dyes to the polymer chains. The surface-exposed amines of the VLP were derivatized with azido-*N*-hydroxysuccinimide ester and the polymers were conjugated to these functional groups. With an increasing ratio between polyoxazolines and Qβ, the diameter of the protein–polymer conjugates increased from 27 nm (no polymer) to a maximum of approximately 38 nm, i.e. a polymer shell of up to 5 nm thickness formed around the protein particle. Multi-point attachment of polymers increased the thermal stability of the protein cage to more than 100 °C, while VLPs that had polymer chains attached at single points disassembled into protein subunits. Unmodified VLPs unfolded at these temperatures (Figure 1.2.4b). These results indicate that cross-linking of the protein subunits by

polymer chains stabilized the assembly of subunits. The protein–polymer core–shell particles could be of interest in materials and biological applications if heat-resistant protein cages are desired. It remains to be elucidated, however, if the modification with poly(2-alkyl-2-oxazoline) increases the biocompatibility of the protein cage and how this modification compares with PEGylated VLPs.

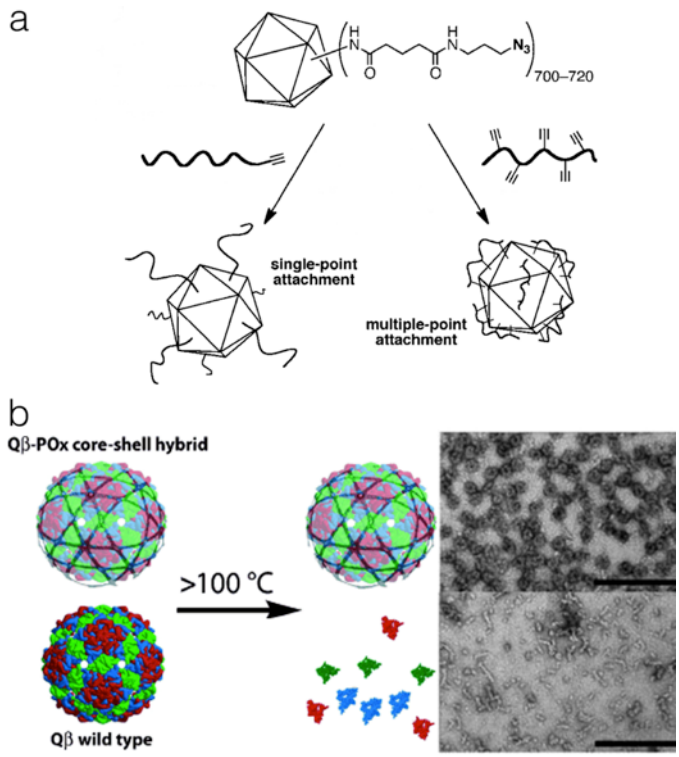

Figure 1.2.4. Different strategies of polymer attachment to Qβ bacteriophage. (a) Schematic view of single-point and multiple-point attachment of oxazoline polymers on the exterior of Qβ bacteriophage. (b) By attaching poly(oxazolines) via multiple-point attachment, the cage structure remains stable upon heating above 100 °C, while the Qβ VLPs without multiple-point attached polymers were disrupted. Left side: Comic representation of the description. Right side: TEM image of intact and stabilized Qβ bacteriophage (top). TEM image of disrupted Qβ protein cages (bottom). Scale bars are 200 nm. Adapted with permission from [310]. Copyright © 2011 WILEY-VCH Verlag GmbH and Co. KGaA, Weinheim.

Poly(*N*-isopropylacrylamide) (PNIPAAm) is the most commonly used temperature-responsive polymer in biomedical research.[311,312] It has a lower critical solution temperature (LCST) of 32 °C,[312,313] i.e. it transforms from a water-soluble polymer at room temperature to a water-insoluble polymer at body temperature. This is a useful property for many drug-delivery applications. Maynard and co-workers synthesized PNIPAAm with a cysteine reactive pyridyl-disulfide group at one polymer chain end and a dansyl group for UV–vis spectroscopic analytical purposes on the other chain end by RAFT polymerization (Figure 1.2.5). This polymer was grafted to the surface

of a cysteine-rich variant of the vault protein cage to create temperature-responsive polymer–protein cage conjugates.[314] The LCST of the hybrid was 35.9 °C, whereas the unmodified vault had no LCST. Heating the conjugate to 40 °C resulted in the formation of micrometre-sized aggregates. The aggregation was reversible. Upon cooling, the aggregates redissolved completely. Moreover, the protein structure stayed intact during the heating and cooling process. This heat-responsive vault–PNIPAAm conjugate could find application in cancer treatment. Local heating of cancer tissue could cause the conjugate to agglomerate and concentrate in cancer tissue, to release therapeutic cargo locally from the vault.[315,316]

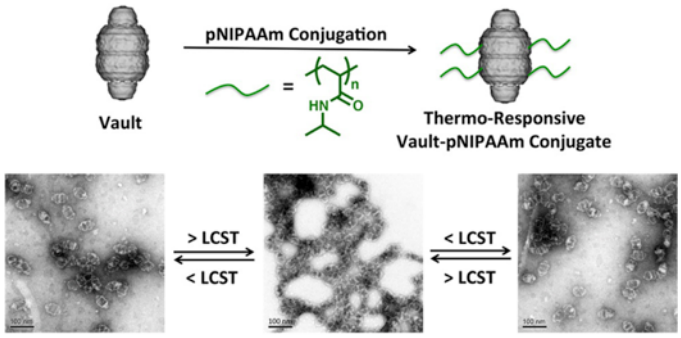

Figure 1.2.5. Schematic depiction of vaults that were modified with the thermoresponsive polymer PNIPAAm and TEM images showing the reversible aggregation of vault–PNIPAAm conjugates. Scale bar is 100 nm. Adapted with permission from [314]. Copyright © 2013, American Chemical Society.

Copolymers of NIPAAm and the UV-cross-linkable monomer 2-(dimethyl maleinimido)-*N*-ethyl-acrylamide (DMIAAm) were synthesized on the exterior surface of horse spleen ferritin.[317] The protein cage was modified with ATRP initiator on the exterior via coupling of 2-bromo-isobutyric acid NHS ester to primary amines. NIPAAm and DMIAAm were randomly copolymerized under ATRP conditions in H_2O:DMF (5:1, v:v) at 4 °C with CuBr and Me_6TREN as catalyst. The ferritin–PNIPAAm-*co*-poly(DMIAAm) conjugate had a phase transition temperature at 32 °C.[312,313] At this temperature, the conjugate precipitated from aqueous solution and the solution became turbid. Dynamic light scattering confirmed a reduction of the hydrodynamic radius of the conjugates from 30 nm at 20 °C to 12 nm at 32 °C. Further increase of the temperature resulted in an increase in hydrodynamic radius due to the formation of aggregates of the collapsed conjugates. The ferritin–polymer conjugate was able to stabilize oil-in-water emulsions. UV-cross-linking of ferritin–polymer conjugates at the oil–water interface

of emulsion droplets led to capsules with an average size of 10 ± 3 μm. Addition of ethanol homogenized the oil-in-water emulsion, but the capsules of cross-linked ferritin–polymer conjugates remained stable. The high stability of the capsules allowed transferring them into solvent of the same polarity as the fluid droplet they were formed on.[176] By starting from oil-in-water and from water-in-oil emulsions, it was therefore possible to create microcontainers that encapsulated hydrophilic compounds in a hydrophilic environment and hydrophobic compounds in a hydrophobic solvent.[176] Extrusion of an emulsion, stabilized by ferritin–polymer conjugates, through a track-etch membrane and subsequent UV irradiation allowed the production of networks of capsule-containing fibres, capsule assemblies and single capsules.[177] The capsules of cross-linked ferritin–polymer conjugates and the macroscopic materials made thereof could find applications as substrates for cell cultivation or as delivery systems, e.g. in cosmetics. Whether the protein remained in its native conformation was, however, not investigated in great detail.[318]

The chemical diversity of polymers extends well beyond 'classic' polymers such as PEG, POX, polymethacrylates and polyacrylamides. Tailor-made polymers with functional groups in their main chain and in their side chains can add another level of functionality. Kim et al. modified Adv with a biodegradable poly(disulfide amine) on which arginine was grafted (ABP–polymer) (Figure 1.2.6).[161] In addition to the biodegradable backbone, the polymer featured primary amines in its side chains. It was designed to enhance the protein's cellular uptake through electrostatic interactions and at the same time to minimize the immune response to the virus. Two types of Adv were used in this study: Adv that delivered genes for the expression of green fluorescent protein (GFP), and YKL-1001, an oncolytic, hepatoma-targeting Adv that kills only these cells. GFP expression was approximately threefold higher with ABP-modified Adv compared with unmodified Adv. The best GFP expression was achieved with an Adv:ABP ratio of 1:5. GFP expression was reduced at a higher Adv:ABP ratio (1:10), most likely because the larger number of positive charges interfered with the Adv infection pathways following cell binding. The higher charge density could also increase cell death, as known from other cationic polymers,[319]which could also contribute to the observed lower GFP expression.[319] Oncologic YKL-1001 with conjugated ABP–polymers remained longer in blood circulation and caused an increased hepatoma cell death compared with unmodified YKL-1001. The latter is in good agreement with the higher transduction efficiency

caused by the ABP–polymer. Concluding, the Adv–polymer conjugate could become a powerful gene delivery vector in oncological therapy because of its higher efficiency compared with unconjugated virus particles.

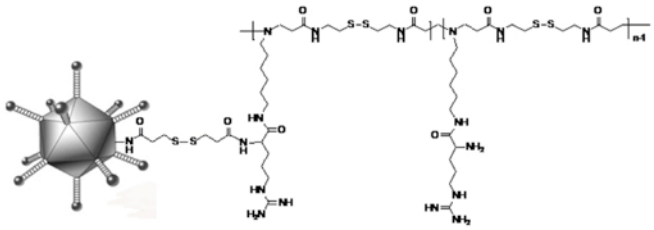

Figure 1.2.6. Schematic view of Adv–ABP–polymer conjugate. The ABP–polymer contained bioreducible disulfide bonds for cleavage and primary amines to promote cellular uptake. Adapted with permission from [161]. Copyright © 2011, Elsevier Ltd.

Another approach to coat Adv with polymers containing primary amines was reported by Ramsey and co-workers.[320] Adv was complexed with synthetic polymers used in gene delivery to allow for cellular uptake into cells that lack the receptors for Adv. To this end, linear and branched polyethyleneimine (PEI) and poly(ethylene glycol)-grafted polyethyleneimine (PEG-g-PEI) were non-covalently bound to the viral capsid by electrostatic interactions. The PEI was modified with PEG to overcome the intrinsic toxicity and other drawbacks associated with pure PEI.[321,322] Indeed, the complexes of Adv and PEG-g-PEI polymer were less toxic than Adv modified with pure PEI, as was shown by cytotoxicity assays. The polymer–Adv complexes were able to shuttle their cargo into CAR-negative NIH 3T3 cells, which Adv alone cannot infect. Gene transduction efficiency was slightly better for Adv with PEG-g-PEI polymers compared with Adv complexed with plain PEI. PEG-g-PEI copolymers composed of linear PEI showed a better performance than those made from branched PEI.

Later, Adv was also complexed with PEI by Yao et al. with variation of the polymer to protein ratio.[165] They managed to create Adv–PEI particles that showed no cytotoxicity under the investigated conditions and an enhanced cell uptake by mesenchymal stem cells compared with unmodified Adv.

Lyophilized proteins are usually solid materials. However, modification of proteins with polymers allows alteration of their state of matter. Mann and co-workers tuned the surface of ferritin with a polymer surfactant and were able create protein liquids, i.e. solvent-free protein melts.[175] The polymer chains were attached to ferritin via

electrostatic interactions (Figure 1.2.7a). Ferritin was first cationized on its surface by binding *N*,*N*-dimethyl-1,3-propanediamine to surface-exposed carboxylic acid groups via *N*-(3-dimethylaminopropyl)-*N*-ethylcarbodiimide hydrochloride (EDC) coupling. Then, the anionic polymer poly(ethylene glycol)-4-nonylphenyl 3-sulfopropyl ether was complexed with the cationized ferritin. Lyophilization (Figure 1.2.7b) and subsequent annealing at 50 °C yielded a red viscous liquid that remained liquid after cooling to room temperature (Figure 1.2.7c). Transmission electron microscopy (TEM) indicated that the protein cage retained its structure in this liquid. This report opened the door to a new class of protein materials with a huge potential in bionanomaterials research.[171] For example, protein liquids represent a very concentrated form for the storage, handling and modification of proteins.

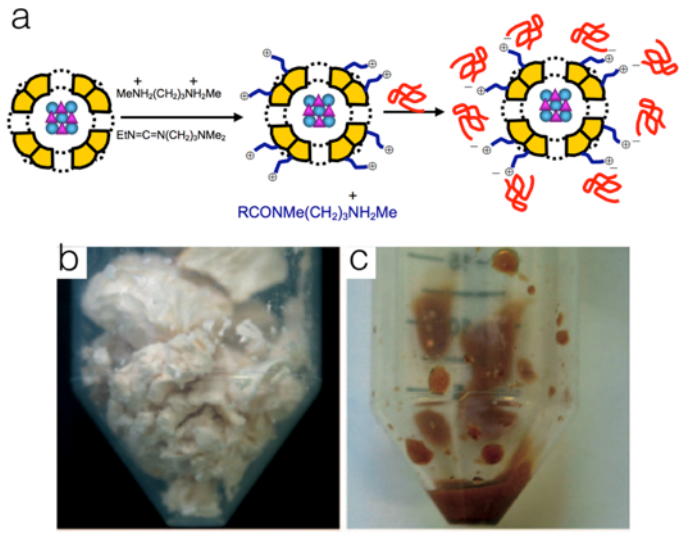

Figure 1.2.7. Modification of ferritin resulted in liquid proteins. (a) Preparation of a protein liquid by cationization of ferritin and electrostatic binding of anionic polymers to the external surface of the protein cage. (b) Lyophilized mixture of cationized ferritin and the anionic polymer. (c) After annealing at 50 °C, the mixture formed a viscous liquid. It remained liquid even after cooling to room temperature. Adapted with permission from [175]. Copyright © 2009, Wiley-VCH Verlag GmbH and Co. KGaA, Weinheim.

1.4.4 Polymer cages as functional additives in polymeric materials

Protein cages are robust biological nanoparticles that have a variety of properties that are difficult or impossible to achieve with synthetic nanocapsules. Therefore, protein cages were incorporated into synthetic polymeric materials with the aim to create functional hybrid materials.

Self-reporting (or self-sensing) materials can autonomously report micron-scale damage and have therefore high potential as safety features in load-bearing components in the aerospace, automotive, construction and medical materials sectors. Self-reporting materials were achieved by incorporating force-responsive molecules or nanostructures into polymeric materials that cause a change in colour, fluorescence or electrical conductivity when being deformed.[323,324] The well-defined three-dimensional (3-D) structure of biological macromolecules results in well-defined mechanical deformation pathways. Thus, they can be used as force and strain sensors if they are intrinsically fluorescent or when combined with fluorescent markers.[325-327] The first protein that was used to create self-reporting materials was the protein cage THS (Figure 1.2.8d).[166,328] It encapsulated a pair of fluorescent proteins and served as a scaffold to bring enhanced cyan fluorescent protein (eCFP) and enhanced yellow fluorescent protein (eYFP) into proximity for fluorescence resonance energy transfer (FRET) (Figure 1.2.8a-c). Moreover, the equatorial plane of chaperonins is mechanically weak, which allows separating the two hemispheres from each other.[329] Lysine residues on the THS were modified with acrylamide groups so that the protein could be copolymerized with acrylamide and bis-acrylamide in aqueous solution to form a gel. Upon drying, optically transparent and brittle specimens were obtained. Uniaxial deformation of these materials resulted in the formation of microcracks and fracture of the material. Fluorescence microscopy of the area surrounding the fracture face revealed an increased FRET efficiency in the vicinity of cracks, which was additionally confirmed by fluorescence lifetime imaging (FLIM) (Figure 1.2.8e). Most likely, polymerization and sample drying caused internal stress in the polymers that deformed the protein cage, increased the distance between the encapsulated fluorescent proteins and therefore lowered FRET. Crack formation allowed the polymer and the protein cage to relax, thus leading to the observed increase in FRET. The system proved that the structure and mechanical response of protein cages can be exploited to engineer polymer–protein hybrid materials with advanced functionalities.

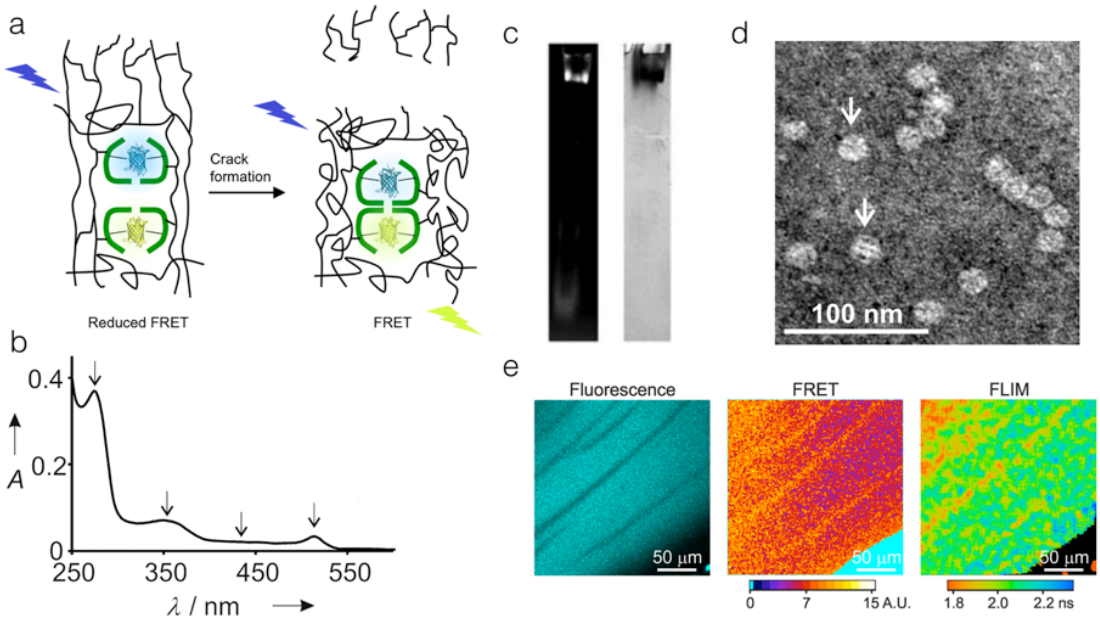

Figure 1.2.8. Integration of a protein cage that encapsulated fluorescent proteins into a polymer matrix yields materials with self-reporting functionality. (a) Schematic depiction of the chaperonin THS (green lines) with a FRET pair of fluorescent proteins embedded into a polymer matrix. Damage in the polymer results in relaxation of the polymer matrix and of the disturbed THS, leading to an increased FRET signal. (b) UV–vis spectrum of the THS–eCFP/eYFP conjugate in solution: the arrows indicate the absorption due to eYFP (513 nm), eCFP (439 nm), bisaryl hydrazone linker between THS and the fluorescent proteins (354 nm) and of all proteins (276 nm). (c) Native PAGE of the conjugate showing that fluorescent proteins are encapsulated in the THS (left: gel imaged in fluorescence mode; right: Coomassie Brilliant Blue stained gel). (d) TEM image of the conjugate with particles in top (top arrow) and side view (lower arrow). (e) Microscopy images of self-reporting PAAm-THS-eCFP/eYFP hybrid materials after uniaxial deformation and fracture (blue fluorescence channel, FRET and FLIM). Adapted with permission from [166]. Copyright © 2009, Wiley-VCH Verlag GmbH and Co. KGaA, Weinheim.

Functional hybrid nanofibres can be prepared by electrospinning of polymer–protein solutions. For the application of such fibres, e.g. in nanotechnology[330] or drug delivery,[331,332] it is important to know if the incorporated biological compounds survive the fabrication procedure of the material. In a study conducted by Zussman and co-workers, bacterial viruses (T4, T7 and bacteriophage λ) and bacteria were encapsulated into hydrophilic poly(vinyl alcohol) (PVA) nanofibres.[333] The electrospinning process, which was used for nanofibre fabrication, reduced the viability of the incorporated viruses to 1–6% of the value before electrospinning, most likely because the tails of the bacteriophages could not withstand the high shear forces during spinning. Nevertheless, a portion of the viruses remained biologically active and retained this activity during storage for three months at –20 °C and –55

°C. This finding let the authors conclude that the electrospinning process is suitable for fabrication of nanofibres in which biological material is integrated. Protein cages can enhance the mechanical properties of electrospun nanofibres. Lee and co-workers incorporated ferritin into PVA nanofibres.[334] The protein cage was homogeneously distributed within the fibre. Ferritin interacted with PVA through hydrogen-bond formation between the hydroxyl group of the polymer and amine and carboxyl groups of the protein, resulting in a twofold increased elastic modulus compared with pure PVA nanofibres, as determined by atomic force microscopy (AFM). Electrospinning of hydrophilic polymers can be used to prepare mats of nanofibres that are highly porous hydrogels. Hybrid ferritin–PVA nanofibre hydrogels showed fast water absorption and had good mechanical properties.[173] The strength of swollen ferritin–PVA hydrogels increased by 113%, the strain at break by 227% and the elastic modulus by 151% compared with wet PVA gels that lacked ferritin. According to the authors, the mechanical properties were even better than those of PVA hydrogels reinforced with carbon nanotubes. Hydrogels with incorporated apoferritin instead of ferritin had a similar modulus but lower strength and strain at break than ferritin–PVA hydrogels. Thus, the iron core of ferritin is an important factor for the reinforcement of these hybrid materials.[333,335] Incorporation of ferritin into a nanofibre hydrogel results in biocompatible and degradable materials with superparamagnetic properties that give good contrast in MRI. The advantage of using ferritin, compared with synthetic contrast agents, is that it does not pose toxicity risks. [336] 3-D porous nanofibre hydrogels were fabricated by electrospinning of ferritin–PVA solutions.[173] Elevated temperatures (e.g. 80 °C) during mixing of the spinning solution were used to denature partially the protein cage so that clusters of ferritin formed. Nanofibres with these clusters had enhanced superparamagnetic properties and the fibre hydrogels showed a high contrast in in vitro and in vivo imaging. In addition to the application as MRI contrast agent, ferritin-containing hydrogels have also been applied as an actuator towards the development of artificial muscles.[168] Electrospun ferritin–PVA and PVA nanofibre hydrogels reversibly expanded and contracted when the pH was cycled between pH 4 and pH 9. In contrast, bulk PVA hydrogels do not show this pH-dependent swelling, indicating that the electrospinning process causes the formation of ionizable functional groups on the polymer. The pH-induced volume change of the electrospun hydrogels was independent of the presence of ferritin. However, ferritin–PVA

hydrogels did not show creep-induced elongation during several extension and contraction cycles, while the PVA hydrogels gradually increased in length after each cycle. Ferritin reinforced the PVA matrix by hydrogen-bond interactions, resulting in the superior mechanical properties of the polymer–protein hybrid material. Lack of creep is a very important property for artificial muscle development, rendering the ferritin–PVA hydrogels interesting candidates for this kind of application.

Kim and co-workers followed a similar electrospinning approach for the fabrication of ferritin-containing nanofibres (Figure 1.2.9).[335] Instead of PVA as the polymer, they used the polyelectrolyte poly(2-acrylamino-2-methyl-1-propane sulfonic acid) (PAMPS). However, ferritin precipitated in PAMPS solution, so that glycerol had to be used as a stabilizer for the protein cage. Coaxial electrospinning of a PAMPS and a ferritin–glycerol solution allowed fabrication of very thin (<50 nm) nanofibres in which ferritin formed the core. Such nanofibres have potential in applications ranging from batteries to biosensors and nanoelectronics.[335]

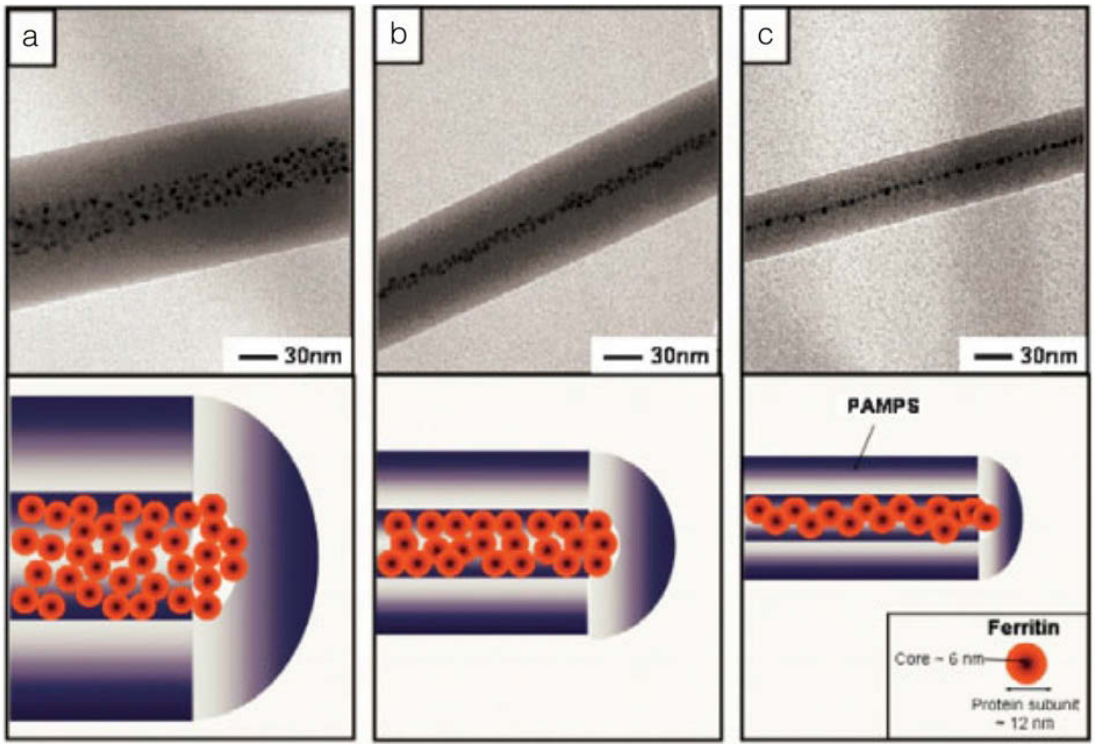

Figure 1.2.9. The integration of ferritin into PAMPS fibers. Top panels (a) – (c) Transmission electron microscopy (TEM) of PAMPS fibers with different widths and incorporated ferritins in the fiber core. Bottom panels (a) – (c) Schematic representation of the ferritin distribution in the core of the PAMPS fibres in dependence of the fibre width. Adapted with permission from.[335] Copyright © 2008, WILEY-VCH Verlag & Co. KGaA, Weinheim.

Carbon nanotubes (CNTs) are known to enhance the mechanical strength of polymeric materials.[337,338] However, it can be difficult to disperse them homogeneously into a polymer. Moreover, low interfacial adhesion between the polymer and CNTs can reduce the performance of the materials. Saboungi and co-workers addressed these problems by covalently attaching ferritin to the sidewalls of CNTs.[339] The carbon–protein hybrids could be homogeneously incorporated into a hydrophilic PVA matrix that was cast into free-standing composite films. The protein significantly enhanced the mechanical properties of the material. Compared with pure PVA, an increase of 108% in the storage modulus was measured.[339]

PVA, PAMPS and PAAm are water-soluble polymers and therefore mix readily with protein cages. For many applications it would be desirable, however, to use hydrophobic polymers that can be cast from organic solvents. PEGylation is a means to render viruses and non-viral protein cages soluble in non-aqueous media.[13,295] TMV was modified with PEG of a molar mass of 2×10^3 g mol^{-1}.[13] The resulting capsid–polymer conjugates dissolved in chloroform, while the unmodified virus was not soluble. TMV solubilized in organic solvents had a markedly increased thermal stability of at least 160 °C compared with PEGylated TMV in water. The organo-soluble virus was cast into polystyrene, opening a route to solid polymer–protein hybrid materials.[340] While TMV is, strictly speaking, not a protein cage in the sense of this review, it is easy to envision that similar strategies could be applied to solubilize protein cages in non-aqueous media. Indeed, ferritin was modified with 750 g mol^{-1} PEG chains on the exterior carboxylic acid groups.[295] The modified ferritin was soluble in dichloromethane, whereas the unmodified protein cage was not. In addition, ferritin was also alkylated on the exterior (C_9 to C_{14} chains coupled to primary amines).[341] Both types of modified ferritin were incorporated into a polymer blend of PEG and a hydrophobic poly(desaminotyrosyl tyrosine dodecyl ester carbonate) (PDTD).[295] The PEGylated ferritin accumulated in the PEG polymer of the blend due to PEG–PEG interactions, while the alkylated ferritins accumulated in PDTD.[295] Therefore, it is possible to direct the location of a protein cage in a phase-separated material by carefully selecting the type of protein modification. Organo-soluble protein–polymer conjugates can alter the morphology of block copolymer films, as shown by the interaction of PEGylated ferritin with poly(2-vinylpyridine)-*block*-poly(ethylene oxide) block copolymers (P2VP-*b*-PEO).[174] The P2VP-*b*-PEO film had a microphase separated lamellar structure with the lamella

oriented parallel to the surface. When ferritin–PEG was added, it interacted with the PEO domains of the block copolymer and prevented their crystallization. As a result, the microdomains reoriented perpendicular to the surface. In another study, the distribution of PEGylated ferritin in thin films of the block copolymer polystyrene-*block*-poly(ethylene oxide) (PS-*b*-PEO) was investigated.[159] PS-*b*-PEO self-assembled into structures in which the PEO blocks form cylinders that were oriented perpendicular to the surface. Ferritin–PEG accumulated in the PEO cylinders. Different PEG chain lengths on ferritin changed the centre-to-centre distance between the PEO cylindrical domains.

Another potential application of organo-soluble protein cages would be their use as nanoreactors for reactions in non-aqueous media.[342] Although this is an intriguing possibility to influence, e.g. the selectivity of chemical reactions, the use of nanoscale protein-based reaction compartments in hydrophobic media has not yet been reported.

The presented examples show strategies to incorporate protein cages into polymeric materials and highlight some interesting properties of the resulting hybrid materials. However, many of the intriguing functionalities of protein cages, such as their ability to encapsulate and release guests, the electronic and magnetic properties of ferritin derivatives and the intrinsic ability of protein cages to self-assemble into 2-D or 3-D arrays have not yet been exploited to create functional polymer–protein hybrid materials. Thus, opportunities for innovation are plentiful.

1.4.5 Protein cages adsorbed to polymer surfaces

Most polymeric materials, when brought into contact with a solution of proteins, will adsorb some of the biomacromolecules at their surface. The investigation of this phenomenon is important, e.g. for medical device development, as adsorbed protein layers determine the biological response towards the material.[343] Ferritin is a good model protein for such studies because it is very stable and easily imaged by TEM. The protein cage was adsorbed on a phase-separated blend of PDTD and poly(ε -caprolactone) (PCL).[344] Both polymers have been studied for medical applications.[345] At physiological pH, native ferritin adsorbed mainly on the hydrophobic PDTD areas. Ferritin and partially hydrolysed PCL are both negatively charged at this pH, so that the protein is repelled from PCL domains. At pH 3.5, i.e. below the isoelectric

point of ferritin, it adsorbed equally well on both polymers.[167] To understand the influence of protein modification on its adsorption behaviour, the carboxylic groups of ferritin were alkylated with dodecylamine.[167] As a result, the alkylated ferritin was positively charged at pH 5.8, in contrast to native ferritin, which was negatively charged at this pH. Alkylated ferritin adsorbed on the PCL phase of the blend due to positive charges, while the native ferritin mainly adsorbed on the PDTD phase. Selective adsorption of ferritin on a polymer was also observed on thin films of polystyrene-*block*-poly(methyl methacrylate) block copolymers (PS-*b*-PMMA).[169] The polymer film was treated with UV light and acetic acid, which etched the PMMA domains. As a result, trenches and ridges were created on the material. Ferritin adsorbed on the PS domains and not on PMMA. This was due to the repulsion between the negative charges of ferritin and the negative charges of edged PMMA. These studies show that protein adsorption is governed by an intricate interplay between the surface properties of the material and of the protein. Moreover, they identify polymer morphology as a very important parameter in biomaterial development because it can influence the distribution of a protein layer on a surface and therefore affect the behaviour of a polymeric material in a biological environment.

1.4.6 Protein cages that encapsulate polymers

1.4.6.1 General considerations

Because of their hollow structure, protein cages can encapsulate a variety of guests, including polymers. These macromolecules can be either synthesized directly in the cavity of a protein cage or preformed polymers can be incorporated into cages during self-assembly or through large pores. If the polymers are homogeneously distributed within the cavity of the protein cage, core–shell particles with a polymer core and a protein shell are obtained. The polymer core can be a cross-linked polymer network, a dense polymer particle or a solution of polymer. If the polymers strongly interact with the protein's inner surface or if short polymer chains are attached to it, the synthetic macromolecule will form a layer that coats the inner surface of the protein cage. The resulting structure is a hollow nanoparticle with a protein–polymer hybrid shell.

The strength of interaction between protein and polymer can be adjusted by the choice of polymer and by engineering the inner protein surface. This allows tailoring the inner structure of protein cage–polymer hybrids. While such an approach is already state-of-the-art for other hollow nanoobjects, such as polymer-filled lipid vesicles,[346] deliberate tuning of the inner structure of polymer-filled protein cages has not been addressed yet. Another interesting challenge for future research could be to prepare stimuli-responsive hybrid particles that transform from a capsule-like structure with the polymer lining the cavity to a structure where the polymer is homogeneously distributed throughout the cavity. This could result in new approaches for the triggered release of therapeutic cargo from protein cages

1.4.6.2 Non-covalent encapsulation of polymers in protein cages: Tuning the size and morphology virus-like particles with polyanionic polymers

Because viruses are protein cages that encapsulate RNA, i.e. a natural macromolecule with anionic phosphate backbone, it is not surprising that successful attempts were made to replace nucleic acids with a synthetic polyanionic polymer. Already in the 1960s, Hohn used poly(vinyl sulfate) to assemble protein subunits of the bacteriophage fr,[347] while Bancroft et al. reassembled CCMV, BMV and BBMV around poly(vinyl sulfate) and dextran sulfate.[348] Their results proved that the phosphate backbone of nucleic acids is not required for the assembly of viral coat proteins into virus-like structures. Both groups also observed that the reassembled particles varied in size, giving a first indication that the structure of reassembled VLPs is influenced by the polyanion. However, detailed studies on the interplay of synthetic polymers and VLPs were only reported in more recent times, pioneered by a study by Douglas and Young. They encapsulated the anionic polymer poly(anetholesulfonic acid) into CCMV.[197] To this end, CCMV at pH 7.5, i.e. in its swollen state, was incubated with the polymer. The pH was lowered to 4.5, which caused a deswelling of CCMV, closed the pores in the protein shell and entrapped the polymer into the viral capsid. In a control experiment, CCMV was incubated with the polymer at pH 4.5 resulting in no encapsulation.

The interior cavity surface of many viral capsids is highly positively charged, while the outer surface of the proteins carries a smaller number of charged residues. Thus, electrostatic interactions with polyanions favour their inclusion into the assembling protein cage. Moreover, the attraction of oppositely charged residues facilitates and

directs the self-assembly of VLPs. Thus, particles that differ from the wild-type capsids in their shape, size and number of subunits can be prepared when using synthetic polymers as scaffold. Cornelissen and co-workers found that poly(styrene sulfonate) (PSS) with a molar mass of 9.9×10^3 g mol^{-1} induces the formation of monodisperse icosahedral CCMV VLPs with a diameter of 16 nm ($T = 1$). At a pH of 7.5, the wild-type virus has a diameter of 28 nm ($T = 3$ particle).[196,197,349] Therefore, under these conditions the polymer causes the formation of VLPs that are smaller than the native capsid.

Knobler and co-workers investigated the influence of different PSS chain lengths on the formation of CCMV VLPs at pH 4.8 (Figure 1.2.10a).[157,350] Polymers with a molar mass of 3.8×10^4 g mol^{-1} are small enough to pack more than one chain into VLPs. Reassembly of the viral coat proteins around PSS with a molar mass of 3.8×10^4 g mol^{-1} resulted in VLPs with a bimodal size distribution.[350] By using a fluorescently labelled polymer, the number of polymer chains per particle could be determined. VLPs with a size of approximately 19 nm ($T = 1$ structure) encapsulated two chains, whereas VLPs with a diameter of 21 nm ($T = 2$ structure) incorporated three polymers. PSS that had a comparable size or were larger than the capsid resulted in the formation of larger VLPs.[157] PSS with a molar mass between 4×10^5 g mol^{-1} and 1×10^6 g mol^{-1} yielded VLPs with a diameter of 22–23 nm ($T = 2$ particles) (Figure 1.2.10b+c, left diagram), whereas polymers with a molar mass between 2×10^6 g mol^{-1} and 3.4×10^6 g mol^{-1} induced the formation of VLPs with a diameter of 27–28 nm ($T = 3$ particles) (Figure 1.2.10b, right diagram). Thus, the virion adapted to the size of the encapsulated cargo. Larger polymers resulted in larger VLPs. A direct comparison of these results to the assembly into $T = 1$ particles reported by Cornelissen[349] is difficult because assembly was carried out at a different pH and the viral coat proteins differed in their N-terminus.

a

Properties of PSS used in packaging experiments

Reaction	Mol. mass (kDa)	Polydispersity index*	Hydrodynamic radius† (nm)
1	408	1.24	18.3
2	691	1.16	25.0
3	1010	1.18	32.6
4	2040	1.07	36.6
5	3441	1.01	42.8

*Polydispersity index data were supplied by Scientific Polymer Products.
†Hydrodynamic radii of PSS were measured by dynamic light scattering in the viral assembly buffer.

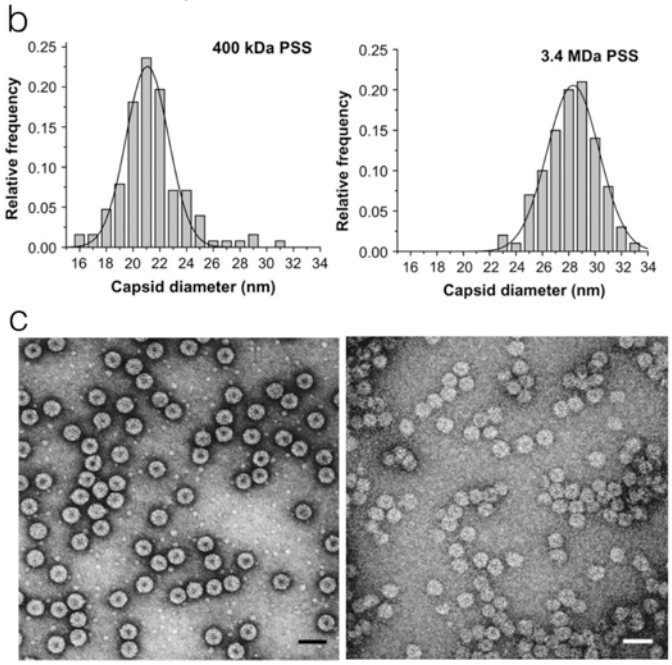

Figure 1.2.10. CCMV size modulation using PSS with different molecular weights.(a) Table of VLP size distributions with various PSS that were applied for the formation of CCMV VLPs. (b) Normalized capsid size distribution histograms showing the influence of polymer chain length on VLP size. Left diagram: CCMV that was assembled with 4×10^5 g mol^{-1} PSS. Right diagram: CCMV that was assembled with 3.4×10^6 g mol^{-1} PSS. (c) Left image: TEM image showing wild-type (wt) CCMV capsids. Right image: TEM image showing CCMV VLPs that were assembled with 3.4×10^6 g mol^{-1} PSS. Scale bars are 50 nm. Adapted with permission from [157]. Copyright © 2008, The Biophysical Society.

Polymers can control not only the size, but also the shape of VLPs. Icosahedral VLPs form when CCMV coat proteins assemble around flexible polyanionic polymers such as single-stranded RNA[351,352], a combination of RNA and DNA[353] or PSS.[157,349,350] However, rigid dsDNA induces the formation of rod-shaped structures.[354] These different VLP morphologies can be selectively accessed by a single type of polymer if it is possible to switch the polymer between a condensed coil and a more expanded conformation.[355] The water-soluble, fluorescent and semiconducting poly(2-methoxy-5-propyloxy sulfonate phenylene vinylene) (MPS–PPV) adapts a coiled and aggregated conformation in aqueous solutions of high ionic strength due to counter-

ion condensation, whereas at low ionic strength the coils expand.[356] In the absence of NaCl, the interplay between MPS–PPV and CCMV coat proteins causes the formation of rod-shaped VLPs (Figure 1.2.11a).[355] Addition of 0.1 M NaCl to the self-assembly buffer resulted in a mixture of spherical and rod-like structures. At 1.0 M NaCl, mostly spherical VLPs were observed (Figure 1.2.11b). Control experiments with PSS as scaffold resulted in spherical structures, independent of the ionic strength of the solution. These results suggest that it is not the ionic strength per se that is responsible for different VLP structures, but rather that the conformation of the polymer dictates the shape of the VLP. Moreover, the protein cage also influences the properties of the polymer. The fluorescent properties of semiconducting polymers such as MPS–PPV depend on the polymer's chain conformation. In the spherical VLPS the polymer is encapsulated as a coil, resulting in blue fluorescence. Rod-shaped VLPs stretch the polymer chains. This leads to a red-shift in fluorescence.

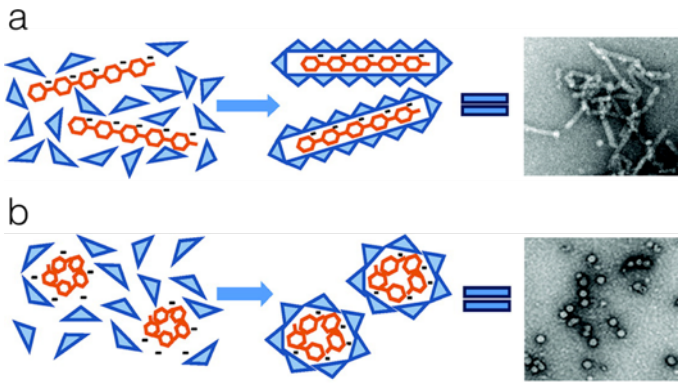

Figure 1.2.11. The concentration of NaCl in the presence of an anionic polymer can influence the morphology of CCMV VLPs. (a) Rod-shaped VLPs were formed in the presence of MPS–PPV without NaCl. Left panel: schematic representation of rod-shaped VLP formation. Right panel: TEM image of rod-shaped CCMV VLPs. (b) Spherical VLPs were formed in the presence of MPS–PPV at 1.0 M NaCl. Left panel: schematic representation of spherical VLP formation. Right panel: TEM image of spherical CCMV VLPs. Adapted with permission from [355]. Copyright © 2011 American Chemical Society.

Polyanionic polymers such as PSS can be used to promote self-assembly of PEGylated CCMV coat proteins.[292] The resulting VLPs encapsulate a synthetic polymer and carry another type of polymer on their outside. PEG was selectively conjugated to the outside surface of coat proteins by reacting fully assembled RNA-containing viral capsids with NHS-ester PEG. PEGylation caused the virus to disassemble slowly, probably because the polymer disrupted interactions between

protein subunits. Disassembly was irreversible unless PSS was added to the protein solution. After removal of the RNA, PSS with a molar mass of 7×10^5 g mol^{-1} yielded fully assembled $T = 1$ particles with an average diameter of 18 nm (Figure 1.2.12). In conclusion, the presence of PSS in the interior of the VLP renders it robust enough to overcome the destabilization by PEG. The method paves the way for multifunctional VLPs, as both the polymer on the outside of the capsid and the polymer on its inside could be designed to feature functional groups, such as targeting ligands and chelators for contrast agents.

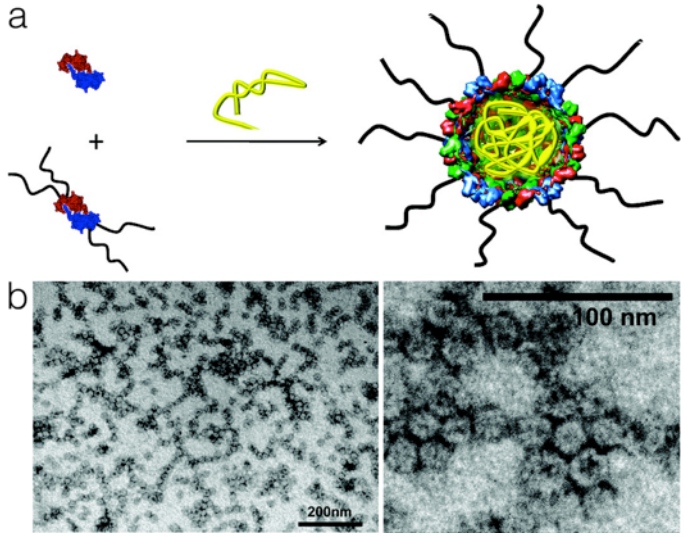

Figure 1.2.12. Self-assembly of CCMV-PEG using PSS (a) Schematic representation of reassembling PEGylated and non-modified CCMV coat proteins into VLPs by polyanionic PSS. (b) Left panel: TEM image of PSS–CCMV–PEG $T = 1$ particles. Scale bar is 200 nm. Right panel: zoomed TEM image of PSS–CCMV–PEG $T = 1$ particles. Scale bar is 100 nm. Adapted with permission from [292]. Copyright © 2013 American Chemical Society.

The anionic polymers discussed so far as scaffolds for self-assembly of viral capsids were linear chains. Recently, de la Escosura and co-workers used anionic Fréchet-type dendrimers to direct the morphology of CCMV and to add functionality to the CCMV–polymer particle.[170] The idea was that zinc and ruthenium phthalocyanine dendrimers[357] could convert molecular oxygen into singlet oxygen and in addition drive the self-assembly of CCMV coat proteins to VLPs. Thus, the protein would form a capsule around the phthalocyanine catalysts. Zn phthalocyanides with four dendrimers attached to the phthalocyanide macrocycle and Ru phthalocyanides with two dendrimers axially co-ordinated to the metal centre were tested for their ability to assemble coat protein into VLPs. Moreover, dendrimers of different generations were used. π -Stacked dimers of Zn phthalocyanides with zero-generation

dendrimers and individual Ru phthalocyanides with first-generation dendrimers were efficient templates for VLP formation (Figure 1.2.13). A possible explanation is that both species carry 16 negative charges, which match the number of positive charges on coat protein dimers. T = 1 particles with a diameter of 18 nm were obtained. Phthalocyanides can produce singlet oxygen, which is used in photodynamic therapy as reactive species. Therefore, these CCMV–phthalocyanine–dendrimer particles have a high potential for biomedical applications.

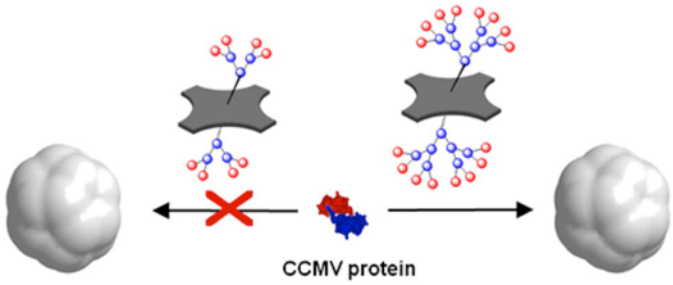

Figure 1.2.13. Schematic representation of VLP formation using Ru phthalocyanine dendrimers. Depending on the dendrimer, VLP formation is favoured. Adapted with permission from [170]. Copyright © 2015 American Chemical Society.

1.4.6.3 Non-covalent encapsulation of polymers in protein cages other than viral capsids

Non-covalent encapsulation of polymers into the cavity of protein cages is not limited to VLPs. Protein cages that have pores wide enough to allow macromolecules to enter their cavity can take up polymers from solution. The vault protein has a barrel-like structure with a large internal cavity.[239] However, the nature and size of pores that connect its interior with the surrounding solution are unknown. To explore whether polymers can enter into vaults, MPS–PPV of unknown molecular weight was incubated with vault particles.[158] The photophysical properties of the fluorescent polymer depend on the polarity of its environment,[356,358] making it a useful tool to study its interaction with proteins. Fluorescence intensity measurements, TEM and small-angle X-ray scattering (SAXS) suggest that the polymer was encapsulated into the vault and did not alter the structure of the protein cage (Figures 1.2.14a–d). Encapsulation of the polymer within the native protein cage was furthermore confirmed with the cationic fluorescence quencher, methyl viologen. A much lower quenching efficacy was observed when the quencher was added to a mixture of polymer and vault compared with a polymer solution that did not contain protein

cages. Thus, the vault restricted access of the quencher to the fluorescent polymer, which implies that the polymer is located inside the protein capsule. For comparison, some of the experiments were repeated with vaults composed of cross-linked protein subunits. The polymer could not enter into cross-linked protein particles, as evidenced by the fact that the fluorescence quenching efficacy with methyl viologen,[359,360] was similar to pure polymer solution. However, vaults could be first loaded with MPS–PPV and then cross-linked, e.g. to prevent leakage of polymer from the protein cage. The significance of this study is that fully assembled vaults can encapsulate and entrap synthetic polymers. As vaults are of human origin, they could become useful delivery vehicles for macromolecular therapeutics.

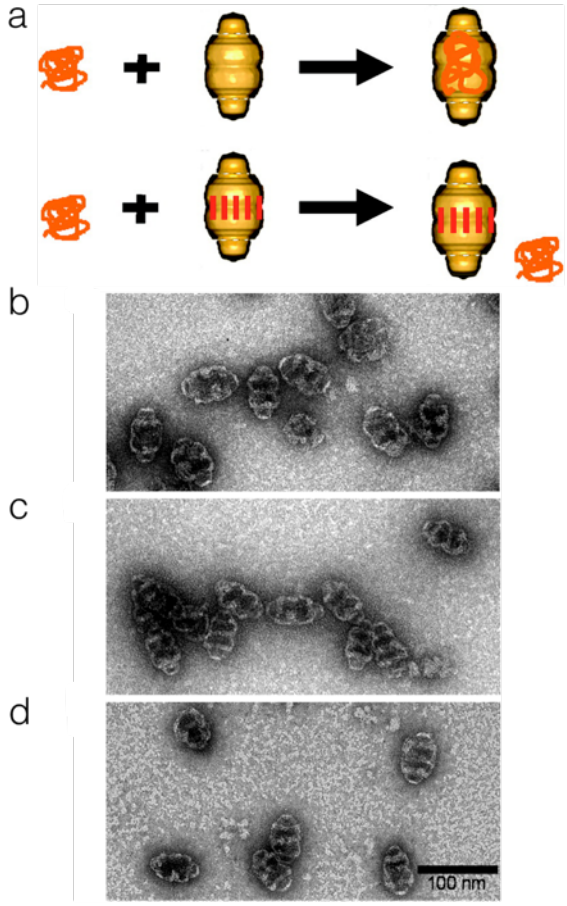

Figure 1.2.14. Integration of a polymer into a vault protein cage.(a) Schematic representation of a vault protein cage (top) and vault protein cage with cross-linked subunits (bottom), showing that non-cross-linked vaults are able to encapsulate MPS–PPV, while the polymer cannot enter the cavity of cross-linked vaults. (b)–(d) TEM images showing (b) vaults in the absence of polymers, (c) vaults that encapsulate MPS–PPV and (d) vaults that were loaded with MPS–PPV and subsequently cross-linked. Scale bar is 100 nm. Adapted with permission from [158]. Copyright © 2008, American Chemical Society

1.4.6.4 Encapsulated polymers that are covalently bound to the interior of the cavity of a protein cage

Non-covalent encapsulation of polymers into protein cages most often relies on electrostatic interactions between the charged inner surface of protein cages and oppositely charged

polymers. Thus, this approach is limited to charged polymers, e.g. polyelectrolytes. The scope of polymers can be significantly broadened if polymers are covalently bound into protein cages, which prevents them from leaching out of the protein's cavity. To this end, selective attachment points, e.g. cysteine residues, have to be genetically engineered to the inner surface of the proteins. These residues allow the introduction of initiators for polymerization reactions into the cage, so that polymer chains can be grown from the protein within its cavity. Moreover, the attachment points can bind preformed polymers via established linker chemistries. In both cases, protein–polymer conjugates are obtained that encapsulate the polymer within the protein cage.

The group of Douglas pioneered the synthesis of polymers inside protein cages by a 'grafting-from' approach. Interestingly, their first reports encompassed an uncommon method to synthesize polymers, the step-wise growth of polymers by repeated click-chemistry reactions.[111,160,361,362] Only later they turned to one of the routine methods of modern polymer chemistry, atom transfer radical polymerization (ATRP).[113,115,148,162,172]

The heat-shock protein (Hsp) from *Methanococcus jannaishii* was used as a scaffold to synthesize branched and cross-linked polymers within its cavity.[160,361] The aim was to prepare drug-delivery and imaging vehicles in which the polymer core provides a high density of binding sites for therapeutics. A genetically modified variant of Hsp (HspG41C) that features a cysteine residue on the inner surface of each subunit was selected.[363] This modification allowed selective attachment of functional molecules into the protein cage. *N*-propargyl bromoacetamide was conjugated to these cysteines to act as an alkyne initiator for polymerizations.[160] However, bromoacetamides can also react with primary amines (e.g. of lysine residues) and the imidazole ring of histidine. There are 11 lysines and one histidine on each subunit of Hsp. To limit the reaction sites of *N*-propargyl bromoacetamide, lysines were passivated with *N*-hydroxysuccinimide acetate before modification of

cysteines with the initiator. Step-wise polymer synthesis via click chemistry of tripropargyl azide and 2-azido-1-azidomethyl-ethylamine within the cavity was performed using a Cu(I) catalyst. Branched and cross-linked polymers that contained primary amines as functional handles were obtained (Figure 1.2.15a). Analytical results of passivated and non-passivated Hsp–polymer conjugates showed similar results in size exclusion chromatography (SEC), dynamic light scattering (DLS) and TEM for all generations of step-growth (G0.5–G2.5) (Figures 1.2.15b-d). The size of the polymer-filled cage was the same as the empty Hsp, indicating that the polymer does not disturb the protein cage structure. The polymer networks increased the temperature stability of the protein cage from 70 °C to ≥120 °C because several protein subunits were covalently connected through the polymer.

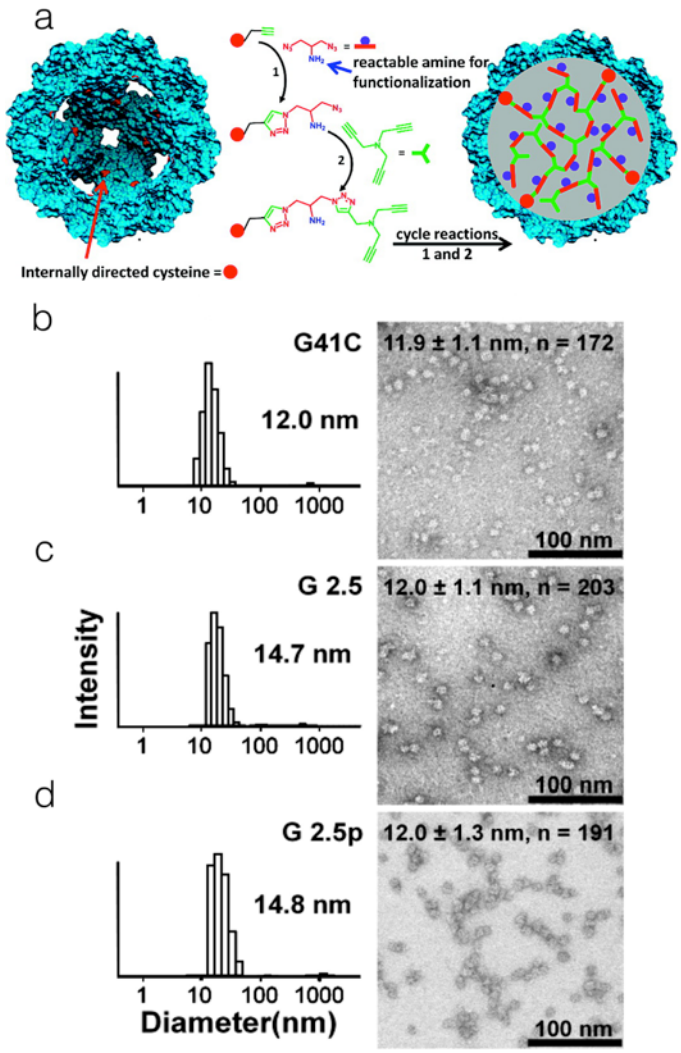

Figure 1.2.15. Step-wise grafting-from approach within Hsp. a) Sectional image of the mutated HspG21C variant, showing the interior of the cavity with cysteine residues (red dots) and step-wise polymerization of 2-azido-1-azidomethyl-ethylamine and tripropargyl amine within the protein cage. (b)–(d) DLS (left panels) and TEM images (right panels) of (b) native HspG41C, (c) non-passivated

HspG41C with G2.5 branched polymer and (d) passivated Hsp41C with G2.5 branched polymer. Scale bar for TEM images is 100 nm. Adapted with permission from [160]. Copyright © 2009 American Chemical Society.

In a next step, functionality was introduced to the Hsp–polymer hybrid particles and they were converted into MRI contrast agents.[361] Diethylenetriamine pentaacetic acid (DTPA) was conjugated to the primary amines of the cross-linked polymer. DTPA is a chelator that is capable of binding metal ions such as gadolinium ions (Gd^{3+}). The functionalized protein cages contained up to 159 Gd^{3+} ions per particle with a maximum T_1 particle relaxivity value of r_1 = 4,200 mM^{-1} s^{-1}. As a comparison, pure DTPA–Gd has an r_1 value of 4 mM^{-1} s^{-1}. This was at the time the second highest relaxivity that was achieved for contrast agents based on protein cages. A higher r_1 value (r_1 = 7,200 mM^{-1} s^{-1}) was achieved with the MS2 viral capsid by conjugation of DTPA ligands to the lysines of MS2.[364] However, taking into account that MS2 has a 12 times bigger volume than Hsp, the relaxivity per volume of the Hsp–polymer conjugate was seven times bigger than that of MS2. The branched polymer network within the cage enabled this high loading capacity for gadolinium ions.

The Hsp–polymer conjugates were also modified with 1,10-phenanthroline (phen).[362] The ligand allowed complexation of metal ions like Fe^{2+}, generating branched co-ordinating polymers within the protein cage that contained 0.3 iron ions per protein subunit (Figure 1.2.16). The hybrid particles could be used as catalysts[365] or in drug-delivery applications, where drugs could be entrapped within and released from the metal–organic networks. [366,367]

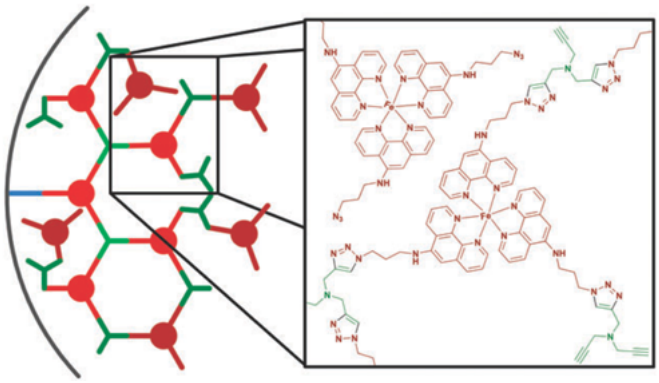

Figure 1.2.16. Schematic representation of the co-ordination polymers created by modifying a branched polymer network with phenanthroline within Hsp G41C. Adapted with permission from [362]. Copyright © 2010, The Royal Society of Chemistry.

The step-wise click-chemistry synthesis of polymers was applied to the P22 viral capsid to create a protein–polymer contrast agent with a larger size and therefore a greater relaxivity than Hsp.[111] The P22 capsid in its WB morphology is 64 nm in diameter and therefore much larger than Hsp with a diameter of 12 nm. In addition, it has pores that have a diameter of 10 nm.[269] It was assumed that bigger pores allow a better exchange of molecules between interior and exterior than smaller pores. This is beneficial for MRI applications because water molecules have to be exchanged as fast as possible between the interior with the Gd^{3+} complexes and the exterior to achieve high relaxivity rates. A branched and cross-linked polymer was synthesized in a P22 mutant (K118C), which had a cysteine residue engineered into each of the 420 subunits. The polymer was synthesized first by introducing alkyne groups to the cysteines as initiating site. The bifunctional azide monomer 2-azido-1-azidomethylethylamine (DAA) with attached 2-(4-isothiocyanatobenzyl)-diethylenetriamine pentaacetic acid gadolinium (*p*-SCN-Bn-DTPA-Gd) was coupled to the alkynes. Prior to the coupling reaction, the *p*-SCN-Bn-DTPA-Gd ligand was attached to the primary amine of DAA (DAA-DTPA-Gd). Trialkyne as branching agent was coupled to the second azide of DAA-DTPA-Gd. The procedure of alkyne–azide coupling was conducted until theoretically seven ligands (DAA-DTPA-Gd) per subunit were introduced. Subsequent modification of the polymer's primary amines with DTPA allowed for complexation of Gd^{3+} ions. While the mass of the protein cage increased due to the presence of the polymer, its size did not change, as confirmed by SEC. The polymers enabled a payload of 1900 Gd^{3+} ions per capsid, which resulted in a very high relaxivity of r_1 = 41,300 mM^{-1} s^{-1} per particle. Moreover, the P22-polymer-DTPA construct slows down molecular tumbling due to its size, which is important to achieve high relaxivities.[368] These results demonstrate the potential of virus–polymer MRI contrast agents. The disadvantage of this kind of step-growth polymerization is, however, that it takes a lot of effort to synthesize larger polymers within the cavity of a protein cage.

For this reason, Douglas and co-workers switched to ATRP for the synthesis of polymers within the P22 capsid,[148] as it allows preparation of real polymers in a single synthesis step (Figure 1.2.17).[22] To ensure that all polymers are within the cavity, a new mutant of P22 was created by single-point mutation. Serine on position 39 of each subunit was exchanged by cysteine ($P22_{S39C}$). All cysteine residues are exposed on the interior of the capsid, in contrast to the K118C mutant, [269] which also

has some cysteines on the exterior surface of the capsid. ATRP initiators were conjugated to the cysteines of the $P22_{S39C}$ mutant in its expanded morphology. Then, 2-aminoethyl methacrylate (AEMA) was copolymerized with the cross-linker bis-acrylamide, resulting in a cross-linked polymer network (xAEMA) that contained primary amines (Figures 1.2.17a-c). An additional difference to the previous reported study that used the click approach for polymer synthesis, the P22 cage was not applied in its WB morphology, but in its expanded (EX) morphology. The diameter in both structures is the same, but the WB lacks the penton subunits. The EX form is similar to the infectious virus in vivo, therefore it was used in this study. To evaluate the number of accessible primary amines on the polymer chains, $P22_{S39C}$–xAEMA conjugates were incubated with FITC. Because FITC attaches to every amine, lysines were also modified. To overcome this issue, $P22_{S39C}$ without polymers was incubated with FITC. The number of amines from $P22_{S39C}$ was subtracted from the total number of $P22_{S39C}$–xAEMA. Thus, it was possible to calculate the number of primary amines in the polymer chains that could be modified. In addition to FITC, which was used as an analytical marker and for quantification purposes, Gd-DTPA-isothiocyanate (Gd-DTPA-NCS) was attached to the amines as MRI contrast agent. The number of Gd-DTPA per $P22_{S39C}$–xAEMA was determined by attaching Gd-DTPA-SCN to the primary amines and as a control to $P22_{S39C}$. $P22_{S39C}$–xAEMA revealed a 28 times higher Gd^{3+} content than $P22_{S39C}$ as determined by inductively coupled plasma–optical emission spectroscopy (ICP–OES). Thus, most of the contrast agent was bound to the polymers. To exclude electrostatic binding of Gd-DTPA with the polymer chains, $P22_{S39C}$–xAEMA was incubated with the contrast agent Gd-DPTA (Magnevist, Bayer Schering Pharma). The $P22_{S39C}$–xAEMA sample incubated with Gd-DTPA-NCS showed a shift to higher molecular weight in native agarose gel electrophoresis compared with the unmodified $P22_{S39C}$–xAEMA. The $P22_{S39C}$–xAEMA sample that was incubated with Magnevist on the other hand showed the same electrophoretic mobility as the $P22_{S39C}$–xAEMA conjugate. These results led to the conclusion that Gd-DTPA was covalently bound to the polymers and not just by electrostatic interaction. The loading capacity of the capsid was 9,100 ± 800 Gd^{3+} ions and resulted in a particle relaxivity of r_1 = 200,000 mM^{-1} s^{-1}. Thus, these ATRP-derived polymers allowed a fivefold higher Gd^{3+} content and relaxivity per VLP than the previously reported click-chemistry-derived polymers.[111] Unfortunately, the WB form of P22 with cross-linked AEMA was not investigated in

this study as in the previously reported study. It would be interesting to see the differences, because the WB morphology has, due to the lack of capsid pentons, larger pores that should allow a better exchange of water molecules between the interior of the Gd^{3+}-loaded capsid and the external environment.

Differences in the location of initiator sites between the K118C and S39C mutants of P22 were demonstrated by homopolymerization of the monomer AEMA[148] and *N*-tris(hydroxymethyl)methyl acrylamide from protein-bound ATRP initiators.[172] Polymerization yielded protein–polymer conjugates in both cases. The size of the $P22_{S39C}$ remained constant during polymerization. However, the diameter of the K118C mutant increased, indicating that in the first case polymer chains formed solely inside the capsid, while in the latter case polymer chains grew on the exterior and the interior surface of the protein cage.

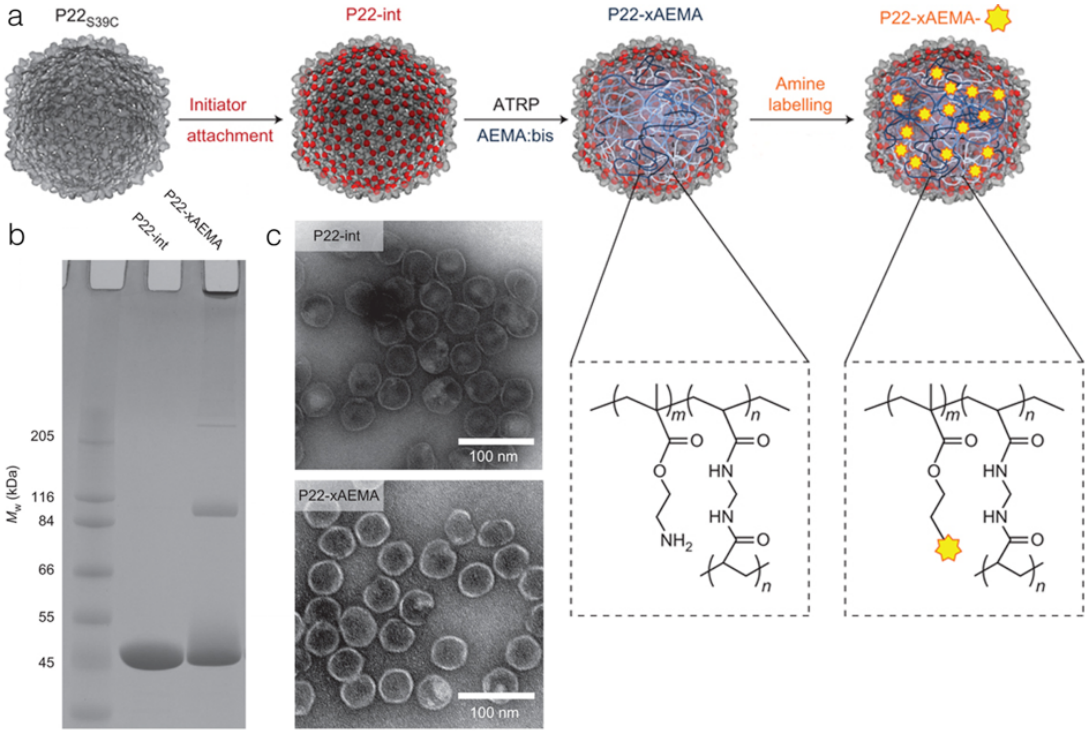

Figure 1.2.17. Synthesis and labelling of $P22_{S39C}$–xAEMA. (a) Schematic representation of 'grafting-from' ATRP inside the protein cage P22 to yield protein–polymer conjugates in which a cross-linked polymer (xAEMA) is encapsulated in a protein shell. The polymer bears amine groups that can be further modified, e.g. with fluorescent dyes or MRI contrast agents. (b) SDS–PAGE showing P22-initiator and P22 with cross-linked AEMA (P22–xAEMA). The latter shows cross-linked subunits at the top of the gel, and streaking of the subunit band to higher molecular weight, indicating the formation of protein–polymer conjugates. (c) TEM images of P22–initiator and P22–xAEMA reveal that the protein cage remains intact after polymerization within the cavity. Scale bars are 100 nm. Adapted with permission from [148]. Copyright © 2012, Nature Publishing Group.

A recent study with the P22–xAEMA-DTPA-Gd construct compared the relaxivity values r_1 and r_2 at different MRI field strengths in dependence of the Gd-loading capacity of the P22 cage.[113] The protein cage gives at least a three times better positive contrast (r_1 value) than free DTPA-Gd at magnetic fields that are used in clinics (≤3 T). Therefore, the P22–polymer conjugate can be applied as T1 contrast agent. At high magnetic fields of 7 T and a loading capacity of 10300 Gd^{3+} per cage, the P22–xAEMA-DTPA-Gd has an r_2/r_1 ratio of approximately 8, which is almost as high as for superparamagnetic (T2) contrast agents ($r_2/r_1 > 10$). Thus, the P22-capsid has high potential as MRI contrast agent.

Because of its high relaxivity, the VLP was used to image vascular inflammation in atherosclerosis mouse models.[162] For comparison, experiments with free DTPA-Gd complex were also carried out. At the same Gd concentrations (20 μmol Gd/kg in mice, corresponding to one-fifth the typical clinical dose), P22–xAEMA-DTPA-Gd resulted in a much stronger contrast in magnetic resonance angiography of vascular systems.[162] In addition, arginine–glycine–aspartic acid (RGD) peptides were attached to the exterior of P22–xAEMA-DTPA-Gd for active targeting of $\alpha V \beta 3$ integrin, which is upregulated on activated macrophages.[162] RGD is a proven targeting ligand for specific targeting in vascular inflammation (e.g. vascular cancer).[369] RGD-modified P22–xAEMA-DTPA-Gd showed enhanced uptake for the targeted cells, as proven by MRI measurements. These results, although so far only published as a conference proceeding, show that the ATRP-derived P22–polymer conjugate can be applied for in vivo MRI and that it is capable of targeting specific cells when modified with a targeting moiety.

Because gadolinium-based contrast agents are linked with nephrogenic system fibrosis due to the possibility of free Gd^{3+}, a less toxic system was developed by Douglas and co-workers based on P22–xAEMA.[115] The protein–polymer conjugate was modified with manganese(III) protoporphyrin (MnPP) on the accessible amines of P22–xAEMA (amines of lysines and xAEMA). A relaxivity per particle of 7098 mM^{-1} s^{-1} with a loading of 3646 MnPP molecules per capsid was achieved. According to the Solomon–Bloembergen–Morgan theory[368] the MnPP containing P22 capsid should have a higher ionic relaxivity than free MnPP because molecular tumbling is slowed down. However, their relaxivity was similar. A hypothesis for this result is that MnPP molecules within the cage interact and block access of water molecules to the metal site, slowing down or preventing exchange of water

molecules with the complex. The relaxivity of Mn-based systems was lower than that of Gd-based systems. Nevertheless, the Mn-based system could be a good alternative to the Gd-based systems because of manganese's lower toxicity. As suggested by the authors, targeting moieties on the exterior of the P22 cage could lead to higher contrasts at desired places of action.[115] Another proposition to enhance the properties of the contrast agent is to disrupt interactions between MnPP molecules within the cavity of the protein cage to allow better access of water molecules to the Mn sites. Furthermore, it would be possible to label the P22–polymer conjugate with Mn–porphyrin complexes of higher relaxivity (e.g. manganese(III) tetrakis(4-sulfonatophenyl)porphyrin).

P22–polymer conjugates that encapsulate cross-linked AEMA were not only explored as contrast agents, but also as nanoreactors for photocatalytic applications.[172] AEMA, bis-acrylamide and [ruthenium(5-methacrylamidophenanthroline)$_3$]$^{2+}$ ([(Ru(meth-phen)$_3$]$^{2+}$) were copolymerized by ATRP in P22$_{S39C}$ to create protein–polymer conjugates with photocatalytic activity (Figures 1.2.18a+b). Photoreduction of methyl viologen (MV^{2+}), using EDTA or ethanol as sacrificial reductants,[359,360] was monitored by UV–vis spectroscopy (Figure 1.2.18c). Absorbance at 395 nm increased as the reaction proceeded (Figure 18c). In contrast, P22–xAEMA that lacked [(Ru(meth-phen)$_3$]$^{2+}$ could not catalyse the reduction of MV^{2+}. The results show that copolymerization of functionalized monomers inside the P22 capsid can yield core–shell particles in which a catalytically active cross-linked polymer core is encapsulated in a protein cage. It remains to be elucidated, however, how the catalytic performance of the protein–polymer conjugates compares with other catalysts.

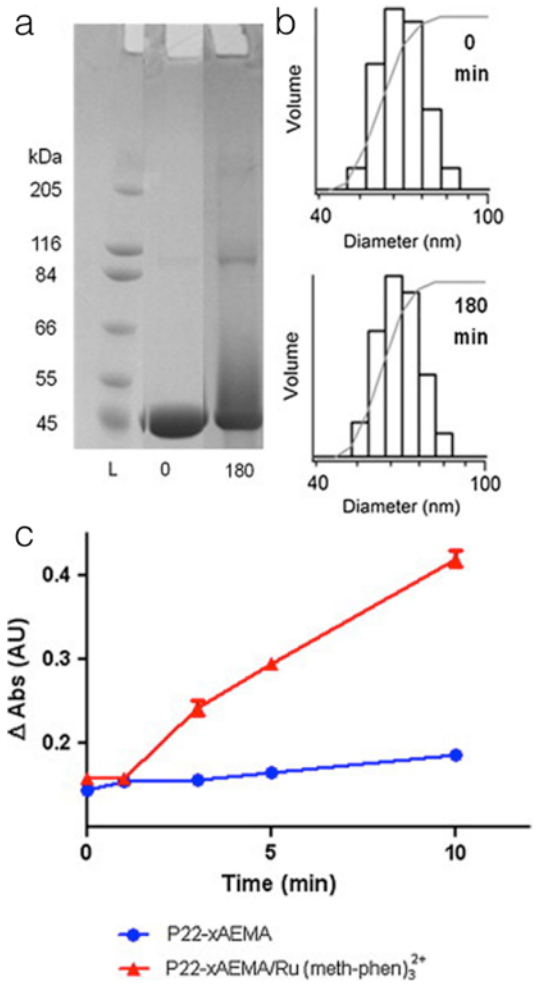

Figure 1.2.18. P22–xAEMA as catalyst for photoreductions. (a) SDS–PAGE of $P22_{S39C}$ initiator after 0 min and 180 min polymerization time. (b) DLS of $P22_{S39C}$ after 0 min and 180 min polymerization shows the same size distribution, indicating that the polymer formed inside the cage. (c) Photocatalytic reduction of MV^{2+} by $P22_{S39C}$–xAEMA-co-$[(Ru(meth\text{-}phen)_3]^{2+}$ as monitored by UV–vis spectroscopy. In contrast, $P22_{S39C}$–xAEMA that lacked $[(Ru(meth\text{-}phen)^{2+}]_3$ did not reduce the substrate. Adapted with permission from [172]. Copyright © 2013 Elsevier Ltd. All rights reserved.

A complementary study to the grafting-from ATRP of amine-containing monomers within a viral capsid by Douglas and co-workers,[111,148,162,172] was conducted by Finn and co-workers (Figure 1.2.19).[114] A modified variant of Qβ bacteriophage was expressed that had the unnatural amino acid azidohomoalanine (AHA) instead of methionine residues on the interior. This mutant (T93AHA) allowed the attachment of ATRP initiators to the interior via click chemistry (Figuure 1.2.19a). The viral RNA was removed prior to quantification of binding sites and conjugation of initiators to AHA. The number of available AHAs was determined by letting the capsid react with fluorescein–alkyne dye in a copper-catalysed azide–alkyne cycloaddition. A quantity of approximately 147 dye molecules per Qβ was

measured. ATRP initiators with alkyne groups were bound to the AHAs, followed by polymerization of 2-dimethyamino ethyl methacrylate (DMAEMA) in the interior of Qβ bacteriophage. Two Qβ–poly(DMAEMA) conjugates were synthesized, one with 250 monomers per subunit (T93@250×) and another with 1000 monomers per subunit (T93@1000×) (Figure 1.2.19b). Qβ–poly(DMAEMA) conjugates increased slightly in diameter (17.3 nm for T93@250× and 22.3 nm for T93@1000×) (Figure 1.1.19c) compared with the protein macroinitiator (16 nm). The increase might be caused by disruption of the capsid structure by the polymer chains or by chains that protruded from the cage. However, DLS and TEM proved that the cages stayed intact after polymerization (Figure 19c). To verify that polymer chains were within the interior of the VLP, the terminal bromines on the polymer chains were exchanged with azides and then labelled with biotin. Biotinylated polymer–protein particles showed weak interaction with streptavidin in an ELISA assay in comparison with Qβ VLPs that were modified on the exterior with biotin, indicating that the majority of polymer chain ends was encapsulated in the protein cage. By changing the pH from 7.0 to 11.0, the initiator-bearing VLP increased in size, while the T93@1000× conjugate decreased in size. This observation could be explained with a transition of poly(DMAEMA) from a swollen to collapsed state when the pH is increased.[370] As additional experiments, a cyclic RGD (cRGD) derivative with a PEG spacer was attached to the exterior to enhance cellular uptake. Uptake into HeLa cells was enhanced compared with Qβ bacteriophage without cRGD and poly(DMAEMA). Surprisingly, Qβ–poly(DMAEMA) conjugates that lacked cRGD on the surface showed a similar overall cell uptake to the protein–polymer conjugate with cRGD. Thus, it can be concluded that the poly(DMAEMA) in the interior had an influence on cellular uptake. A possibility might be that some of the cationic polymer chains protruded from the protein cage and improved cellular uptake. A difference between cRGD and poly(DMAEMA) uptake was, however, observed. While cRGD-decorated VLPs showed a receptor-mediated endolysosomal uptake, Qβ–poly(DMAEMA) VLPs were not found in endolysosomes. The Qβ–poly(DMAEMA) conjugates were applied as transfection agents for small interfering RNA (siRNA) into HeLa cells that expressed GFP. Indeed, a silencing effect of GFP was observed. However, it is difficult for a 21-mer siRNA (≈7 nm length, 2 nm thickness)[371] to enter and leave the cavity through pores with a diameter of 1.5 nm. Moreover, complexes of 40 siRNAs

per VLP were formed. It is unlikely that all siRNAs were encapsulated into the capsid, as this number of nucleotides does not fit into a 22 nm VLP. It is more likely that some siRNA were encapsulated but the major part formed a complex with the exterior of Qβ, probably enhanced by the cationic polymer chains that protruded from the protein cage. Nevertheless, Finn and co-workers showed that a protein cage with polymers in the cavity could be applied for nucleotide delivery.

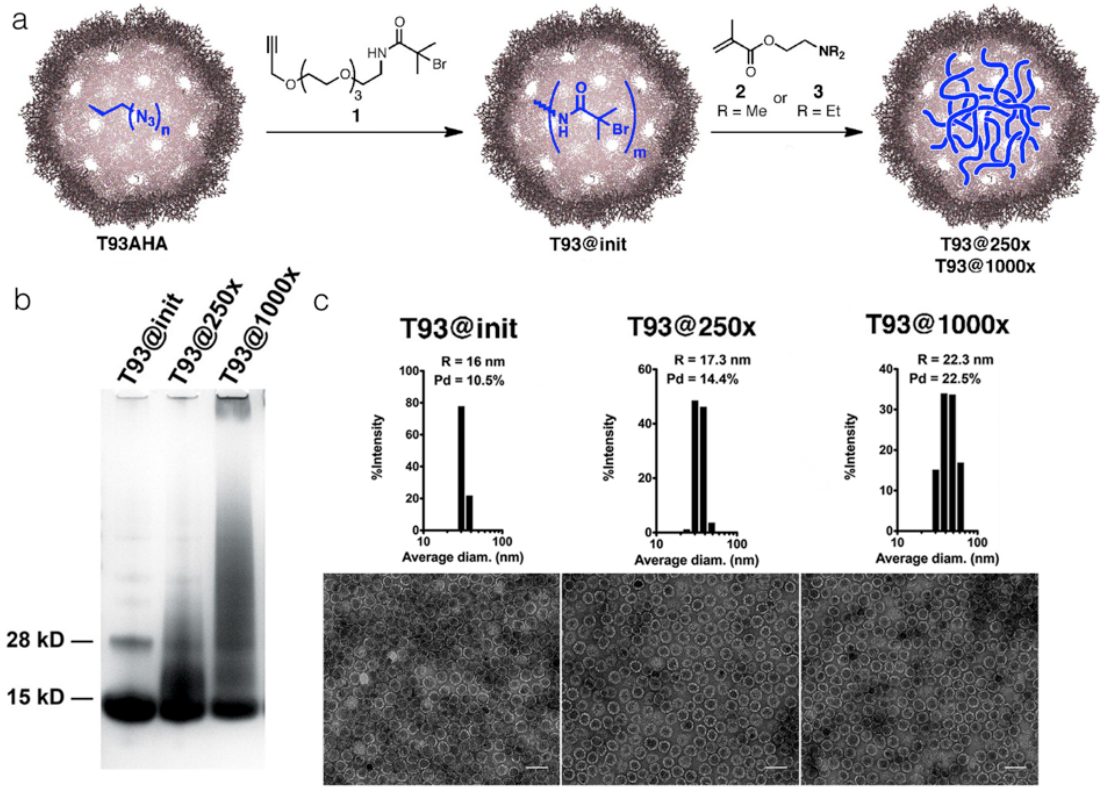

Figure 1.2.19. Synthesis of polymers in the cavity of Qβ bacteriophage. (a) Schematic representation of initiator conjugation in the cavity of the protein cage and subsequent ATRP. (b) SDS–PAGE of the protein macroinitiator (T93@init), a sample that was synthesized with 250 monomers per subunit (T93@250×) and a sample that was synthesized with 1000 monomers per subunit (T93@1000×). (c) DLS (top) and TEM images (bottom) of T93@init, T93@250× and T93@1000×. Scale bars of TEM images are 50 nm. Adapted with permission from [114]. Copyright © 2014 American Chemical Society.

Direct polymerization from protein-bound initiators is a versatile approach to prepare functional protein cage–polymer conjugates. However, well-controlled polymerizations that yield polymers of predetermined molecular weight and narrow molecular weight distribution on the surface of proteins can be difficult to achieve.[29] Moreover, characterization of the synthesized polymers by gel permeation chromatography or mass spectrometry is hampered by the covalently bound protein. An alternative strategy to prepare protein cages that encapsulated polymers is

covalently to link preformed polymers to the inside of protein cages. The advantage of this 'grafting-to' approach is that the polymers are synthesized, purified and characterized in solution, so that their molecular characteristics are well defined. Of course, this strategy will only work for protein cages that feature large pores in their protein shell through which macromolecules can enter into the fully assembled cage, or for polymer–protein conjugates that self-assemble into polymer cages.

The natural function of chaperonins is to refold denatured proteins by providing a folding chamber into which proteins can diffuse. Our group took advantage of this feature and conjugated dendritic poly(amidoamine) (PAMAM, fourth generation) into the cavities of THS, a chaperonin from *T. acidophilum* to prepare delivery agents for siRNA (Figure 1.2.20).[163] PAMAM is a common transfection agent in gene delivery and can bind and release oligonucleotides and a variety of drugs.[372] However, the high density of positive charges on the surface of PAMAM initiates uncontrolled cell uptake and can induce cytotoxicity.[373-375] Moreover, PAMAM often forms non-defined aggregates with DNA and siRNA, leading to particles that are too large for efficient gene delivery.[376] To overcome these disadvantages of PAMAM, it was incorporated into the cavity of THS. The cage shields cells from the positive charges on the polymer, while still allowing the polymer to bind and release siRNA. In contrast to other PAMAM-based siRNA transfection systems, the THS–polymer conjugate has a well-defined and monodisperse size of approximately 16 nm, which is defined by the size of the protein cage. Therefore, it fits well into the therapeutic size window (10–200 nm) for nanoparticles.[377,378] To bind PAMAM into THS, a genetically engineered variant of THS that only carried cysteines on its inside was functionalized with maleimido trioxa-6-formyl benzamide (MTFB). In parallel, PAMAM was functionalized with succinimidyl-6-hydrazino-nicotinamide (S-HyNic). Subsequently, PAMAM-S-HyNic and THS-MTFB were mixed. The polymer diffused into the protein cage where the linkers reacted to form a bis-aryl hydrazone bond, i.e. a resonance stabilized Schiff's base, between the polymer and the protein (Figure 1.2.20a). On average, approximately four PAMAM molecules were bound into THS. The THS–PAMAM hybrid was able to bind therapeutic siRNA and protect it from degradation by RNase (Figure 1.2.20b). Moreover, it could deliver siRNA to U-87 MG cancer cells, inducing siRNA-related inhibition of proliferation (Figure 1.2.20c). By modifying the exterior of THS-PAMAM with the cell-penetrating peptide TAT, siRNA-loaded THS-PAMAM was also taken up by

prostate cancer cells (PC-3) and induced RNA interference in these cells.[379] It was shown that TAT was crucial to initiate RNA interference in PC-3 cells, as protein cage–polymer conjugates that lacked the cell-penetrating peptide did not enter those cells. SiRNA has a big potential to tread different diseases, because it can silence disease-specific proteins.[379] This THS-PAMAM system enables to overcome the inherent hurdles in siRNA delivery, such as fast degradation of siRNA in the blood, rapid clearing by the kidney due to its small size and the inability of siRNA to cross cell membranes.[380]

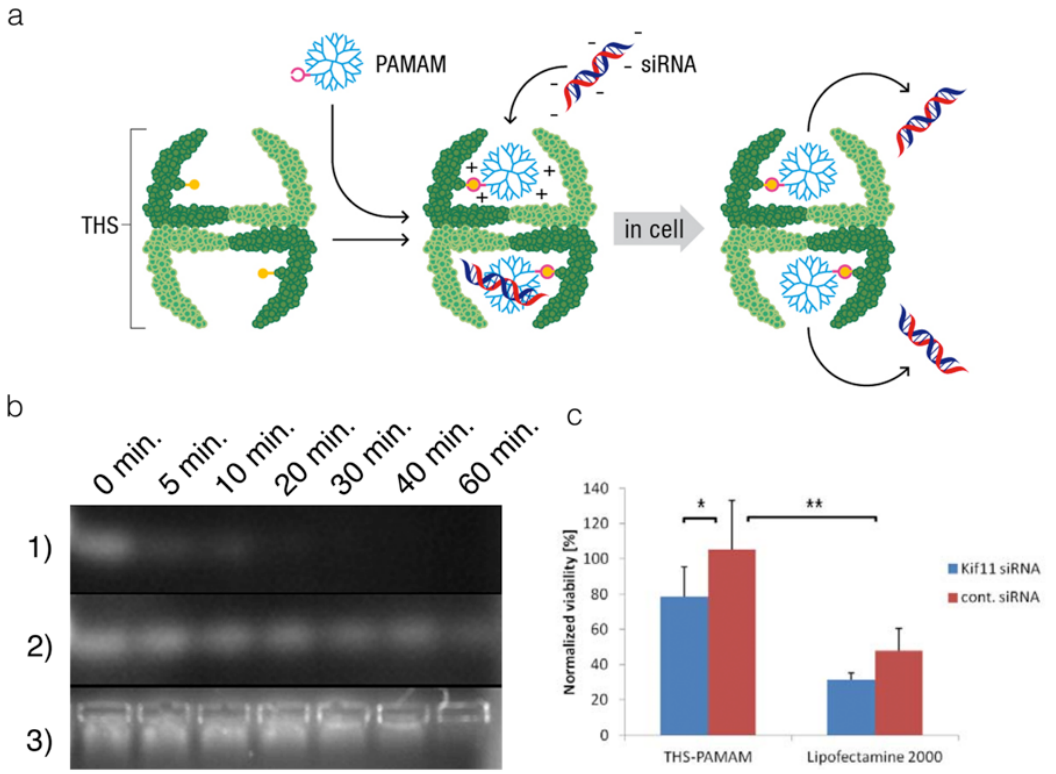

Figure 1.2.20. THS-PAMAM as transporter for siRNA into cells. (a) Conceptional view of THS–PAMAM hybrid as siRNA delivery agent. PAMAM incorporates the sensitive cargo, while the protein shell protects cells from positive charges of the polymer. (b) Degradation of siRNA by RNAse A, as followed by electrophoresis: 1) Free siRNA, 2) PAMAM-siRNA and 3) THS–PAMAM–siRNA. The results show that THS–PAMAM protects its cargo, similar to PAMAM. (c) U-87 MG cells transfected with KIF11 siRNA (blue) or scrambled siRNA (red) with either THS-PAMAM or Lipofectamine 2000 demonstrate the ability of transfecting siRNA by THS-PAMAM. Adapted with permission from [379].

Nanoreactors are very small reaction vessels that confine chemical reactions into a nanoscale reaction volume.[54] They can be created by encapsulation of catalysts into, e.g. polymer vesicles, inorganic capsules, phase-separated polymer networks and protein cages.[51-58,61,72,381,382] Reactions in nanoreactors can be controlled in

unprecedented ways, allowing for enhanced reaction rates, suppressed side reactions, shape- and size-templated synthesis, as well as control of the reaction on a single-molecule level.[51-54,58,72,381] Therefore, nanoreactors have attracted much interest and were explored to conduct biocatalytic transformations in non-aqueous media,[382] to investigate reactions on the single-molecule level[220] and as artificial organelles.[383] With their hollow structure and their well-defined pores, protein cages are very promising nanoreactors. While most investigations concentrated on the conversion of small organic molecules in protein nanoreactors,[51-54,58,72] recent reports suggest that protein cages can also be used as reaction vessels for the formation of polymers.[61,62]

Substituted poly(phenylacetylene)s[384,385] are conjugated polymers that can be used e.g. as material for active layers in organic light-emitting diodes (OLEDs)[386] or as dynamic helical polymers to amplify chirality of guest molecules.[387] To increase control over the polymerization of phenylacetylenes, Watanabe and co-workers complexed the catalyst rhodium norbornadiene (Rh(nbd)) to the inside of apoferritin (Figure 1.2.21a).[62] The 24 subunits bound Rh(nbd) by interaction with cysteine, histidine and glutamic acid on the inside surfaces, as revealed by crystal structure analysis. Each subunit carried three Rh atoms, as determined by ICP–OES. The successful polymerization of phenylacetylene was confirmed by a colour change of the reaction mixture from colourless to pale yellow, indicating the presence of poly(phenylacetylene). Further, the apo-Fr cage kept its structure during polymerization, as indicated by similar elution volumes in size-exclusion column chromatography compared with unmodified apo-Fr (Figure 1.2.21b). The polymer was extracted from the ferritin by disassembling the protein cage into its subunits at pH 2. Poly(phenylacetylene) with a stereoregular cis-transoidal main chain, a number-average molar mass (M_n) of 1.31×10^4 g mol^{-1} and a polydispersity index ($Đ$) of 2.6 was obtained. For comparison, polymerization catalysed by free Rh(nbd)Cl_2 yielded a stereoregular polymer with $M_n = 6.37 \times 10^4$ g mol^{-1} and $Đ$ = 21.4. These results demonstrate that the discrete reaction space within the protein beneficially influences the polymerization of phenylacetylene towards lower M_n and smaller $Đ$ compared with polymerization in the absence of apo-Fr.

Several other derivatives of phenylacetylene were tested as monomers. Although phenylacetylene bearing an amino group was polymerized in the protein nanoreactor, monomers with carboxylic or phosphonic acid substituents did not react. Most likely, this selectivity stems from electrostatic repulsion between anionic molecules and

positively charged pores of ferritin, i.e. the anionic monomers were repelled from the protein cage. Therefore, it can be envisioned to use apoferritin as a selective nanoreactor for neutral and cationic acetylene monomers.

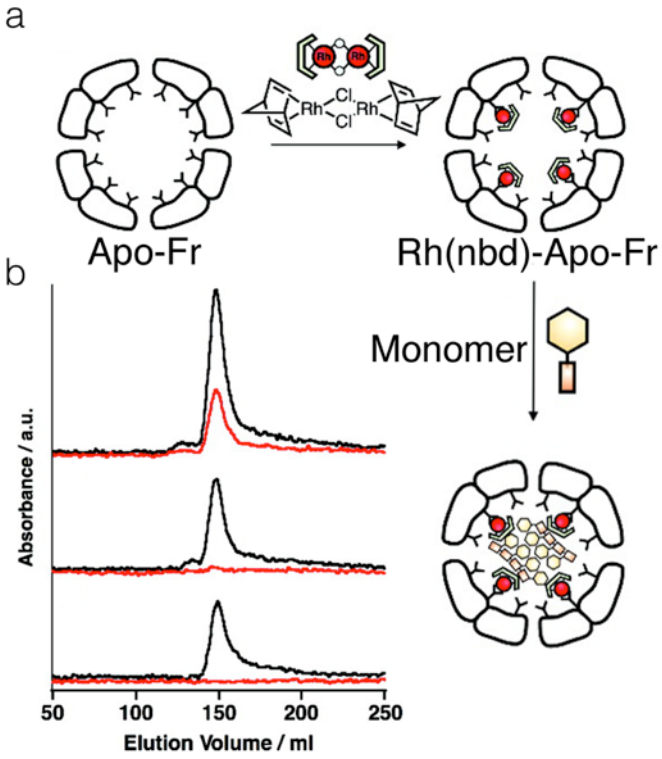

Figure 1.2.21. Apoferritin as nanoreactor for the polymerization of phenylacetylenes. (a) Schematic view of complex formation between apo-Fr and [Rh(nbd)Cl_2] and subsequent polymerization of phenylacetylene. (b) Size-exclusion chromatograms of Rh(nbd)-apo-Fr after polymerization of phenylacetylene (top), Rh(nbd)-apo-Fr (middle) and apo-Fr (bottom). The elution was monitored at 383 nm (red), which is caused by poly(phenylacetylene), and at 280 nm (black) where protein and polymer absorb light. Adapted with permission from [62]. Copyright © 2009, American Chemical Society.

Polymethacrylates and vinyl polymers are usually prepared by radical polymerization. The advent of reversible-deactivation radical polymerization (controlled/living radical polymerizations) such as ATRP and RAFT has paved the way for the precise synthesis of these polymers.[22,47,388] However, conducting ATRP in water can be challenging, as several side reactions might occur.[44] A possibility to increase the performance of ATRP is to conduct the polymerization in nanoreactors.[389] The first example of a protein cage–catalyst conjugate as a nanoreactor for controlled/living radical polymerizations was reported by Bruns and co-workers (Figure 1.2.22a).[61] They bound an ATRP catalyst covalently to the cysteines of an engineered thermosome from *T. acidophilum* (THS). These

attachment points were present on the inside of every beta-subunit of the chaperonin. The ligand for the Cu(I) catalyst was synthesized by functionalizing *N*,*N*,*N*′,*N*′-tetraethyldiethylenetriamine (TEDETA) with an aromatic aldehyde. In parallel, the hetero-bifunctional linker 3-maleimido-6-hydraziniumpyridine hydrochloride (MHPH) was reacted with THS. Then, the ligand and the protein were mixed, which caused the hydraziniumpyridine to react with the aromatic aldehyde, forming a resonance-stabilized bis-aryl hydrazone bond between THS and ligand. The ligand was subsequently used to complex copper ions, yielding THS-L_xCu. SAXS confirmed that the copper complex was only attached on the inside of the protein cage. The THS was in an open conformation, allowing the exchange of polymers between the inside and outside of the protein cage. This enabled the synthesis of polymers inside the THS and their subsequent release into the surroundings. Compared with polymerizations in ferritin (vide supra) it was therefore not necessary to disassemble the protein cage to extract the polymer from the protein. Having a confined reaction space that allows the product to be released into the surrounding medium through large pores is an advantage of THS over many other protein cages. THS-L_xCu was used as a catalyst for ATRP of NIPAAm in water. It resulted in PNIPAAm with M_n of 1.5×10^3 g mol^{-1} and $Đ$ of 1.11. The polymerization of oligo(ethylene glycol)methyl ether acrylate (OEGA) in the presence of 30% THF as organic co-solvent yielded a polymer of $M_n = 1.4 \times 10^3$ g mol^{-1} and $Đ = 1.06$ (Figure 1.2.22b). The synthesis of polymers within THS was compared with polymerizations in which the globular protein bovine serum albumin (BSA) served as the carrier of the copper catalyst (Figure 1.2.22b). BSA-L_xCu gave PNIPAAm with $M_n = 4.26 \times 10^5$ g mol^{-1} ($Đ = 1.92$) and poly(OEGA) with M_n of 1.49×10^5 g mol^{-1} ($Đ$ of 1.84). Thus, polymers synthesized within the protein nanoreactor had a lower molecular weight and narrower molecular weight distribution than their counterparts produced in solution. These findings are in line with the observations for the polymerization of phenylacetylene in ferritin (vide supra).[62] Native and SDS–PAGE, as well as TEM (Figure 22c) confirmed the integrity of the protein cage also under harsh synthesis conditions, i.e. in aqueous solutions that contained 30% organic co-solvent.

Both examples (Rh(nbd)-apo-Fr and THS-L_x-Cu) demonstrate that polymerizations can be confined in protein cages by attaching catalysts to the inner surface of the proteins. The nanoscale reaction space within these engineered protein cages results in polymers with lower and more narrowly distributed molecular weight compared

with polymerizations catalysed by freely accessible catalysts in solution. Reasons for this observation could be that the growth of polymer chains is limited by the rate of diffusion of monomers into the protein cage and that the nanoreactors hold the growing polymer chain and catalyst in close spatial proximity.

Protein nanoreactors offer the opportunity to gain new insights into polymerization reactions. The mechanism of the reactions and the growth of polymer chains could be studied with sequestered single polymer chains. Furthermore, triggers to open and close pores in protein cages could be used to alter the rate of polymerization or to start and stop polymerizations on demand. This could lead to new possibilities to influence polymerization reactions.

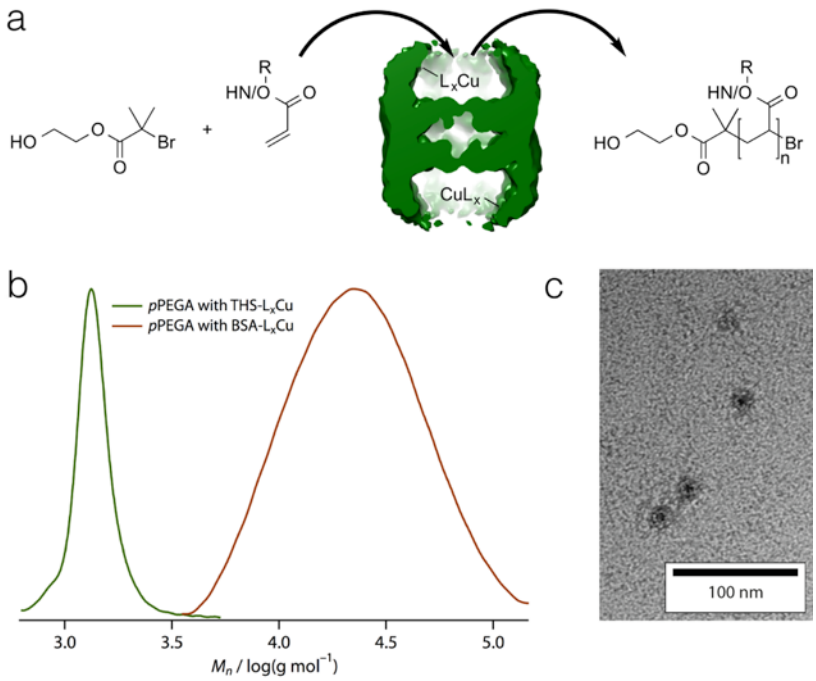

Figure 1.2.22. Polymer synthesis in the cavity of THS. (a) THS as nanoreactor for ATRP of *N*-isopropyl acrylamide and poly(ethylene glycol) methyl ether acrylate. (b) Comparison of GPC traces from poly(OEGA) synthesized within THS-L_xCu (green) or with BSA-L_xCu (brown) in the presence of 30% THF. (c) TEM image of THS-L_xCu after polymerization, showing that after reaction the protein cage is still intact. Adapted with permission from [61]. Copyright © WILEY-VCH 2014, Weinheim.

1.4.7 Conclusion and Outlook

Many of today's technical and healthcare challenges can be addressed by developing functional nanomaterials, e.g. as drug-delivery devices, as templates for electronic and energy materials or as advanced catalysts. A fascinating route to novel

nanomaterials is to take advantage of the rich variety of functional, self-assembled protein structures found in nature. Of particular interest are protein cages, as these capsules offer the possibility to host, protect, transport and release therapeutic cargo, metal nanoparticles, macromolecules, catalysts and many other guests. Moreover, they have very well-defined structures and sizes, which e.g. fit well in the therapeutic size window for long circulation time. Protein cages spontaneously self-assemble from a small number of protein subunits that can be overexpressed in suitable host organisms (e.g. *E. coli*). Some cages can be obtained from abundant natural sources (e.g. certain viral capsids from plants or ferritin from blood). Thus, protein cages are easily and widely accessible in sufficient quantities to be useful tools and building blocks for bionanotechnology. Although protein cages can be used on their own, their full power is unlocked if they are paired with synthetic polymers. In biomedical applications, e.g. as drug- or gene-delivery agents, biocompatible polymer chains on the surface of protein cages are essential to lower the risk of immunogenic responses against the proteins. Moreover, polymers can act as flexible spacers through which targeting ligands can be attached to the surface of the proteins. Protein cages can act as functional additives in polymeric materials, e.g. to create self-reporting materials or to increase the mechanical properties of hydrogels. A major breakthrough in the design of protein cage-based therapeutics was to synthesize polymers in their inside to enhance greatly their loading capacity for small molecule drugs or for MRI contrast agents. In a related approach, cationic polymers were used as anchor groups within the cavity of proteins to bind nucleic acids, so that siRNA delivery with non-viral cages became possible. Synthetic polymers not only increase the potential of protein cages in biomedical applications, but can also guide the self-assembly of viral subunits into nanostructures that differ in their size or shape from their native counterparts. If certain technical applications require a higher heat stability of protein cages, polymer chains can be used to achieve this, e.g. by multi-point attachment of synthetic macromolecules on the exterior surface or by step-growth polymerization and cross-linking of polymers within the cavity of protein cages. Polymerizations within protein cages proceed with fewer unwanted side reactions, so that the proteins have been used as nanoreactors for the synthesis of polymers or of polymer-filled protein nanoparticles.

This review summarizes and discusses many fascinating protein cage–polymer hybrid systems and their (potential) applications. But what lies ahead? The symbiosis

of polymers with protein cages opens up new opportunities for creative solutions in bionanotechnology and paves the road to novel building blocks for nanomaterials. Only a limited number of protein cages have been explored and the selection of appropriate cages for a particular application is often guided by their availability in the research groups that are active in this field. However, many more hollow protein structures are known in the biochemical literature, which can considerably increase the range of sizes and shapes of functional protein–polymer conjugates. For example bacterial microcompartments[192-194] or giant viruses[390-395] have not yet been explored as scaffolds to create protein–polymer hybrid nanoparticles, although such large structures would allow encapsulation of a much higher amount of functional cargo, such as polymer-bound catalyst, polymer-bound semiconducting nanoparticles, drugs or MRI contrast agents. Polymerization of conducting polymers in rod-shaped viruses would create polymer-based nanowires. Another interesting possibility is to create designer protein nanostructures from scratch by engineering of protein subunits or oligomers.[76,396-399] Very recently, this approach has led to highly porous protein cubes[76] and unilamellar hollow spheres,[399] but these structures have not been combined with synthetic polymers yet. While most work on protein cages has focused on using their intriguing structures as scaffolds or as capsules, the function of protein cages has seldom been explored. For example, chaperonins provide a folding chamber for unfolded proteins.[227] This environment might therefore also fold single polymer chains, which would be a major contribution to the field of single-chain polymer particles.[400] Moreover, many cages feature gated pores, but this property has not yet been exploited widely to create gated nanoreactors or triggerable drug-release vehicles. The pores in protein cages could also be rendered responsive to non-native stimuli by blocking them with a stimulus-responsive polymer. This would allow, for example creation of controlled drug-delivery cages that release their cargo in response to temperature changes, pH changes or any other of the many stimuli that are well known in polymer chemistry.[401-403] Polymers would also allow loading protein cages with a high density of catalyst molecules, so that highly reactive nanoreactors can be envisioned. They could be used to conduct cascade reactions with improved yield and reduced side reactions. Moreover, such catalyst-loaded cages could be immobilized on the surface of a lab-on-a-chip device, e.g. for biosensing applications. Polymers grafted to the surface of protein cages can render them soluble in organic solvents.[13] If such proteins could be loaded with catalysts,

they could be used as nanoreactors for reactions in organic solvents. A further promising field of research is to use protein cage nanoparticles as templates for nanostructured materials. Protein cages can be self-assembled into 2-D and 3-D arrays. Such arrays could be used as templates to create polymeric materials with a highly ordered and well-defined internal structure. This might result in materials with novel optical or electronic properties, especially when the protein scaffolds are combined with conducting polymers. Engineering of the contact area between individual protein cage particles in such arrays would allow self-assembling of the protein cages into defined orientations, giving rise for an unprecedented degree of control over the position and orientation of encapsulated cargo, such as polymeric or inorganic nanoparticles.

In conclusion, the combination of protein cages with polymers results in novel hybrid nanosystems that combine the advantages of these biomacromolecules and of tailor-made synthetic polymers. Exciting applications, ranging from drug delivery to the preparation of advanced materials, have been addressed in the past and a variety of protein cage–polymer hybrids have been reported. However, this research field is far from maturity, allowing for many new concepts to be developed and explore

Chapter 2

2 Research projects

2.1 Synthesis of functional polymers within a chaperonin for encapsulation and release of biomacromolecules

This chapter will be published as: Rother M., Nussbaumer M. G., Duskey J. T., Postupalenko V. Meier W., Bruns N., Synthesis of functional polymers within a chaperonin by atom-transfer radical polymerization for encapsulation and release of biomacrololecules, **2016**

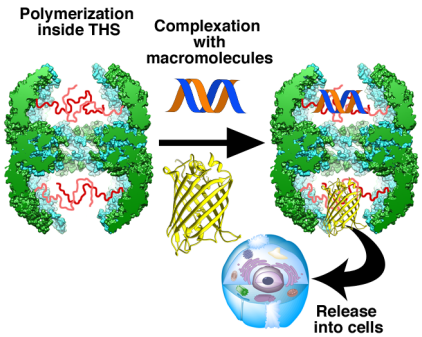

In this chapter, cationic and fluorescent polymers were synthesized in the interior of the protein cage thermosome, a group II chaperonin. This thermosome-polymer conjugate was explored in its interaction with biomacromolecules and their release into mammalian cells. Moreover, the cage structure shielded the cells from toxicity of the cationic charges of the polymer.

2.1.1 Introduction

Nature provides us with different and versatile types of proteins that carry out specific functions such as enzymes,[404-406] membrane proteins,[407,408] antibodies,[409,410] or protein cages.[228,411-413] Protein cages are hollow nanometer sized assemblies from protein subunits.[228,411-413] They are kept together by covalent and non-covalent subunit interactions. Depending on their origin, they play important roles in catalysis, nucleic acid storage and delivery, folding of denatured proteins and molecular storage and regulation.[77,78,234,414-416] Protein cages have recently attracted great

interest as functional and structurally well-defined building blocks for bionanotechnology[77]. They are highly uniform hollow nanoparticles whose structure has been, in many cases, resolved with high resolution. Therefore, they can be site-selectively functionalized on their exterior and their interior via genetic and chemical methods.[78,101] This is an advantage over hollow nano vehicles based on organic or inorganic materials, which have a broader size distribution and cannot be site-selectively modified with that ease as protein cages.[72,81,82] Moreover, they have a remarkable high stability[81] and are biodegradable and biocompatible.[72,149] The properties of protein cages make them ideal candidates for development of nano carriers that can transport cargo to a specific cellular target,[74,82] and as nano reactors for the synthesis of inorganic[60,137,417] or organic materials.[61,62] Protein cages have viral or non-viral origin. The most studied ones are virus-like particles (VLPs) that are derived from viruses and bacteriophages by removing their cargo DNA/RNA.[74,95,105,418] Non-viral protein cages are, for example, ferritins[77], heat-shock proteins,[185,186,213,234,419] chaperonins[187,188,228,235] or vault proteins.[242,316]

Protein cages can be combined with synthetic macromolecules in order to create new hybrid materials that widen the possible applications of these nanostructures.[420,421] Polymers can be attached on the outside of protein cages to alter the properties of the proteins (e.g. prolonged circulation time) or they can be equipped with additional functionalities such as targeting ligands to enhance cellular uptake.[153,154,164,282,283,285,294,297,310,314,322] A constantly growing field are protein cage-polymer conjugates where the polymers are located in the interior of the cages. This allows introducing a higher density of functional molecules into the protein cages, e.g. to create highly efficient magnetic resonance contrast agents, protein cage-polymer conjugates with catalytic activity or gene delivery vehicles.[111,113-115,148,162,163,172,361,362] Commonly used polymerization methods to synthesize protein-polymer conjugates are atom-transfer radical polymerization (ATRP) and radical-addition fragmentation chain transfer (RAFT) polymerization.[15,22,29,33,35,39,40,179,275,422,423]

Many native protein cages have static pores. Ferritin's pores are 0.4 nm in diamter,[211] the pores of Qβ bacteriophage 2.5 nm[264,265] and small heat shock proteins have pores with a diameter of approx. 3 nm.[212,213] However, these pores are too small to allow macromolecular therapeutic cargo, e.g. proteins (~ 50 kDa, approx. 2.5 nm)[424] or duplex 21-mer siRNA (~7 nm length, 2 nm diameter)[371,425-427] to enter the cavity.

From all native protein cages, the pores of chaperonins range among the largest. The thermosome (THS) from *Thermoplasma acidophilum*, a group II chaperonin that was used in this work, is assembled from alternating α- and β-subunits in an eightfold symmetry and has a barrel shape structure, which is approx. 16 nm in outer diameter.[428] In the open state, THS has two large pores (~ 8-10 nm in diameter)[236,237,429] that allow macromolecules like globular proteins (up to 50 kDa)[235] or polymers[61] to enter and leave the cavity (Scheme 1 a & b).

Thus, the THS cage is ideally suited for encapsulation, transport and release of macromolecules. However, macromolecules do not stay permanently in native THS, as they can diffuse out of the cavity when THS is in its open state. In order to address this challenge, cationic polymers can be inserted as an anchor into the THS cavity. The polymer can bind therapeutic macromolecules via electrostatic interactions and therefore prevents the premature release of the cargo from the cavity. A mutated variant (K316C) of native THS was used (Figure 2.1.2a+b).[30] It carries a cysteine (Cys) on the inside of every β-subunit, which allowed covalent attachment of functional molecules in the protein cage. In our previous study, poly(amidoamine) (PAMAM)[430], a cationic dendrimer, was bound to the cysteines via a "grafting-to"-approach in order to bind siRNA within THS.[163] SiRNA was chosen as an example for a biomacromolecule because of its therapeutic properties and importance.[431-433] The oligonucleotide was kept within the THS via electrostatic interactions. However, the PAMAM-approach has its limitations. Being a presynthesized dendrimer, PAMAM cannot include even small amounts of other functional units, is inflexible in its folding and has a very limited scope for further modifications.

In addition, the bulky dendrimer occupies much space in the cavity, limiting the amount of macromolecules (e.g. siRNA) that can be encapsulated. Furthermore, the THS-PAMAM-siRNA complex formed undesired aggregates, most likely because the cargo is not fully encapsulated in the protein cage due to steric reasons. To overcome these issues, a different method was applied in which linear polymers were synthesized in the cavity by a "grafting-from" approach. Maleimide-ATRP initiators were coupled to accessible cysteines (Cys) via Michael-Addition.[434] Then, cationic 2-(dimethylamino)ethyl methacrylate (DMAEMA) was polymerized within the cavity of THS via activators regenerated by electron transfer atom transfer radical polymerization (ARGET ATRP) (Figure 2.1.1a).[46] Copolymerization of DMAEMA with the fluorescent monomer methacryloxyethyl thiocarbamoyl rhodamine B

(RhBMA) (Figure 2.1.1b) allowed synthesizing a polymer with dual functionality within the cage. PDMAEMA is known to bind to negatively charged molecules like nucleic acids and is used for their delivery.[435] The linear polymer chains allowed the entrapment of two times more siRNA into the THS than with the PAMAM-approach. Moreover, cationic polymers were utilized for intracellular delivery of proteins.[436]

The THS-pDMAEMA and THS-pDMAEMA-co-RhBMA conjugates were explored as a delivery platform for siRNA into mammalian U87 cells (Figure 2.1.2c). In addition, enhanced yellow fluorescent protein (eYFP)[437] and a modified variant of the green fluorescent protein (TurboGFP)[438] were complexed to extend our strategy to protein delivery.[439,440]

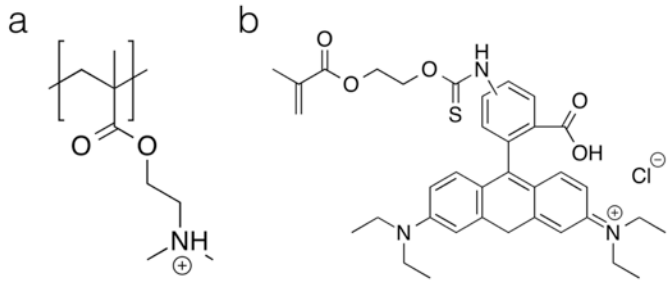

Figure 2.1.1. Chemical structures. (a) pDMAEMA and (b) methacryloxyethyl thiocarbamoyl rhodamine B.

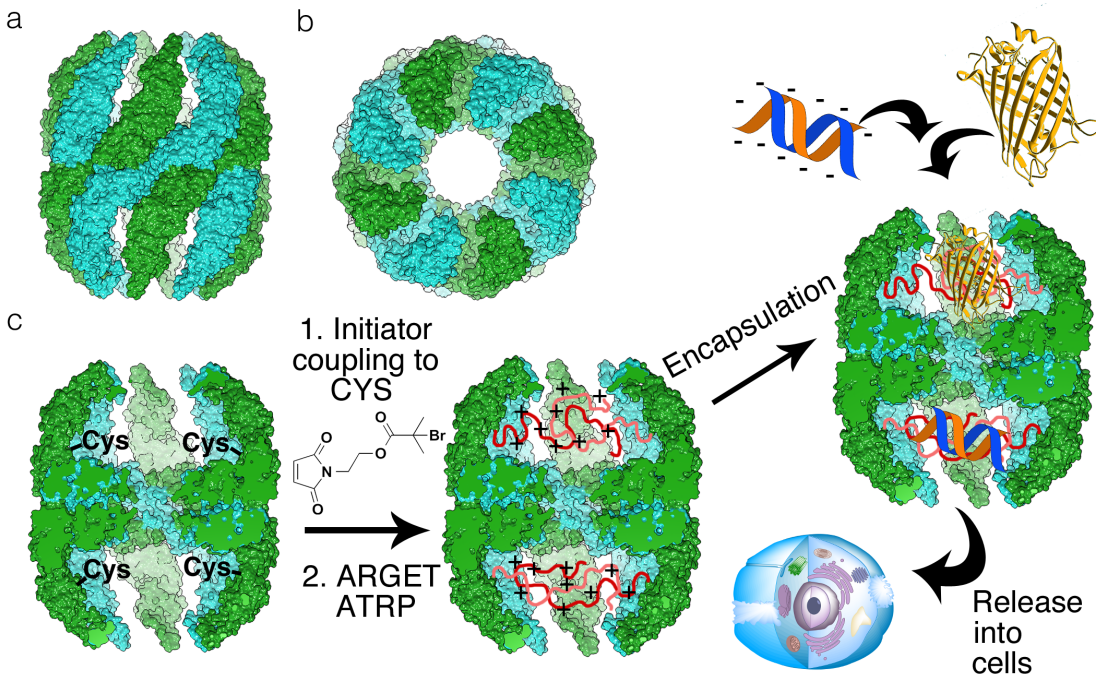

Figure 2.1.2. Structure of THS, polymerization within the cavity of THS, and use of the protein-polymer conjugate to bind and deliver biomacromolecules. Cryo-electron microscopy (cryo-EM) density map of a thermosome in its sideview (a) and top view (b). (c) Cross section of the mutated variant of the native THS, which had one accessible cysteine (Cys) on every β- subunit. Maleimide ATRP-initiators were coupled to the cysteines and the resulting macroinitiator was used for homopolymerization of 2-dimethylaminoethyl methacrylate (DMAEMA) or for copolymerization of DMAEMA with methacryloxyethyl thiocarbamoyl rhodamine B (RhBMA) under ARGET ATRP conditions. Subsequently, siRNA or fluorescent proteins (eYFP, TurboGFP) were complexed within the cavity via electrostatic interaction and delivered into U87 cells.

2.1.2 Results and Discussion

2.1.2.1 Synthesis and characterization of THS-pDMAEMA and THS-pDMAEMA-co-pRhBMA conjugate

Common ATRP reagents with different combinations were tested (Figure 2.1.3), in order to find out at which conditions the cage structure is stable and which lead to degradation (see Tables 2.1.1-2.1.3 and the experimental section for further details). Protein cages were incubated with different single reagents and their combinations in degased H_2O under argon atmosphere for 48 h. After incubation time, the samples were analysed by sodium dodecyl sulphate polyacrylamide gel electrophoresis (SDS-PAGE) and basic native polyacrylamide gel electrophoresis (BN-PAGE). The influence of Cu(I) and Cu(II) on the cage structure in presence and absence of two different ligands (1,1,4,7,10,10-hexamethyltriethylenetetramine (HMTETA)[22] and

tris(2-pyridylmethyl)amine (TPMA)[32] was tested (Figure 2.1.3a+b). Then, we wanted to know the influence of reducing agents (sodium ascorbate (NaAsc) and tin(II)ethyl hexanoate) for Cu(II) complexes, which are commonly applied in ARGET ATRP, on the cage structure (Figure 2.1.3a+b). Moreover, to the tested reagents in various combinations, monomers (hydroxyethyl acrylate (HEA)), ATRP-initiators were added in order to test if the cage keeps its structure under ARGET ATRP conditions (Figures 2.1.3a-c). The THS subunits did not degrade in the presence of Cu(II) (Figure 2.1.2a, lane 2), whereas subunit degradation could be observed in the presence of Cu (I) (Figure 2.1.3a, lane 6). Even when Cu(I) was complexed with HMTETA, subunit degradation could be observed by the appearance of smearing bands (Figure 2.1.3a, lane 8), which was not the case for Cu(II) (Figure 2.1.3a, lane 5). In a comparison between the ligands HMTETA and TPMA, the samples with HMTETA showed no degradation of subunits (e.g. Figure 2.1.3c lane 2), while TPMA showed degradation of the subunits by a smearing (e.g. Figure 2.1.3c, lane 3) in the SDS-PAGE gels. No difference in cage structure was found after treating THS with the reducing agents sodium ascorbate (NaAsc) and tin(II)ethylhexanoate in presence of Cu(II) and HMTETA as ligand. When TPMA was used as ligand, decomposition of the cage was stronger with tin(II)ethylhexanoate (Figure 2.1.3c, lane 9) than with NaAsc (Figure 2.1.3c, lane 8).

THS is stable in the presence of radicals (ARGET ATRP conditions, Figures 2.1.3a-c) as well as in 50 vol% dimethylsulfoxide (DMSO) (Figure 2.1.3d) and 5 vol% methacrylate monomers (Figure 2.1.3e), which is approx. 75’000 monomer units per initiator at 4 initiators per cage (see below). Moreover, a high concentration of Cu (I), even when bound to a ligand, caused disruption of the cage structure. As a consequence, we used HMTETA as ligand and kept the amount of copper very low. At the same time it was desired to generate enough radicals for polymerization within the cavity of THS. Thus, we chose activators regenerated by electron transfer atom transfer radical polymerization (ARGET ATRP) as our polymerization method of choice.[41,46,441] DMSO was chosen as a co-solvent, because preliminary experiments showed a slightly better control over molecular weight of the polymers than with tetrahydrofuran (THF).

From the stability experiments we derived the ARGET ATRP conditions. Copper concentration (as $CuBr_2$ complexed with HMTETA in a 1:1.3-ratio) was chosen to be four times higher than initiators to have an adequate amount of copper that can

create radicals within the cavity of THS. The concentration of the reducing agent NaAsc was chosen to be four times higher than of the Cu-complex. This guaranteed a constant generation of radicals even though concentration of reactants, except monomers, was kept low. We know that the cage structure is stable at a monomer concentration of 5 vol%. For this reason, the monomer concentration was kept below 5 vol% in order not to eventually disrupt the cage structure at higher concentrations.

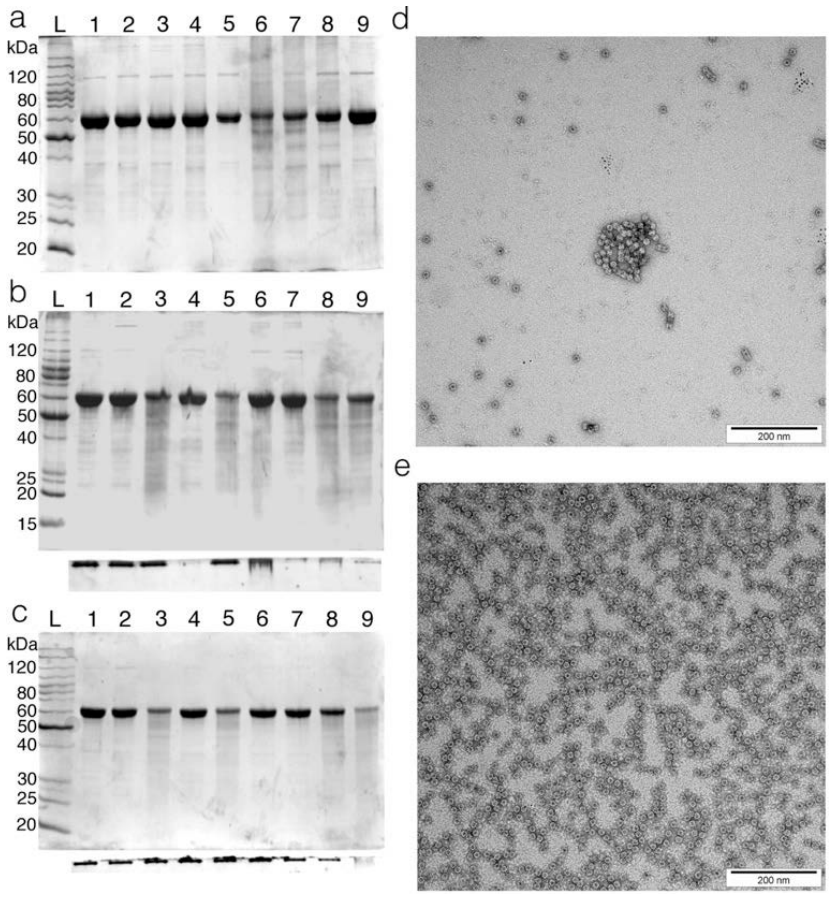

Figure 2.1.3. THS protein cage stability tests to find out at which polymerization conditions the cage remains intact. (a) SDS-PAGE of THS at different reagent compositions. The influence of Cu(I) + Cu(II) in absence and presence of the Ligand HMTETA and reducing agent sodium ascorbate on the cage structure was investigated. In addition, it was tested if the cage structure is stable in presence of radicals. L = protein ladder. Details of the conditions are shown in table 1(b) SDS-PAGE (top) and BN-PAGE (bottom) of THS at different conditions. The influence of Cu (I) + Cu(II) in absence and presence of the Ligand TPMA and reducing agent sodium ascorbate on the cage structure was investigated also in the presence of radicals. Details of the conditions are shown in table 2 (c) SDS-PAGE (top) and BN-PAGE (bottom) of THS at different conditions. The ligands HMTETA and TPMA were compared at various ATRP-conditions. Moreover, the influence of radicals on the cage structure was investigated. Details of the conditions are shown in table 3 (d) THS in DMSO:H_2O 1:1 (v:v). (e) THS in presence of 5 vol% oligo(ethylene glycol) methylether methacrylate (OEGMA, M_n = 480 g mol^{-1}).

Table 2.1.1 (to Figure 2.1.2a). Influence of different parameters (Cu (I) / Cu (II) in presence/absence of HMTETA and presence/absence of Na-ascorbate (NaAsc) on the structure of THS subunits

Figure S 1a	**Lane 1**	**Lane 2**	**Lane 3**	**Lane 4**	**Lane 5**	**Lane 6**	**Lane 7**	**Lane 8**	**Lane 9**
Sample & reagent concentrations	THS (1.1µM)	THS (1.1 µM) $CuBr_2$ (166 µM)	THS (1.1µM) $CuBr_2$ (166 µM) HMTETA (877 µM)	THS (1.1µM) $CuBr_2$ (166 µM) Na-Ascorbate (194 µM)	THS (1.1µM) $CuBr_2$ (166 µM) HMTETA (877 µM) Na-Ascorbate (194 µM)	THS (1.1µM) CuBr (166 µM)	THS (1.1µM) CuBr (166 µM) Na-Ascorbate (194 µM)	THS (1.1µM) CuBr (166 µM) HMTETA (877 µM) Na-Ascorbate (194 µM)	THS (1.1µM) $CuBr_2$ (166 µM) HMTETA (877 µM) Na-Ascorbate (194 µM) Hydroxyethyl acrylate (223 µM) 2-Bromopropionitrile (15µM)
Subunit structure / remarks	Stable	Stable	Stable	Little degradation	Stable (sample conc. was lower)	Degradation of subunits	Degradation of subunits	Degradation of subunits	Stable; Monomer and a source of radicals were added

Table 2.1.2 (to Figure 2.1.2b). Influence of different parameters (Cu(I) /Cu (II) and TPMA as ligand) on the structure of THS. Investigation if the type of ligand changes THS structure

Figure S1b	**Lane 1**	**Lane 2**	**Lane 3**	**Lane 4**	**Lane 5**	**Lane 6**	**Lane 7**	**Lane 8**	**Lane 9**
Sample & reagent concentrations	THS (1.1 µM)	THS (1.1 µM) $CuBr_2$ (175 µM)	THS (1.1 µM) $CuBr_2$ (175 µM) TPMA (363 µM)	THS (1.1 µM) $CuBr_2$ (175 µM) Na-Ascorbate (455 µM)	THS (1.1 µM) $CuBr_2$ (175 µM) TPMA (363 µM) Na-Ascorbate (455 µM)	THS (1.1 µM) CuBr (545 µM)	THS (1.1 µM) CuBr (545 µM) Na-Ascorbate (900 µM)	THS (1.1 µM) CuBr (545 µM) TPMA (700µM) Na-Ascorbate (900 µM)	THS (1.1 µM) $CuBr_2$ (175 µM) TPMA (363 µM) Na-Ascorbate (455 µM) 2-Bromo propionitrile (100 µM) Hydroxyethyl acrylate (53 mM)
Subunit and cage structure / remarks	Stable	Stable	Cage structure intact according to BN-PAGE, but degradation of subunits (SDS-PAGE)	Cage structure disassembled (BN-PAGE); Subunits did not degrade	Cage structure intact (BN-PAGE), degradation of subunits	BN-Page shows uncommon smearing of the native structure, little degradation of subunits (SDS-PAGE)	Only small amount of cage structure visible in BN-PAGE, most disassembled, almost no degradation of subunits	Degradation of cage structure and subunits	Degradation of cage structure and subunits

Table 2.1.3 (to Figure 2.1.2c). Comparison of the ligands HMTETA and TPMA at different conditions and their influence on the THS cage structure.

Figure S1c	**Lane 1**	**Lane 2**	**Lane 3**	**Lane 4**	**Lane 5**	**Lane 6**	**Lane 7**	**Lane 8**	**Lane 9**
Sample & reagent concentrations	THS (1.1 µM)	THS (1.1 µM) $CuBr_2$ (406 µM) HMTETA (860 µM) Na-Ascorbate (860 µM)	THS (1.1µM) $CuBr_2$ (406 µM) TPMA (860 µM) Na-Ascorbate (860 µM)	THS (1.1 µM) $CuBr_2$ (406 µM) HMTETA (860 µM) Tin(II) 2-Ethylhexanoate (860 µM)	THS (1.1 µM) $CuBr_2$ (406 µM) TPMA (860 µM) Tin(II) 2-Ethylhexanoate (860 µM)	THS (1.1 µM) $CuBr_2$ (406 µM) HMTETA (860 µM) Na-Ascorbate (860 µM) Hydroxyethyl methacrylate (53 mM) 2-Bromo propionitrile (200 µM)	THS (1.1 µM) $CuBr_2$ (406 µM) HMTETA (860 µM) Tin(II) 2-Ethylhexanoate (860 µM) Hydroxyethyl methacrylate (53 mM) 2-Bromo propionitrile (200 µM)	THS (1.1 µM) $CuBr_2$ (406 µM) TPMA (860 µM) Na-Ascorbate (860 µM) Hydroxyethyl methacrylate (53 mM) 2-Bromo propionitrile (200 µM)	THS (1.1 µM) $CuBr_2$ (406 µM) TPMA (860 µM) Tin(II) 2-Ethylhexanoate (860 µM) Hydroxyethyl methacrylate (53 mM) 2-Bromo propionitrile (200 µM)
Subunit and cage structure / remarks	Stable cage and subunits	Stable cage and subunits	Stable cage according to BN-PAGE, but degradation of subunits	Stable cage and subunits	Stable cage according to BN-PAGE, but degradation of subunits.	Stable cage and subunits	Stable cage and subunits	Degradation of cage and subunits	Degradation of cage and subunits

Prior to polymerization within the cavity, macro-initiators (THS-Br) were prepared from mutated THS (K316C) and maleimide functionalized ATRP-initiator,[434] which reacted with the cysteines in the interior. In order to assess the amount of initiators within the cavity, THS and THS-Br were labelled with a cysteine-reactive dye (Alexa488 maleimide).

The labelled samples were purified via spin desalting and spin diafiltration and subsequently analysed by fluorescence correlation spectroscopy (FCS) (Figure 2.1.4a). Fitting of the autocorrelation curves were based on one-population fits including triplet state. The obtained diffusion times of THS (408 ±15 µs) and THS-Br (393 ± 26 µs) were almost equal, while the free dye Alexa488-maleimide had a much lower diffusion time (35 µs ± 3.3 µs). Hydrodynamic diameters and molecular brightness (counts per molecule (CPM)) were then calculated based on equations 1 and the equations in the experimental section. Free dye (Alexa488-maleimide) had a molecular brightness of CPM = 5.6 kHz, and a hydrodynamic diameter of 1.1 ± 0.1 nm. In contrast, labelled THS revealed CPM of 31.2 ± 0.9 kHz, and a hydrodynamic diameter of 13.1 ± 0.5 nm. For THS-Br a CPM value of 12.0 ± 0.5 KHz, and a hydrodynamic diameter of 12.7 ± 0.8 nm was calculated. The number of dyes within the cavity was calculated by comparing CPM values according to equation (1).

$$\frac{CPM_{sample}}{CPM_{free\ dye}} = \#\ dyes\ THS^{-1} \qquad (1)$$

5.6 ± 0.2 dye molecules were obtained per THS, whereas THS-Br contained only 2.1 ± 0.1 dye molecules in average (Figure 2.1.4b). From these values we can conclude that from the 6 available cysteines from THS, 4 could be modified with ATRP-initiators (6 cysteines in THS minus 2 that could be modified in the THS-Br). The initiators could not be bound to all cysteines in the interior. A possible explanation for the deviation from a theoretical value of 8 available cysteines might be that our THS was in average not composed of an equal ratio of 8 α- and β-subunits. It rather had more α-subunits that did not have an assessable cysteine in the interior. Mass spectrometry was unfortunately not conclusive, because the different subunits could not be resolved and merged into one signal.

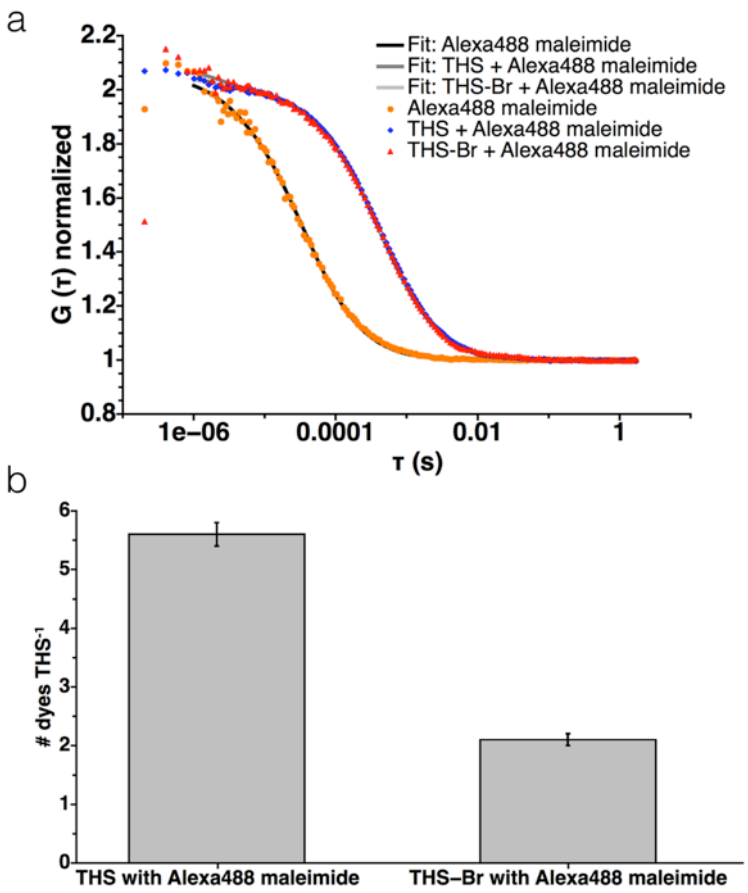

Figure 2.1.4. Determination of available cysteines in THS and THS-Br by coupling of Alexa488 maleimide to Cys and fluorescence correlation spectroscopy (FCS). (a) Normalized autocorrelation curve of Alexa488 maleimide dye, THS that was incubated with Alexa488 dye and THS-Br that was incubated with Alexa488 dye. (b) Calculated number of bound dyes per THS and THS-Br (as derived from the counts per molecule according to equation (1)).

Polymerizations were conducted with the THS-Br macroinitiator. The monomer-to-initiator ratio was varied in order to vary the molecular weight of the THS-polymer conjugates. The different amounts of monomers that were used for the synthesis of the discussed protein-polymer conjugates are combined in Table 4. Homopolymers from 2-dimethylaminoethy methacrylate (DMAEMA) and copolymers of DMAEMA and methacryloxyethyl thiocarbamoyl rhodamine B (RhBMA) were synthesized with the interior. The reaction parameters for the synthesis of protein polymer conjugates are summarized in Table 2 in the experimental section. In this study three different THS-pDMAEMA conjugates were synthesized with an increasing amount of monomers in respect to initiators (from 5'000 monomers per initiator to 15'000) (Table 1). As comparison a bovine serum albumin (BSA, Mw ~ 64'000 g mol^{-1}) pDMAEMA conjugate (BSA-pDMAEMA) with 15'000 monomers per initiator was

synthesized (Table 2.1.4). BSA was chosen, because it is a globular protein that has approximately the same molecular weight as a THS-subunit.

Table 2.1.4. THS-polymer and BSA-polymer conjugates of this study.

Name	n(DMAEMA) per initiator ; n(RhBMA) per initiator amount of initiators: 4 per THS, 1 per BSA
THS-pDMAEMA1	5'000 ; --
THS-pDMAEMA2	10'000; --
THS-pDMAEMA3	15'000; --
BSA-pDMAEMA	15'000; --
THS-pDMAEMA-co-pRhBMA	15'000; 40

Several methods were applied to determine if the synthesized samples contain polymers that are bound to the protein. THS and THS-polymer conjugates were analysed by matrix-assisted laser desorption/ionization time-of-flight mass spectrometry (MALDI-ToF MS) (Figure 2.1.5). The cage structure disassembled most likely due to the impact energy of the laser and therefore only subunits could be analysed by this method. The MS spectrum of THS (Figure 2.1.5a, red curve) doesn`t show two separated masses for the α- and β-subunits as expected, but more an averaged spectrum of both. Therefore, it was not possible to show the attachment of small molecules (e.g. ATRP-initiators) to the β-subunits by mass spectrometry. The presence of polymers attached to the protein subunits could be shown by a clear shift of the subunits to higher molecular weight (Figure 2.1.5a, black curve) when compared with the MS-spectrum of THS (Figure 2.1.5a, red curve). Moreover, only conjugates of reactions in which the molar ratio of DMAEMA to initiator was 50:1 or less could be evaporated and analyzed. It was possible to calculate the size of the polymers by subtracting the MS spectrum of THS from the MS spectrum of the conjugates. For the conjugates with a monomer to initiator ratio of 50:1, most of the

polymers had a molecular weight between 200 - 1400 g mol^{-1}, which in average corresponds to 1.2 to 9 monomers per protein subunit. Higher DMAEMA amounts per initiator decreased the signal of the conjugate dramatically that no analysis was possible.

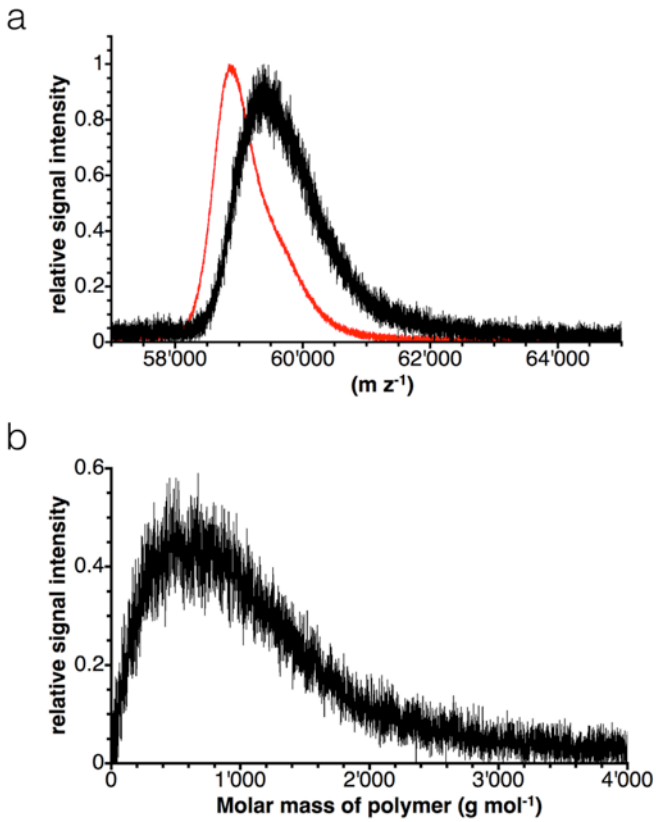

Figure 2.1.5. Matrix-assisted laser desorption ionization mass spectroscopy (MALDI-ToF MS) THS and THS-poly(DMAEMA). (a) MS spectrum of THS (red curve) and MS spectrum of THS-poly(DMAEMA) (black curve) with a ratio of DMAEMA: initiator = 50:1 used for reaction.(b) Calculated spectrum of poly(DMAEMA). Spectrum was calculated by subtracting the MS spectrum of empty THS from THS-poly(DMAEMA).

Sodium dodecyl sulphate polyacrylamide gel electrophoresis (SDS-PAGE) was used to assess the formation of THS-polymer conjugates. Under denaturing conditions, the cage is dissembled into its subunits, which have a molecular weight around 60'000 g mol^{-1} (Figure 2.1.6a). In addition, dimers of the subunits can be observed in a less pronounced band at approx. 120'000 g mol^{-1} and tetramers in an even less pronounced band at approx. 250'000 g mol^{-1}. The tetramer band is more promiment with the THS-pDMAEMA samples (Figure 2.1.6a, lanes 2-4). Dissembled protein cage-polymer conjugate subunits have a higher molecular weight than the subunits with no modification. They have a lower electrophoretic mobility, which can be seen

on the gel. In addition, conjugate samples moved as streaks under electrophoresis conditions due to the attached polymers (Figure 2.1.6a, lanes 3-5).

THS-pDMAEMA conjugates showed weak streaking towards higher molecular weights (Figure 2.1.6a, lanes 3+4), whereas pure THS did not show this smearing of bands (Figure 2.1.6a, lane 1). With an increasing amount of monomers, from 5'000 monomers per initiator (THS-pDMAEMA1, Figure 2.1.6a, lane 2) to 10'000 (THS-pDMAEMA2, Figure 2.1.6a lane 3) and 15'000 (THS-pDMAEMA3, Figure 2.1.6a, lane 4), the smearing of bands to higher molecular weights in the THS-polymer conjugates increased. The increase of smearing bands can be associated with increased polymer chain lengths that are attached to the proteins. This increase is, in addition, visualized as a two-dimensional intensity plot in which the sample density is plotted against the molecular weight (Figure 2.1.6b). In those two-dimensional plots it is visible that the THSpDMAEMA3 sample moved towards higher molecular weights when compared with THS-pDMAEMA2 and especially THS-pDMAEMA1. A molecular weight range between 50'000 g mol^{-1} and 100'000 g mol^{-1} was chosen for the samples, because in this range the single subunits with attached polymers are located. Like in the mass spectrometry analysis a shift to higher molecular weights is visible with the THS-pDMAEMA2 and THS-pDMAEMA3 samples (Figure 2.1.6b). The subunits with polymers of THS-pDMAEMA2 shifted less (500 g mol^{-1}) to higher molecular weights than THS-pDMAEMA3 (1500 g mol^{-1}) in comparison to THS. In addition, the THS-pDMAEMA3 sample covers a higher molecular weight range from approx. 62'000 g mol^{-1} to around 90'000 g $mol^{-1,}$ whereas the THS-pDMAEMA2 sample ranges from around 60'000 g mol^{-1} to 80'000 g mol^{-1}. The THS-pDMAEMA1 sample did not show any shift or streaking like the other conjugate samples. A reason might be that the polymer were so small that gel electrophoresis could not resolve the little difference between the conjugate and THS. Gel electrophoresis has a limited resolution.

From these observations we conclude that with an increasing amount of monomer per initiator the polymer chain length in the conjugates increased. Thus, for our synthesis conditions, the monomer-to-initiator ratio is a parameter that influences the chain lengths of the polymers in protein-polymer conjugate synthesis.

In addition to the monomer-to-initiator parameter that influenced chain growth of the polymers, we wanted to know if the cage structure also influenced the polymerization reaction. From previous investigations in our group, we knew that the

cage structure improved the control of polymer synthesis.[61] However, the difference to our reported study is that polymers were synthesized in THS or with BSA that were not covalently bound to the proteins.[61] For this reason, THS-pDMAEMA3 (Figure 2.1.6a, lane 4) was compared with a BSA-pDMAEMA conjugate (Figure 2.1.6a, lane 5). Both conjugates were synthesized under same conditions and with the same monomer-to-initiator ratio of 15'000:1. The BSA-pDAMEMA conjugate also showed the blurring of bands to higher molecular weights, however, polymers were smaller in the THS-pDMAEMA3 conjugate sample. A direct comparison between THS-pDMAEMA3 (black line) and BSA-pDMAEMA (purple line) in the two-dimensional intensity plot confirms this observation (Figure 2.1.6b). From this observation we conclude that the cage structure has an influence on the polymerization, most likely due to steric hindrance of the protein cage. Access of the catalysts and monomers into the cavity is limited when compared with BSA that does not have a shielding cage structure. Thus, the confined space of THS influenced the polymerization.

From both analytical methods we can conclude that MALDI-ToF is for conjugates with shorter chain lengths. Conjugates with longer chain lengths can not be analysed by MALDI-ToF, but with SDS-PAGE. SDS-PAGE, however, has its limitations with shorter conjugates due to its limitation in resolution.

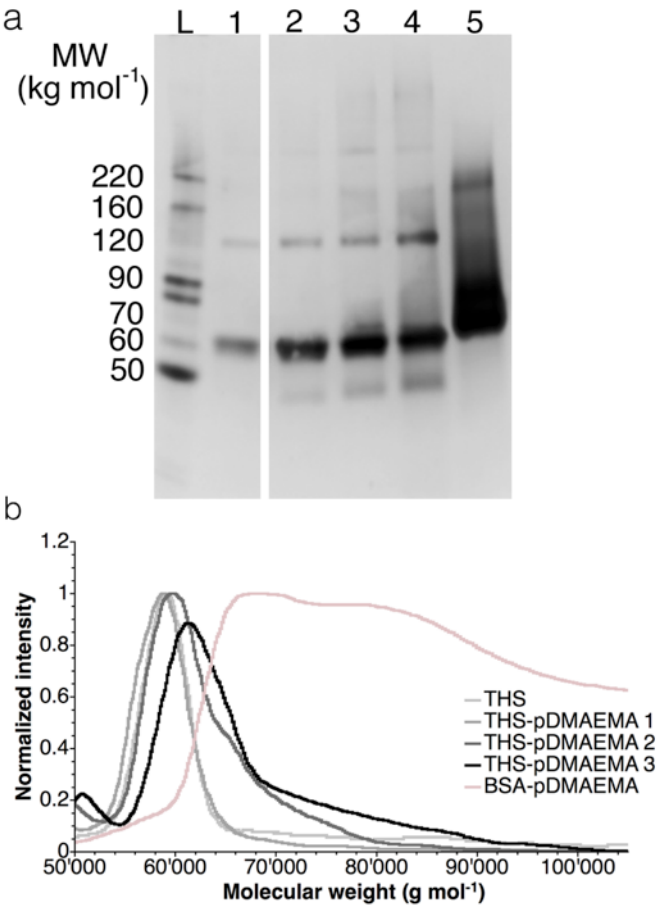

Figure 2.1.6. SDS-PAGE of THS-poly(DMAEMA) and BSA-poly(DMAEMA) conjugates. (a) Lane L = protein ladder, lane 1 = THS, lane 2 = THS-pDMAEMA 1, lane 3 = THS-pDMAEMA 2, lane 4 = THS-pDMAEMA 3, lane 5 = BSA-pDMAEMA. The gel was stained with silver nitrate. (b) Normalized 2D-plots of the SDS-gels of the analysed conjugates shown in a molecular weight range from 50'000 g mol^{-1} to 100'000 g mol^{-1}, i.e. in the range in which the THS subunit-polymer conjugates were located. The calibration curve for determination of molecular weights of the conjugates is shown in the experimental section.

Besides the synthesis of homopolymers also copolymers were synthesized within THS. As comonomer, we chose methacryloxyethyl thiocarbamoyl rhodamine B (RhBMA). THS and THS-pDMAEMA3 have the same absorbance spectrum, while THS-pDMAEMA-co-RhBMA has an additional peak for the RhBMA with an absorbance maximum at 560 nm (Figure 2.1.7a). RhBMA is a fluorescent monomer and can be quantified by UV/Vis (Figure 2.1.7a). For the THS-pDMAEMA-co-RhBMA sample with 15'000 DMAEMA and 40 RhBMA monomers per initiator, an amount of 5 RhBMA molecules per THS-polymer conjugate was calculated. Like THS-pDMAEMA3 (Figure 2.1.7b left gel, lane 2), THS-pDMAEMA-co-RhBMA (Figure 2.1.6b left gel, lane 3) shows a shift to higher molecular weights and a band

streaking in SDS-PAGE. The fluorescence of the conjugate was proven by fluorescence analysis under UV-light of the gel (Figure 2.1.7b right gel, lane 3).

SDS PAGE analysis was complemented by basic native polyacrylamide gel electrophoresis (BN-PAGE) of the conjugates (Figure 2.1.7c). In BN-PAGE proteins are not denatured and therefore it can be used to determine if the cage structure remained intact after polymerization. The empty THS cage (Figure 2.1.7c, left gel, lane 1) had the same electrophoretic mobility than the THS-polymer conjugates (Figure 2.1.7c, left gel, lane 2+3). The results show an intact cage structure of the conjugates. The fluorescence of THS-pDMAEMA-co-RhBMA was also observed in BN-PAGE (Figure 2.1.7c, left gel, lane 3). Furthermore, in BN-PAGE analysis two lines of THS occur in every sample. The two lines are more apparent in the THS-pDMAEMA-co-pRHBMA sample due to the presence of fluorescent molecules (Figure 2.1.7c, right gel, lane 3). At certain conditions, THS can occur in two different open conformations, a fully opened and half-opened, so-called bullet shaped conformation.[238] We assume that the bullet shaped THS is less bulky than the opened THS. The fully open conformation interacts more with the acrylamide gel. Therefore, the bullet-shaped THS migrates further. The band of the bullet-shaped THS is more prominent visible in the gels (Figure 2.1.7c, left gel).

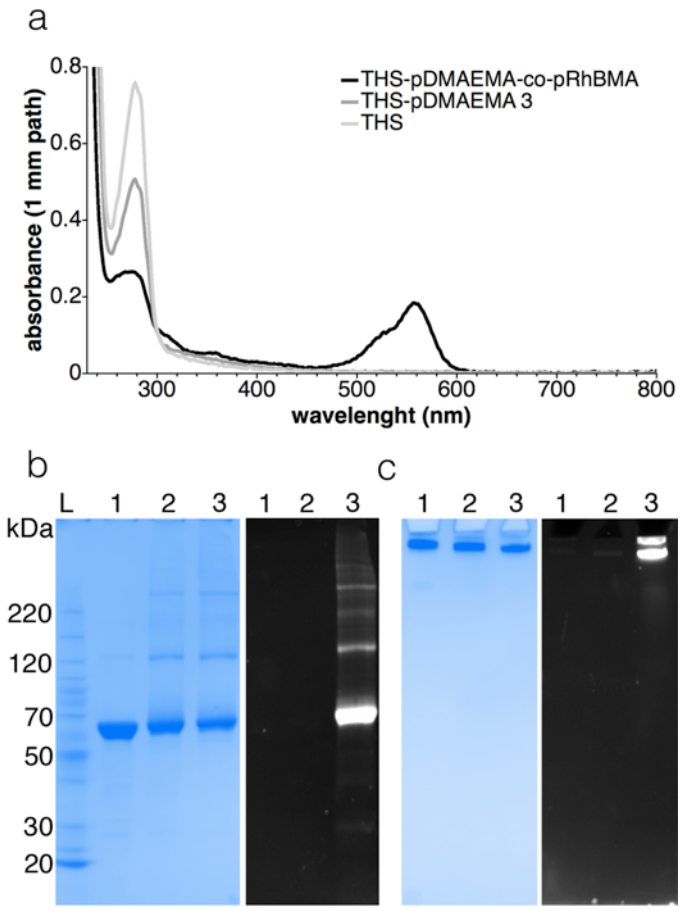

Figure 2.1.7. Spectroscopic and gel electrophoretic characterization of THS and THS-conjugates. (a) UV/Vis of THS, THS-pDMAEMA3 and THS-pDMAEMA-co-pRhBMA. (b) Gel electrophoresis characterization of THS and THS-polymer conjugates. L = protein ladder. (1) = THS protein cage, (2) THS-pDMAEMA 3 (3) THS-pDMAEMA-co-pRhBMA. (a) SDS-PAGE of THS and THS-polymer conjugates. Left gel: Coomassie staining, right gel: fluorescence image (b) BN-PAGE electrophoresis of THS and THS-polymer conjugates. Left gel: coomassie staining, right gel: fluorescence image.

The different cage shapes of the empty THS and THS-polymer conjugates can be seen in the transmission electron microscopy images (Figures 2.1.8–2.1.10). Fully open and bullet-shaped protein cages can be found in the images of the analysed samples.

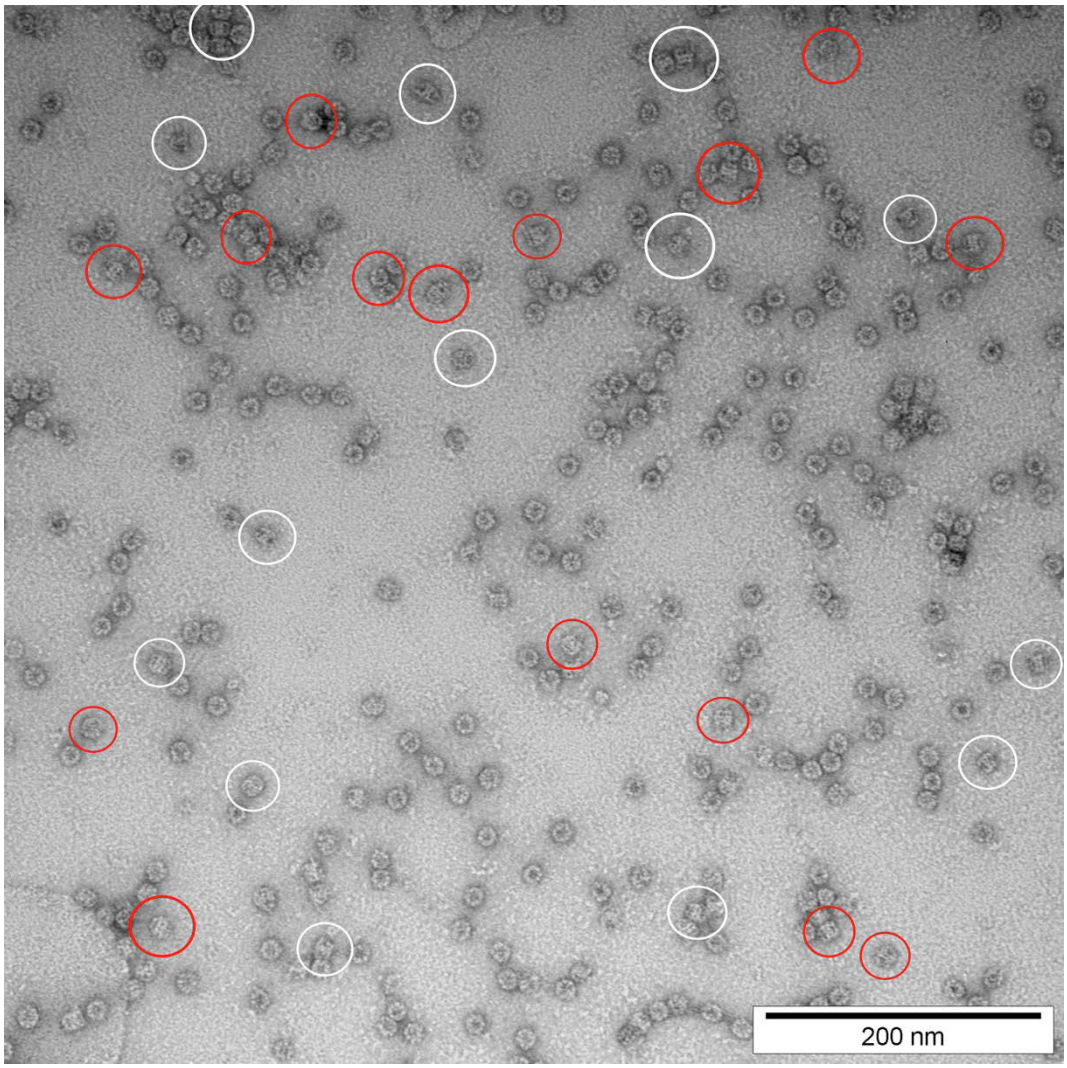

Figure 2.1.8. Transmission electron microscopy images (TEM) of empty THS protein cages. Red circles = side views of bullet-shaped THS, white circles = side views of fully open THS. Scale bar is 200 nm.

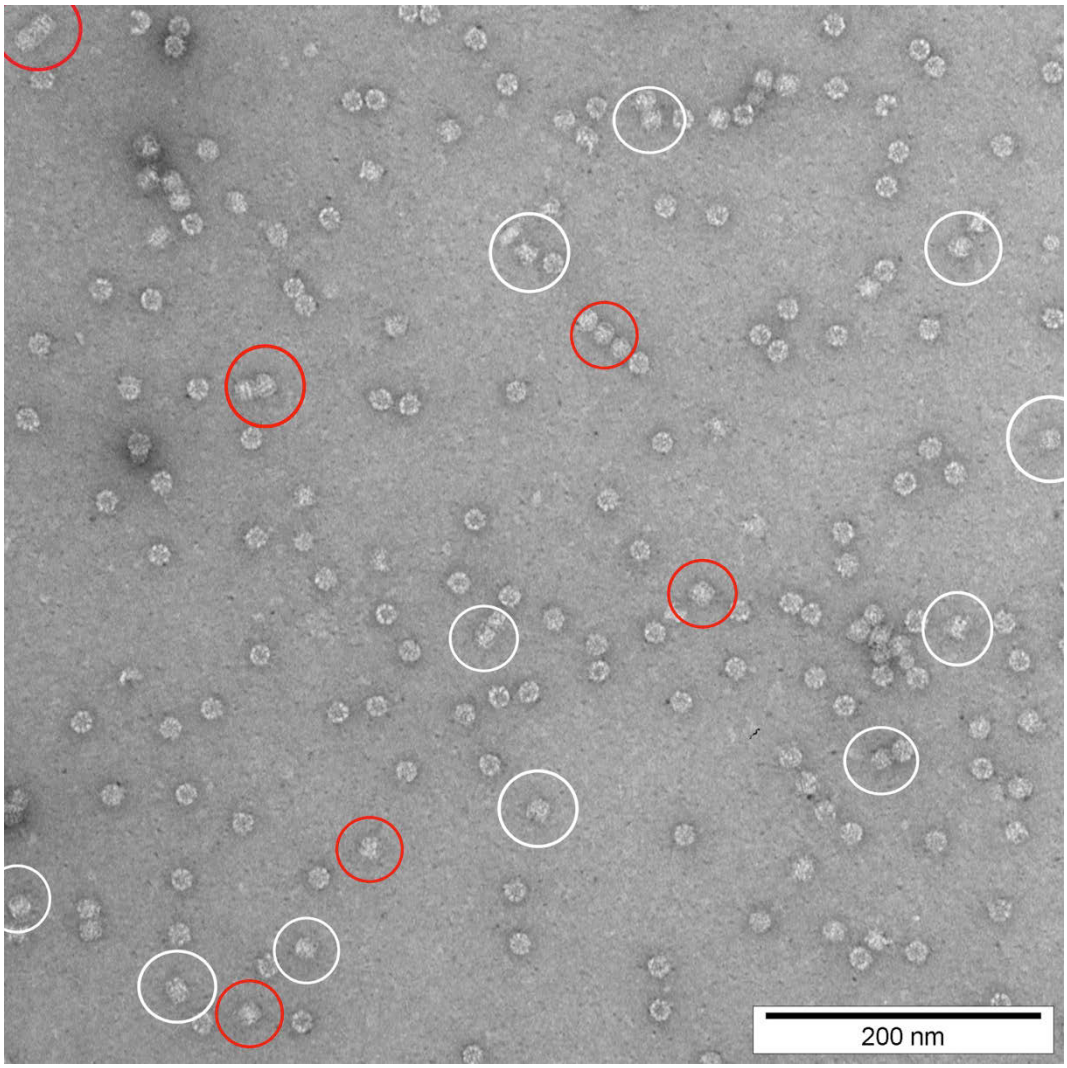

Figure 2.1.9. Transmission electron microscopy images (TEM) of THS-pDMAEMA3 protein cages. Red circles = side views of bullet-shaped THS-pDMAEMA 3, white circles = side views of fully open THS-pDMAEMA 3. Scale bar is 200 nm.

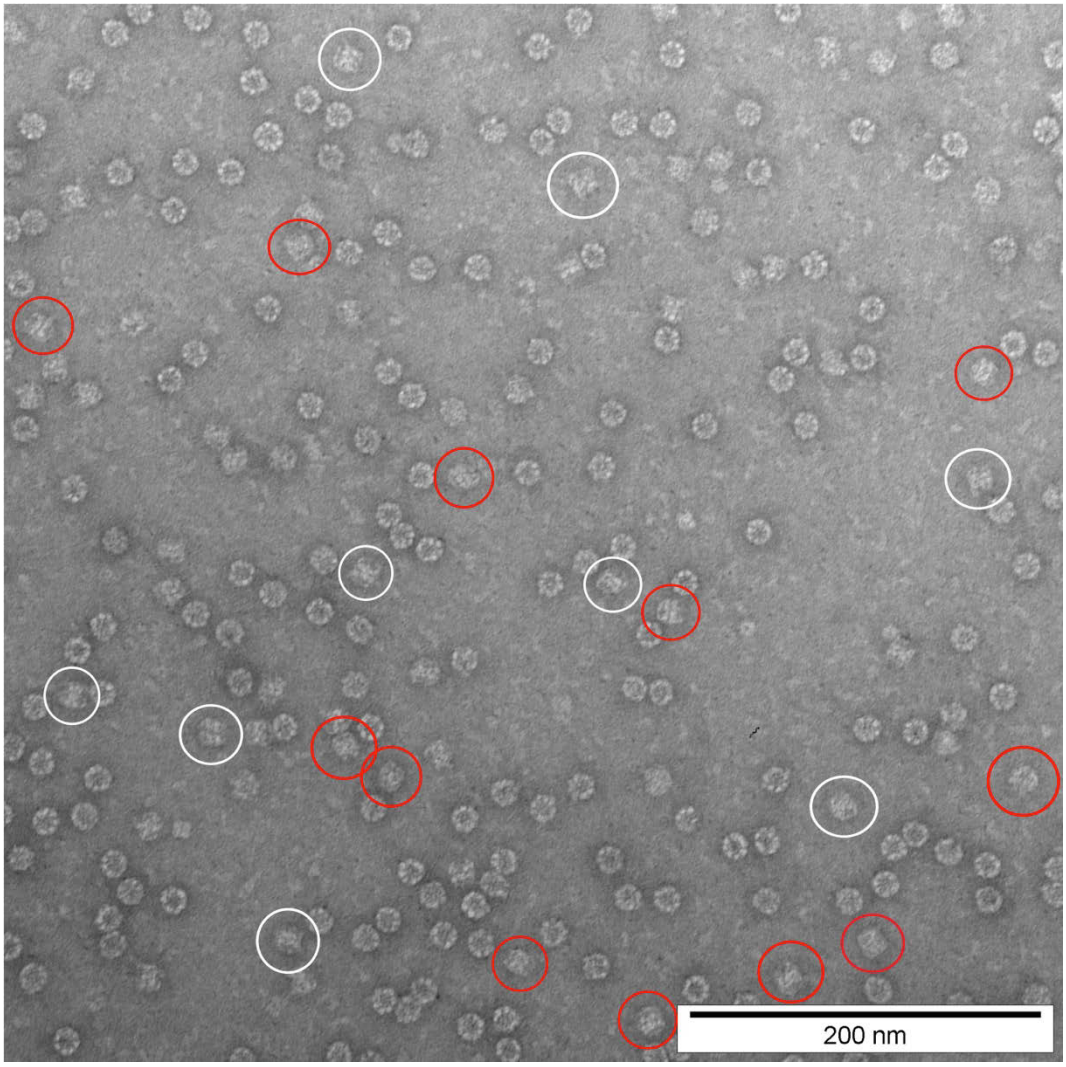

Figure 2.1.10. Transmission electron microscopy images of THS-pDMAEMA-co-RhBMA protein cages. Red circles = side views of bullet-shaped THS-pDMAEMA-co-RhBMA, white circles = side views of fully open THS-pDMAEMA-co-RhBMA. Scale bar is 200 nm.

Dynamic light scattering (DLS) and transmission electron microscopy (TEM) provided additional proof of an intact cage structure after polymerization (Figure 2.1.11a-c). The conjugates have the same size and structure than the empty cage. The DLS and TEM-results are in good agreement with the size and structure of THS reported in literature.[428]

DLS shows, in addition, that the polymer chains are mainly located within the cage because the size of the cage did not increase after polymerization.

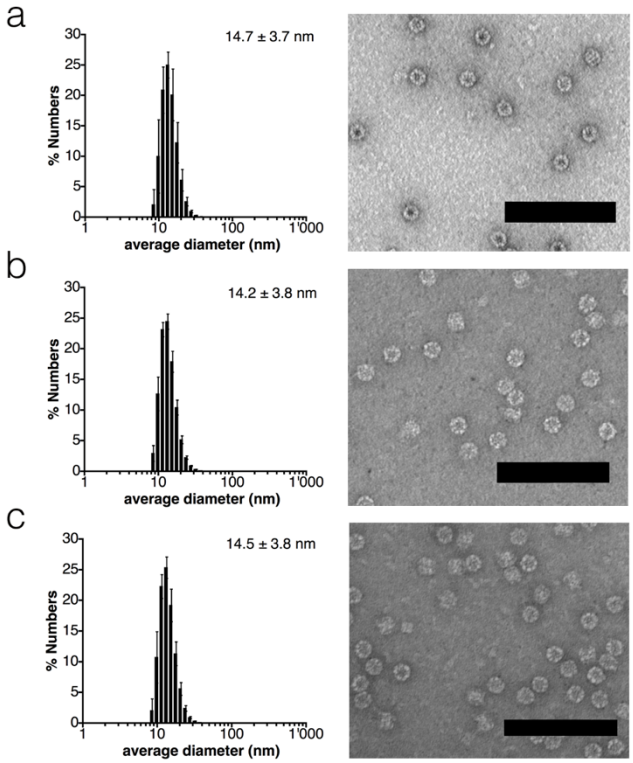

Figure 2.1.11. Dynamic light scattering and transmission electron microscopy of THS and THS-polymer conjugates. (a) THS, (b) THS-pDMAEMA 3 and (c) THS-pDMAEMA-co-pRhBMA. (a) – (c) left panels: DLS measurement of empty THS protein cage (top), THS-pDMAEMA 3 (middle) and THS-pDMAEMA-co-pRhBMA (bottom). (a)-(c) right panels: TEM image of empty THS protein cage (top), THS-pDMAEMA 3 (middle) and THS-pDMAEMA-co-pRhBMA (bottom). TEM scale bars are 100 nm.

2.1.2.2 Interaction of THS-pDMAEMA conjugates with siRNA

PDMAEMA is known to bind DNA and RNA due to its cationic charges that interact with the negative charges of the nucleic acids.[435] We confirm findings from literature that pDMAEMA (Figure 2.1.12a) is capable to bind siRNA (Figure 2.1.12b).[435]

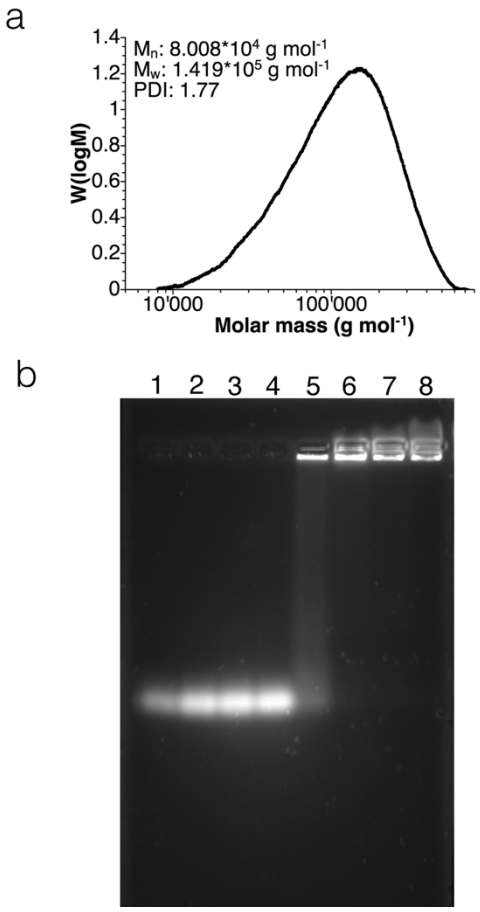

Figure 2.1.12. Characterization of the polymer that was used in this study and its binding capacity to siRNA. (a) Gel-permeation chromatography curve of pDMAEMA, which was synthesized by ARGET ATRP. (b) Agarose gel of pDMAEMA complexed with siRNA.

Moreover, from our previous investigations we know, that macromolecules like siRNA can be encapsulated within THS.[379] To follow up with these results, we were interested, if our new THS-polymer conjugate can be used as siRNA delivery agent. Therefore, we investigated the siRNA binding capacity of the THS-pDMAEMA conjugates. With the electrophoretic mobility shift assay (EMSA), the interaction and binding capacity of a host (THS-pDMAEMA) towards a guest (siRNA) can be estimated.[442] In this agarose gel assay, samples with a constant amount of siRNA were incubated with increasing amounts of THS-pDMAEMA conjugates. For comparison, bare siRNA is shown in lane 1 of the gels. The agarose gels in Figure 2.1.13a show that THS-pDMAEMA 1 did not bind any siRNA at any of the

investigated siRNA-to-THS-pDMAEMA ratios. From a ratio of 1:0.25, THS-pDMAEMA2 bound siRNA, albeit not completely (Figure 2.1.13a, middle gel, lane 4). With THS-pDAMEMA3, binding occured already at the lowest molar ratio (1:0.06) between siRNA and THS-pDAMEMA used for the experiment. Only very little free siRNA was observed in the sample with a siRNA-to-THS-pDAMEMA ratio of 1:0.25 and no free siRNA was observed at a ratio of 1:0.5 (Figure 2.1.13a, right gel, lanes 4+5) and at higher THS-pDMAEMA concentrations. Therefore, full binding of siRNA was achieved with the sample THS-pDMAEMA3. From the results we could estimate that between 2 and 4 siRNAs were encapsulated within the cavity of THS-pDMAEMA3. This estimation is justified with the argument that in the THS-pDMAEMA3 sample with a 1:0.25 ratio, almost no free siRNA could be detected. THS-pDMAEMA does not have any functional groups that actively drag siRNA into its cavity. This means that in a saturated host-guest system, still free species can exist even though most of it could be bound. In addition, a part of the sample migrated in the opposite direction of the normal migration direction of nucleotides (Figure 2.1.13a, left gel, lane 4). This indicates that THS-pDMAEMA3 conjugates in solution existed that had excess in positive charges and did not completely bind the siRNA. Eventually after longer incubation time than in the performed experiment (30 min.) the equilibrium could be shifted towards more binding and thus the disappearing of the weak free siRNA band. The overcompensation of positive charges is even more present in the samples with higher ratios 1:0.5 and 1:0.85 (Figure 2.1.13a, left gel, lane 5 and 6).

From the EMSA assay experiments we found out that THS-pDMAEMA can bind siRNA. In addition, we wanted to know if the THS itself is capable to encapsulate and bind siRNA. This investigation is important to justify the polymers in the cavity of THS. Comparing Figure 2.1.13b, left gel (siRNA, gel red stained) and Figure 2.1.13b right gel (THS, coomassie blue stained) we see that both compounds are separated from each other and do not form a complex. Form this experiment we can conclude that pDMAEMA is necessary for encapsulation and binding of siRNA.

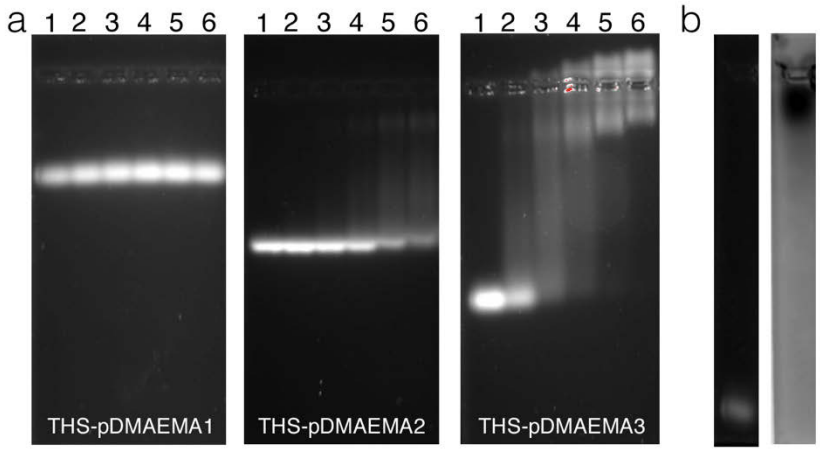

Figure 2.1.13. The presence of polymers and their chain lenght is crucial for siRNA binding. (a) Agarose gels of THS-pDMAEMA samples with different siRNA-to-THS-pDMAEMA ratios. Samples were run for different duration, thus the different migration lengths. The siRNA was stained with GelRed and visualized by fluorescence. The applied ratios between THS-pDMAEMA and siRNA are described in the experimental part. (b) Electrophoretic mobility shift assay (EMSA) of a mixture of siRNA and THS. Left gel: siRNA, gel red stained and fluorescence imaged. Right Gel: THS, coomassie blue stained and imaged with visible light.

The THS-pDMAEMA 3 conjugate is the most promising sample for further investigations. Therefore, we decided to conduct further experiments with this sample. THS-pDMAEMA3 was compared with pDMAEMA in the presence of siRNA. We wanted to know if any structural changes occur when samples are complexed with siRNA. PDMAEMA is a linear polymer and THS-pDMAEMA, in contrast, has the cage structure that shields the polymer chains and can prevent interaction with neighbouring molecules. Dynamic light scattering (DLS) was performed with THS-pDMAEMA3 (Figure 2.1.14a) and for comparison with pDMAEMA in presence of siRNA (Figure 2.1.14b). The size of THS-pDMAEMA 3 complexed with siRNA (14.6 ± 4.0 nm) did not increase in size, compared to THS-pDMAEMA 3 without siRNA (14.2 ± 3.8 nm, Figure 2.1.11b). This result was, in addition, confirmed by TEM (Figure 2.1.15). Another observation from the DLS measurement of THS-pDMAEMA complexed with siRNA was that aggregates of the protein cage were not formed. In contrast, pDMAEMA complexed with siRNA formed larger (~ 600 nm), highly polydisperse aggregates (Figure 2.1.14b). It is known from literature that pDMAEMA complexed with e.g. DNA or RNA can form inhomogeneous aggregates.[443] Aggregate formation was, in addition, observed by the formation of a slightly turbid solution. Since no surrounding structure shielded the

polymer chains, aggregates were formed in a random fashion. The feature that THS-pDMAEMA did not form aggregates is beneficial in delivery applications,[444] because the transporter is more defined in its structure.

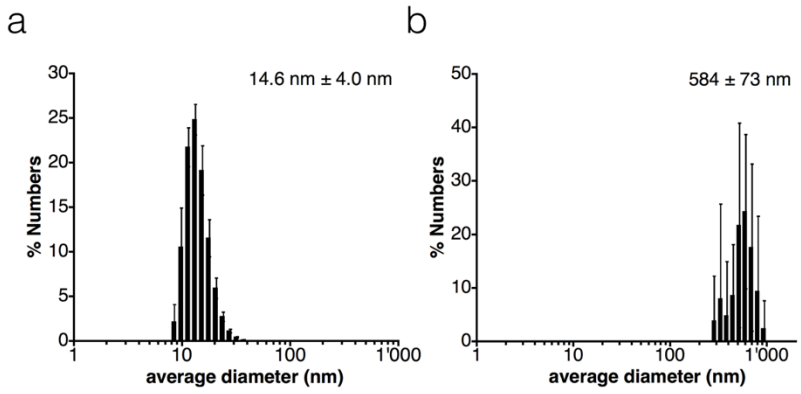

Figure 2.1.14. The cage structure of THS-pDMAEMA prevented aggregate formation when complexed with siRNA. (a) DLS measurement of THS-pDMAEMA3 incubated with siRNA. (b) PDMAEMA incubated with siRNA.

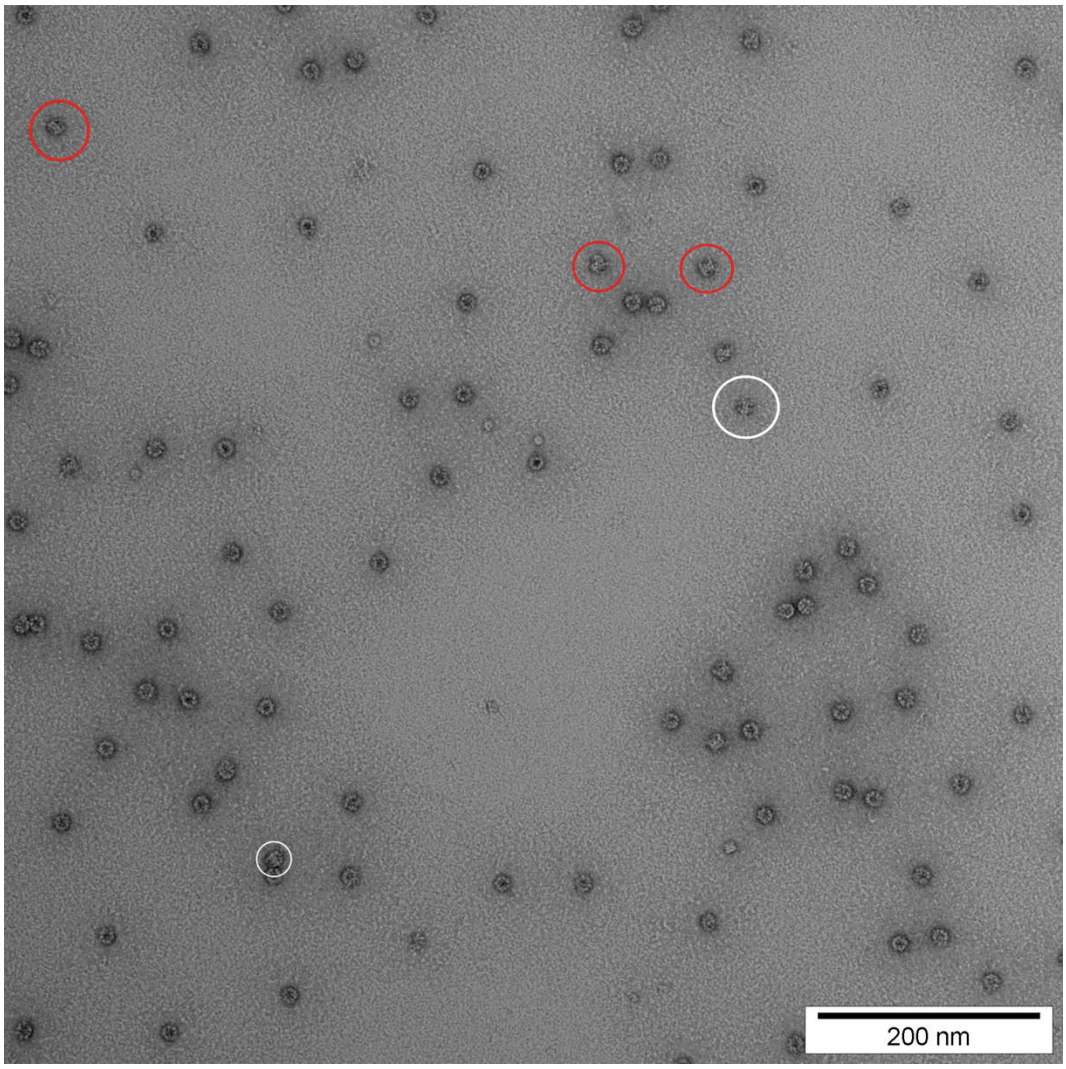

Figure 2.1.15. Transmission electron microscopy (TEM) image of THS-pDMAEMA3 protein cages that were incubated with siRNA. The amount of siRNA was 14 times higher than THS-pDMAEMA3. Red circles = side views of bullet-shaped THS-pDMAEMA-co-RhBMA, white circles = side views of fully open THS-pDMAEMA-co-RhBMA. Scale bar is 200 nm.

2.1.2.3 Protection of siRNA by degradation from RNAses

A further important aspect in siRNA delivery is the protection of siRNA from degrading enzymes (RNAses) that are present in extracellular fluids.[445] In order to assess the protection capability of THS-pDMAEMA3 a digestion experiment was conducted in which THS-pDMAEMA3 was first incubated with siRNA and then RNAse, a RNA degrading enzyme, was added to the solution (Figure 2.1.16a, top gel). As comparison, bare siRNA without any protection was incubated with RNAse (Figure 2.1.16a, bottom gel). At particular time intervals, samples were withdrawn and the degradation reaction stopped. This allowed the quantification of siRNA degradation at specific time points. After 10min. incubation of samples with RNAse,

less than 1 % of THS-pDMAEMA3 protected siRNA was degraded (Figure 2.1.16b, black curve), whereas at the same time, bare siRNA in presence was degraded already to over 80 % of its starting concentration (Figure 2.1.16b, red curve). After 50 min. incubation time, still 50 % of siRNA was intact in the THS-pDMAEMA3 sample, while the amount of unprotected siRNA dropped to 6 % of the starting concentration after this time. The unprotected siRNA was degraded very fast, as can be seen in the graph and also shown by Urban-Klein et al.[446] This result is comparable to our previous THS-PAMAM approach[163] a PAMAM-only approach[447] and with the work of Kong et al,[448] who used a PEGylated pDMAEMA for the complexation of siRNA.

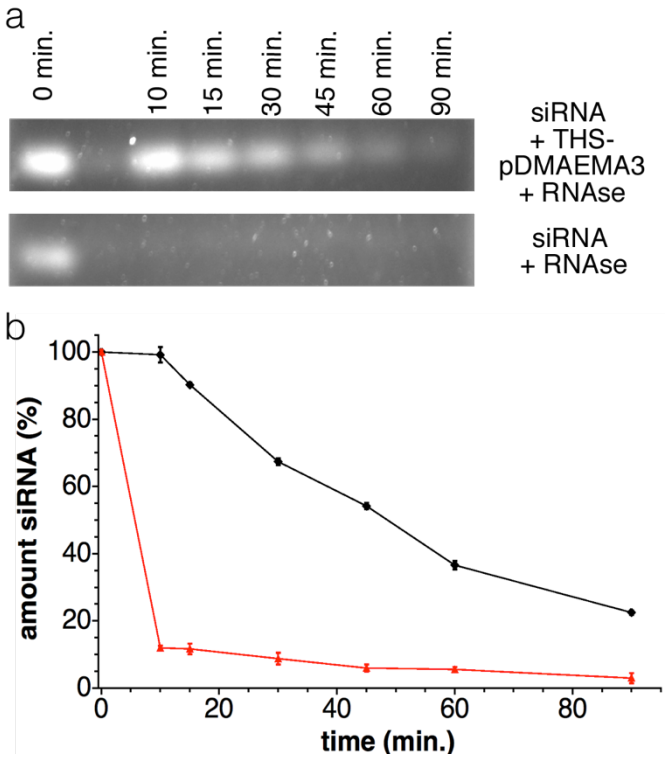

Figure 2.1.16. THS-pDAMEAM3 can protect siRNA from degradation by RNAse II. (a) Agarose gels of siRNA + THS-p(DMAEMA) (upper gel) and of free siRNA (lower gel). (b) Decay curve of siRNA protected by THS-pDMAEMA 3 (black rhomb and line). Decay curve of unprotected siRNA (red triangles and line). The error bars represent the standard error of the evaluation method. Standard deviation errors are between 0.7 % and 2.3 %.

2.1.2.4 Cytotoxicity of THS-pDMAEMA3 and THS-pDMAEMA-co-RhBMA in comparison with

The test for the toxicity of nano objects is very important, if the objects will be used in cell-based assays. A nano transporter that interacts with cells should not cause a toxic reaction. We tested our conjugates (THS-pDMAEMA3 and THS-pDMAEMA-

co-RhBMA) for toxicity and compared them with pDMAEMA (Figures 2.1.17a-c). Cells treated with both conjugates showed same viability as the untreated cells (Figure 2.1.17a + b). PDMAEMA on the other hand showed high toxicity even at the lowest applied concentration (50 μg ml^{-1}), which is consistent with literature (Figure 2.1.17c).[449] From those results we concluded that the cage structure shielded most of the positive charges of pDMAEMA from interaction with the cells.

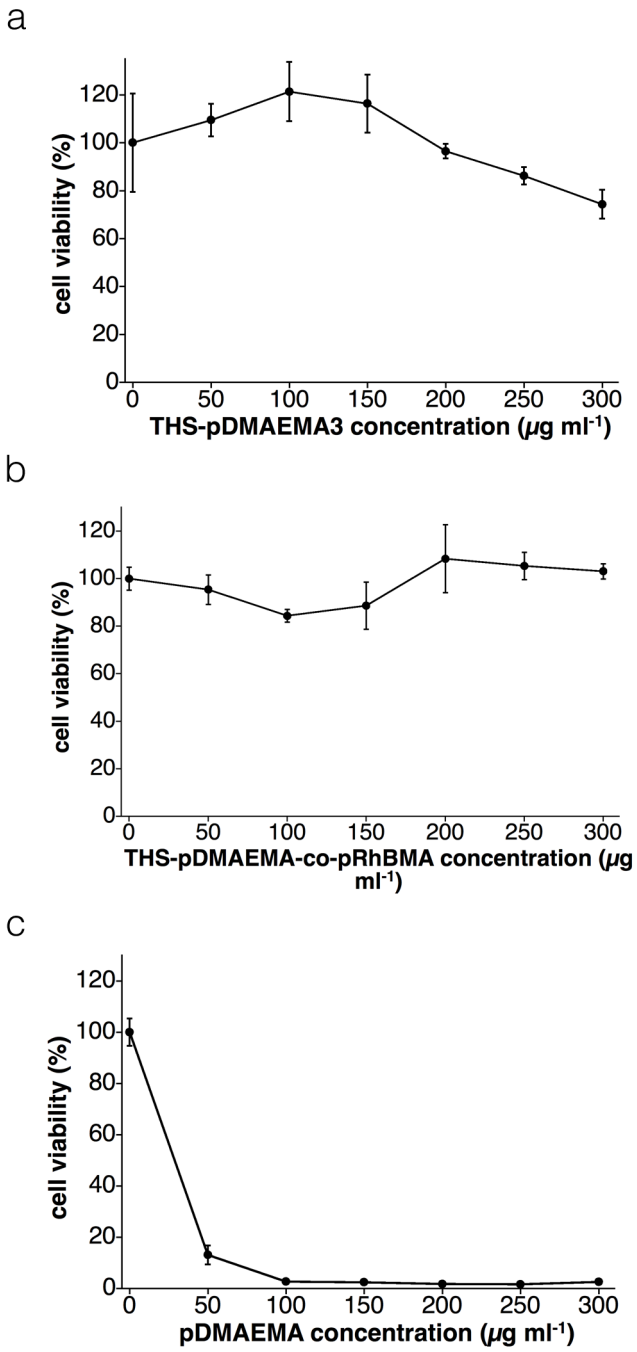

Figure 2.1.17. Toxicity data of THS-polymer conjugates and pDMAEMA. (a) THS-pDMAEMA3 (b) THS-pDMAEMA-co-RhBMA and (c) pDMAEMA.

2.1.2.5 Cellular uptake of THS-pDMAEMA-co-RhBMA

From our previous investigations we know that our pDAMEMA-containing conjugates can entrap siRNA and that they showed promising results from the toxicity assays, which allow going a step further and investigate cellular uptake of our THS-polymer conjugates. From our previous investigations[379] we know that THS-PAMAM is uptaken by U87 cells without further modifications (e.g. cell penetrating peptides).[450,451] For cellular uptake studies into U87 cells (Figure 2.1.18a), we used the THS-pDMAEMA-co-RhBMA conjugate (Figure 2.1.18). This conjugate has fluorescent monomers integrated into its polymer chains that allow the visualization of the particles when uptaken by cells. The conjugate was uptaken by U 87 cells at different conjugate concentrations (Figure 2.1.18b-d). With an increasing concentration from 100 μg ml^{-1} (Figure 2.1.18b) to 500 μg ml^{-1} (Figure 2.1.18d), also the amount of THS-pDMAEMA-co-RhBMA within the cytosol increased.

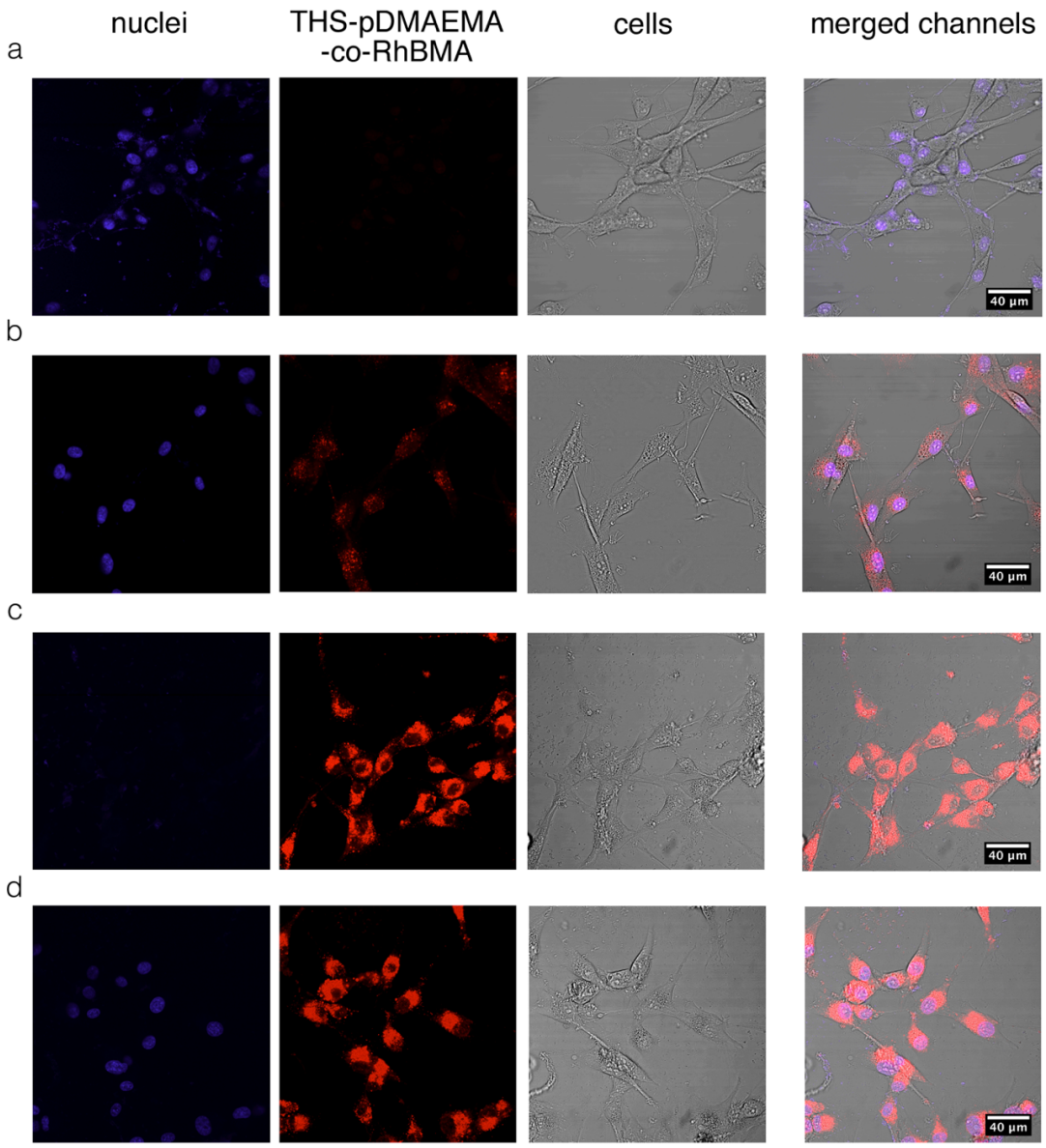

Figure 2.1.18. Cellular uptake of THS-pDMAEMA-co-pRhBMA into U87 cells after 24h. THS-pDMAEMA-co-RhBMA (red areas) and cell nuclei, which were stained with Hoechst 33342 dye (blue compartments). (a) U 87 cells with stained nuclei under the microscope. (b) U87 cells with 100 µg ml^{-1} THS-pDMAEMA-co-pRhBMA. (c) U87 cells with 250 µg ml^{-1} THS-pDMAEMA-co-pRhBMA. (d) U87 cells with 500 µg ml^{-1} THS-pDMAEMA-co-pRhBMA.

2.1.2.6 Complex formation of THS-pDMAEMA-co-RhBMA with fluorescent proteins and its cellular delivery

The thermosome is able to encapsulate macromolecules up to 50'000 g mol^{-1},[235] and there are examples where proteins were delivered into cells with cationic polymers.[436,452,453] Therefore, we explored the capability of THS-polymer conjugates to deliver biological macromolecules peptides or proteins[440,454,455] into U 87 cells. To

show the proof of concept of delivering a protein, we used enhanced yellow fluorescent protein (eYFP) and an improved variant of the green fluorescent protein (TurboGFP). EYFP has an isoelectric point (pI) of around 6.2,[456] and is therefore negatively charged at the physiological pH value used for the experiments (7.2-7.4). EYFP should therefore interact with positive charges of the pDMAEMA. In addition to eYFP, TurboGFP was chosen, because its emission spectrum does not overlap with the emission spectrum of RhBMA in our THS-pDMAMEA-co-RhbMA conjugate. TurboGFP, in addition, has a higher photostability and brightness.[438] Its pK_a-value of 5.2 indicates that it is also negatively charged at physiological pH.[438] Complex-formation between THS-pDMAEMA-co-RhBMA and the proteins was investigated by agarose gel experiments. With a molar excess of THS-pDMAEMA-co-RhBMA to eYFP of 2:1, no free eYFP could be observed in the gel (Figure 2.1.19a lane 2). At higher eYFP concentrations, more free eYFP is visible (Figure 2.1.19a lane3-5). Thus, an excess of conjugate is needed to fully complex eYFP. The agarose gel shown in Figure 2.1.19b shows that TurboGFP could not be complexed with THS-pDMAEMA-co-RhBMA, even with a molar excess (2:1) of THS-pDMAEMA-co-RhBMA. This might be due to the size of TurboGFP, which occurs in solution as dimer and has a molecular weight of 54'000 g mol^{-1}. This is above the maximum molecular weight for proteins that can be encapsulated in the cavity of THS.[235] Moreover, the synthesized polymer in the cavity occupies additional space.

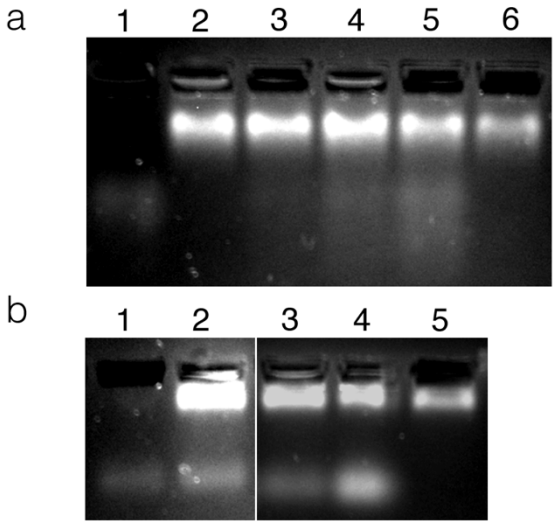

Figure 2.1.19. Agarose gels of THS-pDMAEMA-co-RhBMA with eYFP (a) and TurboGFP (b) to evaluate complex formation. Following conjugate-to-fluorescent protein ratios were applied with a constant conjugate concentration. (a) Lane 1: eYFP only, lane 2: (2:1), lane 3: (1:1), lane 4: (1:2), lane 5: (1:3), lane 6: conjugate only (b) Two separate gels are shown. Lane 1: TurboGFP only, lane 2: (2:1), lane 3: (1:1), lane 4: (1:2), lane 5: conjugate.

With the agarose gel experiment (Figure 2.1.19a) we could show that THS-pDMAEMA-co-RhBMA can complex with eYFP and from toxicity experiments we know that our conjugates did not decrease cell viability. Therefore, a cellular uptake experiment into U87 cells with THS-pDMAEMA-co-RhBMA and eYFP (molar ratio 1:2) was conducted and the uptake efficiency of the conjugate and eYFP was measured by fluorescence-activated cell sorting (FACS) (Figure 2.1.20). The fluorescence intensity of cells containing THS-pDMAEMA-co-RhBMA of the conjugate/eYFP-complex (Figure 2.1.20a, red curve) increased by a factor of around 100, compared to the auto-fluorescence of the U87 cells (Figure 2.1.20a, light blue curve). The fluorescence intensity of eYFP of the conjugate/eYFP-complex increased by a factor of 0.5 (Figure 15b, red curve) compared to the auto-fluorescence of U87 cells (Figure 2.1.20b, light blue curve) and the fluorescence intensity of cells to which only eYFP as sample was added (Figure 2.1.20b, bright green curve). Thus, a slight cellular uptake of eYFP was measured. The relative low increase in fluorescence intensity of uptaken eYFP might be the result of a weak fluorescence of the eYFP-protein in the applied concentrations. Moreover, the complex between THS-pDMAEMA-co-RhBMA and eYFP might not be strong enough in the cell culture medium, so that uptake of eYFP by U87 cells was not very pronounced. Nevertheless, these findings show the potential of the THS-polymer conjugate to deliver proteins, but the delivery has to be investigated in more detail. For example, with a higher concentration of eYFP and THS-pDMAEMA-co-RhBMA the signal-shift of eYFP in FACS could be stronger. A delivery of TurboGFP promoted by THS-pDMAEMA-co-RhBMA could not be measured (Figure 2.1.20c). The signal intensity of TurboGFP (Figure 2.1.20c, red line) is equal to the signal of U87 cells (Figure 2.1.20c, light blue line). No cellular uptake was measured. However, it is possible that TurboGFP was uptaken by some cells, but in the average signal of all cells, the amount of cells with uptaken TurboGFP did not change the overall fluorescence intensity.

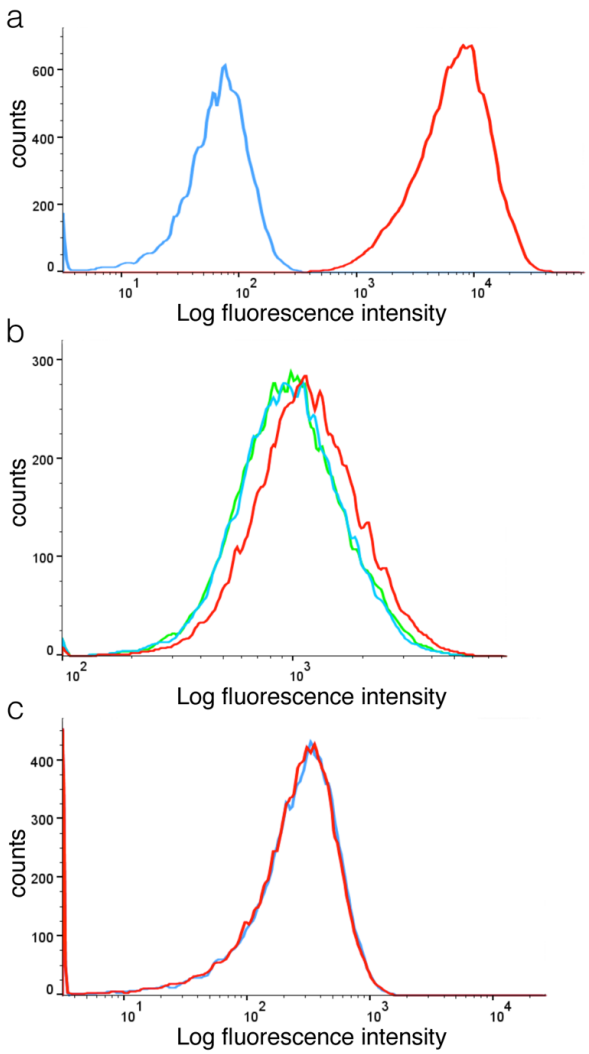

Figure 2.1.20. Fluorescence-activated cell sorting (FACS) of the THS-pDMAEMA-co-RhBMA/eYFP complex uptaken by U87 cells. (a) Fluorescence intensity of THS-pDMAEMA-co-RhBMA (red curve) compared with the fluorescence of the U87 cells (light blue curve). (b) Fluorescence intensity of eYFP from the THS-pDAMEMA-co-RhBMA/eYFP-complex (red curve), eYFP uncomplexed (bright green curve) and fluorescence of U87 cells (light blue curve). (c) Fluorescence intensity of TurboGFP (red curve) and U87 cells (light blue curve) in the presence of THS-pDMAEMA-co-RhBMA.

Even though we could not observe strong complex formation with THS-pDMAEMA-co-RhBMA and TurboGFP (Figure 2.1.19b) and an uptake by FACS, further cell uptake experiments were conducted in order to prove if TurboGFP was uptaken by cells in presence of THS-pDMAEMA-co-RhBMA (Figure 2.1.21). After incubation, cells were imaged by confocal laser scanning microscopy (CLSM). A higher amount of TurboGFP was uptaken into selected U87 cells in the presence of the conjugate (Figure 2.1.21a), when compared with the control of TurboGFP without conjugate (Figure 2.1.21b). A possible explanation for the higher uptake

could be that THS-pDMAEMA-co-RhBMA formed a transient complex with TurboGFP and enhanced the uptake of TurboGFP. Due to the spectral overlap of RhBMA and eYFP, conclusive images could not be recorded by CLSM. This can be resolved by using a different protein and label it with e.g. Alexa488 dye (e.g. horse-radish peroxidase M = 44'000 g mol^{-1}, pI between 3 and 9).[457] The complex formation between fluorescent proteins and THS-pDMAEMA3 could not be observed by gel electrophoresis as well as enhanced cellular uptake with this conjugate. By changing the protein to a more negatively charged at physiological pH (e.g. fluorescent labelled tyrosine aminotransferase, M = 32'000 g mol^{-1}, pI = 4.1)[458], it might be possible to form a complex with this conjugate. Although these initial experiments are promising, they have to be investigated and proven more in detail by repeating experiments and eventually adapt the conditions (e.g. longer incubation time, variation of pH) and the protein (pI around 4.0) to clearly show protein delivery.

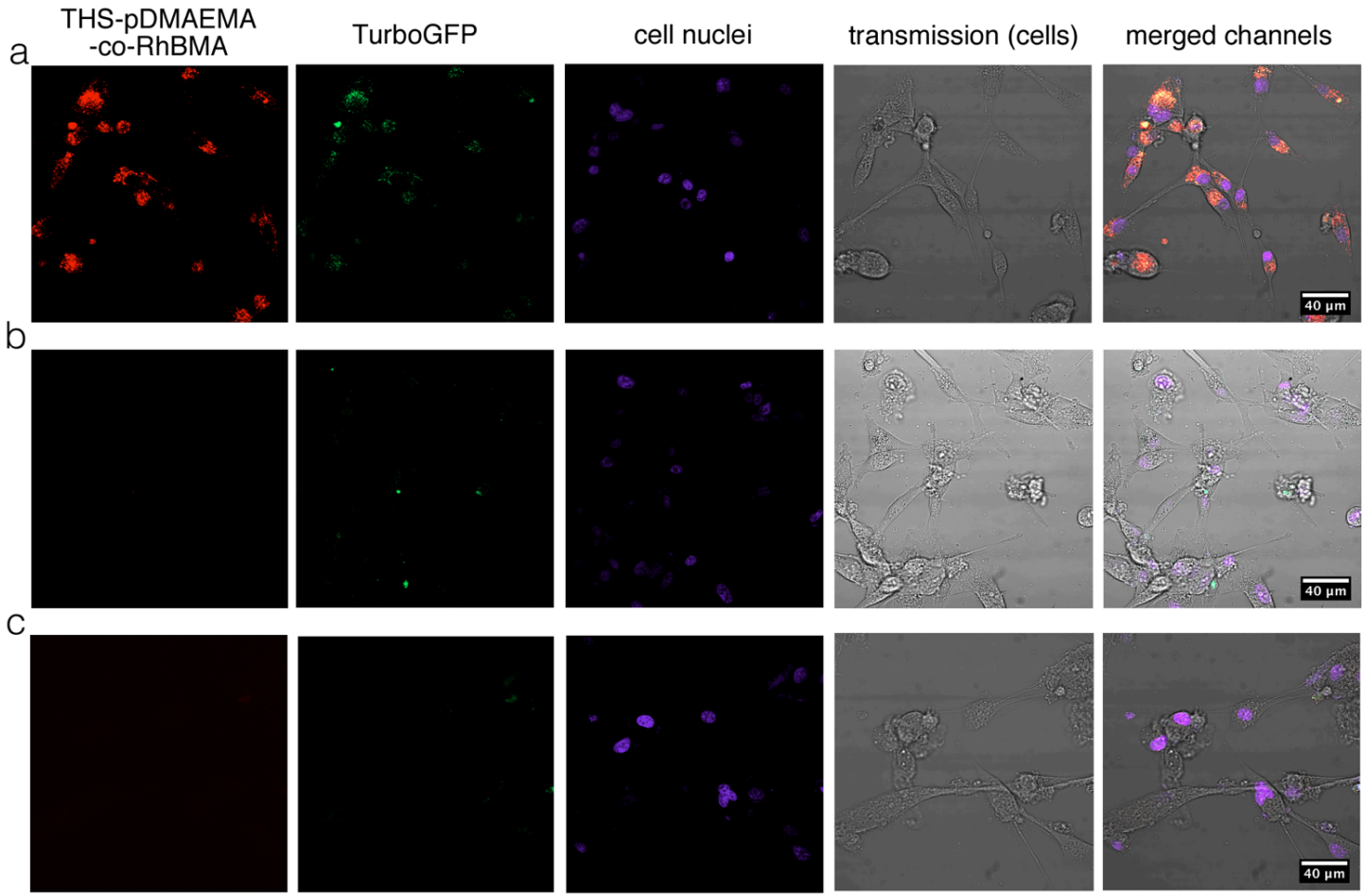

Figure 2.1.21. Cellular uptake of TurboGFP is promoted by THS-pDMAEMA-co-pRhBMA conjugates. Red: THS-pDMAEMA-co-pRhBMA, green: TurboGFP, blue: cell nuclei, grey: transmission of cells, merged: all channels combined (a) THS-pDMAEMA-co-RhBMA enhanced the uptake of TurboGFP into U87 cells (b) TurboGFP control. The amount of TurboGFP was the same as with the THS-pDMAEMA-co-RhBMA + TurboGFP sample. (c) U87 control image

2.1.2.7 SiRNA delivery with THS-pDMAEMA3 into mammalian U87 cells

The ability of THS-pDMAEMA3 to bind and protect negatively charged molecules makes it a good candidate for siRNA delivery. Experiments in which siRNA was deliverd into U87 cells were conducted. This coding siRNA is capable to bind to a specific pattern of the messenger-RNA (mRNA) gene sequence and can knock-down the synthesis of proteins that are synthesized according to the gene sequence by interfering with the mRNA translation.[433,459] This mechanism of silencing a specific gene is known as RNA interference (RNAi). RNAi can be useful in the treatment of cancer and many other human diseases.[460-465] As the silencing target for our experiments, glyceraldehyde-3-phosphate dehydrogenase (GAPDH, M ≈ 37'000 g mol^{-1}) was chosen, which is a protein that is present in all living cells and plays an important role in the cell metabolism.[466] While investigations are still ongoing, initial results show promise that THS-pDMAEMA3 can deliver siRNA into cells and create a maximum knockdown reaching of 80% of intracellular GADPH levels when 5 pmol of siRNA were delivered, remaining the same with higher amounts (Fig 2.1.22a+d). The control experiments show that siRNA alone cannot reduce the GAPDH protein level by gene-silencing (Figure 2.1.22b). Moreover, the loading control protein (M≈ 40'000 g mol^{-1}) was not affected by gene silencing, indicating that the specific knock-down of GAPDH worked (Figure 2.1.22.c). While THS-pDMAEMA3 still required a 5x higher amount of siRNA than the commercially available lipofectamine RNAiMAX reagent (5 pmol compared to 1 pmol respectively), further optimization could lead to improved results.

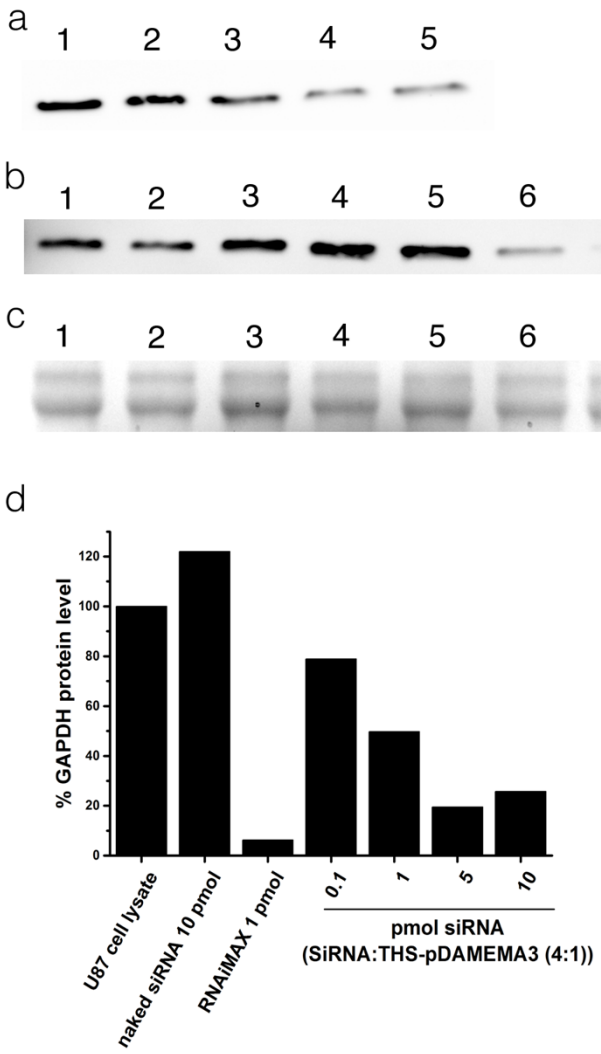

Figure 2.1.22. Delivery of siRNA into U87 cells by THS-pDMAEMA3. (a) GAPDH gene silencing in U87 cells mediated by THS-pDAMEMA3. THS-pDMAEMA3:SiRNA 1:4 with an amount of siRNA of lane 1: 0 pmol, lane2: 0.1 pmol, lane 3: 1 pmol, lane 4: 5 pmol, lane 5: 5 pmol. (b) Control experiments with cell lysate (lane 1), naked siRNA (lanes 2-5) and siRNA deliverd with RNAiMAX (lanes 6-7) with an amount of siRNA of lane 1: 0 pmol, lane 2: 0.1 pmol, lane 3: 1 pmol, lane 4: 5 pmol, lane 5: 10 pmol, lane 6: 0.1 pmol, lane 7: 1 pmol. (c) Control experiment showing that the control protein was not affected by gene-silencing. Samples and lanes correspond to (b). (d) Graph visualizing the data of the different experiments.

2.1.3 Conclusion

With the integration of ATRP-initiators into the cavity of THS, it was possible to synthesize conjugates with functional polymers that could entrap and form complexes with biomacromolecules and enabled particle localization when uptaken by cells. We found that the cavity influences on polymerization. Polymers synthesized within the cavity of THS were smaller than polymers that were synthesized on a protein without having a cage structure. This is in agreement with another study from our group where polymers that were not covalently bound to the protein were synthesized in the THS.[61] Size measurements showed that the cage structure did not increase in size, which is an indication that polymers were in the interior and not exterior. PDMAEMA, the polymer synthesized in the interior of THS, is toxic as known from literature[449] and as confirmed by our own experiments. However, the cage shielded cells from the toxic positive charges of the polymers and reduced their toxicity. Our THS-pDAMEMA3 and THS-pDMAEMA-co-RhBMA conjugates showed same cell viability as the untreated cells in the tested range ($\leq$ 300 $\mu g\ ml^{-1}$). Another important finding for drug delivery applications is that the THS-polymer conjugates did not form aggregates in presence of biomacromolecules such as siRNA, which is important because aggregate formation could lead to less effective delivery.[444] For drug delivery applications, it is important that the cargo is protected from degrading agents in the local biological environment. THS-pDMAEMA3 can entrap siRNA and protect it from degradation by enzymes. Moreover, the delivery of siRNA into cells by THS-pDAMEMA3 and gene knock-down was shown. The encapsulation strategy for biomacromolecules was extended by complex formation of the THS-polymer conjugates with fluorescent proteins and their delivery into cells. We took fluorescent proteins as the proof-of-concept, because of their fluorescence and therefore possibility of detection by confocal laser scanning microscopy in living cells. The results show that protein delivery into cells is possible, but currently has limitations that have to be investigated in more detail. We showed the potential behind a protein cage with polymers that are synthesized within its cavity. The monomer to be polymerized within the cavity can be chosen to suit the desired needs. Polymers allow having a high density of functional groups within a protein cage. Therefore, customized bio nano particles can be created for applications like drug delivery,[114,379] magnetic resonance imaging[111,148] or catalysis.[172]

2.1.4 Experimental section

2.1.4.1 Materials

All Chemicals were purchased from Sigma-Aldrich with the highest purity and used as received, unless stated otherwise. Water used for buffers was produced with a water purification system (ELGA PureLab DV25). Methacryloxyethyl thiocarbamoyl rhodamine B (RhBMA) was purchased from PolySciences Europe (Germany). Scrambled siRNA with following sequence delivered as double stranded siRNA (5'-AGG UAG UGU AAU CGC CUU GTT-3')[467] was purchased from Microsynth AG (Switzerland). DMEM, optimum, Fetal calf serum (FCS), non-essential amino acids (NEAA), and PEN/strep were purchased from Gibco. TEMED, Bovine serum albumin (≥ 96 %)Leupeptin, aprotinin, pepstatin, and PMSF were purchased from Sigma-Aldrich. The U87 cell line was obtained from ATCC (USA). Sodium dodecyl sulphate (SDS) and the TGX stain free acrylamide kit (10%) were obtained from Bio-Rad (Switzerland). Supersignal molecular weight protein ladder, lipofectamine RNAiMAX reagent, monoclonal mouse antiGADPH antibody and goat anti mouse HRP conjugated secondary antibody were purchased from Life Technologies (USA). Nitrocellulose membranes and gel-blotting paper were purchased from GE Healthcare (USA). Micro BCA protein assay kit and Supersignal west Pico chemiluminescent substrate, DMEM, opti-MEM and Silencer select GAPDH siRNA as well as 6X MassRuler DNA Loading Dye, Hoechst 33342 and SimplyBlue Safe Stain, Alexa 488 maleimide, nuclease free PBS buffer (10x), nuclease free water and spin desalting colums (Zeba Spin Desalting Columns, MWCO = 7'000 g mol^{-1}) were purchased from Thermo Scientific (USA). Argon used for the glove box (99.998 %, Argon 48) was obtained from Carbagas (Switzerland).The centrifugal filters (Amicon) with various molecular weight cutoff values (MWCO) were purchased from Merck Millipore (Ireland). RNAse A (RNAse II;activity 50 U mg^{-1}) was purchased from Roche (Switzerland) and GelRed agarose gel staining from Biotium (USA). The nuclease free PBS buffer (10x Ambion) was and diluted with nuclease free water Gradient gels with 4 – 20 % acrylamide content (Mini-PROTEAN TGX Precast Gels) for electrophoresis were obtained from BioRad (USA). Spin desalting colums (Zeba Spin Desalting Columns, MWCO = 7'000 g mol^{-1}) were obtained from Thermo Scientific (USA).Recombinant TurboGFP (rTurboGFP) (M = 54'000 g mol^{-1}, ε_{482} = 70'000 M^{-1} cm^{-1})[438] was obtained from Evrogen (Russia). The protein eYFP

(M = 27'000 g mol^{-1}, ε_{514} = 36'500) was expressed in our group according to published protocols.[468]

2.1.4.2 ATRP-initiator:

The maleimide functionalized ATRP-initiator was synthesized according to the protocol by Le Droumaguet *et al.*,[434] with slight modification. Instead of petrol ether, a 1:1 mixture of hexane and ethyl acetate was used for chromatography.

2.1.4.3 THS expression

A mutated variant of the thermosome (THS) from *Thermoplasma acidophilum* was expressed and purified as reported by Bruns *et al* .[61,166] The mutated variant (K316C) of THS had a Cys residue on the inside of every β-subunit, which allowed covalent attachment of functional molecules. For purification and concentration centrifugal filters with a MWCO of 100'000 g mol^{-1} were used. The purified THS stock solution was kept at 4°C in a 100 mM sodium phosphate buffer (pH 7.4, 150 mM NaCl, 0.01 % NaN_3)

2.1.4.4 Methods

Indicated concentrations are given as end concentrations in the sample/reaction mixtures. Structures of protein cages were rendered with UCSF chimera software (Version 1.9).[274] Since no structural data of the THS cage in its open state is available in the databases, as alternative the cryo-electron microscopy structure of the similar chaperonin Mn-Cpn from *Methanococcus maripaludis* (PDB: 3IZH) in its open conformation was taken for vizualization.[469]

2.1.4.5 UV/Vis spectroscopy

If not stated otherwise, a Nanodrop 2000c spectrometer (Thermo Scientific, USA) was used for concentration determination. Following extinction coefficients were used for calculations: THS ε_{280} = 210 880 M^{-1} cm^{-1} [30], RhBMA ε_{552} = 38'460 M^{-1} cm^{-1} ± 1'060 M^{-1} cm^{-1} (determined by absorption measurements at different concentrations and slope calculation).

2.1.4.6 THS stability studies

Stability studies of the THS in presence of common (ARGET) ATRP reagents and organic solvents were performed at a THS concentration of 1.1 µM (1 mg ml^{-1}). Experiments were conducted in degased H_2O under argon with 48 h incubation time at room temperature. After incubation time, samples were analysed by SDS-PAGE and BN-PAGE.

2.1.4.7 Macroinitiator synthesis (THS-Br)

Prior to maleimide initiator attachment to Cys, the buffer (100 mM sodium phosphate pH 7.4) was exchanged to 100 mM sodium phosphate pH 6.5 using centrifugal filters with a MWCO of 100 kDa. After buffer exchange, the THS was diluted in 100 mM sodium phosphate buffer (pH 6.5 + 150 mM NaCl + 0.01 % NaN_3) to a concentration of 1 mg mL^{-1} (1.1 µM, 6.6µM Cys). To the diluted THS solution, 4% DMSO (v/v) was added. Afterwards, ATRP-initiator dissolved in DMSO (200 mM stock solution) was added with a 40-times molar excess in respect to Cys. The solution was incubated over night at room temperature with shaking at 400 rpm (BioShake iQ, Quantifol Instruments). Unreacted products were removed and the buffer was exchanged to 100 mM sodium phosphate buffer (pH 7.4, 150 mM NaCl, 0.01 % NaN_3) using centrifugal filters (AMICON, MWCO = 100'000 g mol^{-1}) with at least 6 dilution-concentration cycles. The bovine serum albumin (BSA) macroinitiator (BSA-Br) was synthesized in the same way. The phosphate buffer was exchanged to degased water before the macro-initiators were used for conjugate synthesis.

2.1.4.8 Labeling of THS and THS-Br with Atto-488 maleimide for FCS measurements:

THS and THS-Br were diluted in 100 mM sodium phosphate buffer (pH 6.5 + 150 mM NaCl + 0.01 % NaN_3) and 4 % DMSO to a concentration of 1 mg ml^{-1} (1.1 µM). Atto-488 maleimide dissolved in DMSO (200mM) was added in an amount, that was 40-times higher than the β-subunits of THS (6 per THS, 6.6µM). The sample was incubated over night and purified by spin desalting followed by two cycles of spin diafiltration.

2.1.4.9 THS-pDMAEMA synthesis

Synthesis of THS-polymer conjugates was performed in a glove box (Labstar, MBRAUN, Germany) at < 0.5 - 1 ppm O_2-level, < 0.5 - 1 ppm H_2O-level, an argon over pressure of 1.2 – 1.6 mbar and at a room temperature of 20 ± 2 °C. Solvents and reagents were degassed with argon for 30 min. before use. The monomer DMAEMA was purified by filtration over basic aluminium oxide and degassed with argon before application. The ligand 1,1,4,7,10,10-hexamethyltriethylenetetramine (HMTETA) was distilled before use and kept in the fridge at 4°C under argon. The macroinitiator (THS-Br) was degassed by at least 5 centrifugation filtration (Amicon, MWCO = 30'000 g mol^{-1}) cycles with degassed H_2O.

The tube and filter with THS-Br were filled with argon prior to centrifugation. Reducing agent (sodium ascorbate, NaAsc) and catalyst (HMTETA + $CuBr_2$) stock solutions were prepared in 10 ml two-neck round bottom flasks connected to a Schlenk line. Flasks were evacuated and re-filled with argon in at least 4 cycles before dissolving the reagents in 5 ml deoxygenized ELGA water H_2O under stirring. All reactants were transferred into the glovebox. First H_2O was added into the reaction tube followed by the addition of the calculated amount of THS-Br. Afterwards DMSO was added to a final concentration of 20 % (v/v). The calculated amount of DMAEMA was added as well as an aliquot of the catalyst stock solution. The reaction was started by the addition of an aliquot of reducing agent stock solution. The reaction tubes were shaken at 500 rpm (BioShake iQ, Quantifol Instruments, Germany) at room temperature for 16 h. THS-Br concentration was 1 mg ml^{-1} (1.1 μM) or expressed in a total concentration of bound initiators: 4 x 1.1μM = 4.4 μM. Concentrations of reactants were calculated based on the initiator concentrations. The ratios were [Initiator]:[Catalyst]:[Reducing agent]:[Monomer] = [1]:[4.1]:[16.1]:[various]. Experimental details are summarized in Table 2.

The reaction was quenched by addition of non-deoxygenized H_2O and exposure to air. Polymerization reaction samples were concentrated and the solvent was exchanged to 100 mM phosphate buffer (pH 7.4 + 150 mM NaCl + 0.01% NaN_3) by centrifugal filters (MWCO = 100'000 g mol^{-1}) with at least 6 dilution-concentration cycles.

2.1.4.10 THS-pDMAEMA-co-pRhBMA:

Synthesis was performed according to the protocol for THS-pDMAEMA. In addition, after 10min. reaction time initiated by addition of Na-Asc, an aliquot of RhBMA dissolved in DMSO (c_{RhBMA} = 100 mM) was added. Amount of RhBMA in reaction solution corresponded to 40 monomers per initiator. The amount of RhBMA in THS-poly(DMAEMA-co-RhBMA) was determined from A($RhBMA_{552}$) and with ε($RhBMA_{552}$). In order to be able to calculate the amount of THS in THS-poly(DMAEMA-co-RhBMA), first a ratio from A($RhBMA_{280}$) / A($RhBMA_{552}$) of RhBMA was calculated. With this ratio (mean value = 0.370) and the known concentration of RhBMA it was possible to calculate the signal amount of RhBMA at 280 nm within the total signal intensity at 280 nm. Subtraction of the signal amount of RhBMA at 280 nm from the total sample signal at 280 nm gave the absorbance of THS at 280 nm.

Table 2.1.5. Experimental conditions for THS-pDMAEMA, THS-pDMAEMA-co-pRHBA and BSA-pDMAEMA. Polymerization reactions were conducted in a solvent mixture of 80 % degased H_2O and 20 % DMSO.

Reagents / Sample	c (THS-Br) [µM]	c(initiators per THS) [µM]	BSA-Br [µM]	c(HMTETA) = 1.2 × c($CuBr_2$) [µM]	c ($CuBr_2$) [µM]	Amount of $CuBr_2$ molecules per initiator	c (Na-Ascorbate) [µM]	Amount of Na-Ascorbate molecules per initiator	c (DMAEMA) [mM]	Amount of DMAEMA molecules per initiator	c (RhBMA) [µM]	Amount of RhBMA molecules per initiator
THS-pDMAEMA1	1.1	4.4	--------	21.6	18.0	4.1	71.0	16.1	22	5’000	--------	--------
THS-pDMAEMA2	1.1	4.4	--------	21.6	18.0	4.1	71.0	16.1	44	10’000	--------	--------
THS-pDMAEMA3	1.1	4.4	--------	21.6	18.0	4.1	71.0	16.1	66	15’000	--------	--------
THS-pDMAEMA-pRhBMA	1.1	4.4	--------	21.6	18.0	4.1	71.0	16.1	66	15’000	176	40
BSA-pDMAEMA	--------	--------	4.4	21.6	18.0	4.1	71.0	16.1	66	15’000	--------	--------

2.1.4.11 SDS-PAGE

Acrylamide gels were prepared based on the protocol published by Laemmli.[470] The amount of protein or protein-polymer conjugate per sample well was 5 – 7 µg. If necessary, samples were diluted with either water or PBS buffer. 8 µl 2x loading buffer (130 mM Tris/HCl pH 6.8, 200 mM dithiothreitol, 20 % (v/v) glycerine, 4 % (w/v) SDS, 0.01 % (w/v) bromophenol blue) was added to 8 µl sample, followed by heating at 95°C for 3 min. After denaturing, samples were loaded on a 12 % acrylamide SDS-PAGE gel or 4 - 20 % gradient gel if not otherwise mentioned (Mini-PROTEAN TGX Precast Gels, BioRad) and run with a constant voltage of 200 V for 55 min. (Mini Protean Tetra cell, BioRad). The running buffer for these experiments was 25 mM Tris, 250 mM glycine pH 8.3 + 0.1 % SDS buffer. For Coomassie staining a ready-to-use solution was used (SimplyBlue™ SafeStain, Life Technologies) and samples were stained according to the manufacturer's protocol. Silver staining was performed according to the protocol by Nesterenko et al .[471]

Conjugate bands were plottet as two-dimensional (2D) plots with the software imageJ (1.47v). For the calibration of the molecular weights, the x-y-cooridinates of the 2D-plots were converted into into a signal-to-molecular weight relation. With the software qTi-plot, an equation was determined that could convert x-coordinates into molecular weights. The exponential equation in Figure 2.1.22 below was determined by iterative analysis.

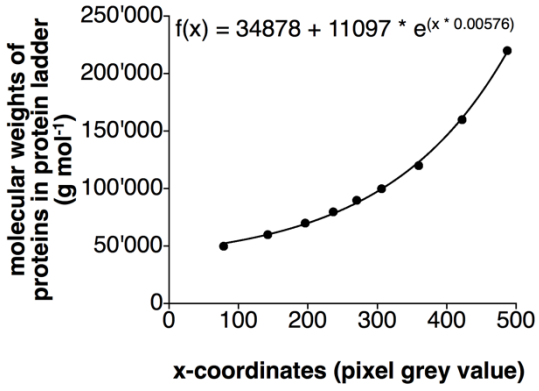

Figure 2.1.23. Kalibration curve and equation for molecular weight calculation in SDS-PAGE.

2.1.4.12 Basic native PAGE:

The amount of samples was calculated to have a total mass of 5-7µg of protein or protein-polymer conjugate per well and that all wells have equal amounts of protein and volumes. If necessary, samples were diluted with H_2O or PBS buffer. A volume of 2 µL of 5x sample buffer (150mM Tris/HCl pH 6.8, 70 % glycerol, 0.01 % w/v bromo phenol blue) was added to 8 µl of samples and mixed. Samples were pipetted into the wells of a 4-20% gradient gel and the gel was run at constant 100V for 100 min.

Gel imaging: Electrophoresis gels were imaged using an automated imager (Gel Doc™ EZ system, BioRad) with the Image Lab™ software.

2.1.4.13 Fluorescence correlation spectroscopy (FCS):

FCS measurements were conducted on a Confocor 2 (Carl Zeiss, Germany) with an Ar^+-laser for excitation at 488 nm with a LP505 filter. An 40× C-apchromat water immersion objective with a numeric aperture of 1.2 was used for laser beam focussing. The fluorescence intensity was recorded with an avalanche photodiode (APD). Measurements were conducted at a constant temperature of 20 °C and a sample volume of 5µl. Raw data processing was done with the software ConfoCor 3. Measured samples were fitted with one-component fits including triplet state according to the following equation:

$$G(\tau)_{fit} = 1 + \left(1 + \frac{T}{1-T} e^{-\frac{\tau}{\tau_{trip}}}\right) \frac{1}{N} \left[\frac{1}{1+\frac{\tau}{\tau_D}} \frac{1}{\sqrt{1+R^2\frac{\tau}{\tau_D}}}\right]$$

In this equation τ_D describes the diffusion time. T is the fluorophore fraction that is in the triplet state with the appropriate triplet time τ_{trip}. R is the structural parameter that is determined after measuring the free dye molecules and N describes the number of particles.

The diffusion coefficients (D) were calculated according to the relation between the diffusion time (τ_D) and the x-y dimension of the confocal volume ω_{xy}.

$$\tau_D = \frac{{\omega_{xy}}^2}{4D}$$

The hydrodynamic radii (R_H) of the samples were calculated with the Einstein-Stokes equation in which k_B is the Boltzman constant, η the viscosity of the solvent and T the absolute temperature in Kelvin.

$$D = \frac{k_B T}{6\pi\eta R_H}$$

The counts per molecule (*CPM*) value can be calculated with the count rate (*CR*), which is the amount of photons that reach the detector and the number of molecules *N* with following equation:

$$CPM = \frac{CR}{N}$$

2.1.4.14 Dynamic light scattering

Size determination of the THS, poly(DMAEMA), THS-polymer conjugates and THS-polymer conjugates with encapsulated siRNA were performed on a Zetasizer ZSP (Malvern, UK). Following instrument parameters were used: backscattering (173°), dispersant: 1x PBS, equilibrium time: 30 sec. temperature: 25 °C. For measurements UV-cuvettes micro (Brand, Germany) with a volume of 70 µl and following dimensions (12.5 x 12.5 x 45 mm) were used. Particle size distribution (PSD) was calculated according to the number of particles. The mean value of the diameter was calculated according to 4 measurement cycles with 14 single measurements per cycle. The standard deviations from the mean value were calculated the same way. Experiments were performed with a protein concentration of 0.7 µM (0.63 mg ml^{-1}) THS or THS-polymer conjugates diluted in nuclease free PBS buffer (pH 7.4). Complexation reactions with siRNA were conducted at a THS-pDMAEMA 3 concentration of 0.7 µM and a siRNA concentration of 10 µM. Samples were incubated at 37 °C for 30 min. prior to measurement. Experiments with pDMAEMA and siRNA were carried out at a pDMAEMA concentration of 0.5 mg ml^{-1} and a siRNA concentration of 10 µM. The pDMAEMA + siRNA sample was incubated at room temperature for 10 min. and measured. Incubation time and temperature was lower with pDMAEMA because, at longer incubation time and higher temperature, larger aggregates were formed that made a measurement impossible. The THS-poly(DMAEMA) conjugate did not form any aggregates. It stayed intact and kept the cage architecture, whereas the polymer formed aggregates

in presence of siRNA. Furthermore, aggregate formation was observed by visible turbidity in solution.

2.1.4.15 Transmission electron microscopy (TEM)

TEM analysis was done on a FEI Morgani 268D. Sample preparation: A 5 µl drop of sample was placed on a glow-discharged specimen grid (Cu 400 mesh, coated with 2 % palladium and carbon (Stork Veco, Netherlands)) and allowed to be absorbed for 60 sec. Excess of liquid was gently removed via a filter paper. Afterwards the absorbed sample was washed two times with H_2O. Samples were two times stained with a 2% Uranylacetate solution. For the first staining, the 2 % Uranylacetate drop was kept on the sample for 1 sec. and removed with a filter paper. For the second staining, the was kept on the sample for 10 sec. and then removed by a filter paper. Binding capacity of siRNA and pDMAEMA with Mn = 80080 g mol^{-1} and PDI = 1.77 in dependence of increasing N/P-ratios at pH 7.4 . Concentration of siRNA in all samples was 2 µM. The used siRNA was a 21-mer doublestrand and had therefore 42 negative charges. Samples were incubated for 30 min. at 37 °C prior to analysis.(1) bare siRNA (2) N/P = 0.1 : 1 (3) N/P = 0.5 : 1 (4) N/P = 1 : 1 (5) N/P = 3 : 1 (6) N/P = 6 : 1 (7) N/P = 8 : 1 (8) N/P = 10 : 1

2.1.4.16 Electrophoretic mobility shift assay (EMSA) with pDMAEMA samples and siRNA

EMSA[442,472] were performed at pH 7.4, constant voltage of 100V, but different time intervals. Sample volumes were kept at 10 µl, if necessary diluted with PBS buffer (pH 7.4) and 2 µl loading dye (6x Mass Ruler DNA loading dye) was added prior to electrophoresis. Agarose gels were stained with GelRed dye (Biotinum, USA). Concentration of siRNA was kept constant at 2 µM. In all gels, lane 1 was siRNA only. Following ratios [siRNA]:[THS-pDMAEMA 3] were used: Lane 2) [1] : [0.06] Lane 3) [1] : [0.125] Lane 4) [1] : [0.25] Lane 5) [1] : [0.5] Lane 6) [1] : [0.85].

For the control reaction with THS and siRNA a molar ratio of 1:1; [2 µM] : [2 µM] was used.

2.1.4.17 RNAse protection assay

SiRNA (c = 2 µM) was incubated with or without THS-pDMAEMA 3 (c = 3 µM) for 30 min. at 37 °C in a nuclease free PBS Buffer (pH 7.4) in order to encapsulate

the siRNA. A slightly higher concentration of THS-pDMAEMA 3 compared to the EMSA was chosen to make sure that all siRNA is encapsulated. It was assumed that better protection would be achieved by a little excess of THS-pDMAEMA 3 over siRNA. A stock solution (10 µl) of RNAse II with an activity of 500 U ml^{-1} and a concentration of 10 mg ml^{-1} was prepared and incubated for 30 min. at 37°C. (The enzymatic activity U ml^{-1} (1 U = 1 µmol min^{-1}) describes the conversion rate of a substrate by an enzyme.) After the incubation time, an aliquot (7 µl) of the RNAse stock solution was added to the THS-pDMAEMA 3 + siRNA solution. The RNAse concentration in the reaction tube (THS-pDMAEMA 3 + siRNA + RNAse) was 1 mg ml^{-1} with an activity of 50 U ml^{-1}. After specific time intervals of incubation at 37 °C (0 min., 10 min., 15 min., 30 min., 45 min., 60 min., 90 min.), 10 µl aliquots were withdrawn from the reaction solution and 1 µl of 4 % SDS was added to the samples to a final concentration of approx. 0.4 %. Addition of SDS inactivated the RNAse and released encapsulated siRNA from THS-poly(DMAEMA) for better analysis. Samples were kept at 4°C until gel electrophoresis. To all samples 2 µl loading dye (6x Mass Ruler DNA loading dye) was added. In order to analyse the samples an agarose gel electrophoresis (AGE) was performed. Samples were run for 25 min. at 100 V constant. Afterwards the gels were stained using a fluorescent dye (GelRed, Biotium, USA) and an incubation time of 30 min. in the GelRed solution. The GelRed staining solution was prepared according to the manufacturers protocol. The gels were imaged with a fluorescence imager (GelDoc EZ Imager, Bio-Rad, Switzerland). Fluorescence intensity was analysed with the software imageJ 1.47v (NIH, USA) by plotting intensity plots of the samples and measuring the area under curve (AUC). For the decay graph, the AUC from the sample at 0 min. incubation time was normalized to 100 % siRNA content in the reaction mixture. AUCs of the other samples were compared to the 100% siRNA sample and proportionate calculated. Error bars were calculated according to the analysis method of the gels using imageJ (v.147).[473] The bands were depicted as 2D-plots. Signal intensity was determined by measuring the area under the curve (AUC). Depending on the integration, for the same peak, different AUCs were measured. The standard deviation of N = 5 AUC measurements represents the error.

2.1.4.18 Agarose gel electrophoresis (AGE) of THS-pDMAEMA-co-RhBMA conjugates and fluorescent proteins (FPs):

Prior to analysis, samples of THS-polymer conjugates were incubated in constant amounts of THS-pDMAEMA-co-RhBMA and various amounts of fluorescent proteins for 3h. The amount of THS-pDMAEMA-co-RhBMA in the experiments was 4.4 pmol for each well. The volume for each sample/well was 10µl. If necessary, the sample was diluted with PBS buffer to 10µl. The ratios between conjugate and eYFP are summarized in table 6 and between the conjugate and TurboGFP in table 7.

Table 2.1.6. Molar ratios between THS-pDMAEMA-co-RhBMA and eYFP

Sample 1	Sample 2	Sample 3	Sample 4	Sample 5	Sample 6
eYFP (13.2 pmol)	THS-poly:eYFP 2:1	THS-poly:eYFP 1:1	THS-poly:eYFP 1:2	THS-poly:eYFP 1:3	THS-poly (4.4 pmol)

Table 2.1.7. Molar ratios between THS-pDMAEMA-co-RhBMA and TurboGFP.

Sample 1	Sample 2	Sample 3	Sample 4	Sample 5
TurboGFP (2.2 pmol)	THS-poly:TurboGFP 2:1	THS-poly:TurboGFP 1:1	THS-poly:TurboGFP 1:2	THS-poly (4.4 pmol)

2.1.4.19 Cell culture

U87 glioblastoma cell line was maintained at 37 °C in a 5% CO_2 humidified atmosphere. Cells were grown in Dulbecco's modified eagle medium (DMEM) with 10% fetal bovine serum (FBS), 1% non-essential amino acids, 100 units mL^{-1} penicillin, 100 µg mL^{-1} streptomycin and 2 mM L-glutamine.

2.1.4.20 Cell viability assay

Cytotoxicity testing was performed using the Promega CellTiter 96 AQueous Non-Radioactive Cell Proliferation (MTS) assay to determine the number of viable cells in culture. An amount of 10’000 U87 cells were cultured in a 96-well plate for 24 h prior to the experiment. Thermosome-polymer conjugates (50 – 300 µg ml^{-1}) were added to the cells and incubated for 24h at 37°C with 5% CO_2. Next, a MTS mixture (20 µL/well) was added to the cells and then incubated for 1.5 h. Cell viability was calculated by measuring the absorbance at 490 nm using a 96-well plate reader. Two internal controls were set up for each experiment: untreated cells and medium without cells. Background absorbance due to the non-specific reaction between test

compounds and the MTS reagent was deducted from exposed cell values. Each experiment was performed in triplicate.

For THS-pDMAEMA-co-pRhBMA, in addition, wells without the MTS reagent with the same concentrations as for the cell viability test were prepared. The absorption values from those wells were taken as blank values for each concentration and were subtracted from the values that were measured with the samples where the MTS reagent was added.

2.1.4.21 Sample preparation for protein delivery

To an aliquot of THS-pDMAEMA-co-pRHBMA (10.0 µg, 10.8 pmol), TurboGFP (1.16 µg, 21.6 pmol) was added in a molar ratio of 1:2. For eYFP samples the molar ratio was also 1:2 (THS-polymer conjugates: 15.0 µg,16.6 pmol and eYFP 0.9µg, 33.3 pmol). The incubation and complex formation was done in PBS buffer at 4°C over night.with a total sample volume of 10 µl. Control samples had the same concentration of either eYFP or TurboGFP, but were without THS-polymer conjugates. For FACS measurements, the sample amount was increased by a factor of three.

2.1.4.22 Cellular uptake

Freshly trypsinized U87 cells ($4x10^4$ cells in 300 µL cell culture medium) were seeded into 8-wells chamber 24 h prior to the experiment. The cell culture medium was replaced with a cell culture medium without serum (200 µL) followed by addition of the different amount of THS-pDMAEMA-co-pRhBMA (100, 250, 500 µg ml^{-1}) or THS-pDMAEMA TurboGFP complex (50, 100, 250 µg of THS-polymer conjugates, formed as described earlier). After 4h incubation, the cell culture medium was carefully removed and replaced with serum-containing medium (300 µL). The cells were incubated for additional 20 h. Immediately before live cell imaging, the cell culture medium was replaced with an Opti-MEM. Cell nuclei were stained for 10 min with 2 µL of a 50 µg/mL Hoechst 33342 solution in PBS. The imaging was performed on a commercial Confocor2 (Carl Zeiss, Jena, Germany). Images were taken using a 40x water-immersion objective. The samples were excited at 405 nm (Hoechst 33342), 488 nm (TurboGFP), 543 nm (THS-pDMAEMA-co-pRhBMA) and the emission was collected with a broad pass filter at 420-480 nm (Hoechst 33342), a long pass 505 nm filter (TurboGFP) and a long pass 560 nm filter

(THS-pDMAEMA-co-pRhBMA), respectively. Images were taken with the same acquisition settings for comparison purpose.

If necessary, cell uptake images were adjusted in contrast/brightness with the software imageJ (1.47v). For comparison reasons, settings were the same for each experiment. In order to reduce horizontal streaks in LSM images, the LSM Transmission deblurring plugin was applied. In some cases, the images were deblurred two times with the plugins default settings to remove horizontal streaks.

2.1.4.23 Flow cytometry analysis

U87 cells ($1x10^5$ cells/well) were plated into 24-well tissue culture plates 24 hours prior to the experiment. The cell culture medium was replaced with serum-free medium (464 µL) and 36 µl of the eYFP or THS-pDMAEMA-co-pRhBMA eYFP complex were added. After 4h incubation, the serum-free medium was carefully removed and replaced with 1 ml of medium containing 10% FBS. The cells were then incubated 20h. To prepare the sample cells were trypsinized with 200 µl of trypsin for 10 minutes at 37 °C and 5% CO_2. Following trypsinization, 800 µl PBS were added to the cells, gently mixed by pipetting and transferred into 1.5 mL microcentrifuge tubes. Cells were then pelleted by centrifugation at 200 RCF for five minutes. Subsequently, the media was aspirated and the pellet was resuspended in 250 µl PBS and put on ice. 6 µL of a 50 µg/mL stock solution of Hoechst 33342 was added to each sample. The cells were vortexed gently prior to FACS analysis. FACS measurements were performed by measuring at least 30000 cells with a FACS BD LSR Fortessa, the cells were excited with lasers at 405 nm (Hoechst 33342), 488 nm (eYFP and TurboGFP) and 561 nm (THS-pDMAEMA-co-pRhBMA), the emitted light passed through a Band Pass 450/50 (Hoechst 33342), 542/27 (eYFP), 512/25 (TurboGFP) and 586/15 (THS-pDMAEMA-co-RhBMA) filters, respectively, before reaching the detector. The low pass filter was set to 505 nm for eYFP and TurboGFP. The data were processed with FlowJo Vx (Tree Star, USA) and a histogram of fluorescence intensity of only viable cells was plotted.

2.1.4.24 Cell cultivation for siRNA knockdown experiments

U87 cells were grown in DMEM media containing 10% FBS, 1% penicilin/streptomycin, and 1% NEAA at 5% CO_2 and 37 °C.

2.1.4.25 Western blot analysis of THS-pDMAEMA3-mediated siRNA GAPDH knockdown

The procedure was followed from a previously published peptide siRNA delivery protocol with several modifications.[473] 24 hours before the experiment 5000 U87 cells were plated in 100 µl per well in 96 well plate and incubated at 5 % CO_2 and 37 °C. For every sample 4 wells were plated. After 24 hours, the media was removed and replaced with 100 µl opti-MEM media. Samples were prepared by adding 0.4-40 pmol of siRNA (volume 20 µl) in opti-MEM, and mixing it with either blank opti-MEM, opti-MEM containing Lipofectamine RMAiMAX, or THS-PDMAEMA3 (in a ratio of 4:1 siRNA to THE-PDMAEMA3) in 20 µl (total volume 40 µl) and incubated at room temperature for 30 min. 10 µl of sample were added to each well (final concentrations of 0.1-10 pmol siRNA per well). After 4 hours 100 µl DMEM containing normal cell culture media was added to each well and incubated for 68 more hours (72 total hours). After 72 hours, the media was removed from cells and they were washed with PBS 3x. 60 µl of lysis buffer was added to the first well incubated for 5 minutes and then transferred to the second, third, and fourth well of each sample with 5 minute incubation in each (final volume of 60 µl containing a mixture of the cell lysate of all 4 wells). The cell lysate protein concentration was quantified with the micro BCA protein assay kit. 15 µg total protein of each sample were then mixed in 5x SDS protein loading buffer and heated at 95 °C for 10 minutes. After heating, the samples were loaded into a 10% TGX stain free acrylamide gel and electrophoresed at 120 V for 50 minutes. The gel was removed from the cassette and imaged on an EZdoc one touch imager (BioRAD) using the TGX stain free method activating for 5 min. This image was analysed in imageJ to verify consistant loading of each well by quantifying the band at 40'000 g mol^{-1}. The gels were then transferred to nitrocellulose membranes via a biometra FASTblot semi-dry transfer system at a constant 80 mA for 25 minutes. The membranes were then blocked in 5% milk in TBS buffer overnight at 4 °C. The next morning the blocking solution was removed and 15 mL of 5% milk in TBS containing 1:10'000 mixture of primary monoclonal mouse antiGADPH antibody was added to each membrane and incubated at room temperature for 2 hours. The membranes were then washed in TBST buffer 3x for ten minutes each. The second incubation was also done in 15 ml 5 % milk in TBS containing 1:10'000 goat antimouse HRP conjugated antibody for 1 hour. The membranes were washed 3 more times at 10 minutes each

in TBST buffer and then dried. The supersignal west pico chemiluminescent substrate was added as per manufacturer's directions and imaged on a Bucher biotec fluorescence imaging system equipped with s FujiFilm Las-4000 camera. Images were recorded with the Las-4000 software and quantified using imageJ to determine percent GAPDH-protein level of each sample.

2.2 Self-sealing and puncture resistant breathable membranes for water evaporation applications

This work has been published: Rother, M., Barmettler, J., Reichmuth, A., Araujo, J. V., Rytka, C., Glaied, O., Pieles, U. and Bruns, N., Self-Sealing and Puncture Resistant Breathable Membranes for Water-Evaporation Applications. Adv. Mater. 2015, 27, 6620-6624, DOI: 10.1002/adma.201502761.[1]

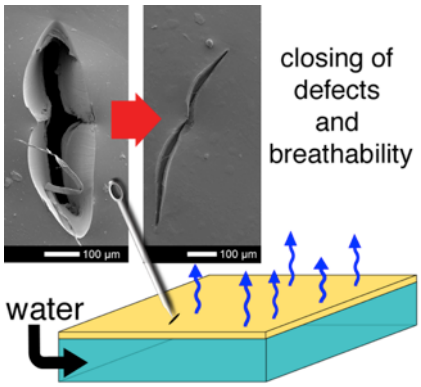

In this chapter a composite membrane was developed, which was based on a thin non-porous poly(ether ester) multi-block copolymer membrane that was covalently bound with an amphiphilic polymer conetwork (APCN), based on the hydrophilic poly(hydroxyl ethyl) acrylate and the hydrophobic poly(dimethylsiloxane). This composite material was capable to let water vapour pass through the membrane, while being capable to seal punctures at applied pressures of at least 1.6 bar. The self-closing properties were investigated with two different APCN compositions. Moreover the breathability was demonstrated on a cooling pad example.

2.2.1 Introduction

Waterproof, but water vapor permeable membranes are thin polymeric membranes that are designed to let water vapor pass, while condensed water is retained. Such waterproof and breathable membranes can be made out of expanded poly(tetrafluorethylene), polyurethane or poly(ether ester) block copolymers.[475,476] They are widely used in the textile industry for weather protective clothing that allow body-generated moisture to pass the membrane while preventing wind and rain from penetrating the fabric, thus keeping the body dry and warm. Their selective

[1] Reprinted (adapted) with permission from reference (474) Rother, M.; Barmettler, J.; Reichmuth, A.; Araujo, J. V.; Rytka, C.; Glaied, O.; Pieles, U.; Bruns, N. Self-Sealing and Puncture Resistant Breathable Membranes for Water-Evaporation Applications. *Adv Mater* **2015**, *27*, 6620-6624. Copyright Wiley-VCH, Weinheim 2015

permeability for water-vapor is not only interesting for apparel, but can also be used in medical applications, e.g. for cooling garments that alleviate symptoms of multiple sclerosis.[477-480] Their working-principle is based on the evaporation of water through a breathable membrane. Evaporative heat loss causes a gentle drop in temperature of the skin and the tissue underneath. Moreover, breathable membranes find application in pervaporation,[481,482] membrane distillation[483] moisture regulation of buildings[484] and in humidification for the conservation of art and paper.[485] They can also be used as part of a sensor for constant electrocardiography monitoring.[486,487] A major drawback of these membranes is that they are sensitive to punctures and mechanical wear and tear. Even a microscopic hole causes the membrane to become leaky for liquid water. To overcome this problem, self-sealing membranes that autonomously close or heal damage would be desirable. The sealing of holes in rubbery materials is well known,[488] e.g. in the case of rubber septa,[489] in waterproofing construction foils that feature a layer of rubberized asphalt,[490] or in self-sealing actuators.[491] The self-sealing effect can be enhanced if the material is not only elastic, but also swellable in a solvent. The volume gain due to swelling can close reasonable large holes. This concept has been used in technical applications, such as bullet proof fuel tank of world war II aircrafts[492] and in self-repairing car tires.[493] Inspiration for self-sealing materials can also be drawn from Nature. The plant *Aristolochia macrophylla*, a northamerican liana, has a mechanism to mechanically close defects.[494] Its tissue expands and swells to seal fissures. Inspired by this phenomenon, Speck and co-workers developed an airtight pneumatic membrane (as used, e.g. in inflatable boats) that is capable to close punctures by the expansion of a polyurethane-foam.[495] Unfortunately, all these materials are not suitable for self-sealing breathable membranes, as a sealing layer on a climate membrane has to be permeable for water in order to retain the original function of the membrane, i.e. the evaporation of moisture.

Here we present a two-layered composite membrane for water evaporation applications that autonomously closes small defects by swelling of a water-swellable elastomeric layer. The self-sealing membrane consisted of a waterproof and breathable, non-porous poly(ether ester) multi-block copolymer membrane (PEE; Sympatex membrane)[476,496] onto which an amphiphilic polymer conetwork (APCN)[497-510] was polymerized. APCNs are water-swellable materials that have much stronger mechanical properties than conventional hydrogels due to the

presence of a reinforcing hydrophobic phase.[497,511-513] Moreover, they have been investigated as membranes for pervaporation,[514,515] nanofiltration,[515,516] chiral separation,[517] and drug delivery.[518,519] We chose APCNs in which hydrophilic poly(2-hydroxyethyl acrylate) (PHEA) was cross-linked with hydrophobic poly(dimethylsiloxane) (PDMS) because these APCNs are rubbery, elastic materials both in dry and wet state.[382,519-522] The combination of PHEA-l-PDMS with a PEE membrane resulted in a composite material, here named APCN/PEE, that effectively closed punctures, while having water evaporation properties similar to unmodified PEE membranes.

2.2.2 Results and Discussion

A precursor method reported by Bruns. et al. was adapted for the synthesis of PHEA-l-PDMS.[521] The APCN/PEE composite membranes were prepared by synthesizing PHEA-l-PDMS conetworks on modified PEE membranes. First, the surface of PEE was activated with oxygen plasma and functionalized with methacrylate groups by condensation of 3-(trimethoxysilyl)propyl methacrylate. This modification ensures a tight bonding between the PEE and the APCN, because the methacrylate groups copolymerize with monomers of the APCN.[521] UV-initiated free radical copolymerization of 2-(trimethylsilyloxy)ethyl acrylate (TMSOEA) with α,ω-dimethacrylate-terminated poly(dimethylsiloxane) (MA-PDMS-MA; M_n = 5050 g mol^{-1}, PDI = 1.11) under argon atmosphere resulted in hydrophobic precursor networks that were covalently bound to PEE. The trimethyl-silyl (TMS) groups of these networks were cleaved by immersing the composite membranes in acidified mixtures of 50% isopropanol (iPrOH) in water, resulting in hydrophilic PHEA chain segments. Successful removal of the TMS groups was confirmed via infrared spectroscopy (See Figure 2.2.1).[521] Our synthesis approach allows to prepare APCNs with a wide range of compositions by adjusting the ratio of the TMSOEA to MA-PDMS-MA in the monomer mixture.[521] A higher hydrophilic content results in a higher degree of swelling in water.[521] As a pronounced swelling should give rise to a good self-sealing effect, we chose to synthesize PHEA-l-PDMS conetworks with 75 wt% and 90 wt% PHEA content. The thickness of the APCN could also influence the self-sealing properties of the composite membrane. Therefore, APCN/PEE were prepared in casting molds of 200 µm and 400 µm height.

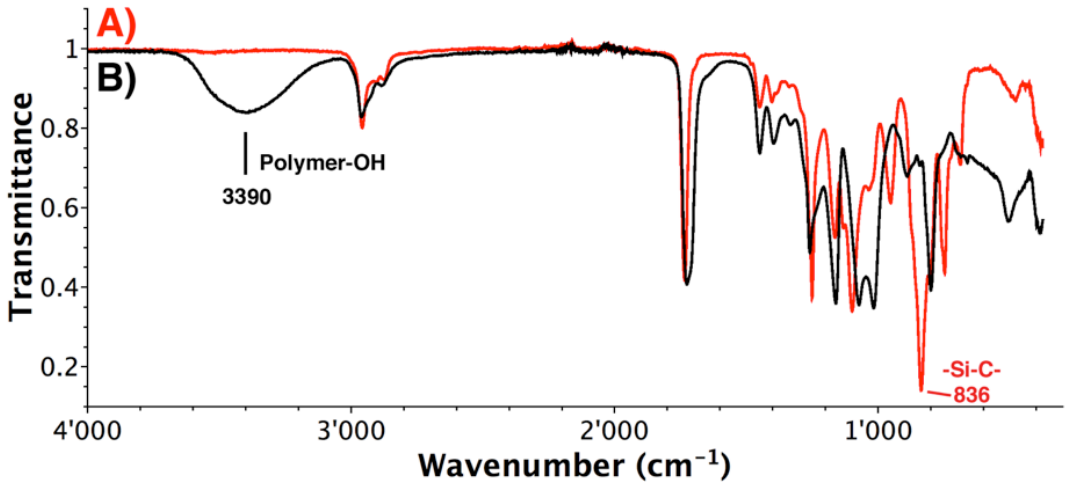

Figure 2.2.1. ATR-FT-IR spectra of APCN/PEE composite membrane with a composition of PHEA:PDMS 90:10 (w/w). The spectra were recorded on the APCN side of the sample. A) PTMSOEA-l-PDMS before treatment in acidified iPrOH:H_2O (1:1); B) The same sample after incubation for 24 h in acidified iPrOH:H_2O (1:1) and subsequent drying. This process cleaved the TMS groups from the PHEA chain segments and yielded an amphiphilic PHEA-l-PDMS conetwork. Removal of the TMS groups resulted in the appearance of the broad OH-Polymer band at 3390 cm^{-1} and disappearance of the –Si-C-band at 836 cm^{-1}.

2.2.2.1 Imaging of the APCN/PEE composite

The produced APCN/PEE composite membranes were imaged by scanning electron microscopy (SEM). The micrograph (Figure 2.2.2a) shows the two layers of the composite material. There is no gap between the PEE-membrane and the APCN, which indicates good binding between the materials. SEM also allowed measuring the thickness of the APCNs. A 400 µm casting mold resulted in PHEA-l-PDMS layers with a thickness of approx. 340 µm, while the 200 µm casting mold yielded approx. 170 µm thick APCNs. This decrease in volume is most likely due to polymerization shrinkage and the cleavage of TMS groups. All synthesized APCNs were optically transparent. This proves that no macroscopic phase separation between the hydrophilic and the hydrophobic polymers occurred, and is consistent with literature reports on the nanophase separated morphologies of APCNs.[497,521] However, the hydrophobic phase can accumulate on the surface of APCNs,[521] which would lead to the formation of a water-impermeable PDMS layer on the surface. Such layer would hamper the ability of the composite membranes to take up and evaporate water. Therefore, the phase morphology on the surface of an APCN/PEE composite membrane was visualized by atomic force microscopy (AFM) in phase mode (Figure 2.2.2b). Dark areas represent soft PDMS domains, whereas bright

areas show harder PHEA domains.[521] AFM revealed a nanophase separated cocontinuous morphology with average domain sizes below 70 nm. The area covered by PDMS is higher than expected from the overall PDMS content of the sample (10 wt%), indicating that the hydrophobic polymer enriched on the surface during synthesis. However, the PDMS does not form a closed layer, so that water can penetrate into the APCN and diffuse through the material.

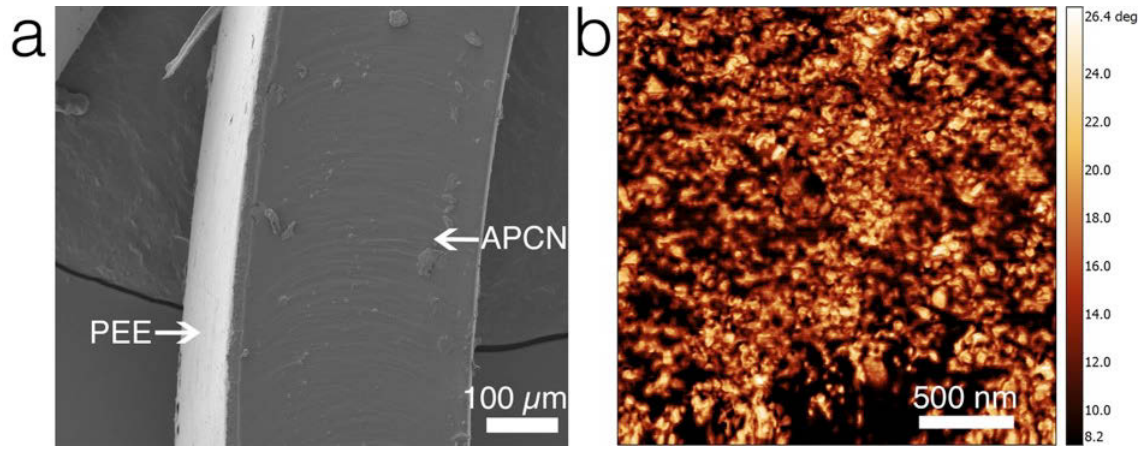

Figure 2.2.2. SEM and AFM characterization of the APCN/PEE composite. (a) SEM image of a dry APCN/PEE composite membrane (side cut). Composition of the material was PHEA:PDMS 90:10 (w/w) with a thickness of approx. 350 µm. (b) AFM image (phase mode) of the surface of the APCN side of an APCN/PEE composite membrane with a composition of (PHEA:PDMS 90:10 (w/w)) and a thickness of 340 µm.

2.2.2.2 Swelling properties of APCN/PEE composites

As expected, PHEA-l-PDMS conetworks swelled in water. Freestanding samples with a composition of PHEA:PDMS 75:25 (w/w) reached an equilibrium degree of swelling Q = 1.57 ± 0.02 and samples with a composition of PHEA:PDMS 90:10 (w/w) swelled to Q = 2.10 ± 0.1.

2.2.2.3 Mechanical properties of APCN/PEE composites

The mechanical properties of composite membranes were investigated by tensile tests (Figure 2.2.3). APCN/PEE membranes with a composition of PHEA:PDMS 90:10 (w/w) behaved like an elastomer with a young modulus of 0.05 ± 0.01 MPa and a stress of 1.74 ± 0.23 MPa at 250 % strain. In contrast, stress-strain curves of neat PEE membranes and of methacrylate-functionalized PEE membranes are typical for thermoplastic polymers. Thus, the predominant load-bearing phase in the composite membranes is the APCN. The elastic modulus and yield strength of PEE

increased significantly after its surface was functionalization with a methacrylate-bearing silane, most likely because of the formation of brittle silica on (and in) the PEE. Similar observations were made for other polymer-silicon oxide hybrid materials.[523,524] PDMS-based APCNs are elastomers.[497,511,525] Addition of the APCN to the PEE resulted in a composite membrane in which the elastomeric PHEA-*l*-PDMS became the predominant load-bearing phase

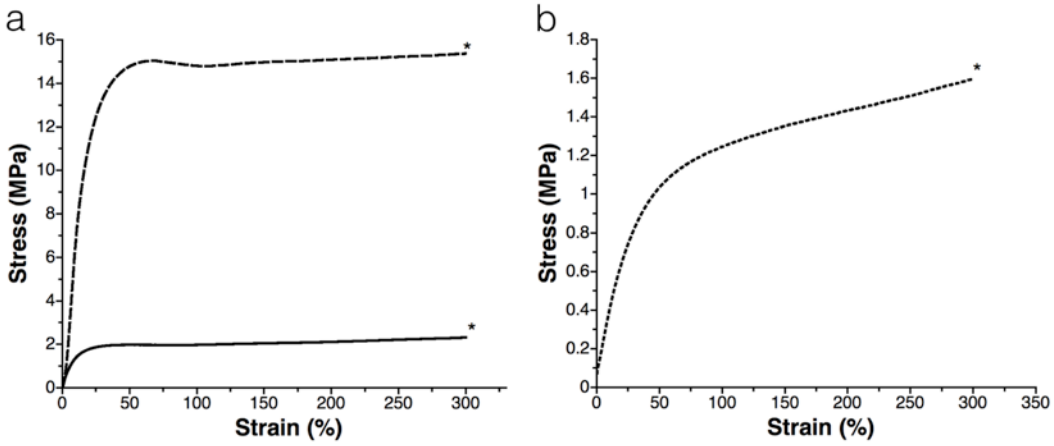

c

	Elastic Modulus[MPa]	Yield Strength [MPa]
PEE	0.20 ± 0.02	1.94 ± 0.09
PEE-methacrylate	1.96 ± 0.33	15.17 ± 0.69
APCN/PEE	0.05 ± 0.01	------

Figure 2.2.3. Mechanical properties of dry membranes. (a) Stress-strain curves of PEE (——) and methacrylate-functionalized PEE (----) membranes; (b) Stress-strain curve of APCN/PEE composite membrane with a composition of PHEA:PDMS 90:10 (w/w) and a thickness of 340 µm (·····). * = Measurements were stopped before the ultimate tensile strength and elongation at break were reached, as the experimental-set-up did not allow to measure at higher strains. (c) Mechanical properties of membranes. Average values from at least five tensile tests per type of membrane and standard deviations are reported.

2.2.2.4 Investigation of self-sealing properties

In order to show that APCN/PEE composite membranes can self-seal small defects, dry membranes were punctured with a needle of 0.6 mm diameter. Figure 2.2.4 and Figure 2.2.5a show SEM pictures of the resulting holes. When the composite membrane was brought into contact with water, the APCN swelled and closed the holes (Figure 2.2.5b). The self-sealing capabilities of APCN/PEE membranes were

quantified by measuring the water flow through damaged membranes. PEE membranes are water-proof to pressures above 4.4 bar, according to the manufacturers specifications.[526]When pierced, a substantial amount of water passes through the hole in the membrane (Figure 2.2.5c and Figure 2.2.6). In contrast, the APCN/PEE composite membranes show no or only little leaking, i.e. they are self-sealing materials. In a first set of experiments, the effect of APCN composition on self-sealing was investigated at water pressures between 0.02 bar and 0.04 bar above atmospheric pressure (Figure 2.2.6). Leaking rates between 8×10^{-5} ml sec^{-1} and 2.2×10^{-3} ml sec^{-1} were determined for APCN/PEE membranes with a composition of PHEA:PDMS 75:25 (w/w) and a thickness 170 µm. This is 450 times lower than the leaking rates of the unmodified PEE-membrane at these pressures (0.035 ml sec^{-1} to 0.1 ml sec^{-1}). Composite membranes with an APCN composition of PHEA:PDMS 90:10 (w/w) had leaking rates that ranged from 0 ml sec^{-1} to 7×10^{-4} ml sec^{-1}, i.e. they were more than three orders of magnitude lower than those of unmodified PEE. APCNs with a PHEA-content of 90% showed a stronger self-sealing effect than those with a PHEA-content of 75%, most likely because a higher hydrophilic content leads to higher swelling of the APCN in water. For this reason, all further self-sealing experiments were carried out with APCN/PEE membranes with a composition of PHEA:PDMS 90:10 (w/w).

The influence of the APCN thickness on the self-sealing performance of APCN/PEE membranes was evaluated at pressures between 0.1 bar and 1.6 bar. With 170 µm thick samples, leaking rates at pressures ≤ 0.5 bar were very low (< 0.006 ml sec^{-1}) (Figure 2.2.5d). Above this threshold, leaking rates increased with pressure, i.e. the 170 µm thick APCN layer was not capable to seal small defects completely. In contrast, the water flow through 340 µm thick membrane stayed between 0 ml sec^{-1} and 0.003 ml sec^{-1} for pressures up to 1.6 bar (Figure 2.2.5e). The 340 µm thick APCN was therefore capable to seal holes in the investigated pressure range. In conclusion, thicker APCN layers lead to a higher pressure tolerance of the self-sealing effect, because more swollen material covers the defect in the PEE.

Although water penetrated through the 170 µm thick APCN/PEE membranes at pressures ≥ 0.6 bar, it should be pointed out that the observed leaking was significantly less than the loss of water through an unmodified PEE membrane. At 0.5, 1.0 and 1.5 bar, respectively, a leaking rate of 0.85 ml sec^{-1}, 1.1 ml sec^{-1} and 2.6 ml sec^{-1} were measured for pierced PEE. Drying of a damaged APCN/PEE

membrane reopens the puncture, because the APCN de-swells. In order to determine if this process would impede the ability of the membrane to seal the hole if rewetted, a punctured membrane was repetitively dried and exposed to water. A self-sealing experiment with a 340 µm thick APCN/PEE was carried out at a pressure of 0.5 bar as described above. No leaking of water was observed (Figure 2.2.5f, cycle 1). After the measurement, the membrane was dried in air over night. Then, water was refilled into the test apparatus, wetting the membrane. Pressure was set to 0.5 bar. The material immediately sealed the puncture, and no water passed through the membrane. These drying and wetting cycles were repeated four more times (Figure 2.2.5f, cycles 2 to 5). Leaking rates remained at 0 ml sec^{-1}, i.e. the composite membrane sealed the puncture completely. Thus, the self-sealing property of APCN/PEE membranes is not affected by repeated drying-swelling cycles.

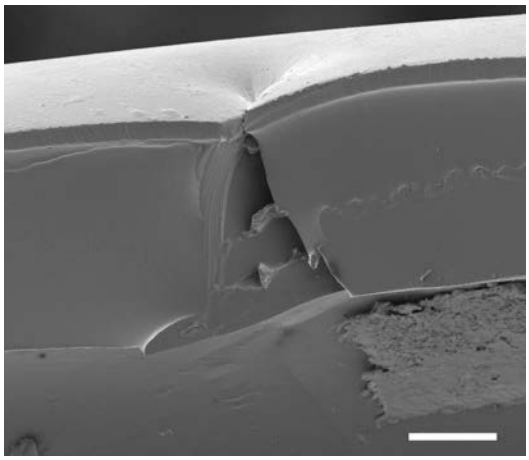

Figure 2.2.4. SEM image of a puncture in a dry APCN/PEE composite membrane (side cut). Composition of the material was PHEA:PDMS 90:10 (w/w). The APCN thickness of this membrane was approx. 200 µm. The membrane was damaged with a syringe needle (diameter 0.6 mm) in the dry state. Scale bar is 100 µm.

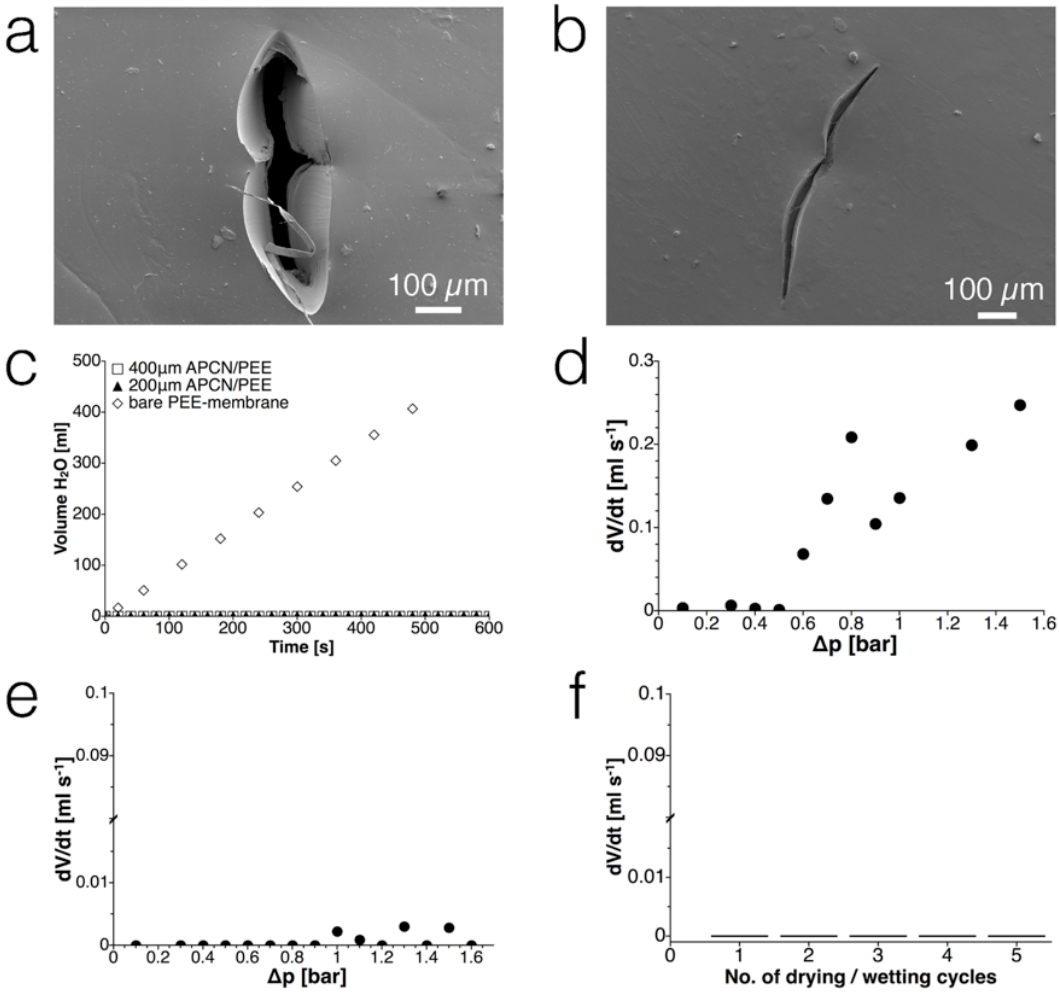

Figure 2.2.5. Self-sealing of APCN/PEE composite membranes with a composition of PHEA:PDMS 90:10 (w/w). (a) Cryo SEM image of a puncture in a dry APCN/PEE membrane with a thickness of 340 µm. (b) Cryo SEM image of a defect after swelling of the APCN in water (thickness of sample 340 µm). (c) Measurement of the water flow through punctured unmodified PEE membrane in comparison to punctured APCN/PEE composite membranes with thicknesses of 170 µm µm and 340 µm at a water pressure of 0.5 bar above atmospheric pressure. Such data was used to determine leaking rates. (d) Leaking rate in dependence of water pressure for punctured APCN/PEE composite membranes with a thickness of 170 µm. (e) Leaking rate in dependence of water pressure for punctured APCN/PEE composite membranes with a thickness of 340 µm. The membranes were damaged by puncturing them with a syringe needle (diameter 0.6 mm) in the dry state. Variations in the leaking rate might be a result of the manual piercing process and small inhomogeneities in the materials' thickness. (f) Effect of repetitive drying/wetting cycles on the ability of an APCN/PEE composite membrane to self-seal. A composite membrane with a thickness of 340 µm was punctured with a syringe needle (diameter 0.6 mm) in the dry state and leaking rates at 0.5 bar water pressure were measured.

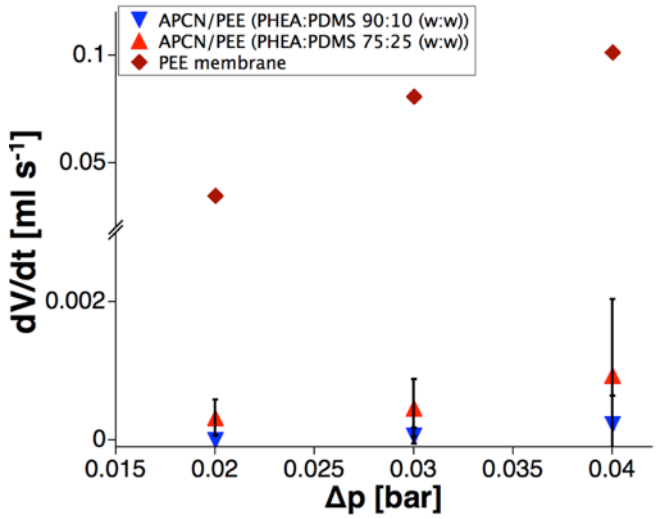

Figure 2.2.6. Leaking rates of 170 µm thick APCN/PEE composite membranes with different compositions and of unmodified PEE at water pressures between 0.02 bar and 0.04 bar.

2.2.2.5 Evaluation of water vapour evaporation through the APCN/PEE

Water evaporation through the composite membranes was measured in order to assess if the layer of APCN on the PEE hampers the functionality of the membrane in cooling garment applications.[477,478,480]

To this end, two types of cooling laminates were produced. One was made with the unmodified PEE membrane and served as reference sample. The other was made using an APCN/PEE composite membrane with a composition of PHEA:PDMS 90:10 (w/w) and a thickness of 170 µm. The fabrication procedure and experimental setup is described in the supporting information. In brief, the membranes were used to enclose a hydrophilic polyethylene terephthalate (PET) fabric in a sandwich laminate (Figure 2.2.7a). The APCN layer was facing inwards, i.e. towards the fabric. Membranes and fabric were glued together with an array of glue spots and the laminates were sealed at their edges. Water that was filled into the laminate was distributed throughout the laminate by the inner fabric. The two laminates were connected to water-reservoirs and placed on a heating plate that was set to the average human skin surface temperature of 34 °C.[527] Evaporation of water through the membranes was measured as loss of water in the reservoirs. In addition, temperature of the cooling laminates was monitored by an infrared (IR) camera. Both types of cooling laminates evaporated water through the membranes (Figure 2.2.7b): APCN/PEE-based laminates with an evaporation area of 20 cm^2 at a rate of 0.0162 ± 0.0006 ml h^{-1} cm^{-1} (and PEE reference laminates at 0.0298 ± 0.0003 ml h^{-1} cm^{-1}).

Evaporation of water from APCN/PEE samples was slower, most likely because the APCN layer transports water to the PEE membrane by diffusion, while unmodified PEE membrane is in direct contact with liquid water. Moreover, the additional material could act as heat resistance that reduced energy transfer from the plate to the surface of the laminate.

The infrared camera measured average temperatures on the APCN/PEE-based and the PEE-based laminates of 26 ± 1 °C and 30 ± 2 °C, respectively (Figure 2.2.5c). The drop in temperature is in accordance with previously reported results for similar cooling devices.[478] The laminates had a lower surface temperature than the heating plate. The temperature was also lower in the middle of the laminates than at their sealed edges, indicating that the evaporation of water resulted in cooling. The heat transfer resistance of the material also contributed to the decrease in surface temperature, which is the reason why the temperature of the thicker APCN/PEE membranes was lower than the temperature of the PEE-based laminate, despite the higher rate of water evaporation in the latter case.

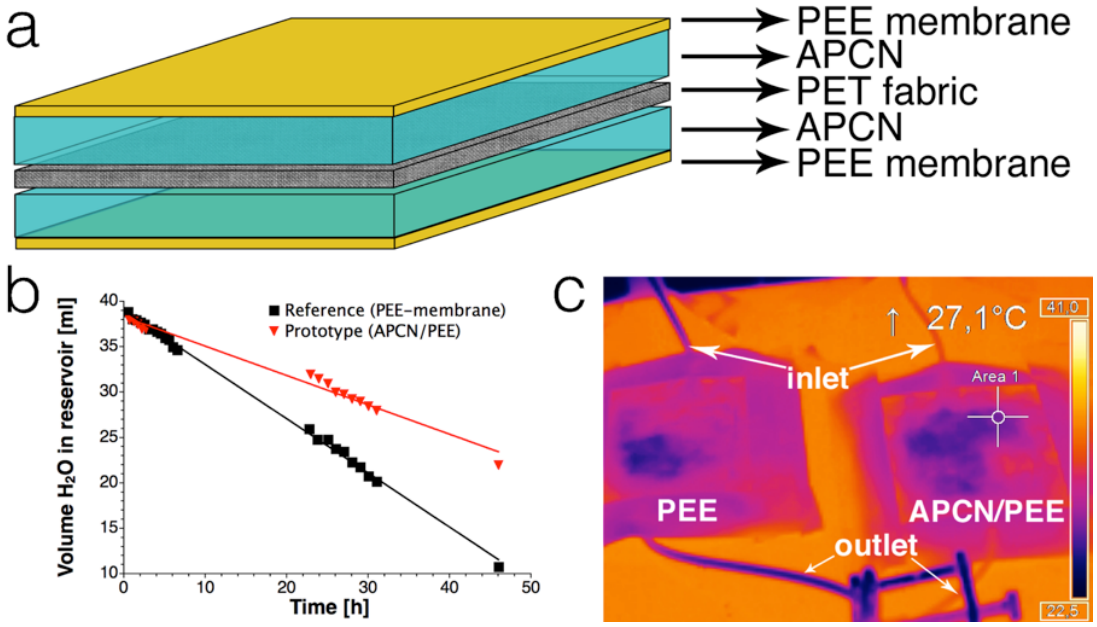

Figure 2.2.7. Water evaporation and cooling due to evaporative heat loss in APCN/PEE-based, water-filled laminates. (a) Schematic view of the three-layer laminate. (b) Water evaporation from APCN/PEE-based and PEE-based laminates, measured as the loss of water in the reservoirs. The laminates had a size of 8 × 7 cm^2 and an evaporation area of 5 × 4 cm = 20 cm^2 (see supporting information for explanation of the evaporation area). (c) Temperature of the cooling laminates during a water evaporation experiment as measured with an IR camera.

2.2.3 Conclusions

In conclusion, we have modified a waterproof, but breathable PEE-membrane with an amphiphilic polymer conetwork in order to equip the membrane with self-sealing properties. When in contact with water, the two-layer APCN/PEE composite membrane was able to seal damages by swelling of the APCN. Thicker and more hydrophilic APCN layers resulted in a more pronounced self-sealing effect. A 340 µm thick APCN/PEE prevented leakage through punctures at pressures of at least 1.6 bar, which corresponds to a water column of >16000 mm. A membrane is considered to be waterproof if it can withstand a pressure of 1300 mm.[526] Thus, the self-sealing effect is strong enough to render the composite membranes waterproof after puncture with a sharp object such as a syringe needle. Cooling laminates were assembled from these membranes. Water evaporation through the composite membrane was similar to the evaporation of water through unmodified PEE membranes and resulted in a gentle drop of surface temperature. We demonstrated the functionality of the composite membrane in the context of cooling garments. However, it is easy to envision that such self-sealing composite membranes can also find applications in other areas, e.g. as pervaporation membranes with prolonged life time, humidification devices for paper conservation, or as robust climate membrane in protective textiles.

2.2.4 Experimental section

2.2.4.1 Materials

All chemicals were used as received unless described otherwise. Isopropanol (iPrOH, EP, PhEur) was purchased from Brenntag Schweizerhall (Switzerland). 3-(Trimethoxysilyl)propyl methacrylate (TMSPMA, ≥98%) was purchased from Sigma-Aldrich. Methacryloxypropyl terminated poly(dimethylsiloxane) (α,ω-dimethacrylate-terminated poly(dimethylsiloxane); MA-PDMS-MA; M_n = 5050 g mol^{-1} (GPC), PDI = 1.11 (GPC), end functionalization ≥ 99 % (^{1}H-NMR)) and 2-(trimethylsilyloxy)ethyl acrylate (TMSOEA, 97%) were purchased from ABCR (Germany). TMSOEA was distilled prior to use in order to remove the polymerization inhibitor at 50 °C and 6.2×10^{-2} mbar. The photoinitiator Irgacure 651 (2,2-dimethoxy-1,2-diphenylethane-1-one) was kindly provided by BASF

(Germany). Self-adhesive poly(propylene)-tape (tesafilm® kristall-klar from Tesa AG, Germany) with a thickness of approx. 50 µm was used. Polyester-polyether (PEE) membrane with a thickness of approx. 20 µm was obtained from Sympatex Technologies (Germany). The polyethylene terephthalate (PET) fabric with a thickness of approx. 50 µm and mesh density of 150 dtex was obtained from Serge Ferrari Tersuisse AG (Switzerland).

2.2.4.2 Functionalization of PEE-membrane

The surface of PEE membrane was functionalized with methacrylate groups in order to allow covalent binding of TMSOEA-l-PDMS to the PEE membrane (see Scheme S1). For this purpose, the PEE membrane was treated with an oxygen plasma at a pressure of 0.0108 mbar and a flow rate of 84.5×10^{-3} Pa m^3 s^{-1} and a radio frequency (RF) power of 50 W. The membranes were treated on both sides for 5 min each side. Subsequently, the membranes were placed between two glass plates (20 × 20 cm). TMSPMA was injected between the activated membrane and the glass plate on both sides with a concentration of 1.7×10^{-5} mol ml^{-1}. The temperature was maintained at 40°C for 2

hours followed by 1 night at room temperature and ambient pressure allowing the condensation of TMSPMA onto the PEE-membrane. The membranes were washed 3 times with EtOH and then dried.

2.2.4.3 Synthesis of APCN/PEE composite membranes

The process of APCN/PEE preparation is depicted in Figure 2.2.8. Synthesis of the composite membranes was carried out in a glove box (Labstar Glove Box Workstation, MBraun) under argon atmosphere ($p(O_2) < 1$ ppm). MA-PDMS-MA was mixed with TMSOEA in a glass vial containing Irgacure 651 with a concentration of 5 mg mL^{-1}. The mixture was thoroughly mixed until the initiator was completely dissolved. Volume ratios between TMSOEA and PDMS were calculated based on the final product after cleavage of the TMS-groups (e.g. PHEA:PDMS 90:10 (w/w)). Table 2.2.1 reports the quantity of reagents used for APCN/PEE composite membranes with a size of 16.3 cm x 10.3 cm and a mold thickness of 200 µm. For the preparation of APCNs in a 400 µm thick mold the amount was doubled.

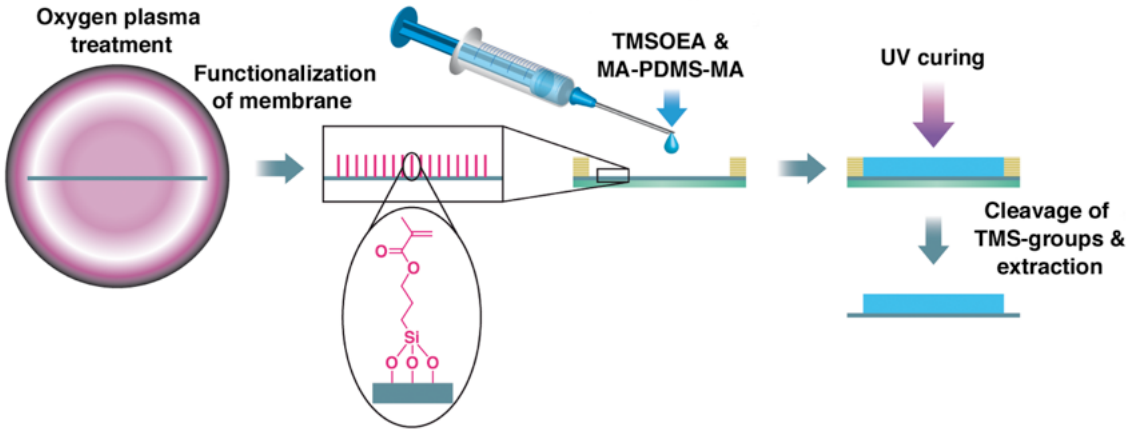

Figure 2.2.8. Fabrication process of APCN/PEE composite membranes. PEE membranes were treated with oxygen plasma and functionalized with methacrylate groups by condensation of TMSPMA. Then, a monomer mixture of TMSOEA, MA-PDMA-MA and photoinitiator Irgacure 651 was casted onto the membrane. The monomer mixture was cured by UV-initiated free radical polymerization. Casting and UV curing was performed under inert atmosphere. Subsequently, the composite membrane was incubated in an acidified H2O:iPrOH (1:1) mixture to cleave TMS groups. The overall process yielded PHEA-l-PDMS amphiphilic polymer conetworks that were covalently attached to the PEE membrane.

Table 2.2.1. Quantity of reagents used for APCNs with the size of 16.3 cm x 10.3 cm and a thickness of 200 µm.

Final composition (PHEA:PDMS, (w/w))	V (MA-PDMS-MA) [µL]	m (MA-PDMS-MA) [mg]	n (MA-PDMS-MA) [µmol]	V (TMSOEA) [µL]	m (TMSOEA) [mg]	n (TMSOEA) [µmol]	m (Irgacure 651) [mg]	n (Irgacure 651) [µmol]
75:25	831	814	163	4169	3961	21035	25	98
90:10	311	305	61	4689	4454	23655	25	98

The functionalized PEE-membrane was moistened with EtOH. The edges of the membrane were fixed onto a glass plate with self-adhesive tape in a way that the membrane was strained after evaporation of EtOH. The tape formed a rectangular mold into which monomer mixtures could be casted. By using several layers of tape, the APCN thickness could be adjusted in 50 µm steps. The monomer mixture was added uniformly onto the PEE-membrane. Curing of the mixture was performed in a curing chamber using a 400 W UV curing lamp (UV Light Technology Limited, Birmingham, UK). Radiation power of the UV lamp at the surface of the sample was 10 mW cm^{-2}. The lamp had an output between 315 nm and 405 nm using the

suppliers black filter glass. The monomer mixture was exposed to UV light for 1 min. Then, the sample was then taken out of the chamber for 2 min to cool down the material. This cycle was repeated 4 times for each sample. Cooling times were important in order to have clear materials with nanoscopic phase seperation. When cooling times were not included in the synthesis procedure, the APCNs became opaque due to larger domains that phase seperate. After synthesis, the sample was incubated for 24 h in a 1:1(v:v) mixture of H_2O and iPrOH that had been acidified with 2-3 drops of HCl (37%) per liter. HCl was added to increase the cleavage rate of TMS-groups.

Free-standing APCNs were prepared as described above, but with no PEE membrane present.

2.2.4.4 Preparation of cooling laminates

Cooling laminates with a size of 8 cm × 7 cm were produced. To this end, APCN/PEE composite membranes with a composition of PHEA:PDMS 90:10 (w/w) and a thickness of 170 µm were glued with an array of dots of Elastosil E43 (Wacker, Germany) (dot diameter = 2 mm, distance between dots = 5 mm) to both sides of a hydrophilic PET fabric with the APCN layers facing towards the PET fabric. The result was a three-layer laminate in which the PET fabric is enclosed by the composite membrane (Figure 3a). The gaps between the dots of glue in combination with the PET fabric allowed water to evenly distribute in the laminate and contact the composite membranes. The edges of the sandwich were sealed with Elastosil E43. Due to sealed edges, the evaporation area, i.e. the area of the membrane that could get in contact with water, was 20 cm^2. In addition, two silicone tubings (MVQ Silicones, Germany) with different diameters (outer diameter = 4.5 mm resp. 2.8 mm; inner diameter = 2 mm resp. 0.8 mm) were fixed in between the two membrane layers using Elastosil E43. The thinner tube acted as an air outlet the thicker as a water inlet.

Reference cooling laminates were prepared as described above, but replacing the APCN/PEE composite membrane with unmodified PEE membrane (thickness ≈ 20 µm) that had briefly been flame treated (one second butane gas flame with a distance of 5 cm to the surface) in order to create reactive groups for a better adhesion of the glue.[528]

2.2.4.5 Methods

Fourier-transform infrared (FT-IR) spectra were recorded on an Alpha FT-IR spectrometer with attenuated total reflection (ATR) module (Bruker Optics, Germany). Spectra were analyzed using OPUS 6.5 software from Bruker.

Atomic force microscopy (AFM) images were recorded using an Agilent 5100 AFM/SPM microscope (PicoLe System, Molecular Imaging, USA) in tapping mode at ambient conditions. Silicon cantilevers (PPP-NCHR; Nanosensors, Switzerland) with nominal spring constant of 42 N m^{-1} were used for measurements. Images were collected with a resolution of 1024 × 1024 pixels at a scan rate of 0.4 lines s^{-1}.

For conventional scanning electron microscopy (SEM), samples were cut with a scalpel. The sample was mounted onto a 45° sample holder in a way that the area of interest did not contact the sample holder. Then, the sample was sputtered with a 20 nm thick gold layer using a Leica EM ACE600 high vacuum coater. SEM images were taken with a FEI NOVA Nano SEM230 Microscope at 5 kV. In order to see the edge of the sample from a top view, the sample holder was tilted. For cryo-SEM, an APCN/PEE membrane sample was mounted on an aluminum cylinder and mechanically fixed with a ring of wire in a way that the APCN side was facing the outside. The cylinder had two drilled holes and the composite membrane was pierced with a syringe needle (Sterican 0.6 mm × 30 mm; B|Braun Melsungen AG, Germany) from the PEE-side. After mounting the cylinder on the cryo holder, the sample was plunge frozen in nitrogen slush and transferred under vaccum to the prechamber of the cryo preparation unit Gatan Alto 2500 (Figure 8). There, it was sputtered with a gold layer of 20 nm and finally transferred to the cryo stage of the SEM, which was cooled to -150°C. Images were taken with a Philips ESEM XL 30 Microscope at 5 kV. For images of water-swollen APCN/PEE membranes, samples were prepared and imaged as described above. In addition, the cylinder with fixed membrane was put into a small dish filled with water prior to freezing. The sample was allowed to swell for 2 h. Then, surface water was removed using a fiber-free tissue and the sample was immersed in nitrogen slush under vacuum. Tensile tests were conducted with a Dynamic Mechanical Analyser (DMA-Q800, TA Instruments). The samples were cut into rectangular strips of 5 x 15 mm^2 and gripped using clamps. Tests were performed with dry samples at 26 ºC, with a strain rate of 5 % min^{-1}, to a final strain of at least 300 % (which represents the maximal strain that could be achieved with the experimental set-up). The Young's moduli for PEE and

methacrylate-functionalized PEE membranes were calculated from the slope of the initial linear region of stress-stain curves. Yield strength for PEE and PEE-methacrylate was determined as the maximum stress value after which the materials began to deform plastically, i.e. at the yield point. At least five specimens were tested for each type of material. Average values and standard deviations are reported.

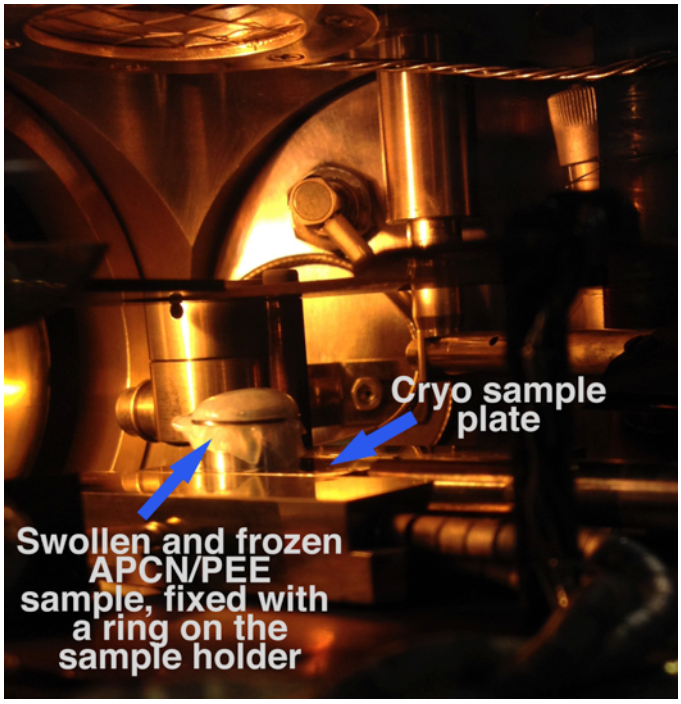

Figure 2.2.9. Inside view of the prechamber of the cryo preparation unit Gatan Alto 2500 with a swollen and frozen APCN/PEE sample that was fixed on a cylindrical sample holder.

2.2.4.6 Swelling and water content measurements

The equilibrium degree of swelling (Q) was calculated from $Q = \frac{m_{swollen}}{m_{dry}}$, whereas $m_{swollen}$ represents the mass of a free-standing APCN sample in its swollen state and m_{dry} is the same sample in dry state. Samples were dried in a vacuum oven at 40°C for 48 h until constant weight. Afterwards, samples were immersed in H_2O for 24 h. Excess of water was removed from the surface of the sample by blotting with laboratory tissue and the swollen APCN was weighted. For each APCN composition, the swelling of at least 3 samples was measured. Average Q and the standard deviation are reported.

2.2.4.7 Self-sealing experiments

For each dataset all experiments were performed with samples of the same batch, i.e. of the same APCN thickness, to ensure that batch-to-batch variations in sample thickness did not influence the measured leaking rates.

Self-sealing at pressures between 0.02 bar and 0.04 bar was evaluated by tightly fixating an APCN/PEE membrane with a rubber band across the cut-of opening of a syringe and connecting the syringe as an adapter to a glass column (3 cm diameter) via luer connections. The APCN was facing towards the water reservoir. A hole was pierced into the membrane in wet conditions from the PEE side using a syringe needle with 0.6 mm diameter (Sterican 0.6 mm × 30 mm; B|Braun Melsungen AG, Germany). The glass column was filled with water to a height of 20 cm, 30 cm, or 40 cm, respectively. The water column defined the applied pressure on the material. Leakage through the pierced membranes was measured by collecting the water in a beaker on an analytical balance (AL204, Mettler-Toledo, Switzerland).

Scheme S2 shows the experimental setup for measurements at pressures between 0.1 bar and 1.6 bar. A small round piece of APCN/PEE membrane (1.00 cm diameter, 0.79 cm^2) was cut out and placed in a custom-made poly(tetrafluoroethylene) (PTFE) adapter. This adapter consisted of two rings with an inner diameter of 0.5 cm and an inner metal plate with a hole of 0.2 cm in diameter. It prevented coiling up of the membrane and undesired leakage. The adapter was placed in a swinny stainless steel syringe filter holder (13 mm; Cat. No. XX3001200; Millipore). A hole was pierced into the membrane in dry conditions from the PEE side using a syringe needle with 0.6 mm diameter. Membranes were pierced after placing the membrane into the filter holder device. The filter holder was connected to a glass chromatography column (height approx. 65 cm, inner diameter 4 cm, max. pressure 2.5 bar) via a syringe adapter so that the APCN faced towards the column. The adapter was composed of rubber tubing in which a half-cut 1 ml syringe was inserted on one side with the male luer part looking out. The adapter was tightened to the column outlet with a clamp. The male luer was connected to the filter holder. The column was then filled to a height of 45 cm with water and pressurized with air. A pressure reduction valve with manometer (DTG-35, Druck & Temperatur Leitenberger GmbH, Germany) was used to regulate and determine the pressure. The manometer was connected with the top of the column by a tube. Primary air pressure was set to 2.0 bar. Leakage rates were

determined by measuring water flow through the membrane using a beaker and an analytical balance (see Figure 2.2.10.).

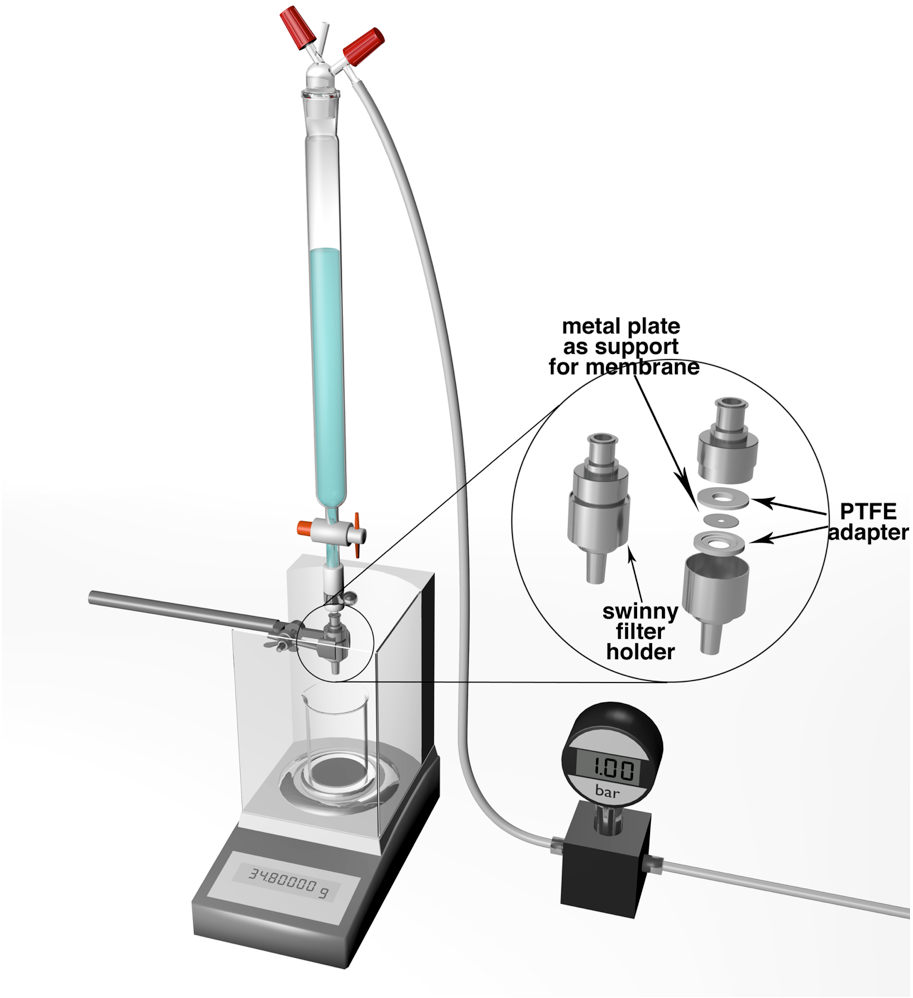

Figure 2.2.10. Schematic depiction of experimental setup for self-sealing experiments. A membrane was placed in a PTFE adapter which was then put into a swinny filter holder. The membranes were punctured in this holder by means of a syringe needle. Then, the filter holder was connected with a flash chromatography column by a piece of rubber tubing in which a syringe adapter was inserted. The column was filled with water and connected to a pressure gas system. The pressure was regulated by a needle valve in a manometer. Leaking rate was measured by collecting the water in a glass beaker on an analytical balance.

2.2.4.8 Effect of repetitive drying/wetting cycles on self-sealing performance of membranes

In order to assess the materials self-sealing performance, an APCN/PEE composite membrane (PHEA:PDMS 90:10 (w/w), thickness 340 m) was punctured in its dry state with a syringe needle (0.6 mm diameter) as described above. Then, the sample was wetted at 0.5 bar water pressure and the leakaging rate was measured as

described above. After the experiment, the swinny filter holder with inserted PTFE-adapter and APCN/PEE membrane was disconnected from the water reservoir and unscrewed. Remaining water drops were gently removed with a lint-free tissue. The PTFE-adapter and the APCN/PEE membrane were kept in the filter holder in order to guarantee the same position of the puncture in the next leakage measurement, i.e. to perform the experiments at same conditions without any changes in the material's position. To ensure drying of the swollen APCN/PEE, the filter holder was left open over night, with the APCN-side exposed to the environment, so that the membrane could dry in air at ambient conditions. A gentle airflow from the work place ventilation aided the drying process. After over night drying, the filter holder was screwed together for the next experiment, connected to the water reservoir and the leaking rate at 0.5 bar was measured as described above. The drying/wetting cycle was performed five times in total with the same sample.

2.2.4.9 Water evaporation tests

Evaporation measurements (air humidity = 50 %, temperature = 23 °C) were conducted in parallel with an APCN/PEE-based laminate and a PEE-based reference laminate. Evaporation tests were performed using a heating plate (Type 0812, Medax Nagel GmbH, Germany) on which the laminates were fixed with self-adhesive tape. Samples were tested for leaking prior to evaporation experiments to guarantee that water loss is only due to evaporation. Water reservoirs were attached to the inlet tubes of the cooling laminates. The reservoirs guaranteed a constant water amount within the samples. Syringes with 20 ml content were used as reservoirs. They were installed on the same height (7 cm) to ensure an equal hydrostatic pressure in both laminates. The laminates were filled with approximately 10 ml water each, the outlet tubes were closed by means of a metal clamp for tubing and the evaporation test was started by setting the heating plate temperature to 34 °C. Monitoring of evaporation started after ca. 0.5 h in order to be sure that the experimental set-up had thermally equilibrated. The evaporation of water out of the laminates was monitored by the loss of water from the water reservoir. Periodically, the water in the reservoirs was refilled. Measurement of surface temperature during evaporation experiments was performed using a contactless infrared camera (Optris PI 160, Optris GmbH, Germany). The temperature was measured with a rectangular IR spot of 2 cm x 2 cm in the center of the membrane, as an average of 3 measurements within 10s.

Chapter 3

3 General conclusions and outlooks

In the first project described in this work, functional homo and copolymers were synthesized from polymerization initiators bound to the interior of a protein cage, the thermosome. Prior to the polymerization, the cage was tested for its stability in presence of different polymerization reagents. From those tests the polymerization conditions within the thermosome were derived. The functionality of the polymers can be described by the cationic charges of protonated tertiary amine groups and in the copolymers with additional fluorescence of Rhodamine B. The polymerization process in the confined space of the cavity of the thermosome was compared with a protein that does not have a cage structure. The cationic charges of the polymers allowed the interaction with negatively charged biomacromolecules. Thus, the polymers acted as anchors. The encapsulation of biomacromolecules was possible, because the thermosome has two large pores that are big enough for macromolecules (up to 50'000 g mol^{-1}) to enter and leave the cavity. The thermosome-polymer conjugates and, in addition, their interaction with biomacromolecules were evaluated with different analytical methods like gel electrophoresis, dynamic light scattering and transmission electron microscopy. As examples for biomacromolecules, siRNA and fluorescent proteins (eYFP and TurboGFP) were selected. Cellular uptake studies of complexes of the thermosome-polymer conjugate and fluorescence proteins or siRNA were conducted.

The central findings of this project work are:

a) ATRP conditions were elaborated in which the protein cage remained stable.
b) Polymers and copolymers were synthesized by ATRP within the protein cage using a grafting from approach from thermosome-bound initiators.
c) With an increasing monomer-to-initiator ratio the polymers within the cavity of the thermosome became larger.
d) Polymers synthesized within the cavity of the thermosome are smaller than those synthesized on albumin under the same conditions. This is most probable

due to the cage structure of the thermosome that restricts access of reactants into the cavity.

e) The size of the protein cage did not change when homo or copolymers were synthesized within its cavities. This finding shows that polymer chains are mainly located within that cavity. Binding of siRNA into the polymer-protein conjugate did also not affect the size of the cage, indicating that macromolecules were and did not stick to the exterior of the protein cage.

f) The homopolymer conjugates could entrap siRNA and protect it from fast degradation by enzymes.

g) Besides synthesis of homopolymers, it was possible to synthesize copolymers of ionizable methacrylate monomers and fluorescent methacrylate monomers. This shows the versatility of the grafting-from-approach, which allows synthesizing tailor-made polymer chains with different functionalities.

h) The homopolymer and copolymer conjugates showed similar cell viability as the untreated control cells. Thus, the cage structure shielded the cells from the cationic charges of the polymers.

i) Complex formation with eYFP was possible and the first preliminary results show a cell uptake of eYFP, which was complexed with the thermosome copolymer conjugate.

j) The delivery of siRNA with thermosome-homopolymer into U87 cells was successful and protein expression could be lowered by gene silencing.

The presented results allow concluding that with the synthesis of polymers within the cavity of a protein cage, it is possible to create nano-transporters that are capable to encapsulate or interact with cargo and release it into cells. Customized polymer synthesis gives a higher flexibility towards the possible applications. The results will help in further advancements in the development of the thermosome-polymer conjugates as nano-transporter and can be a source of inspiration for other researchers to device protein cage-polymer conjugates as drug delivery vehicles.

In order to advance the developments of the thermosome-polymer conjugates, further investigations should look more in detail of the polymerization process. As observed during the experimental work, a high amount of monomers (10’000 - 15’000 per initiator) was needed in order to synthesize polymers with longer (approx. 60-160 monomer units) chains. This is different to a reported work in the field of protein cage-polymer conjugates in which longer polymer chains could be synthesized with

a lower amount of monomers (250 – 1000 per initiator) by classical ATRP with a bipyridine ligand instead of ARGET ATRP.[114] Another alternative would be AGET ATRP in which just a part of the catalysts is generated by the addition of reducing agents.[32]

Moreover, the temperature of polymer synthesis might be an important parameter in the synthesis of THS-pDMAEMA conjugates. In two samples that were synthesized during days, when the average room temperature was 5 °C – 7 °C higher than in the results reported herein, an additional band at higher molecular weights (300 000 g mol^{-1}) was observed in SDS-PAGE. Those samples formed aggregates (approx. 100 nm) when incubated with siRNA, whereas samples synthesized at normal room temperature did not show this property. In addition, samples synthesized at higher temperature showed higher toxicity. The data for the conjugates that were synthesized at higher temperature was not included in this thesis, because further investigations have to be conducted. Therefore, for further developments of synthesis of thermosome-polymer conjugates, the polymerization reaction temperature should be taken into account.

For future ideas, it would be desirable to implement more amino acids (e.g. cysteines) on each subunit in the interior to which polymerization initiators can be bound. This should allow the synthesis of a higher density of polymers within the cavity of the thermosome. A higher amount of positively charged polymer chains could possibly bind more negatively charged macromolecules or a higher degree of functionalities could be implemented. Moreover, the probability of protruding polymer chains interacting with the surrounding (e.g. cells) could possibly be lowered.

In this work, the thermosome was in its apo state, i.e. the cage structure remained fully open or half-open in all steps. The cage of the thermosome can be completely closed with ATP-derivates (e.g. ATP•AlF_x).[238] The protection of (e.g. siRNA) can eventually be improved with a fully closed cage.

Cell experiments with the conjugates in this thesis were conducted with a cell line that was previously shown to uptake thermosome. Other cell lines should be tested in order to evaluate the uptake of the thermosome-polymer conjugates and the possible influence of protruding polymers on the cellular uptake.

The uptake experiments with fluorescent proteins have to be investigated more in detail by repeating experiments, adapt the complexation conditions or by changing the protein to a different one (e.g. fluorescence labeled horseradish peroxidase or tyrosine aminotransferase).

Since polymers can be synthesized within the cavity depending on the application, for entrapment purposes also anionic polymer could be synthesized that allow the encapsulation of macromolecules with positive charges at physiological pH (e.g. anti-HIV and anti-tumor protein MAP30, M ≈ 30'000 g mol^{-1}, pI = 9.12).[529-531]

In the second project of this dissertation, a thin semipermeable membrane (poly(ester ether)) was equipped with a water-swellable polymer layer (amphiphilic conetwork) in order to add a self-closing feature to the composite material without hampering water vapor evaporation through it. Prior to composite material synthesis, the poly(ester ether membrane) was functionalized with methacrylate groups for covalent binding with the amphiphilic conetwork. The synthesized composite membrane was tested for its water-swellability and self-sealing properties at over pressures up to 1.6 bar. With the composite membrane a laminate was fabricated in order to show its water evaporation capability. This capability is important in e.g. medical applications.[477]

The central findings of this project are:

a) The higher the content of hydrophilic monomers the higher the swelling of the amphiphilic conetwork in water.
b) The self-closing property is related to the thickness of the amphiphilic conetwork and becomes more pronounced with thicker amphiphilic polymer conetworks.
c) A punctured membrane keeps its full self-closing property even after five drying/wetting cycles.
d) Water vapour could evaporate through the membrane.

The presented results allow concluding that by the attachment of a polymer layer onto a thin climate membrane, properties can be added that extend the field of possible applications and make the material more durable. The developed membrane showed self-closing properties at overpressures to at least 1.6 bar, therefore it could be applied in fields where such features are necessary (e.g. medical applications,

membrane filtration). The generated results should give an example of composite material development and how to improve an already existing material by the addition of another.

The next step in further development of this composite membrane is to implement self-healing properties and keeping the water vapour evaporation feature. This can be done by the integration of groups that form donor-acceptor interactions (e.g. nucleic acids, boronate-catechol complexation[533]). Another idea is to integrate subunits of viruses or other protein cages into the polymer network material. The interaction of virus subunits is very strong and they have to withstand internal pressures of the DNA of approx. 50 bar when the virus is fully packed with DNA.[534] Thus, the integration of virus-like particles or viral subunits into an amphiphilic conetwork could add self-healing property.

Chapter 4

4 Bibliography

(1) Klok, H. A. Peptide/Protein-Synthetic Polymer Conjugates: Quo Vadis. *Macromolecules* **2009**, *42*, 7990-8000.

(2) Grover, G. N.; Maynard, H. D. Protein-polymer conjugates: synthetic approaches by controlled radical polymerizations and interesting applications. *Curr. Opin. Chem. Biol.* **2010**, *14*, 818-827.

(3) Jung, B.; Theato, P. Chemical Strategies for the Synthesis of Protein-Polymer Conjugates. *Adv. Polym. Sci.* **2013**, *253*, 37-70.

(4) Abuchowski, A.; McCoy, J. R.; Palczuk, N. C.; van Es, T.; Davis, F. F. Effect of covalent attachment of polyethylene glycol on immunogenicity and circulating life of bovine liver catalase. *J. Biol. Chem.* **1977**,*252*,3582-3586.

(5) Grace, M. J.; Lee, S.; Bradshaw, S.; Chapman, J.; Spond, J.; Cox, S.; Delorenzo, M.; Brassard, D.; Wylie, D.; Cannon-Carlson, S.; Cullen, C.; Indelicato, S.; Voloch, M.; Bordens, R. Site of pegylation and polyethylene glycol molecule size attenuate interferon-alpha antiviral and antiproliferative activities through the JAK/STAT signaling pathway. *J. Biol. Chem.* **2005**, *280*, 6327-6336.

(6) Pelegri-O'Day, E. M.; Lin, E. W.; Maynard, H. D. Therapeutic protein-polymer conjugates: advancing beyond PEGylation. *J. Am. Chem. Soc.* **2014**, *136*, 14323-14332.

(7) Keefe, A. J.; Jiang, S. Y. Poly(zwitterionic)protein conjugates offer increased stability without sacrificing binding affinity or bioactivity. *Nat. Chem.* **2012**, *4*, 60-64.

(8) Cummings, C.; Murata, H.; Koepsel, R.; Russell, A. J. Dramatically Increased pH and Temperature Stability of Chymotrypsin Using Dual Block Polymer-Based Protein Engineering. *Biomacromolecules* **2014**, *15*, 763-771.

(9) Thilakarathne, V.; Briand, V. A.; Zhou, Y. X.; Kasi, R. M.; Kumar, C. V. Protein Polymer Conjugates: Improving the Stability of Hemoglobin with Poly(acrylic acid). *Langmuir* **2011**, *27*, 7663-7671.

(10) Gauthier, M. A.; Klok, H. A. Polymer-protein conjugates: an enzymatic activity perspective. *Polym. Chem.* **2010**, *1*, 1352-1373.

(11) De, P.; Li, M.; Gondi, S. R.; Sumerlin, B. S. Temperature-regulated activity of responsive polymer-protein conjugates prepared by grafting-from via RAFT polymerization. *J. Am. Chem. Soc.* **2008**, *130*, 11288-11289.

(12) Fernandez-Lafuente, R. Stabilization of multimeric enzymes: Strategies to prevent subunit dissociation. *Enzyme and Microb. Technol.* **2009**, *45*, 405-418.

(13) Schlick, T. L.; Ding, Z.; Kovacs, E. W.; Francis, M. B. Dual-Surface Modification of the Tobacco Mosaic Virus. *J. Am. Chem. Soc.* **2005**, *127*, 3718-3723.

(14) Mabrouk, P. A.: The Use of Poly(ethylene glycol)-Enzymes in Nonaqueous Enzymology. In *Poly(ethylene glycol)*; *ACS Symposium Series 680*; American Chemical Society, 1997; Vol. 680; pp 118-133.

(15) Cobo, I.; Li, M.; Sumerlin, B. S.; Perrier, S. Smart hybrid materials by conjugation of responsive polymers to biomacromolecules. *Nat. Mat.* **2015**, *14*, 143-159.

(16) Lu, H.; Wang, D.; Kazane, S.; Javahishvili, T.; Tian, F.; Song, F.; Sellers, A.; Barnett, B.; Schultz, P. G. Site-specific antibody-polymer conjugates for siRNA delivery. *J. Am. Chem. Soc.* **2013**, *135*, 13885-13891.

(17) Torchilin, V. P.; Lukyanov, A. N. Peptide and protein drug delivery to and into tumors: challenges and solutions. *Drug Discovery Today* **2003**, *8*, 259-266.

(18) Boyer, C.; Huang, X.; Whittaker, M. R.; Bulmus, V.; Davis, T. P. An overview of protein-polymer particles. *Soft Matter* **2011**, *7*, 1599-1614.

(19) Rosendahl, M. S.; Doherty, D. H.; Smith, D. J.; Carlson, S. J.; Chlipala, E. A.; Cox, G. N. A long-acting, highly potent interferon alpha-2 conjugate created using site-specific PEGylation. *Bioconjug. Chem.* **2005**, *16*, 200-207.

(20) Hirao, A.; Goseki, R.; Ishizone, T. Advances in Living Anionic Polymerization: From Functional Monomers, Polymerization Systems, to Macromolecular Architectures. *Macromolecules* **2014**, *47*, 1883-1905.
(21) Aoshima, S.; Kanaoka, S. A Renaissance in Living Cationic Polymerization. *Chem. Rev.* **2009**, *109*, 5245-5287.
(22) Matyjaszewski, K. Atom Transfer Radical Polymerization (ATRP): Current Status and Future Perspectives. *Macromolecules* **2012**, *45*, 4015-4039.
(23) Hill, M. R.; Carmean, R. N.; Sumerlin, B. S. Expanding the Scope of RAFT Polymerization: Recent Advances and New Horizons. *Macromolecules* **2015**, *48*, 5459-5469.
(24) Guegain, E.; Guillaneuf, Y.; Nicolas, J. Nitroxide-Mediated Polymerization of Methacrylic Esters: Insights and Solutions to a Long-Standing Problem. *Macrom. Rapid Commun.* **2015**, *36*, 1227-1247.
(25) Aliferis, T.; Iatrou, H.; Hadjichristidis, N. Living polypeptides. *Biomacromolecules* **2004**, *5*, 1653-1656.
(26) Huang, J.; Rempel, G. L. Ziegler-Natta Catalysts for Olefin Polymerization - Mechanistic Insights from Metallocene Systems. *Prog. Polym. Sci.* **1995**, *20*, 459-526.
(27) Bielawski, C. W.; Grubbs, R. H. Living ring-opening metathesis polymerization. *Prog. Polym. Sci.* **2007**, *32*, 1-29.
(28) Zhao, W. G.; Liu, F.; Chen, Y.; Bai, J.; Gao, W. P. Synthesis of well-defined protein-polymer conjugates for biomedicine. *Polymer* **2015**, *66*, A1-A10.
(29) Wallat, J. D.; Rose, K. A.; Pokorski, J. K. Proteins as substrates for controlled radical polymerization. *Polym. Chem.* **2014**, *5*, 1545-1558.
(30) Bruns, N.; Pustelny, K.; Bergeron, L. M.; Whitehead, T. A.; Clark, D. S. Mechanical Nanosensor Based on FRET within a Thermosome: Damage-Reporting Polymeric Materials. *Angew. Chem., Int. Ed.* **2009**, *48*, 5666-5669.
(31) Thordarson, P.; Le Droumaguet, B.; Velonia, K. Well-defined protein-polymer conjugates--synthesis and potential applications. *Appl. Microbiol. Biotechnol.* **2006**, *73*, 243-254.
(32) Averick, S.; Simakova, A.; Park, S.; Konkolewicz, D.; Magenau, A. J. D.; Mehl, R. A.; Matyjaszewski, K. ATRP under Biologically Relevant Conditions: Grafting from a Protein. *ACS Macro Lett.* **2012**, *1*, 6-10.
(33) Moad, G. Mechanism and Kinetics of Dithiobenzoate-Mediated RAFT Polymerization – Status of the Dilemma. *Macrom. Chem. Phys.* **2014**, *215*, 9-26.
(34) Baskaran, D.; Müller, A. H. E.: Anionic Vinyl Polymerization. In *Controlled and Living Polymerizations*; Wiley-VCH Verlag GmbH & Co. KGaA, 2009; pp 1-56.
(35) Averick, S.; Simakova, A.; Park, S.; Konkolewicz, D.; Magenau, A. J. D.; Mehl, R. A.; Matyjaszewski, K. ATRP under Biologically Relevant Conditions: Grafting from a Protein. *ACS Macro Lett.* **2011**, *1*, 6-10.
(36) Sumerlin, B. S. Proteins as Initiators of Controlled Radical Polymerization: Grafting-from via ATRP and RAFT. *ACS Macro Lett.* **2011**, *1*, 141-145.
(37) Liu, J. Q.; Bulmus, V.; Herlambang, D. L.; Barner-Kowollik, C.; Stenzel, M. H.; Davis, T. P. In situ formation of protein-polymer conjugates through reversible addition fragmentation chain transfer polymerization. *Angew. Chem., Int. Ed.* **2007**, *46*, 3099-3103.
(38) Lele, B. S.; Murata, H.; Matyjaszewski, K.; Russell, A. J. Synthesis of Uniform Protein−Polymer Conjugates. *Biomacromolecules* **2005**, *6*, 3380-3387.
(39) Matyjaszewski, K.; Tsarevsky, N. V. Macromolecular Engineering by Atom Transfer Radical Polymerization. *J. Am. Chem. Soc.* **2014**, *136*, 6513-6533.
(40) Boyer, C.; Bulmus, V.; Davis, T. P.; Ladmiral, V.; Liu, J.; Perrier, S. Bioapplications of RAFT Polymerization. *Chem. Rev.* **2009**, *109*, 5402-5436.
(41) Tsarevsky, N. V.; Matyjaszewski, K. "Green" atom transfer radical polymerization: From process design to preparation of well-defined environmentally friendly polymeric materials. *Chem. Rev.* **2007**, *107*, 2270-2299.
(42) Haas, M.; Solari, E.; Nguyen, Q. T.; Gautier, S.; Scopelliti, R.; Severin, K. A bimetallic ruthenium complex as a catalyst precursor for the atom transfer radical polymerization of methacrylates at ambient temperature. *Adv. Synth. Catal.* **2006**, *348*, 439-442.
(43) Moineau, G.; Minet, M.; Dubois, P.; Teyssie, P.; Senninger, T.; Jerome, R. Controlled radical polymerization of (meth)acrylates by ATRP with NiBr2(PPh3)(2) as catalyst. *Macromolecules* **1999**, *32*, 27-35.
(44) Tsarevsky, N. V.; Matyjaszewski, K. “Green” Atom Transfer Radical Polymerization: From Process Design to Preparation of Well-Defined Environmentally Friendly Polymeric Materials. *Chem. Rev.* **2007**, *107*, 2270-2299.
(45) Flemming, C. A.; Trevors, J. T. Copper Toxicity and Chemistry in the Environment - a Review. *Water. Air. Soil. Poll.* **1989**, *44*, 143-158.

(46) Simakova, A.; Averick, S. E.; Konkolewicz, D.; Matyjaszewski, K. Aqueous ARGET ATRP. *Macromolecules* **2012**, *45*, 6371-6379.
(47) Keddie, D. J. A guide to the synthesis of block copolymers using reversible-addition fragmentation chain transfer (RAFT) polymerization. *Chem. Soc. Rev.* **2014**, *43*, 496-505.
(48) Boyer, C.; Bulmus, V.; Liu, J.; Davis, T. P.; Stenzel, M. H.; Barner-Kowollik, C. Well-defined protein-polymer conjugates via in situ RAFT polymerization. *J. Am. Chem. Soc.* **2007**, *129*, 7145-7154.
(49) Chiefari, J.; Chong, Y. K.; Ercole, F.; Krstina, J.; Jeffery, J.; Le, T. P. T.; Mayadunne, R. T. A.; Meijs, G. F.; Moad, C. L.; Moad, G.; Rizzardo, E.; Thang, S. H. Living free-radical polymerization by reversible addition-fragmentation chain transfer: The RAFT process. *Macromolecules* **1998**, *31*, 5559-5562.
(50) Mayadunne, R. T. A.; Rizzardo, E.; Chiefari, J.; Chong, Y. K.; Moad, G.; Thang, S. H. Living radical polymerization with reversible addition-fragmentation chain transfer (RAFT polymerization) using dithiocarbamates as chain transfer agents. *Macromolecules* **1999**, *32*, 6977-6980.
(51) Vriezema, D. M.; Aragones, M. C.; Elemans, J. A. A. W.; Cornelissen, J. J. L. M.; Rowan, A. E.; Nolte, R. J. M. Self-Assembled Nanoreactors. *Chem. Rev.* **2005**, *105*, 1445-1489.
(52) de la Escosura, A.; Nolte, R. J. M.; Cornelissen, J. J. L. M. Viruses and protein cages as nanocontainers and nanoreactors. *J. Mat. Chem.* **2009**, *19*, 2274.
(53) Kim, K. T.; Meeuwissen, S. A.; Nolte, R. J. M.; van Hest, J. C. M. Smart Nanocontainers and Nanoreactors. *Nanoscale* **2010**, *2*, 844-858.
(54) Renggli, K.; Baumann, P.; Langowska, K.; Onaca, O.; Bruns, N.; Meier, W. Selective and Responsive Nanoreactors. *Adv. Funct. Mater.* **2011**, *21*, 1241-1259.
(55) Tanner, P.; Baumann, P.; Enea, R.; Onaca, O.; Palivan, C.; Meier, W. Polymeric Vesicles: From Drug Carriers to Nanoreactors and Artificial Organelles. *Acc. Chem. Res.* **2011**, *44*, 1039-1049.
(56) Palivan, C. G.; Fischer-Onaca, O.; Delcea, M.; Itel, F.; Meier, W. Protein-Polymer Nanoreactors for Medical Applications. *Chem. Soc. Rev.* **2012**, *41*, 2800-2823.
(57) Marguet, M.; Bonduelle, C.; Lecommandoux, S. Multicompartmentalized polymeric systems: towards biomimetic cellular structure and function. *Chem. Soc. Rev.* **2013**, *42*, 512-529.
(58) Maity, B.; Fujita, K.; Ueno, T. Use of the confined spaces of apo-ferritin and virus capsids as nanoreactors for catalytic reactions. *Curr. Op. Chem. Biol.* **2015**, *25*, 88-97.
(59) Priebe, M.; Fromm, K. M. Nanorattles or Yolk-Shell Nanoparticles-What Are They, How Are They Made, and What Are They Good For? *Chem. Eur. J.* **2015**, *21*, 3854-3874.
(60) Li, S.; Lee, A. R.; Park, S. J.; Kim, J. H. Preparation of ZnSe Quantum Dots by Ferritin. *Sci. Adv. Mater.* **2014**, *6*, 2590-2594.
(61) Renggli, K.; Nussbaumer, M. G.; Urbani, R.; Pfohl, T.; Bruns, N. A Chaperonin as Protein Nanoreactor for Atom-Transfer Radical Polymerization. *Angew. Chem., Int. Ed.* **2014**, *53*, 1443-1447.
(62) Abe, S.; Hirata, K.; Ueno, T.; Morino, K.; Shimizu, N.; Yamamoto, M.; Takata, M.; Yashima, E.; Watanabe, Y. Polymerization of Phenylacetylene by Rhodium Complexes within a Discrete Space of apo-Ferritin. *J. Am. Chem. Soc.* **2009**, *131*, 6958-6960.
(63) Reichhardt, C.; Uchida, M.; O'Neil, A.; Li, R.; Prevelige, P. E.; Douglas, T. Templated assembly of organic-inorganic materials using the core shell structure of the P22 bacteriophage. *Chem. Commun.* **2011**, *47*, 6326-6328.
(64) Priebe, M.; Fromm, K. M. One-Pot Synthesis and Catalytic Properties of Encapsulated Silver Nanoparticles in Silica Nanocontainers. *Part. Part. Syst. Charact.* **2014**, *31*, 645-651.
(65) Tanner, P.; Onaca, O.; Balasubramanian, V.; Meier, W.; Palivan, C. G. Enzymatic Cascade Reactions inside Polymeric Nanocontainers: A Means to Combat Oxidative Stress. *Chemistry* **2011**, *17*, 4552-4560.
(66) Gunkel-Grabole, G.; Sigg, S.; Lomora, M.; Lorcher, S.; Palivan, C. G.; Meier, W. P. Polymeric 3D nano-architectures for transport and delivery of therapeutically relevant biomacromolecules. *Biomater. Sci.* **2014**, 3, 25-40.
(67) Brinkhuis, R. P.; Rutjes, F. P. J. T.; van Hest, J. C. M. Polymeric vesicles in biomedical applications. *Polym. Chem.* **2011**, *2*, 1449-1462.
(68) Egli, S.; Schlaad, H.; Bruns, N.; Meier, W. Functionalization of Block Copolymer Vesicle Surfaces. *Polymers* **2011**, *3*, 252-280.
(69) Mellal, D.; Zumbuehl, A. Exit-strategies - smart ways to release phospholipid vesicle cargo. *J. Mater. Chem. B* **2014**, *2*, 247-252.
(70) Skirtach, A. G.; Yashchenok, A. M.; Mohwald, H. Encapsulation, release and applications of LbL polyelectrolyte multilayer capsules. *Chem. Commun.* **2011**, *47*, 12736-12746.

(71) Heddle, J. G. Protein cages, rings and tubes: useful components of future nanodevices? *Nanotechnol., Sci. Appl.* **2008**, *1*, 67-78.
(72) Uchida, M.; Klem, M. T.; Allen, M.; Suci, P.; Flenniken, M.; Gillitzer, E.; Varpness, Z.; Liepold, L. O.; Young, M.; Douglas, T. Biological Containers: Protein Cages as Multifunctional Nanoplatforms. *Adv. Mater.* **2007**, *19*, 1025-1042.
(73) Bode, S. A.; Minten, I. J.; Nolte, R. J.; Cornelissen, J. J. Reactions inside nanoscale protein cages. *Nanoscale* **2011**, *3*, 2376-2389.
(74) Ma, Y.; Nolte, R. J. M.; Cornelissen, J. J. L. M. Virus-based nanocarriers for drug delivery. *Adv. Drug Delivery Rev.* **2012**, *64*, 811-825.
(75) Molino, N. M.; Wang, S.-W. Caged protein nanoparticles for drug delivery. *Curr. Opin. Biotechnol.* **2014**, *28*, 75-82.
(76) Lai, Y.-T.; Reading, E.; Hura, G. L.; Tsai, K.-L.; Laganowsky, A.; Asturias, F. J.; Tainer, J. A.; Robinson, C. V.; Yeates, T. O. Structure of a designed protein cage that self-assembles into a highly porous cube. *Nat. Chem.* **2014**, *6*, 1065-1071.
(77) Jutz, G.; van Rijn, P.; Miranda, B. S.; Boker, A. Ferritin: A Versatile Building Block for Bionanotechnology. *Chem. Rev.* **2015**, *115*, 1653-1701.
(78) Putri, R. M.; Cornelissen, J. J. L. M.; Koay, M. S. T. Self-Assembled Cage-Like Protein Structures. *ChemPhysChem* **2015**, *16*, 911-918.
(79) Kushner, D. J. Self-Assembly of Biological Structures. *Bacteriol. Rev.* **1969**, *33*, 302-&.
(80) Kaiser, C. R.; Flenniken, M. L.; Gillitzer, E.; Harmsen, A. L.; Jutila, M. A.; Douglas, T.; Young, M. J. Biodistribution studies of protein cage nanoparticles demonstrate broad tissue distribution and rapid clearance in vivo. *Int. J. Nanomedicine* **2007**, *2*, 715-733.
(81) Maham, A.; Tang, Z.; Wu, H.; Wang, J.; Lin, Y. Protein-based nanomedicine platforms for drug delivery. *Small* **2009**, *5*, 1706-1721.
(82) Molino, N. M.; Wang, S. W. Caged protein nanoparticles for drug delivery. *Curr. Opin. Biotechnol.* **2014**, *28*, 75-82.
(83) Falkner, J. C.; Turner, M. E.; Bosworth, J. K.; Trentler, T. J.; Johnson, J. E.; Lin, T. W.; Colvin, V. L. Virus crystals as nanocomposite scaffolds. *J. Am. Chem. Soc.***2005**, *127*, 5274-5275.
(84) Jaafar, M.; Aljabali, A. A. A.; Berlanga, I.; Mas-Balleste, R.; Saxena, P.; Warren, S.; Lomonossoff, G. P.; Evans, D. J.; de Pablo, P. J. Structural Insights into Magnetic Clusters Grown Inside Virus Capsids. *ACS Appl. Mater. & Interfaces* **2014**, *6*, 20936-20942.
(85) Aljabali, A. A. A.; Barclay, J. E.; Cespedes, O.; Rashid, A.; Staniland, S. S.; Lomonossoff, G. P.; Evans, D. J. Charge Modified Cowpea Mosaic Virus Particles for Templated Mineralization. *Adv. Funct. Mater.* **2011**, *21*, 4137-4142.
(86) Kumar, K.; Doddi, S. K.; Arunasree, M. K.; Paik, P. CPMV-induced synthesis of hollow mesoporous SiO2 nanocapsules with excellent performance in drug delivery. *Dalton Transactions* **2015**, *44*, 4308-4317.
(87) Blum, A. S.; Soto, C. M.; Wilson, C. D.; Cole, J. D.; Kim, M.; Gnade, B.; Chatterji, A.; Ochoa, W. F.; Lin, T. W.; Johnson, J. E.; Ratna, B. R. Cowpea mosaic virus as a scaffold for 3-D patterning of gold nanoparticles. *Nano Lett.* **2004**, *4*, 867-870.
(88) Douglas, T.; Young, M. Virus particles as templates for materials synthesis. *Adv. Mater.* **1999**, *11*, 679-681.
(89) Patterson, D. P.; Schwarz, B.; Waters, R. S.; Gedeon, T.; Douglas, T. Encapsulation of an Enzyme Cascade within the Bacteriophage P22 Virus-Like Particle. *ACS Chem. Biol.* **2014**, *9*, 359-365.
(90) Glasgow, J. E.; Capehart, S. L.; Francis, M. B.; Tullman-Ercek, D. Osmolyte-Mediated Encapsulation of Proteins inside MS2 Viral Capsids. *ACS Nano* **2012**, *6*, 8658-8664.
(91) Capehart, S. L.; Coyle, M. P.; Glasgow, J. E.; Francis, M. B. Controlled integration of gold nanoparticles and organic fluorophores using synthetically modified MS2 viral capsids. *Abstr. Pap. Am. Chem. Soc.* **2013**, *245*.
(92) Capek, I. Viral nanoparticles, noble metal decorated viruses and their nanoconjugates. *Adv. Coll. Interf. Sci.* **2015**, *222*, 119-134.
(93) Ludwig, C.; Wagner, R. Virus-like particles-universal molecular toolboxes. *Curr. Opin. Biotechnol.* **2007**, *18*, 537-545.
(94) Teunissen, E. A.; de Raad, M.; Mastrobattista, E. Production and biomedical applications of virus-like particles derived from polyomaviruses. *J. Controlled Release* **2013**, *172*, 305-321.
(95) Garcea, R. L.; Gissmann, L. Virus-like particles as vaccines and vessels for the delivery of small molecules. *Curr. Opin. Biotechnol.* **2004**, *15*, 513-517.
(96) Steinmetz, N. F. Viral nanoparticles as platforms for next-generation therapeutics and imaging devices. *Nanomedicine: Nanotechology, Biology, Medicine* **2010**, *6*, 634-641.

(97) Waehler, R.; Russell, S. J.; Curiel, D. T. Engineering targeted viral vectors for gene therapy. *Nat. Rev. Gen.* **2007**, *8*, 573-587.
(98) Choi, K.-m.; Choi, S.-H.; Jeon, H.; Kim, I.-S.; Ahn, H. J. Chimeric Capsid Protein as a Nanocarrier for siRNA Delivery: Stability and Cellular Uptake of Encapsulated siRNA. *ACS Nano* **2011**, *5*, 8690-8699.
(99) Lilavivat, S.; Sardar, D.; Jana, S.; Thomas, G. C.; Woycechowsky, K. J. In Vivo Encapsulation of Nucleic Acids Using an Engineered Nonviral Protein Capsid. *J. Am. Chem. Soc.* **2012**, *134*, 13152-13155.
(100) Brown, S. D.; Fiedler, J. D.; Finn, M. G. Assembly of Hybrid Bacteriophage Qβ Virus-like Particles. *Biochemistry* **2009**, *48*, 11155-11157.
(101) Schoonen, L.; van Hest, J. C. M. Functionalization of protein-based nanocages for drug delivery applications. *Nanoscale* **2014**, *6*, 7124-7141.
(102) Lee, L. A.; Niu, Z.; Wang, Q. Viruses and virus-like protein assemblies—Chemically programmable nanoscale building blocks. *Nano Res.* **2009**, *2*, 349-364.
(103) Strable, E.; Finn, M. G.: Chemical Modification of Viruses and Virus- Like Particles. In *Curr Top Microbiol*; Manchester, M., Steinmetz, N., Eds.; Curr. Top. . Microbiol. Immunol.; Springer Berlin Heidelberg, 2009; Vol. 327; pp 1-21.
(104) Lee, L. A.; Wang, Q. Adaptations of nanoscale viruses and other protein cages for medical applications. *Nanomedicine : Nanotechnology, Biology, Medicine* **2006**, *2*, 137-149.
(105) Douglas, T.; Young, M. Viruses: making friends with old foes. *Science* **2006**, *312*, 873-875.
(106) Zhang, J.; Baker, M. L.; Schroder, G. F.; Douglas, N. R.; Reissmann, S.; Jakana, J.; Dougherty, M.; Fu, C. J.; Levitt, M.; Ludtke, S. J.; Frydman, J.; Chiu, W. Mechanism of folding chamber closure in a group II chaperonin. *Nature* **2010**, *463*, 379-383.
(107) Shan, L.; Cui, S.; Du, C.; Wan, S.; Qian, Z.; Achilefu, S.; Gu, Y. A paclitaxel-conjugated adenovirus vector for targeted drug delivery for tumor therapy. *Biomaterials* **2012**, *33*, 146-162.
(108) Moon, H.; Lee, J.; Min, J.; Kang, S. Developing Genetically Engineered Encapsulin Protein Cage Nanoparticles as a Targeted Delivery Nanoplatform. *Biomacromolecules* **2014**, *15*, 3794-3801.
(109) Koudelka, K. J.; Ippoliti, S.; Medina, E.; Shriver, L. P.; Trauger, S. A.; Catalano, C. E.; Manchester, M. Lysine Addressability and Mammalian Cell Interactions of Bacteriophage λ Procapsids. *Biomacromolecules* **2013**, *14*, 4169-4176.
(110) Zhen, Z.; Tang, W.; Chen, H.; Lin, X.; Todd, T.; Wang, G.; Cowger, T.; Chen, X.; Xie, J. RGD-Modified Apoferritin Nanoparticles for Efficient Drug Delivery to Tumors. *ACS Nano* **2013**, *7*, 4830-4837.
(111) Qazi, S.; Liepold, L. O.; Abedin, M. J.; Johnson, B.; Prevelige, P.; Frank, J. A.; Douglas, T. P22 viral capsids as nanocomposite high-relaxivity MRI contrast agents. *Mol. Pharm.* **2013**, *10*, 11-17.
(112) Toita, R.; Murata, M.; Abe, K.; Narahara, S.; Piao, J. S.; Kang, J.-H.; Ohuchida, K.; Hashizume, M. Biological evaluation of protein nanocapsules containing doxorubicin. *Int. J. Nanomed.* **2013**, *8*, 1989-1999.
(113) Usselman, R. J.; Qazi, S.; Aggarwal, P.; Eaton, S. S.; Eaton, G. R.; Russek, S.; Douglas, T. Gadolinium-Loaded Viral Capsids as Magnetic Resonance Imaging Contrast Agents. *Appl. Magn. Reson.* **2015**, *46*, 349-355.
(114) Hovlid, M. L.; Lau, J. L.; Breitenkamp, K.; Higginson, C. J.; Laufer, B.; Manchester, M.; Finn, M. G. Encapsidated Atom-Transfer Radical Polymerization in Qβ Virus-like Nanoparticles. *ACS Nano* **2014**, *8*, 8003-8014.
(115) Qazi, S.; Uchida, M.; Usselman, R.; Shearer, R.; Edwards, E.; Douglas, T. Manganese(III) porphyrins complexed with P22 virus-like particles as T1-enhanced contrast agents for magnetic resonance imaging. *JBIC* **2014**, *19*, 237-246.
(116) Moradi, M.; Li, Z.; Qi, J.; Xing, W.; Xiang, K.; Chiang, Y.-M.; Belcher, A. M. Improving the Capacity of Sodium Ion Battery Using a Virus-Templated Nanostructured Composite Cathode. *Nano Lett.* **2015**, *15*, 2917-2921.
(117) Allen, M.; Bulte, J. W. M.; Liepold, L.; Basu, G.; Zywicke, H. A.; Frank, J. A.; Young, M.; Douglas, T. Paramagnetic viral nanoparticles as potential high-relaxivity magnetic resonance contrast agents. *Mag. Res. Med.* **2005**, *54*, 807-812.
(118) Flenniken, M. L.; Liepold, L. O.; Crowley, B. E.; Willits, D. A.; Young, M. J.; Douglas, T. Selective attachment and release of a chemotherapeutic agent from the interior of a protein cage architecture. *Chem. Commun.* **2005**, 447-449.
(119) Liepold, L.; Anderson, S.; Willits, D.; Oltrogge, L.; Frank, J. A.; Douglas, T.; Young, M. Viral capsids as MRI contrast agents. *Mag. Res. Med.* **2007**, *58*, 871-879.

(120) Barnhill, H. N.; Claudel-Gillet, S.; Ziessel, R.; Charbonniere, L. J.; Wang, Q. Prototype protein assembly as scaffold for time-resolved fluoroimmuno assays. *J. Am. Chem. Soc.* **2007**, *129*, 7799-7806.

(121) Gillitzer, E.; Willits, D.; Young, M.; Douglas, T. Chemical modification of a viral cage for multivalent presentation. *Chem. Commun.* **2002**, 2390-2391.

(122) Lee, W.; Seo, J.; Kwak, S.; Park, E. J.; Na, D. H.; Kim, S.; Lee, Y. M.; Kim, I. S.; Bae, J. S. A Double-Chambered Protein Nanocage Loaded with Thrombin Receptor Agonist Peptide (TRAP) and gamma-Carboxyglutamic Acid of Protein C (PC-Gla) for Sepsis Treatment. *Adv. Mater.* **2015**, *27*, 6637-6643.

(123) Uchida, M.; Flenniken, M. L.; Allen, M.; Willits, D. A.; Crowley, B. E.; Brumfield, S.; Willis, A. F.; Jackiw, L.; Jutila, M.; Young, M. J.; Douglas, T. Targeting of cancer cells with ferrimagnetic ferritin cage nanoparticles. *J. Am. Chem. Soc.* **2006**, *128*, 16626-16633.

(124) Anand, P.; O'Neil, A.; Lin, E.; Douglas, T.; Holford, M. Tailored delivery of analgesic ziconotide across a blood brain barrier model using viral nanocontainers. *Sci. Rep.* **2015**, *5,* 1-10.

(125) Uchida, M.; Kosuge, H.; Terashima, M.; Willits, D. A.; Liepold, L. O.; Young, M. J.; McConnell, M. V.; Douglas, T. Protein Cage Nanoparticles Bearing the LyP-1 Peptide for Enhanced Imaging of Macrophage-Rich Vascular Lesions. *ACS Nano* **2011**, *5*, 2493-2502.

(126) Toita, R.; Murata, M.; Tabata, S.; Abe, K.; Narahara, S.; Piao, J. S.; Kang, J. H.; Hashizume, M. Development of Human Hepatocellular Carcinoma Cell-Targeted Protein Cages. *Bioconjug. Chem.* **2012**, *23*, 1494-1501.

(127) Luo, Y.; Wang, X.; Du, D.; Lin, Y. Hyaluronic acid-conjugated apoferritin nanocages for lung cancer targeted drug delivery. *Biomat. Sci.* **2015**, 3, 1386-1394.

(128) Suci, P.; Kang, S.; Gmür, R.; Douglas, T.; Young, M. Targeted Delivery of a Photosensitizer to Aggregatibacter actinomycetemcomitans Biofilm. *Antimicrob. Agents Chemother.* **2010**, *54*, 2489-2496.

(129) Schwarz, B.; Madden, P.; Avera, J.; Gordon, B.; Larson, K.; Miettinen, H. M.; Uchida, M.; LaFrance, B.; Basu, G.; Rynda-Apple, A.; Douglas, T. Symmetry Controlled, Genetic Presentation of Bioactive Proteins on the P22 Virus-like Particle Using an External Decoration Protein. *ACS Nano* **2015**, *9*, 9134-9147.

(130) Stephanopoulos, N.; Tong, G. J.; Hsiao, S. C.; Francis, M. B. Dual-Surface Modified Virus Capsids for Targeted Delivery of Photodynamic Agents to Cancer Cells. *ACS Nano* **2010**, *4*, 6014-6020.

(131) Love, A. J.; Makarov, V.; Yaminsky, I.; Kalinina, N. O.; Taliansky, M. E. The use of tobacco mosaic virus and cowpea mosaic virus for the production of novel metal nanomaterials. *Virology* **2014**, *449*, 133-139.

(132) Courchesne, N. M. D.; Klug, M. T.; Huang, K. J.; Weidman, M. C.; Cantu, V. J.; Chen, P. Y.; Kooi, S. E.; Yun, D. S.; Tisdale, W. A.; Fang, N. X.; Belcher, A. M.; Hammond, P. T. Constructing Multifunctional Virus-Templated Nanoporous Composites for Thin Film Solar Cells: Contributions of Morphology and Optics to Photocurrent Generation. *J. Phys. Chem. C* **2015**, *119*, 13987-14000.

(133) Ueno, T.; Suzuki, M.; Goto, T.; Matsumoto, T.; Nagayama, K.; Watanabe, Y. Size-selective olefin hydrogenation by a Pd nanocluster provided in an apo-ferritin cage. *Angew. Chem., Int. Ed.* **2004**, *43*, 2527-2530.

(134) Patterson, D. P.; Schwarz, B.; Waters, R. S.; Gedeon, T.; Douglas, T. Encapsulation of an Enzyme Cascade within the Bacteriophage P22 Virus-Like Particle. *ACS Chem. Biol.* **2013**, *9*, 359-365.

(135) Glasgow, J. E.; Asensio, M. A.; Jakobson, C. M.; Francis, M. B.; Tullman-Ercek, D. Influence of Electrostatics on Small Molecule Flux through a Protein Nanoreactor. *ACS Synth. Biol.* **2015**, 4, 1011-1019.

(136) Patterson, D. P.; Prevelige, P. E.; Douglas, T. Nanoreactors by Programmed Enzyme Encapsulation Inside the Capsid of the Bacteriophage P22. *ACS Nano* **2012**, *6*, 5000-5009.

(137) Meldrum, F. C.; Wade, V. J.; Nimmo, D. L.; Heywood, B. R.; Mann, S. Synthesis of Inorganic Nanophase Materials in Supramolecular Protein Cages. *Nature* **1991**, *349*, 684-687

(138) Douglas, T.; Strable, E.; Willits, D.; Aitouchen, A.; Libera, M.; Young, M. Protein Engineering of a Viral Cage for Constrained Nanomaterials Synthesis. *Adv. Mat.* **2002**, *14*,415-418.

(139) Ishii, D.; Kinbara, K.; Ishida, Y.; Ishii, N.; Okochi, M.; Yohda, M.; Aida, T. Chaperonin-mediated stabilization and ATP-triggered release of semiconductor nanoparticles. *Nature* **2003**, *423*, 628-632.

(140) Suzuki, M.; Abe, M.; Ueno, T.; Abe, S.; Goto, T.; Toda, Y.; Akita, T.; Yamada, Y.; Watanabe, Y. Preparation and catalytic reaction of Au/Pd bimetallic nanoparticles in Apo-ferritin. *Chem. Commun.* **2009**, 4871-4873.

(141) Behrens, S.; Heyman, A.; Maul, R.; Essig, S.; Steigerwald, S.; Quintilla, A.; Wenzel, W.; Bürck, J.; Dgany, O.; Shoseyov, O. Constrained Synthesis and Organization of Catalytically Active Metal Nanoparticles by Self-Assembled Protein Templates. *Adv. Mater* **2009**, *21*, 3515-3519.

(142) Huggins, K. N. L.; Schoen, A. P.; Arunagirinathan, M. A.; Heilshorn, S. C. Multi-Site Functionalization of Protein Scaffolds for Bimetallic Nanoparticle Templating. *Adv. Funct. Mater.* **2014**, *24*, 7737-7744.

(143) Malyutin, A. G.; Easterday, R.; Lozovyy, Y.; Spilotros, A.; Cheng, H.; Sanchez-Felix, O. R.; Stein, B. D.; Morgan, D. G.; Svergun, D. I.; Dragnea, B.; Bronstein, L. M. Viruslike Nanoparticles with Maghemite Cores Allow for Enhanced MRI Contrast Agents. *Chem. Mater.* **2015**, *27*, 327-335.

(144) Bedwell, G. J.; Zhou, Z. Y.; Uchida, M.; Douglas, T.; Gupta, A.; Prevelige, P. E. Selective Biotemplated Synthesis of TiO2 Inside a Protein Cage. *Biomacromolecules* **2015**, *16*, 214-218.

(145) Ma-Ham, A.; Wu, H.; Wang, J.; Kang, X.; Zhang, Y.; Lin, Y. Apoferritin-based nanomedicine platform for drug delivery: equilibrium binding study of daunomycin with DNA. *J. Mater. Chem.* **2011**, *21*, 8700-8708.

(146) Garimella, P. D.; Datta, A.; Romanini, D. W.; Raymond, K. N.; Francis, M. B. Multivalent, High-Relaxivity MRI Contrast Agents Using Rigid Cysteine-Reactive Gadolinium Complexes. *J. Am. Chem. Soc.* **2011**, *133*, 14704-14709.

(147) Tong, G. J.; Hsiao, S. C.; Carrico, Z. M.; Francis, M. B. Viral Capsid DNA Aptamer Conjugates as Multivalent Cell-Targeting Vehicles. *J. Am. Chem. Soc.* **2009**, *131*, 11174-11178.

(148) Lucon, J.; Qazi, S.; Uchida, M.; Bedwell, G. J.; LaFrance, B.; Prevelige, P. E., Jr.; Douglas, T. Use of the interior cavity of the P22 capsid for site-specific initiation of atom-transfer radical polymerization with high-density cargo loading. *Nat. Chem.* **2012**, *4*, 781-788.

(149) Kaiser, C. R.; Flenniken, M. L.; Gillitzer, E.; Harmsen, A. L.; Harmsen, A. G.; Jutila, M. A.; Douglas, T.; Young, M. J. Biodistribution studies of protein cage nanoparticles demonstrate broad tissue distribution and rapid clearance in vivo. *Int. J. of Nanomed.* **2007**, *2*, 715-733.

(150) Singh, P.; Prasuhn, D.; Yeh, R. M.; Destito, G.; Rae, C. S.; Osborn, K.; Finn, M. G.; Manchester, M. Bio-distribution, toxicity and pathology of cowpea mosaic virus nanoparticles in vivo. *J. Controlled Release* **2007**, *120*, 41-50.

(151) Ranford, J. C.; Coates, A. R. M.; Henderson, B. Chaperonins are cell-signalling proteins: the unfolding biology of molecular chaperones. *Expert Rev. Mol. Med.* **2000**, *2*, 1-17.

(152) O'Riordan, C. R.; Lachapelle, A.; Delgado, C.; Parkes, V.; Wadsworth, S. C.; Smith, A. E.; Francis, G. E. PEGylation of Adenovirus with Retention of Infectivity and Protection from Neutralizing Antibody in Vitro and in Vivo. *Human Gene Ther.* **1999**, *10*, 1349-1358.

(153) Steinmetz, N. F.; Manchester, M. PEGylated Viral Nanoparticles for Biomedicine: The Impact of PEG Chain Length on VNP Cell Interactions In Vitro and Ex Vivo. *Biomacromolecules* **2009**, *10*, 784-792.

(154) Raja, K. S.; Wang, Q.; Gonzalez, M. J.; Manchester, M.; Johnson, J. E.; Finn, M. G. Hybrid Virus−Polymer Materials. 1. Synthesis and Properties of PEG-Decorated Cowpea Mosaic Virus. *Biomacromolecules* **2003**, *4*, 472-476.

(155) Vllasaliu, D.; Fowler, R.; Stolnik, S. PEGylated nanomedicines: recent progress and remaining concerns. *Expert Opin. Drug Deliv.* **2014**, *11*, 139-154.

(156) Minten, I. J.; Ma, Y.; Hempenius, M. A.; Vancso, G. J.; Nolte, R. J. M.; Cornelissen, J. J. L. M. CCMV capsid formation induced by a functional negatively charged polymer. *Org. Biomol. Chem.* **2009**, *7*, 4685-4688.

(157) Hu, Y.; Zandi, R.; Anavitarte, A.; Knobler, C. M.; Gelbart, W. M. Packaging of a polymer by a viral capsid: the interplay between polymer length and capsid size. *Biophys. J.* **2008**, *94*, 1428-1436.

(158) Ng, B. C.; Yu, M.; Gopal, A.; Rome, L. H.; Monbouquette, H. G.; Tolbert, S. H. Encapsulation of Semiconducting Polymers in Vault Protein Cages. *Nano Lett.* **2008**, *8*, 3503-3509.

(159) Hu, Y. X.; Samanta, D.; Parelkar, S. S.; Hong, S. W.; Wang, Q. A.; Russell, T. P.; Emrick, T. Ferritin-Polymer Conjugates: Grafting Chemistry and Integration into Nanoscale Assemblies. *Adv. Funct. Mater.* **2010**, *20*, 3603-3612.

(160) Abedin, M. J.; Liepold, L.; Suci, P.; Young, M.; Douglas, T. Synthesis of Cross-Linked Branched Polymer Network in the Interior of a Protein Cage. *J. Am. Chem. Soc.* **2009**, *131*, 4346-4354.
(161) Kim, P. H.; Kim, J.; Kim, T. I.; Nam, H. Y.; Yockman, J. W.; Kim, M.; Kim, S. W.; Yun, C. O. Bioreducible polymer-conjugated oncolytic adenovirus for hepatoma-specific therapy via systemic administration. *Biomaterials* **2011**, *32*, 9328-9342.
(162) Kosuge, H.; Uchida, M.; Lucon, J.; Qazi, S.; Douglas, T.; McConnell, M. V. High-Gd-Payload P22 protein cage nanoparticles for imaging vascular inflammation. *J. Cardiovasc. Magn. Res.* **2013**, *15*.
(163) Nussbaumer, M. G.; Rother, M.; Renggli, K.; Chami, M.; Bruns, N. Chaperonin-dendrimer conjugates for siRNA delivery. *submitted* **2015**.
(164) Eto, Y.; Yoshioka, Y.; Ishida, T.; Yao, X.; Morishige, T.; Narimatsu, S.; Mizuguchi, H.; Mukai, Y.; Okada, N.; Kiwada, H.; Nakagawa, S. Optimized PEGylated Adenovirus Vector Reduces the Anti-vector Humoral Immune Response against Adenovirus and Induces a Therapeutic Effect against Metastatic Lung Cancer. *Biol. Pharm. Bull.***2010**, *33*, 1540-1544.
(165) Yao, X.; Zhou, N.; Wan, L.; Su, X.; Sun, Z.; Mizuguchi, H.; Yoshioka, Y.; Nakagawa, S.; Zhao, R. C.; Gao, J.-Q. Polyethyleneimine-coating enhances adenoviral transduction of mesenchymal stem cells. *Biochem. Biophys. Res. Commun.* **2014**, *447*, 383-387.
(166) Nabatoff, R. A. Surgical technique for stripping the long saphenous vein. *Surg. Gynecol. Obstet.* **1977**, *145*, 81-87.
(167) Sengonul, M.; Sousa, A.; Libera, M. Selective adsorption of surface-modified ferritin on a phase-separated polymer blend. *Coll. Surf. B* **2009**, *73*, 152-155.
(168) Shin, M. K.; Spinks, G. M.; Shin, S. R.; Kim, S. I.; Kim, S. J. Nanocomposite Hydrogel with High Toughness for Bioactuators. *Adv. Mater.* **2009**, *21*, 1712-1715.
(169) Ibrahim, S.; Ito, T. Surface Chemical Properties of Nanoscale Domains on UV-Treated Polystyrene-Poly(methyl methacrylate) Diblock Copolymer Films Studied Using Scanning Force Microscopy. *Langmuir* **2010**, *26*, 2119-2123.
(170) Setaro, F.; Brasch, M.; Hahn, U.; Koay, M. S. T.; Cornelissen, J. J. L. M.; de la Escosura, A.; Torres, T. Generation-Dependent Templated Self-Assembly of Biohybrid Protein Nanoparticles around Photosensitizer Dendrimers. *Nano Lett.* **2015**, *15*, 1245-1251.
(171) Perriman, A. W.; Mann, S. Liquid proteins--a new frontier for biomolecule-based nanoscience. *ACS Nano* **2011**, *5*, 6085-6091.
(172) Lucon, J.; Edwards, E.; Qazi, S.; Uchida, M.; Douglas, T. Atom transfer radical polymerization on the interior of the P22 capsid and incorporation of photocatalytic monomer crosslinks. *Eur. Polym. J.* **2013**, *49*, 2976-2985.
(173) Shin, M. K.; Kim, S. I.; Kim, S. J.; Kim, B. J.; So, I.; Kozlov, M. E.; Oh, J.; Baughman, R. H. A tough nanofiber hydrogel incorporating ferritin. *Appl. Phys. Lett.* **2008**, *93*.
(174) Lin, Y.; Boker, A.; He, J.; Sill, K.; Xiang, H.; Abetz, C.; Li, X.; Wang, J.; Emrick, T.; Long, S.; Wang, Q.; Balazs, A.; Russell, T. P. Self-directed self-assembly of nanoparticle/copolymer mixtures. *Nature* **2005**, *434*, 55-59.
(175) Perriman, A. W.; Colfen, H.; Hughes, R. W.; Barrie, C. L.; Mann, S. Solvent-free protein liquids and liquid crystals. *Angew. Chem., Int. Ed.* **2009**, *48*, 6242-6246.
(176) van Rijn, P.; Mougin, N. C.; Franke, D.; Park, H.; Boker, A. Pickering emulsion templated soft capsules by self-assembling cross-linkable ferritin-polymer conjugates. *Chem. Commun.* **2011**, *47*, 8376-8378.
(177) van Rijn, P.; Mougin, N. C.; Boker, A. Hierarchical structures via self-assembling protein-polymer hybrid building blocks. *Polymer* **2012**, *53*, 6045-6052.
(178) Pelegri-O'Day, E. M.; Lin, E. W.; Maynard, H. D. Therapeutic Protein-Polymer Conjugates: Advancing Beyond PEGylation. *J. Am. Chem. Soc.* **2014**.
(179) Qi, Y.; Chilkoti, A. Growing polymers from peptides and proteins: a biomedical perspective. *Polym. Chem.* **2014**, *5*, 266-276.
(180) Sumerlin, B. S. Proteins as Initiators of Controlled Radical Polymerization: Grafting-from via ATRP and RAFT. *ACS Macro Lett.* **2012**, *1*, 141-145.
(181) Zeltins, A. Construction and characterization of virus-like particles: a review. *Mol. Biotech.* **2013**, *53*, 92-107.
(182) Mateu, M. G. Assembly, stability and dynamics of virus capsids. *Arch. of Biochem. Biophys.* **2013**, *531*, 65-79.
(183) Theil, E. C. Ferritin: the protein nanocage and iron biomineral in health and in disease. *Inorg. Chem.* **2013**, *52*, 12223-12233.
(184) Rome, L. H.; Kickhoefer, V. A. Development of the Vault Particle as a Platform Technology. *ACS Nano* **2012**, *7*, 889-902.

(185) De Maio, A.; Vazquez, D. Extracellular heat shock proteins: a new location, a new function. *Shock* **2013**, *40*, 239-246.
(186) De Maio, A. Heat Shock Proteins: Facts, Thoughts, and Dreams. *Shock* **1999**, *11*.
(187) Dekker, C.; Willison, K. R.; Taylor, W. R. On the evolutionary origin of the chaperonins. *Proteins* **2011**, *79*, 1172-1192.
(188) Horwich, A. L.; Fenton, W. A.; Chapman, E.; Farr, G. W. Two families of chaperonin: physiology and mechanism. *Ann. Rev. Cell Dev. Biol.* **2007**, *23*, 115-145.
(189) Ritsert, K.; Huber, R.; Turk, D.; Ladenstein, R.; Schmidt-Baese, K.; Bacher, A. Studies on the lumazine synthase/riboflavin synthase complex of Bacillus subtilis: crystal structure analysis of reconstituted, icosahedral β-subunit capsids with bound substrate analog inhibitor at 2.4 Å resolution. *J. Mol. Biol.* **1995**, *253*, 151-167.
(190) Sutter, M.; Boehringer, D.; Gutmann, S.; Guenther, S.; Prangishvili, D.; Loessner, M. J.; Stetter, K. O.; Weber-Ban, E.; Ban, N. Structural basis of enzyme encapsulation into a bacterial nanocompartment. *Nat. Struct. Mol. Biol.* **2008**, *15*, 939-947.
(191) Rahmanpour, R.; Bugg, T. D. H. Assembly in vitro of Rhodococcus jostii RHA1 encapsulin and peroxidase DypB to form a nanocompartment. *FEBS Journal* **2013**, *280*, 2097-2104.
(192) Cheng, S. Q.; Liu, Y.; Crowley, C. S.; Yeates, T. O.; Bobik, T. A. Bacterial microcompartments: their properties and paradoxes. *Bioessays* **2008**, *30*, 1084-1095.
(193) Tanaka, S.; Sawaya, M. R.; Yeates, T. O. Structure and mechanisms of a protein-based organelle in Escherichia coli. *Science* **2010**, *327*, 81-84.
(194) Corchero, J.; Cedano, J. Self-assembling, protein-based intracellular bacterial organelles: emerging vehicles for encapsulating, targeting and delivering therapeutical cargoes. *Microb. Cell Fact.* **2011**, *10*, 92.
(195) Namba, K.; Stubbs, G. Structure of Tobacco Mosaic-Virus at 3.6-a Resolution - Implications for Assembly. *Science* **1986**, *231*, 1401-1406.
(196) Wang, Q.; Lin, T.; Tang, L.; Johnson, J. E.; Finn, M. G. Icosahedral Virus Particles as Addressable Nanoscale Building Blocks. *Angew. Chem., Int. Ed.* **2002**, *41*, 459-462.
(197) Douglas, T.; Young, M. Host-guest encapsulation of materials by assembled virus protein cages. *Nature* **1998**, *393*, 152-155.
(198) Speir, J. A.; Munshi, S.; Wang, G.; Baker, T. S.; Johnson, J. E. Structures of the native and swollen forms of cowpea chlorotic mottle virus determined by X-ray crystallography and cryo-electron microscopy. *Structure* **1995**, *3*, 63-78.
(199) Valegard, K.; Liljas, L.; Fridborg, K.; Unge, T. The three-dimensional structure of the bacterial virus MS2. *Nature* **1990**, *345*, 36-41.
(200) Golmohammadi, R.; Valegård, K.; Fridborg, K.; Liljas, L. The Refined Structure of Bacteriophage MS2 at 2.8 Å Resolution. *J. Mol. Biol* **1993**, *234*, 620-639.
(201) Saban, S. D.; Nepomuceno, R. R.; Gritton, L. D.; Nemerow, G. R.; Stewart, P. L. CryoEM structure at 9Å resolution of an adenovirus vector targeted to hematopoietic cells. *J. Mol. Biol.* **2005**, *349*, 526-537.
(202) Liu, H.; Jin, L.; Koh, S. B. S.; Atanasov, I.; Schein, S.; Wu, L.; Zhou, Z. H. Atomic Structure of Human Adenovirus by Cryo-EM Reveals Interactions Among Protein Networks. *Science* **2010**, *329*, 1038-1043.
(203) Reddy, V. S.; Natchiar, S. K.; Stewart, P. L.; Nemerow, G. R. Crystal Structure of Human Adenovirus at 3.5 Å Resolution. *Science* **2010**, *329*, 1071-1075.
(204) Mao, C.; Solis, D. J.; Reiss, B. D.; Kottmann, S. T.; Sweeney, R. Y.; Hayhurst, A.; Georgiou, G.; Iverson, B.; Belcher, A. M. Virus-Based Toolkit for the Directed Synthesis of Magnetic and Semiconducting Nanowires. *Science* **2004**, *303*, 213-217.
(205) Niu, Z.; Liu, J.; Lee, L. A.; Bruckman, M. A.; Zhao, D.; Koley, G.; Wang, Q. Biological templated synthesis of water-soluble conductive polymeric nanowires. *Nano Lett.* **2007**, *7*, 3729-3733.
(206) Lee, S.-Y.; Lim, J.-S.; Harris, M. T. Synthesis and application of virus-based hybrid nanomaterials. *Biotech. Bioeng.* **2012**, *109*, 16-30.
(207) Culver, J. N.; Brown, A. D.; Zang, F.; Gnerlich, M.; Gerasopoulos, K.; Ghodssi, R. Plant virus directed fabrication of nanoscale materials and devices. *Virology* **2015**, *479–480*, 200-212.
(208) Fischlechner, M.; Donath, E. Viruses as building blocks for materials and devices. *Chem., Int. Ed.* **2007**, *46*, 3184-3193.
(209) Caspar, D. L.; Klug, A. Physical principles in the construction of regular viruses. *Cold. S pring. Harb. Symp. Quant. Biol.* **1962**, *27*, 1-24.
(210) Prasad, B. V. V.; Schmid, M. F. Principles of Virus Structural Organization. *Adv. Exp. Med. Biol.* **2012**, *726*, 17-47.

(211) Gallois, B.; d'Estaintot, B. L.; Michaux, M.-A.; Dautant, A.; Granier, T.; Précigoux, G.; Soruco, J.-A.; Roland, F.; Chavas-Alba, O.; Herbas, A.; Crichton, R. R. X-ray structure of recombinant horse L-chain apoferritin at 2.0 Å resolution: implications for stability and function. *JBIC* **1997**, *2*, 360-367.
(212) Kim, K. K.; Yokota, H.; Santoso, S.; Lerner, D.; Kim, R.; Kim, S.-H. Purification, Crystallization, and Preliminary X-Ray Crystallographic Data Analysis of Small Heat Shock Protein Homolog from Methanococcus jannaschii,a Hyperthermophile. *J. Struct. Biol.* **1998**, *121*, 76-80.
(213) Kim, K. K.; Kim, R.; Kim, S.-H. Crystal structure of a small heat-shock protein. *Nature* **1998**, *394*, 595-599.
(214) Teschke, C. M.; McGough, A.; Thuman-Commike, P. A. Penton Release from P22 Heat-Expanded Capsids Suggests Importance of Stabilizing Penton-Hexon Interactions during Capsid Maturation. *Biophys. J.* **2003**, *84*, 2585-2592.
(215) Galvez, N.; Sanchez, P.; Dominguez-Vera, J. M. Preparation of Cu and CuFe Prussian Blue derivative nanoparticles using the apoferritin cavity as nanoreactor. *Dalton Trans.* **2005**, 2492-2494.
(216) Basu, G.; Allen, M.; Willits, D.; Young, M.; Douglas, T. Metal binding to cowpea chlorotic mottle virus using terbium(III) fluorescence. *JBIC* **2003**, *8*, 721-725.
(217) Tama, F.; Brooks, C. L. The Mechanism and Pathway of pH Induced Swelling in Cowpea Chlorotic Mottle Virus. *J. Mol. Biol.* **2002**, *318*, 733-747.
(218) Verduin, B. J. M. The preparation of CCMV-protein in connection with its association into a spherical particle. *FEBS lett.* **1974**, *45*, 50-54.
(219) Johnson, J. E.; Speir, J. A. Quasi-equivalent viruses: a paradigm for protein assemblies. *J. Mol. Biol.* **1997**, *269*, 665-675.
(220) Comellas-Aragones, M.; Engelkamp, H.; Claessen, V. I.; Sommerdijk, N. A. J. M.; Rowan, A. E.; Christianen, P. C. M.; Maan, J. C.; Verduin, B. J. M.; Cornelissen, J. J. L. M.; Nolte, R. J. M. A Virus-Based Single-Enzyme Nanoreactor. *Nature Nanotech.* **2007**, *2*, 635-639.
(221) Liu, G.; Wang, J.; Wu, H.; Lin, Y. Versatile Apoferritin Nanoparticle Labels for Assay of Protein. *Anal. Chem.* **2006**, *78*, 7417-7423.
(222) Liu, G.; Wang, J.; Lea, S. A.; Lin, Y. Bioassay Labels Based on Apoferritin Nanovehicles. *ChemBioChem* **2006**, *7*, 1315-1319.
(223) Lin, X.; Xie, J.; Niu, G.; Zhang, F.; Gao, H.; Yang, M.; Quan, Q.; Aronova, M. A.; Zhang, G.; Lee, S.; Leapman, R.; Chen, X. Chimeric Ferritin Nanocages for Multiple Function Loading and Multimodal Imaging. *Nano Lett.* **2011**, *11*, 814-819.
(224) Waldmann, T.; Nitsch, M.; Klumpp, M.; Baumeister, W. Expression of an archaeal chaperonin in E. coli: formation of homo- (α, β) and hetero-oligomeric (α + β) thermosome complexes. *FEBS lett.* **1995**, *376*, 67-73.
(225) Webb, B.; Frame, J.; Zhao, Z.; Lee, M. L.; Watt, G. D. Molecular Entrapment of Small Molecules within the Interior of Horse Spleen Ferritin. *Arch. Biochem. Biophys.* **1994**, *309*, 178-183.
(226) Saibil, H. R.; Fenton, W. A.; Clare, D. K.; Horwich, A. L. Structure and Allostery of the Chaperonin GroEL. *J. Mol. Biol.* **2013**, *425*, 1476-1487.
(227) Bigotti, M. G.; Clarke, A. R. Chaperonins: The hunt for the Group II mechanism. *Arch. Biochem. Biophys.* **2008**, *474*, 331-339.
(228) Lopez, T.; Dalton, K.; Frydman, J. The Mechanism and Function of Group II Chaperonins. *J. Mol. Biol.* **2015**.
(229) Meyer, A. S.; Gillespie, J. R.; Walther, D.; Millet, I. S.; Doniach, S.; Frydman, J. Closing the Folding Chamber of the Eukaryotic Chaperonin Requires the Transition State of ATP Hydrolysis. *Cell* **2003**, *113*, 369-381.
(230) Lawson, D. M.; Artymiuk, P. J.; Yewdall, S. J.; Smith, J. M. A.; Livingstone, J. C.; Treffry, A.; Luzzago, A.; Levi, S.; Arosio, P.; et al. Solving the structure of human H ferritin by genetically engineering intermolecular crystal contacts. *Nature* **1991**, *349*, 541-544.
(231) Stefanini, S.; Cavallo, S.; Wang, C.-Q.; Tataseo, P.; Vecchini, P.; Giartosio, A.; Chiancone, E. Thermal stability of horse spleen apoferritin and human recombinant H apoferritin. *Arch. Biochem. Biophys.* **1996**, *325*, 58-64.
(232) Listowsky, I.; Blauer, G.; Englard, S.; Betheil, J. J. Denaturation of horse spleen ferritin in aqueous guanidinium chloride solutions. *Biochemistry* **1972**, *11*, 2176-2182.
(233) Kim, R.; Kim, K. K.; Yokota, H.; Kim, S.-H. Small heat shock protein of Methanococcus jannaschii, a hyperthermophile. *Proc. Natl. Acad. Sci. U.S.A.* **1998**, *95*, 9129-9133.
(234) Hartl, F. U.; Hayer-Hartl, M. Molecular chaperones in the cytosol: from nascent chain to folded protein. *Science* **2002**, *295*, 1852-1858.

(235) Ditzel, L.; Löwe, J.; Stock, D.; Stetter, K.-O.; Huber, H.; Huber, R.; Steinbacher, S. Crystal Structure of the Thermosome, the Archaeal Chaperonin and Homolog of CCT. *Cell* **1998**, *93*, 125-138.
(236) Schoehn, G.; Hayes, M.; Cliff, M.; Clarke, A. R.; Saibil, H. R. Domain rotations between open, closed and bullet-shaped forms of the thermosome, an archaeal chaperonin. *J. Mol. Biol.* **2000**, *301*, 323-332.
(237) Booth, C. R.; Meyer, A. S.; Cong, Y.; Topf, M.; Sali, A.; Ludtke, S. J.; Chiu, W.; Frydman, J. Mechanism of lid closure in the eukaryotic chaperonin TRiC/CCT. *Nat. Struct. Mol. Biol.* **2008**, *15*, 746-753.
(238) Douglas, N. R.; Reissmann, S.; Zhang, J.; Chen, B.; Jakana, J.; Kumar, R.; Chiu, W.; Frydman, J. Dual action of ATP hydrolysis couples lid closure to substrate release into the group II chaperonin chamber. *Cell* **2011**, *144*, 240-252.
(239) Rome, L. H.; Kickhoefer, V. A. Development of the Vault Particle as a Platform Technology. *ACS Nano* **2013**, *7*, 889-902.
(240) Kedersha, N. L. Vaults. III. Vault ribonucleoprotein particles open into flower-like structures with octagonal symmetry. *J. Cell Biol.* **1991**, *112*, 225-235.
(241) Slesina, M.; Inman, E.; Moore, A.; Goldhaber, J.; Rome, L.; Volknandt, W. Movement of vault particles visualized by GFP-tagged major vault protein. *Cell Tissue Res.* **2006**, *324*, 403-410.
(242) Mikyas, Y.; Makabi, M.; Raval-Fernandes, S.; Harrington, L.; Kickhoefer, V. A.; Rome, L. H.; Stewart, P. L. Cryoelectron microscopy imaging of recombinant and tissue derived vaults: localization of the MVP N termini and VPARP. *J. Mol. Biol.* **2004**, *344*, 91-105.
(243) Zhou, Z. H.; McCarthy, D. B.; O'Connor, C. M.; Reed, L. J.; Stoops, J. K. The remarkable structural and functional organization of the eukaryotic pyruvate dehydrogenase complexes. *Proc. Natl. Acad. of Sci. U.S.A.* **2001**, *98*, 14802-14807.
(244) Izard, T.; Ævarsson, A.; Allen, M. D.; Westphal, A. H.; Perham, R. N.; de Kok, A.; Hol, W. G. J. Principles of quasi-equivalence and Euclidean geometry govern the assembly of cubic and dodecahedral cores of pyruvate dehydrogenase complexes. *Proc. Natl. Acad. Sci. U.S.A.* **1999**, *96*, 1240-1245.
(245) Dalmau, M.; Lim, S.; Chen, H. C.; Ruiz, C.; Wang, S.-W. Thermostability and molecular encapsulation within an engineered caged protein scaffold. *Biotech. Bioeng.* **2008**, *101*, 654-664.
(246) Rowe, W. P.; Huebner, R. J.; Gilmore, L. K.; Parrott, R. H.; Ward, T. G. Isolation of a Cytopathogenic Agent from Human Adenoids Undergoing Spontaneous Degeneration in Tissue Culture. *P. Soc. Exp. Biol. Med.* **1953**, *84*, 570-573.
(247) Reddy, V. S.; Natchiar, S. K.; Stewart, P. L.; Nemerow, G. R. Crystal Structure of Human Adenovirus at 3.5 Å Resolution. *Science* **2010**, *329*, 1071-1075.
(248) Martin, C. S. Latest Insights on Adenovirus Structure and Assembly. *Viruses-Basel* **2012**, *4*, 847-877.
(249) Jiang, H.; Gomez-Manzano, C.; Lang, F. F.; Alemany, R.; Fueyo, J. Oncolytic Adenovirus: Preclinical and Clinical Studies in Patients with Human Malignant Gliomas. *Curr. Gene. Ther.* **2009**, *9*, 422-427.
(250) Rainov, N. G.; Heidecke, V. Clinical Development of Experimental Virus-Mediated Gene Therapy for Malignant Glioma. *Anti-Cancer Agents Med. Chem.* **2011**, *11*, 739-747.
(251) Castro, M. G.; Lowenstein, P. R. Neuro-Oncology The long and winding road-gene therapy for glioma. *Nat. Rev. Neurol.* **2013**, *9*, 609-610.
(252) Yan, Y.; Li, S. Y.; Jia, T. T.; Du, X. H.; Xu, Y. X.; Zhao, Y. S.; Li, L.; Liang, K.; Liang, W. T.; Sun, H. W.; Li, R. Combined therapy with CTL cells and oncolytic adenovirus expressing IL-15-induced enhanced antitumor activity. *Tumor. Biol.* **2015**, *36*, 4535-4543.
(253) Sainsbury, F.; Canizares, M. C.; Lomonossoff, G. P. Cowpea mosaic Virus: The Plant Virus-Based Biotechnology Workhorse. *Annu. Rev. Phytopathol.* **2010**, *48*, 437-455.
(254) Wang, Q.; Kaltgrad, E.; Lin, T. W.; Johnson, J. E.; Finn, M. G. Natural supramolecular building blocks: Wild-type cowpea mosaic virus. *Chem. Biol.* **2002**, *9*, 805-811.
(255) Lin, T. W.; Chen, Z. G.; Usha, R.; Stauffacher, C. V.; Dai, J. B.; Schmidt, T.; Johnson, J. E. The refined crystal structure of cowpea mosaic virus at 2.8 Å resolution. *Virology* **1999**, *265*, 20-34.
(256) Lucas, R. W.; Larson, S. B.; McPherson, A. The crystallographic structure of brome mosaic virus. *J. Mol. Biol.* **2002**, *317*, 95-108.
(257) Larson, S. B.; Lucas, R. W.; McPherson, A. Crystallographic structure of the T=1 particle of brome mosaic virus. *J. Mol. Biol.* **2005**, *346*, 815-831.

(258) Finch, J. T.; Klug, A. Structure of Broad Bean Mottle Virus. I. Analysis of Electron Micrographs and Comparison with Turnip Yellow Mosaic Virus and Its Top Component. *J. Mol. Biol.* **1967**, *24*, 289-302.
(259) Yamazaki, H.; Bancroft, J.; Kaesberg, P. Biophysical Studies of Broad Bean Mottle Virus. *Proc. Natl. Acad. Sci. U.S.A.* **1961**, *47*, 979-983.
(260) Finch, J. T.; Leberman, R.; Berger, J. E. Structure of Broad Bean Mottle Virus. II. X-Ray Diffraction Studies. *J. Mol. Biol.* **1967**, *27*, 17-24.
(261) Bayer, M. E.; Bocharov, A. F. The capsid structure of bacteriophage lambda. *Virology* **1973**, *54*, 465-475.
(262) Lander, G. C.; Evilevitch, A.; Jeembaeva, M.; Potter, C. S.; Carragher, B.; Johnson, J. E. Bacteriophage lambda stabilization by auxiliary protein gpD: Timing, location, and mechanism of attachment determined by cryo-EM. *Structure* **2008**, *16*, 1399-1406.
(263) Dokland, T.; Murialdo, H. Structural Transitions during Maturation of Bacteriophage-Lambda Capsids. *J. Mol. Biol.* **1993**, *233*, 682-694.
(264) Golmohammadi, R.; Fridborg, K.; Bundule, M.; Valegård, K.; Liljas, L. The crystal structure of bacteriophage Qβ at 3.5 Å resolution. *Structure* **1996**, *4*, 543-554.
(265) Takamatsu, H.; Iso, K. Chemical evidence for the capsomeric structure of phage q beta. *Nature* **1982**, *298*, 819-824.
(266) Cielens, I.; Ose, V.; Petrovskis, I.; Strelnikova, A.; Renhofa, R.; Kozlovska, T.; Pumpens, P. Mutilation of RNA phage Q beta virus-like particles: from icosahedrons to rods. *FEBS lett.* **2000**, *482*, 261-264.
(267) Orlova, E. V.: Bacteriophages and their structural organisation. In *Bacteriophages*; Kurtboke, I., Ed.; InTech: Rijeka, Croatia, 2012; pp 3-30.
(268) Jiang, W.; Li, Z.; Zhang, Z.; Baker, M. L.; Prevelige, P. E., Jr.; Chiu, W. Coat protein fold and maturation transition of bacteriophage P22 seen at subnanometer resolutions. *Nature Struct. Biol.* **2003**, *10*, 131-135.
(269) Kang, S.; Uchida, M.; O'Neil, A.; Li, R.; Prevelige, P. E.; Douglas, T. Implementation of P22 Viral Capsids as Nanoplatforms. *Biomacromolecules* **2010**, *11*, 2804-2809.
(270) Chang, J.; Weigele, P.; King, J.; Chiu, W.; Jiang, W. Cryo-EM asymmetric reconstruction of bacteriophage P22 reveals organization of its DNA packaging and infecting machinery. *Structure* **2006**, *14*, 1073-1082.
(271) Mattevi, A.; Obmolova, G.; Kalk, K. H.; Teplyakov, A.; Hol, W. G. J. Crystallographic Analysis of Substrate Binding and Catalysis in Dihydrolipoyl Transacetylase (E2p). *Biochemistry* **1993**, *32*, 3887-3901.
(272) Tanaka, H.; Kato, K.; Yamashita, E.; Sumizawa, T.; Zhou, Y.; Yao, M.; Iwasaki, K.; Yoshimura, M.; Tsukihara, T. The Structure of Rat Liver Vault at 3.5 Å Resolution. *Science* **2009**, *323*, 384-388.
(273) Chen, D. H.; Baker, M. L.; Hryc, C. F.; DiMaio, F.; Jakana, J.; Wu, W. M.; Dougherty, M.; Haase-Pettingell, C.; Schmid, M. F.; Jiang, W.; Baker, D.; King, J. A.; Chiu, W. Structural basis for scaffolding-mediated assembly and maturation of a dsDNA virus. *Proc. Natl. Acad. Sci. U.S.A.* **2011**, *108*, 1355-1360.
(274) Pettersen, E. F.; Goddard, T. D.; Huang, C. C.; Couch, G. S.; Greenblatt, D. M.; Meng, E. C.; Ferrin, T. E. UCSF Chimera—A visualization system for exploratory research and analysis. *J. Comp. Chem.* **2004**, *25*, 1605-1612.
(275) Moad, G.; Rizzardo, E.; Thang, S. H. Living Radical Polymerization by the RAFT Process – A Third Update. *Austr. J. Chem.* **2012**, *65*, 985-1076.
(276) Lewis, J. D.; Destito, G.; Zijlstra, A.; Gonzalez, M. J.; Quigley, J. P.; Manchester, M.; Stuhlmann, H. Viral nanoparticles as tools for intravital vascular imaging. *Nature Med.* **2006**, *12*, 354-360.
(277) Heredia, K. L.; Maynard, H. D. Synthesis of protein-polymer conjugates. *Org. Biomol. Chem.* **2007**, *5*, 45-53.
(278) Lutz, J.-F.; Börner, H. G. Modern trends in polymer bioconjugates design. *Prog. Polym. Sci.* **2008**, *33*, 1-39.
(279) Gauthier, M. A.; Klok, H.-A. Peptide/protein-polymer conjugates: synthetic strategies and design concepts. *Chem. Commun.* **2008**, 2591-2611.
(280) Broyer, R. M.; Grover, G. N.; Maynard, H. D. Emerging synthetic approaches for protein-polymer conjugations. *Chem. Commun.* **2011**, *47*, 2212-2226.
(281) Obermeyer, A. C.; Olsen, B. D. Synthesis and Application of Protein-Containing Block Copolymers. *ACS Macro Lett.* **2015**, *4*, 101-110.
(282) Yao, X.; Yoshioka, Y.; Morishige, T.; Eto, Y.; Watanabe, H.; Okada, Y.; Mizuguchi, H.; Mukai, Y.; Okada, N.; Nakagawa, S. Systemic administration of a PEGylated adenovirus

vector with a cancer-specific promoter is effective in a mouse model of metastasis. *Gene Ther.* **2009**, *16*, 1395-1404.

(283) Kovacs, E. W.; Hooker, J. M.; Romanini, D. W.; Holder, P. G.; Berry, K. E.;Francis, M. B. Dual-Surface-Modified Bacteriophage MS2 as an Ideal Scaffold for a Viral Capsid-Based Drug Delivery System. *Bioconjug. Chem.* **2007**, *18*, 1140-1147.

(284) Yao, X.; Yoshioka, Y.; Morishige, T.; Eto, Y.; Narimatsu, S.; Kawai, Y.; Mizuguchi, H.; Gao, J. Q.; Mukai, Y.; Okada, N.; Nakagawa, S. Tumor vascular targeted delivery of polymer-conjugated adenovirus vector for cancer gene therapy. *Mol. Ther.* **2011**, *19*, 1619-1625.

(285) Pokorski, J. K.; Breitenkamp, K.; Liepold, L. O.; Qazi, S.; Finn, M. G. Functional virus-based polymer-protein nanoparticles by atom transfer radical polymerization. *J. Am. Chem. Soc.* **2011**, *133*, 9242-9245.

(286) Suh, J.; Choy, K.-L.; Lai, S. L.; Suk, J. S.; Tang, B. C.; Prabhu, S.; Hanes, J. PEGylation of nanoparticles improves their cytoplasmic transport. *Int. J. Nanomed.* **2007**, *2*, 735-741.

(287) Wattendorf, U.; Merkle, H. P. PEGylation as a tool for the biomedical engineering of surface modified microparticles. *J. Pharm. Sci.* **2008**, *97*, 4655-4669.

(288) Li, W. J.; Zhan, P.; De Clercq, E.; Lou, H. X.; Liu, X. Y. Current drug research on PEGylation with small molecular agents. *Prog. Polym. Sci.* **2013**, *38*, 421-444.

(289) Ginn, C.; Khalili, H.; Lever, R.; Brocchini, S. PEGylation and its impact on the design of new protein-based medicines. *Future Med. Chem.* **2014**, *6*, 1829-1846.

(290) Alconcel, S. N. S.; Baas, A. S.; Maynard, H. D. FDA-approved poly(ethylene glycol)-protein conjugate drugs. *Polym. Chem.* **2011**, *2*, 1442-1448.

(291) Wang, Q.; Raja, K. S.; Janda, K. D.; Lin, T.; Finn, M. G. Blue Fluorescent Antibodies as Reporters of Steric Accessibility in Virus Conjugates. *Bioconjug. Chem.* **2003**, *14*, 38-43.

(292) Comellas-Aragonès, M.; de la Escosura, A. s.; Dirks, A. J.; van der Ham, A.; Fusté-Cuñé, A.; Cornelissen, J. J. L. M.; Nolte, R. J. M. Controlled Integration of Polymers into Viral Capsids. *Biomacromolecules* **2009**, *10*, 3141-3147.

(293) Farkas, M. E.; Aanei, I. L.; Behrens, C. R.; Tong, G. J.; Murphy, S. T.; O'Neil, J. P.; Francis, M. B. PET Imaging and Biodistribution of Chemically Modified Bacteriophage MS2. *Mol. Pharm.* **2013**, *10*, 69-76.

(294) Kim, P.-H.; Sohn, J.-H.; Choi, J.-W.; Jung, Y.; Kim, S. W.; Haam, S.; Yun, C.-O. Active targeting and safety profile of PEG-modified adenovirus conjugated with herceptin. *Biomaterials* **2011**, *32*, 2314-2326.

(295) Sengonul, M.; Ruzicka, J.; Attygalle, A. B.; Libera, M. Surface modification of protein nanocontainers and their self-directing character in polymer blends. *Polymer* **2007**, *48*, 3632-3640.

(296) Kulmashiro, Y.; Ikezoe, Y.; Tamada, K.; Hara, M. Dynamic interfacial properties of poly(ethylene glycol)-modified ferritin at the solid/liquid interface. *J. Phys. Chem. B* **2008**, *112*, 8291-8297.

(297) Molino, N. M.; Bilotkach, K.; Fraser, D. A.; Ren, D.; Wang, S.-W. Complement Activation and Cell Uptake Responses Toward Polymer-Functionalized Protein Nanocapsules. *Biomacromolecules* **2012**, *13*, 974-981.

(298) Yao, X.; Yoshioka, Y.; Morishige, T.; Eto, Y.; Narimatsu, S.; Mizuguchi, H.; Mukai, Y.; Okada, N.; Nakagawa, S. Adenovirus vector covalently conjugated to polyethylene glycol with a cancer-specific promoter suppresses the tumor growth through systemic administration. *Biol. Pharm. Bull.* **2010**, *33*, 1073-1076.

(299) Yao, X. L.; Yoshioka, Y.; Ruan, G. X.; Chen, Y. Z.; Mizuguchi, H.; Mukai, Y.; Okada, N.; Gao, J. Q.; Nakagawa, S. Optimization and internalization mechanisms of PEGylated adenovirus vector with targeting peptide for cancer gene therapy. *Biomacromolecules* **2012**, *13*, 2402-2409.

(300) Daniels, T. R.; Bernabeu, E.; Rodriguez, J. A.; Patel, S.; Kozman, M.; Chiappetta, D. A.; Holler, E.; Ljubimova, J. Y.; Helguera, G.; Penichet, M. L. The transferrin receptor and the targeted delivery of therapeutic agents against cancer. *Biochim. Biophys. Acta* **2012**, *1820*, 291-317.

(301) Bruckman, M. A.; Randolph, L. N.; VanMeter, A.; Hern, S.; Shoffstall, A. J.; Taurog, R. E.; Steinmetz, N. F. Biodistribution, pharmacokinetics, and blood compatibility of native and PEGylated tobacco mosaic virus nano-rods and -spheres in mice. *Virology* **2014**, *449*, 163-173.

(302) Zeng, Q.; Li, T.; Cash, B.; Li, S.; Xie, F.; Wang, Q. Chemoselective derivatization of a bionanoparticle by click reaction and ATRP reaction. *Chem. Commun.* **2007**, 1453-1455.

(303) Hatakeyama, H.; Akita, H.; Harashima, H. The Polyethyleneglycol Dilemma: Advantage and Disadvantage of PEGylation of Liposomes for Systemic Genes and Nucleic Acids Delivery to Tumors. *Biol. Pharm. Bull.* **2013**, *36*, 892-899.
(304) Pelaz, B.; del Pino, P.; Maffre, P.; Hartmann, R.; Gallego, M.; Rivera-Fernández, S.; de la Fuente, J. M.; Nienhaus, G. U.; Parak, W. J. Surface Functionalization of Nanoparticles with Polyethylene Glycol: Effects on Protein Adsorption and Cellular Uptake. *ACS Nano* **2015**, *9*, 6996-7008.
(305) Verhoef, J. J. F.; Carpenter, J. F.; Anchordoquy, T. J.; Schellekens, H. Potential induction of anti-PEG antibodies and complement activation toward PEGylated therapeutics. *Drug Disc. Today* **2014**, *19*, 1945-1952.
(306) Yang, Q.; Lai, S. K. Anti-PEG immunity: emergence, characteristics, and unaddressed questions. *Interdiscip. Rev. Nanomed. Nanobiotechnol.* **2015**, *7*, 655-677.
(307) Sedlacek, O.; Monnery, B. D.; Filippov, S. K.; Hoogenboom, R.; Hruby, M. Poly(2-Oxazoline)s – Are They More Advantageous for Biomedical Applications Than Other Polymers? *Macromol. Rapid Commun.* **2012**, *33*, 1648-1662.
(308) Adams, N.; Schubert, U. S. Poly(2-oxazolines) in biological and biomedical application contexts. *Adv. Drug Delivery Rev.* **2007**, *59*, 1504-1520.
(309) Lava, K.; Verbraeken, B.; Hoogenboom, R. Poly(2-oxazoline)s and click chemistry: A versatile toolbox toward multi-functional polymers. *Eur. Polym. J.* **2015**, *65*, 98-111.
(310) Manzenrieder, F.; Luxenhofer, R.; Retzlaff, M.; Jordan, R.; Finn, M. G. Stabilization of Virus-like Particles with Poly(2-oxazoline)s. *Angew. Chem., Int. Ed.* **2011**, *50*, 2601-2605.
(311) Alarcon, C. d. l. H.; Pennadam, S.; Alexander, C. Stimuli responsive polymers for biomedical applications. *Chem. Soc. Rev.* **2005**, *34*, 276-285.
(312) Ward, M. A.; Georgiou, T. K. Thermoresponsive Polymers for Biomedical Applications. *Polymers* **2011**, *3*, 1215-1242.
(313) Schild, H. G. Poly (N-Isopropylacrylamide) - Experiment, Theory and Application. *Prog. Polym. Sci.***1992**, *17*, 163-249.
(314) Matsumoto, N. M.; Prabhakaran, P.; Rome, L. H.; Maynard, H. D. Smart Vaults: Thermally-Responsive Protein Nanocapsules. *ACS Nano* **2012**, *7*, 867-874.
(315) Xu, J.; Liu, S. Polymeric nanocarriers possessing thermoresponsive coronas. *Soft Matter* **2008**, *4*, 1745-1749.
(316) Kickhoefer, V. A.; Garcia, Y.; Mikyas, Y.; Johansson, E.; Zhou, J. C.; Raval-Fernandes, S.; Minoofar, P.; Zink, J. I.; Dunn, B.; Stewart, P. L.; Rome, L. H. Engineering of vault nanocapsules with enzymatic and fluorescent properties. *Proc. Natl. Acad. Sci. U.S.A.* **2005**, *102*, 4348-4352.
(317) Mougin, N. C.; van Rijn, P.; Park, H.; Muller, A. H. E.; Boker, A. Hybrid Capsules via Self-Assembly of Thermoresponsive and Interfacially Active Bionanoparticle-Polymer Conjugates. *Adv. Funct. Mater.* **2011**, *21*, 2470-2476.
(318) Nash, M. E.; Carroll, W. M.; Nikoloskya, N.; Yang, R. B.; Connell, C. O.; Gorelov, A. V.; Dockery, P.; Liptrot, C.; Lyng, F. M.; Garcia, A.; Rochev, Y. A. Straightforward, One-Step Fabrication of Ultrathin Thermoresponsive Films from Commercially Available pNIPAm for Cell Culture and Recovery. *ACS Appl. Mater. Interf.* **2011**, *3*, 1980-1990.
(319) Lv, H. T.; Zhang, S. B.; Wang, B.; Cui, S. H.; Yan, J. Toxicity of cationic lipids and cationic polymers in gene delivery. *J. Controlled Release* **2006**, *114*, 100-109.
(320) Singarapu, K.; Pal, I.; Ramsey, J. D. Polyethylene glycol–grafted polyethylenimine used to enhance adenovirus gene delivery. *J. Biomed. Mater. Res. Part A* **2013**, *101A*, 1857-1864.
(321) Fischer, D.; Li, Y.; Ahlemeyer, B.; Krieglstein, J.; Kissel, T. In vitro cytotoxicity testing of polycations: influence of polymer structure on cell viability and hemolysis. *Biomaterials* **2003**, *24*, 1121-1131.
(322) Paul, A.; Eun, C.-J.; Song, J. M. Cytotoxicity mechanism of non-viral carriers polyethylenimine and poly-l-lysine using real time high-content cellular assay. *Polymer* **2014**, *55*, 5178-5188.
(323) Chung, D. D. L. Carbon materials for structural self-sensing, electromagnetic shielding and thermal interfacing. *Carbon* **2012**, *50*, 3342-3353.
(324) Caruso, M. M.; Davis, D. A.; Shen, Q.; Odom, S. A.; Sottos, N. R.; White, S. R.; Moore, J. S. Mechanically-induced chemical changes in polymeric materials. *Chem. Rev.* **2009**, *109*, 5755-5798.
(325) Brantley, J. N.; Bailey, C. B.; Wiggins, K. M.; Keatinge-Clay, A. T.; Bielawski, C. W. Mechanobiochemistry: harnessing biomacromolecules for force-responsive materials. *Polym. Chem.* **2013**, *4*, 3916-3928.

(326) Makyła, K.; Müller, C.; Lörcher, S.; Winkler, T.; Nussbaumer, M. G.; Eder, M.; Bruns, N. Fluorescent Protein Senses and Reports Mechanical Damage in Glass-Fiber-Reinforced Polymer Composites. *Adv. Mater.* **2013**, *25*, 2701-2706.
(327) Lörcher, S.; Winkler, T.; Makyła, K.; Ouellet-Plamondon, C.; Burgert, I.; Bruns, N. Mechanical unfolding of a fluorescent protein enables self-reporting of damage in carbon-fibre-reinforced composites. *J. Mater. Chem. A* **2014**, *2*, 6231-6237.
(328) Bruns, N.; Clark, D. S. Self-Reporting Materials: Protein- Mediated Visual Indication of Damage in a Bulk Polymer. *Chimia* **2011**, *65*, 245-249.
(329) Valle, F.; DeRose, J. A.; Dietler, G.; Kawe, M.; Plückthun, A.; Semenza, G. AFM structural study of the molecular chaperone GroEL and its two-dimensional crystals: an ideal "living" calibration sample. *Ultramicroscopy* **2002**, *93*, 83-89.
(330) Huang, Z. M.; Zhang, Y. Z.; Kotaki, M.; Ramakrishna, S. A review on polymer nanofibers by electrospinning and their applications in nanocomposites. *Compos. Sci. Technol.* **2003**, *63*, 2223-2253.
(331) Hu, X.; Liu, S.; Zhou, G.; Huang, Y.; Xie, Z.; Jing, X. Electrospinning of polymeric nanofibers for drug delivery applications. *J. Controlled Release* **2014**, *185*, 12-21.
(332) Sebe, I.; Szabo, P.; Kallai-Szabo, B.; Zelko, R. Incorporating small molecules or biologics into nanofibers for optimized drug release: A review. *Int. J. Pharm.* **2015**, Ahead of Print.
(333) Salalha, W.; Kuhn, J.; Dror, Y.; Zussman, E. Encapsulation of bacteria and viruses in electrospun nanofibres. *Nanotechnology* **2006**, *17*, 4675-4681.
(334) Shin, M. K.; Kim, S. I.; Kim, S. J.; Kim, S. K.; Lee, H. Reinforcement of polymeric nanofibers by ferritin nanoparticles. *Appl. Phys. Lett.* **2006**, *88*.
(335) Kim, M. S.; Shin, K. M.; Kim, S. I.; Spinks, G. M.; Kim, S. J. Controlled array of ferritin in tubular nanostructure. *Macromol. Rapid Commun.* **2008**, *29*, 552-556.
(336) Shin, M. K.; Kim, S. I.; Kim, S. J.; Park, S. Y.; Hyun, Y. H.; Lee, Y.; Lee, K. E.; Han, S.-S.; Jang, D.-P.; Kim, Y.-B.; Cho, Z.-H.; So, I.; Spinks, G. M. Controlled Magnetic Nanofiber Hydrogels by Clustering Ferritin. *Langmuir* **2008**, *24*, 12107-12111.
(337) De Volder, M. F. L.; Tawfick, S. H.; Baughman, R. H.; Hart, A. J. Carbon Nanotubes: Present and Future Commercial Applications. *Science* **2013**, *339*, 535-539.
(338) Coleman, J. N.; Khan, U.; Blau, W. J.; Gun'ko, Y. K. Small but strong: A review of the mechanical properties of carbon nanotube-polymer composites. *Carbon* **2006**, *44*, 1624-1652.
(339) Bhattacharyya, S.; Sinturel, C.; Salvetat, J. P.; Saboungi, M. L. Protein-functionalized carbon nanotube-polymer composites. *Appl. Phys. Lett.* **2005**, *86*.
(340) Holder, P. G.; Finley, D. T.; Stephanopoulos, N.; Walton, R.; Clark, D. S.; Francis, M. B. Dramatic Thermal Stability of Virus−Polymer Conjugates in Hydrophobic Solvents. *Langmuir* **2010**, *26*, 17383-17388.
(341) Wong, K. K. W.; Colfen, H.; Whilton, N. T.; Douglas, T.; Mann, S. Synthesis and characterization of hydrophobic ferritin proteins. *J. Inorg. Biochem.* **1999**, *76*, 187-195.
(342) Klibanov, A. M. Improving enzymes by using them in organic solvents. *Nature* **2001**, *409*, 241-246.
(343) Vogler, E. A. Protein adsorption in three dimensions. *Biomaterials* **2012**, *33*, 1201-1237.
(344) Sousa, A.; Sengonul, M.; Latour, R.; Kohn, J.; Libera, M. Selective protein adsorption on a phase-separated solvent-cast polymer blend. *Langmuir* **2006**, *22*, 6286-6292.
(345) Deshayes, S.; Kasko, A. M. Polymeric biomaterials with engineered degradation. *J. Polym. Sci. A* **2013**, *51*, 3531-3566.
(346) Stauch, O.; Uhlmann, T.; Frohlich, M.; Thomann, R.; El-Badry, M.; Kim, Y. K.; Schubert, R. Mimicking a cytoskeleton by coupling poly(N-isopropylacrylamide) to the inner leaflet of liposomal membranes: Effects of photopolymerization on vesicle shape and polymer architecture. *Biomacromolecules* **2002**, *3*, 324-332.
(347) Hohn, T. Role of RNA in the assembly process of bacteriophage fr. *J. Mol. Biol.* **1969**, *43*, 191-200.
(348) Bancroft, J. B.; Hiebert, E.; Bracker, C. E. The effects of various polyanions on shell formation of some spherical viruses. *Virology* **1969**, *39*, 924-930.
(349) Sikkema, F. D.; Comellas-Aragones, M.; Fokkink, R. G.; Verduin, B. J.; Cornelissen, J. J.; Nolte, R. J. Monodisperse polymer-virus hybrid nanoparticles. *Org. Biomol. Chem.* **2007**, *5*, 54-57.
(350) Cadena-Nava, R. D.; Hu, Y.; Garmann, R. F.; Ng, B.; Zelikin, A. N.; Knobler, C. M.; Gelbart, W. M. Exploiting fluorescent polymers to probe the self-assembly of virus-like particles. *J. Phys. Chem. B* **2011**, *115*, 2386-2391.
(351) Stockley, P. G.; Twarock, R.; Bakker, S. E.; Barker, A. M.; Borodavka, A.; Dykeman, E.; Ford, R. J.; Pearson, A. R.; Phillips, S. E.; Ranson, N. A.; Tuma, R. Packaging signals in

single-stranded RNA viruses: nature's alternative to a purely electrostatic assembly mechanism. *J. Biol. Phys.* **2013**, *39*, 277-287.

(352) Cadena-Nava, R. D.; Comas-Garcia, M.; Garmann, R. F.; Rao, A. L.; Knobler, C. M.; Gelbart, W. M. Self-assembly of viral capsid protein and RNA molecules of different sizes: requirement for a specific high protein/RNA mass ratio. *J. Virology* **2012**, *86*, 3318-3326.

(353) Garmann, R. F.; Sportsman, R.; Beren, C.; Manoharan, V. N.; Knobler, C. M.; Gelbart, W. M. A Simple RNA-DNA Scaffold Templates the Assembly of Monofunctional Virus-Like Particles. *J. Am. Chem. Soc.* **2015**, *137*, 7584-7587.

(354) Mukherjee, S.; Pfeifer, C. M.; Johnson, J. M.; Liu, J.; Zlotnick, A. Redirecting the coat protein of a spherical virus to assemble into tubular nanostructures. *J. Am. Chem. Soc.* **2006**, *128*, 2538-2539.

(355) Ng, B. C.; Chan, S. T.; Lin, J.; Tolbert, S. H. Using Polymer Conformation to Control Architecture in Semiconducting Polymer/Viral Capsid Assemblies. *ACS Nano* **2011**, *5*, 7730-7738.

(356) Smith, A. D.; Shen, C. K. F.; Roberts, S. T.; Helgeson, R.; Schwartz, B. J. Ionic strength and solvent control over the physical structure, electronic properties and superquenching of conjugated polyelectrolytes. *Res. Chem. Intermediat.* **2007**, *33*, 125-142.

(357) Setaro, F.; Ruiz-Gonzalez, R.; Nonell, S.; Hahn, U.; Torres, T. Synthesis, photophysical studies and O-1(2) generation of carboxylate-terminated zinc phthalocyanine dendrimers. *J. Inorg. Biochem.* **2014**, *136*, 170-176.

(358) Nguyen, T. Q.; Doan, V.; Schwartz, B. J. Conjugated polymer aggregates in solution: Control of interchain interactions. *J. Chem. Phys.* **1999**, *110*, 4068-4078.

(359) Kaneko, M.; Motoyoshi, J.; Yamada, A. Solid phase photoreduction of methylviologen adsorbed on cellulose. *Nature* **1980**, *285*, 468-470.

(360) Ebbesen, T. W.; Levey, G.; Patterson, L. K. Photoreduction of methyl viologen in aqueous neutral solution without additives. *Nature* **1982**, *298*, 545-548.

(361) Liepold, L. O.; Abedin, M. J.; Buckhouse, E. D.; Frank, J. A.; Young, M. J.; Douglas, T. Supramolecular Protein Cage Composite MR Contrast Agents with Extremely Efficient Relaxivity Properties. *Nano Lett.* **2009**, *9*, 4520-4526.

(362) Lucon, J.; Abedin, M. J.; Uchida, M.; Liepold, L.; Jolley, C. C.; Young, M.; Douglas, T. A click chemistry based coordination polymer inside small heat shock protein. *Chem. Commun.* **2010**, *46*, 264-266.

(363) Flenniken, M. L.; Willits, D. A.; Brumfield, S.; Young, M. J.; Douglas, T. The small heat shock protein cage from Methanococcus jannaschii is a versatile nanoscale platform for genetic and chemical modification. *Nano Lett.* **2003**, *3*, 1573-1576.

(364) Anderson, E. A.; Isaacman, S.; Peabody, D. S.; Wang, E. Y.; Canary, J. W.; Kirshenbaum, K. Viral nanoparticles donning a paramagnetic coat: conjugation of MRI contrast agents to the MS2 capsid. *Nano Lett.* **2006**, *6*, 1160-1164.

(365) Manna, K.; Zhang, T.; Greene, F. X.; Lin, W. Bipyridine- and Phenanthroline-Based Metal–Organic Frameworks for Highly Efficient and Tandem Catalytic Organic Transformations via Directed C–H Activation. *J. Am. Chem. Soc.* **2015**, *137*, 2665-2673.

(366) Horcajada, P.; Serre, C.; Maurin, G.; Ramsahye, N. A.; Balas, F.; Vallet-Regi, M.; Sebban, M.; Taulelle, F.; Ferey, G. Flexible porous metal-organic frameworks for a controlled drug delivery. *J. Am. Chem. Soc.* **2008**, *130*, 6774-6780.

(367) Sun, C. Y.; Qin, C.; Wang, X. L.; Su, Z. M. Metal-organic frameworks as potential drug delivery systems. *Expert Opin. Drug Deliv.* **2013**, *10*, 89-101.

(368) Werner, E. J.; Datta, A.; Jocher, C. J.; Raymond, K. N. High-Relaxivity MRI Contrast Agents: Where Coordination Chemistry Meets Medical Imaging. *Angew. Chem., Int. Edit.* **2008**, *47*, 8568-8580.

(369) Danhier, F.; Le Breton, A.; Preat, V. RGD-based strategies to target alpha(v) beta(3) integrin in cancer therapy and diagnosis. *Mol. Pharm.* **2012**, *9*, 2961-2973.

(370) Orakdogen, N. pH-responsive swelling behavior, elasticity and molecular characteristics of poly(N,N-dimethylaminoethyl methacrylate) gels at various initial monomer concentrations. *Polym. Bull.* **2011**, *67*, 1347-1366.

(371) Smith, S. B.; Cui, Y. J.; Bustamante, C. Overstretching B-DNA: The elastic response of individual double-stranded and single-stranded DNA molecules. *Science* **1996**, *271*, 795-799.

(372) Menjoge, A. R.; Kannan, R. M.; Tomalia, D. A. Dendrimer-based drug and imaging conjugates: design considerations for nanomedical applications. *Drug Discov. Today* **2010**, *15*, 171-185.

(373) Biswas, S.; Torchilin, V. P. Dendrimers for siRNA Delivery. *Pharmaceuticals* **2013**, *6*, 161-183.

(374) Perumal, O. P.; Inapagolla, R.; Kannan, S.; Kannan, R. M. The effect of surface functionality on cellular trafficking of dendrimers. *Biomaterials* **2008**, *29*, 3469-3476.
(375) Boas, U.; Heegaard, P. M. Dendrimers in drug research. *Chem. Soc. Rev.* **2004**, *33*, 43-63.
(376) Jensen, L. B.; Pavan, G. M.; Kasimova, M. R.; Rutherford, S.; Danani, A.; Nielsen, H. M.; Foged, C. Elucidating the molecular mechanism of PAMAM–siRNA dendriplex self-assembly: Effect of dendrimer charge density. *Int. J. Pharm.* **2011**, *416*, 410-418.
(377) Alexis, F.; Pridgen, E.; Molnar, L. K.; Farokhzad, O. C. Factors affecting the clearance and biodistribution of polymeric nanoparticles. *Mol. Pharm.* **2008**, *5*, 505-515.
(378) Choi, H. S.; Liu, W.; Misra, P.; Tanaka, E.; Zimmer, J. P.; Itty Ipe, B.; Bawendi, M. G.; Frangioni, J. V. Renal clearance of quantum dots. *Nat. Biotechnol.* **2007**, *25*, 1165-1170.
(379) Nussbaumer, M. The protein cage Thermosome as versatile delivery platform. PhD-Thesis, University of Basel, 2015.
(380) Kanasty, R.; Dorkin, J. R.; Vegas, A.; Anderson, D. Delivery materials for siRNA therapeutics. *Nat. Mater.* **2013**, *12*, 967-977.
(381) Cotanda, P.; Petzetakis, N.; O'Reilly, R. K. Catalytic polymeric nanoreactors: more than a solid supported catalyst. *MRS Commun.***2012**, *2*, 119-126.
(382) Bruns, N.; Tiller, J. C. Amphiphilic Network as Nanoreactor for Enzymes in Organic Solvents. *Nano Lett.* **2005**, *5*, 45-48.
(383) Tanner, P.; Balasubramanian, V.; Palivan, C. G. Aiding Nature's Organelles: Artificial Peroxisomes Play Their Role. *Nano Lett.* **2013**, *13*, 2875-2883.
(384) Pauly, A. C.; Theato, P. Control of reactivity of constitutional isomers of pentafluorophenyl ethynylbenzoates for the synthesis of functional poly(phenylacetylenes). *Polym. Chem.* **2012**, *3*, 1769-1782.
(385) Lam, J. W. Y.; Tang, B. Z. Functional Polyacetylenes. *Acc. Chem. Res.* **2005**, *38*, 745-754.
(386) Lam, J. W. Y.; Dong, Y.; Kwok, H. S.; Tang, B. Z. Light-Emitting Polyacetylenes: Synthesis and Electrooptical Properties of Poly(1-phenyl-1-alkyne)s Bearing Naphthyl Pendants. *Macromolecules* **2006**, *39*, 6997-7003.
(387) Yashima, E.; Maeda, K.; Furusho, Y. Single- and Double-Stranded Helical Polymers: Synthesis, Structures, and Functions. *Acc. Chem. Res.* **2008**, *41*, 1166-1180.
(388) Braunecker, W. A.; Matyjaszewski, K. Controlled/living radical polymerization: Features, developments, and perspectives. *Prog. Polym. Sci.* **2007**, *32*, 93-146.
(389) Zetterlund, P. B. Controlled/living radical polymerization in nanoreactors: compartmentalization effects. *Polym. Chem.* **2011**, *2*, 534-549.
(390) La Scola, B.; Audic, S.; Robert, C.; Jungang, L.; de Lamballerie, X.; Drancourt, M.; Birtles, R.; Claverie, J. M.; Raoult, D. A giant virus in amoebae. *Science* **2003**, *299*, 2033-2033.
(391) Aherfi, S.; La Scola, B.; Pagnier, I.; Raoult, D.; Colson, P. The expanding family Marseilleviridae. *Virology* **2014**, *466*, 27-37.
(392) Boyer, M.; Yutin, N.; Pagnier, I.; Barrassi, L.; Fournous, G.; Espinosa, L.; Robert, C.; Azza, S.; Sun, S. Y.; Rossmann, M. G.; Suzan-Monti, M.; La Scola, B.; Koonin, E. V.; Raoult, D. Giant Marseillevirus highlights the role of amoebae as a melting pot in emergence of chimeric microorganisms. *Proc. Natl. Acad. Sci. U.S.A.* **2009**, *106*, 21848-21853.
(393) Xiao, C. A.; Chipman, P. R.; Battisti, A. J.; Bowman, V. D.; Renesto, P.; Raoult, D.; Rossmann, M. G. Cryo-electron microscopy of the giant mimivirus. *J. Mol. Biol.* **2005**, *353*, 493-496.
(394) Van Etten, J. L.; Lane, L. C.; Dunigan, D. D. DNA Viruses: The Really Big Ones (Giruses). *Annu. Rev. Microbiol.* **2010**, *64*, 83-99.
(395) Klose, T.; Rossmann, M. G. Structure of large dsDNA viruses. *Biol. Chem.* **2014**, *395*, 711-719.
(396) Glover, D. J.; Giger, L.; Kim, J. R.; Clark, D. S. Engineering protein filaments with enhanced thermostability for nanomaterials. *Biotechnol. J.* **2013**, *8*, 228-236.
(397) Dordick, J. S. Functional nanoscale biomolecular materials. *Biotechnol. J.* **2013**, *8*, 165-166.
(398) Regan, L.; Caballero, D.; Hinrichsen, M. R.; Virrueta, A.; Williams, D. M.; O'Hern, C. S. Protein design: Past, present, and future. *Peptide Sci.* **2015**, *104*, 334-350.
(399) Fletcher, J. M.; Harniman, R. L.; Barnes, F. R. H.; Boyle, A. L.; Collins, A.; Mantell, J.; Sharp, T. H.; Antognozzi, M.; Booth, P. J.; Linden, N.; Miles, M. J.; Sessions, R. B.; Verkade, P.; Woolfson, D. N. Self-Assembling Cages from Coiled-Coil Peptide Modules. *Science* **2013**, *340*, 595-599.
(400) Altintas, O.; Barner-Kowollik, C. Single Chain Folding of Synthetic Polymers by Covalent and Non-Covalent Interactions: Current Status and Future Perspectives. *Macromol Rapid Commun.* **2012**, *33*, 958-971.
(401) Stuart, M. A. C.; Huck, W. T. S.; Genzer, J.; Muller, M.; Ober, C.; Stamm, M.; Sukhorukov, G. B.; Szleifer, I.; Tsukruk, V. V.; Urban, M.; Winnik, F.; Zauscher, S.; Luzinov, I.; Minko,

S. Emerging applications of stimuli-responsive polymer materials. *Nat. Mater.* **2010**, *9*, 101-113.
(402) Cabane, E.; Zhang, X.; Langowska, K.; Palivan, C.; Meier, W. Stimuli-Responsive Polymers and Their Applications in Nanomedicine. *Biointerphases* **2012**, *7*, 1-27.
(403) Schattling, P.; Jochum, F. D.; Theato, P. Multi-stimuli responsive polymers - the all-in-one talents. *Polym. Chem.* **2014**, *5*, 25-36.
(404) Urlacher, V. B.; Lutz-Wahl, S.; Schmid, R. D. Microbial P450 enzymes in biotechnology. *Appl. Microbiol. Biotechnol.* **2004**, *64*, 317-325.
(405) Cech, T. R. The Chemistry of Self-Splicing Rna and Rna Enzymes. *Science* **1987**, *236*, 1532-1539.
(406) Neurath, H. Evolution of proteolytic enzymes. *Science* **1984**, *224*, 350-357.
(407) Koebnik, R.; Locher, K. P.; Van Gelder, P. Structure and function of bacterial outer membrane proteins: barrels in a nutshell. *Mol. Microbiol.* **2000**, *37*, 239-253.
(408) von Heijne, G. Membrane-protein topology. *Nat. Rev. Mol. Cell Biol.* **2006**, *7*, 909-918.
(409) Woof, J. M.; Burton, D. R. Human antibody - Fc receptor interactions illuminated by crystal structures. *Nat. Rev. Immunol.* **2004**, *4*, 89-99.
(410) Chen, K.; Xu, W.; Wilson, M.; He, B.; Miller, N. W.; Bengten, E.; Edholm, E. S.; Santini, P. A.; Rath, P.; Chiu, A.; Cattalini, M.; Litzman, J.; J, B. B.; Huang, B.; Meini, A.; Riesbeck, K.; Cunningham-Rundles, C.; Plebani, A.; Cerutti, A. Immunoglobulin D enhances immune surveillance by activating antimicrobial, proinflammatory and B cell-stimulating programs in basophils. *Nat. Immunol.* **2009**, *10*, 889-898.
(411) Flenniken, M. L.; Uchida, M.; Liepold, L. O.; Kang, S.; Young, M. J.; Douglas, T. A Library of Protein Cage Architectures as Nanomaterials. *Curr. Top. Microbiol.* **2009**, *327*, 71-93.
(412) Ellis, R. J. Molecular chaperones: assisting assembly in addition to folding. *Trends Biochem. Sci.* **2006**, *31*, 395-401.
(413) Hartl, F. U.; Bracher, A.; Hayer-Hartl, M. Molecular chaperones in protein folding and proteostasis. *Nature* **2011**, *475*, 324-332.
(414) Arosio, P.; Levi, S. Ferritin, iron homeostasis, and oxidative damage. *Free Radical Bio. Med.* **2002**, *33*, 457-463.
(415) Frydman, J. Folding of newly translated proteins in vivo: The role of molecular chaperones. *Annu. Rev. Biochem.* **2001**, *70*, 603-647.
(416) Theil, E. C.; Behera, R. K.; Tosha, T. Ferritins for chemistry and for life. *Coord. Chem. Rev.* **2013**, *257*, 579-586.
(417) Yamashita, I.; Iwahori, K.; Zheng, B.; Kumagai, S. Nanoparticles Synthesized and Delivered by Protein in the Field of Nanotechnology Applications. *Coord. Chem. Protein Cages: Principles, Design, and Applications (eds. T. Ueno and Y. Watanabe)* **2013**, 305-328.
(418) Kang, S.; Lander, G. C.; Johnson, J. E.; Prevelige, P. E. Development of Bacteriophage P22 as a Platform for Molecular Display: Genetic and Chemical Modifications of the Procapsid Exterior Surface. *ChemBioChem* **2008**, *9*, 514-518.
(419) Saibil, H. Chaperone machines for protein folding, unfolding and disaggregation. *Nat. Rev. Mol. Cell Bio.* **2013**, *14*, 630-642.
(420) Cornelissen, J. J. Chemical virology: Packing polymers in protein cages. *Nat. Chem.* **2012**, *4*, 775-777.
(421) Rother, M.; Nussbaumer, M. G.; Renggli, K.; Bruns, N. Protein cages and synthetic polymers: A fruitful symbiosis for bionanotechnology. to be submitted to *Chem. Soc. Rev.* **2016**.
(422) Klok, H.-A. Peptide/Protein−Synthetic Polymer Conjugates: Quo Vadis. *Macromolecules* **2009**, *42*, 7990-8000.
(423) Averick, S. E.; Bazewicz, C. G.; Woodman, B. F.; Simakova, A.; Mehl, R. A.; Matyjaszewski, K. Protein–polymer hybrids: Conducting ARGET ATRP from a genetically encoded cleavable ATRP initiator. *Europ. Polym. J.* **2013**, *49*, 2919-2924.
(424) Erickson, H. P. Size and Shape of Protein Molecules at the Nanometer Level Determined by Sedimentation, Gel Filtration, and Electron Microscopy. *Biol. Proced. Online* **2009**, *11*, 32-51.
(425) Hansen, K. M.; Ji, H. F.; Wu, G. H.; Datar, R.; Cote, R.; Majumdar, A.; Thundat, T. Cantilever-based optical deflection assay for discrimination of DNA single-nucleotide mismatches. *Anal. Chem.* **2001**, *73*, 1567-1571.
(426) Baumann, C. G.; Smith, S. B.; Bloomfield, V. A.; Bustamante, C. Ionic effects on the elasticity of single DNA molecules. *Proc. Natl. Acad. Sci. U.S.A.* **1997**, *94*, 6185-6190.
(427) Sinden, R. R.; Pearson, C. E.; Potaman, V. N.; Ussery, D. W.: DNA: Structure and function. *Adv. Gen. Biol.*; Ram, S. V., Ed.; JAI, **1998**; Vol. Volume 5; pp 1-141.

(428) Ditzel, L.; Lowe, J.; Stock, D.; Stetter, K. O.; Huber, H.; Huber, R.; Steinbacher, S. Crystal structure of the thermosome, the archaeal chaperonin and homolog of CCT. *Cell* **1998**, *93*, 125-138.
(429) Zhang, J. J.; Baker, M. L.; Schroder, G. F.; Douglas, N. R.; Reissmann, S.; Jakana, J.; Dougherty, M.; Fu, C. J.; Levitt, M.; Ludtke, S. J.; Frydman, J.; Chiu, W. Mechanism of folding chamber closure in a group II chaperonin. *Nature* **2010**, *463*, 379-U130.
(430) Kesharwani, P.; Banerjee, S.; Gupta, U.; Mohd Amin, M. C. I.; Padhye, S.; Sarkar, F. H.; Iyer, A. K. PAMAM dendrimers as promising nanocarriers for RNAi therapeutics. *Mater. Today*.**2015,** *18*, 565-572
(431) Whitehead, K. A.; Langer, R.; Anderson, D. G. Knocking down barriers: advances in siRNA delivery. *Nat. Rev. Drug Discov.* **2009**, *8*, 129-138.
(432) Joshi, B. H.; Pachchigar, K. P. siRNA: novel therapeutics from functional genomics. *Biotechnol. Genet. Eng.* **2014**, *30*, 1-30.
(433) Zhou, Y. J.; Zhang, C. L.; Liang, W. Development of RNAi technology for targeted therapy - A track of siRNA based agents to RNAi therapeutics. *J. Controlled Release* **2014**, *193*, 270-281.
(434) Le Droumaguet, B.; Velonia, K. In situ ATRP-Mediated hierarchical formation of giant amphiphile bionanoreactors. *Angew. Chem., Int. Edit.* **2008**, *47*, 6263-6266.
(435) Agarwal, S.; Zhang, Y.; Maji, S.; Greiner, A. PDMAEMA based gene delivery materials. *Mater. Today* **2012**, *15*, 388-393.
(436) Coue, G.; Engbersen, J. F. J. Functionalized linear poly(amidoamine)s are efficient vectors for intracellular protein delivery. *J. Controlled Release* **2011**, *152*, 90-98.
(437) Llopis, J.; McCaffery, J. M.; Miyawaki, A.; Farquhar, M. G.; Tsien, R. Y. Measurement of cytosolic, mitochondrial, and Golgi pH in single living cells with green fluorescent proteins. *Proc. Natl. Acad. of Sci. U.S.A.* **1998**, *95*, 6803-6808.
(438) Evdokimov, A. G.; Pokross, M. E.; Egorov, N. S.; Zaraisky, A. G.; Yampolsky, I. V.; Merzlyak, E. M.; Shkoporov, A. N.; Sander, I.; Lukyanov, K. A.; Chudakov, D. M. Structural basis for the fast maturation of Arthropoda green fluorescent protein. *EMBO Rep.* **2006**, *7*, 1006-1012.
(439) Tang, R.; Kim, C. S.; Solfiell, D. J.; Rana, S.; Mout, R.; Velazquez-Delgado, E. M.; Chompoosor, A.; Jeong, Y.; Yan, B.; Zhu, Z. J.; Kim, C.; Hardy, J. A.; Rotello, V. M. Direct Delivery of Functional Proteins and Enzymes to the Cytosol Using Nanoparticle-Stabilized Nanocapsules. *ACS Nano* **2013**, *7*, 6667-6673.
(440) Fu, A. L.; Tang, R.; Hardie, J.; Farkas, M. E.; Rotello, V. M. Promises and Pitfalls of Intracellular Delivery of Proteins. *Bioconjug. Chem.* **2014**, *25*, 1602-1608.
(441) Min, K.; Gao, H. F.; Matyjaszewski, K. Use of ascorbic acid as reducing agent for synthesis of well-defined polymers by ARGET ATRP. *Macromolecules* **2007**, *40*, 1789-1791.
(442) Hellman, L. M.; Fried, M. G. Electrophoretic mobility shift assay (EMSA) for detecting protein-nucleic acid interactions. *Nat. Protoc.* **2007**, *2*, 1849-1861.
(443) Verbaan, F. J.; Oussoren, C.; van Dam, I. M.; Takakura, Y.; Hashida, M.; Crommelin, D. J. A.; Hennink, W. E.; Storm, G. The fate of poly(2-dimethyl amino ethyl)methacrylate-based polyplexes after intravenous administration. *Int. J. Pharm.* **2001**, *214*, 99-101.
(444) Rodriguez-Lorenzo, L.; Rothen-Rutishauser, B.; Petri-Fink, A.; Balog, S. Nanoparticle Polydispersity Can Strongly Affect In Vitro Dose. *Part. Part. Syst. Char.* **2015**, *32*, 321-333.
(445) Akhtar, S.; Benter, I. F. Nonviral delivery of synthetic siRNAs in vivo. *J. Clin. Invest.* **2007**, *117*, 3623-3632.
(446) Urban-Klein, B.; Werth, S.; Abuharbeid, S.; Czubayko, F.; Aigner, A. RNAi-mediated gene-targeting through systemic application of polyethylenimine (PEI)-complexed siRNA in vivo. *Gene Ther.* **2004**, *12*, 461-466.
(447) Zhou, J. H.; Wu, J. Y.; Hafdi, N.; Behr, J. P.; Erbacher, P.; Peng, L. PAMAM dendrimers for efficient siRNA delivery and potent gene silencing. *Chem. Commun.* **2006**, 2362-2364.
(448) Kong, W. H.; Sung, D. K.; Shim, Y. H.; Bae, K. H.; Dubois, P.; Park, T. G.; Kim, J. H.; Seo, S. W. Efficient intracellular siRNA delivery strategy through rapid and simple two steps mixing involving noncovalent post-PEGylation. *J. Controlled Release* **2009**, *138*, 141-147.
(449) Rawlinson, L. A. B.; O'Brien, P. J.; Brayden, D. J. High content analysis of cytotoxic effects of pDMAEMA on human intestinal epithelial and monocyte cultures. *J. Controlled Release* **2010**, *146*, 84-92.
(450) Raucher, D.; Ryu, J. S. Cell-penetrating peptides: strategies for anticancer treatment. *Trends Mol. Med.* **2015**, *21*, 560-570.
(451) Koren, E.; Torchilin, V. P. Cell-penetrating peptides: breaking through to the other side. *Trends Mol. Med.* **2012**, *18*, 385-393.

(452) Ayame, H.; Morimoto, N.; Akiyoshi, K. Self-assembled cationic nanogels for intracellular protein delivery. *Bioconjug. Chem.* **2008**, *19*, 882-890.
(453) Lee, A. L. Z.; Wang, Y.; Ye, W. H.; Yoon, H. S.; Chan, S. Y.; Yang, Y. Y. Efficient intracellular delivery of functional proteins using cationic polymer core/shell nanoparticles. *Biomaterials* **2008**, *29*, 1224-1232.
(454) Lu, Y.; Sun, W. J.; Gu, Z. Stimuli-responsive nanomaterials for therapeutic protein delivery. *J. Controlled Release* **2014**, *194*, 1-19.
(455) Sun, W. J.; Lu, Y.; Gu, Z. Advances in Anticancer Protein Delivery using Micro-/Nanoparticles. *Part. Part. Syst. Char.* **2014**, *31*, 1204-1222.
(456) Hazarika, P.; Kukolka, F.; Niemeyer, C. M. Reversible binding of fluorescent proteins at DNA-gold nanoparticles. *Angew. Chem., Int. Edit.* **2006**, *45*, 6827-6830.
(457) Shannon, L. M.; Kay, E.; Lew, J. Y. Peroxidase isozymes from horseradish roots. I. Isolation and physical properties. *J. Biol. Chem.* **1966**, *241*, 2166-2172.
(458) Dice, J. F.; Goldberg, A. L. Relationship between in vivo degradative rates and isoelectric points of proteins. *Proc. Natl Acad. Sci. U.S.A.* **1975**, *72*, 3893-3897.
(459) Reynolds, A.; Leake, D.; Boese, Q.; Scaringe, S.; Marshall, W. S.; Khvorova, A. Rational siRNA design for RNA interference. *Nat. Biotechnol.* **2004**, *22*, 326-330.
(460) Devi, G. R. siRNA-based approaches in cancer therapy. *Cancer Gene. Ther.* **2006**, *13*, 819-829.
(461) Boudreau, R. L.; Spengler, R. M.; Davidson, B. L. Rational design of therapeutic siRNAs: minimizing off-targeting potential to improve the safety of RNAi therapy for Huntington's disease. *Mol. Ther.* **2011**, *19*, 2169-2177.
(462) Wittrup, A.; Lieberman, J. Knocking down disease: a progress report on siRNA therapeutics. *Nat. Rev. Genet.* **2015**, *16*, 543-552.
(463) Wu, S. Y.; Lopez-Berestein, G.; Calin, G. A.; Sood, A. K. RNAi therapies: drugging the undruggable. *Sci. Transl. Med.* **2014**, *6*, 240-247.
(464) Mansoori, B.; Sandoghchian Shotorbani, S.; Baradaran, B. RNA interference and its role in cancer therapy. *Adv. Pharm. Bull.* **2014**, *4*, 313-321.
(465) Joo, M. K.; Yhee, J. Y.; Kim, S. H.; Kim, K. The potential and advances in RNAi therapy: Chemical and structural modifications of siRNA molecules and use of biocompatible nanocarriers. *J. Controlled Release* **2014**, *193*, 113-121.
(466) Tristan, C.; Shahani, N.; Sedlak, T. W.; Sawa, A. The diverse functions of GAPDH: views from different subcellular compartments. *Cell Signal.* **2011**, *23*, 317-323.
(467) Gutwein, P.; Schramme, A.; Abdel-Bakky, M. S.; Doberstein, K.; Hauser, I. A.; Ludwig, A.; Altevogt, P.; Gauer, S.; Hillmann, A.; Weide, T.; Jespersen, C.; Eberhardt, W.; Pfeilschifter, J. ADAM10 is expressed in human podocytes and found in urinary vesicles of patients with glomerular kidney diseases. *J. Biomed. Sci.* **2010**, *17*.
(468) Makyla, K.; Muller, C.; Lorcher, S.; Winkler, T.; Nussbaumer, M. G.; Eder, M.; Bruns, N. Fluorescent Protein Senses and Reports Mechanical Damage in Glass-Fiber-Reinforced Polymer Composites. *Adv. Mater.* **2013**, *25*, 2701-2706.
(469) Douglas, N. R.; Reissmann, S.; Zhang, J. J.; Chen, B.; Jakana, J.; Kumar, R.; Chiu, W.; Frydman, J. Dual Action of ATP Hydrolysis Couples Lid Closure to Substrate Release into the Group II Chaperonin Chamber. *Cell* **2011**, *144*, 240-252.
(470) Laemmli, U. K. Cleavage of Structural Proteins during the Assembly of the Head of Bacteriophage T4. *Nature* **1970**, *227*, 680-685.
(471) Nesterenko, M. V.; Tilley, M.; Upton, S. J. A Simple Modification of Blums Silver Stain Method Allows for 30 Minute Detection of Proteins in Polyacrylamide Gels. *J. Biochem. Bioph. Meth.* **1994**, *28*, 239-242.
(472) Fried, M. G. Measurement of Protein-DNA Interaction Parameters by Electrophoresis Mobility Shift Assay. *Electrophoresis* **1989**, *10*, 366-376.
(473) Liang, W.; Mason, A. J.; Lam, J. W.: Western Blot Evaluation of siRNA Delivery by pH-Responsive Peptides. In *Target Identification and Validation in Drug Discovery*; Moll, J., Colombo, R., Eds.; Methods in Molecular Biology; Humana Press, 2013; Vol. 986; pp 73-87.
(474) Rother, M.; Barmettler, J.; Reichmuth, A.; Araujo, J. V.; Rytka, C.; Glaied, O.; Pieles, U.; Bruns, N. Self-Sealing and Puncture Resistant Breathable Membranes for Water-Evaporation Applications. *Adv. Mater.* **2015**, *27*, 6620-6624.
(475) Mukhopadhyay, A.; Vinay Kumar, M. A Review on Designing the Waterproof Breathable Fabrics Part I: Fundamental Principles and Designing Aspects of Breathable Fabrics. *J. Ind. Text.* **2008**, *37*, 225-262.
(476) Gugliuzza, A.; Drioli, E. A review on membrane engineering for innovation in wearable fabrics and protective textiles. *J. Membr. Sci.* **2013**, *446*, 350-375.

(477) Meyer-Heim, A.; Rothmaier, M.; Weder, M.; Kool, J.; Schenk, P.; Kesselring, J. Advanced lightweight cooling-garment technology: functional improvements in thermosensitive patients with multiple sclerosis. *Mult. Scler.* **2007**, *13*, 232-237.
(478) Rothmaier, M.; Weder, M.; Meyer-Heim, A.; Kesselring, J. Design and performance of personal cooling garments based on three-layer laminates. *Med. Biol. Eng. Comp.* **2008**, *46*, 825-832.
(479) Davis, S. L.; Wilson, T. E.; White, A. T.; Frohman, E. M. Thermoregulation in multiple sclerosis. *J. Appl. Physiol.* **2010**, *109*, 1531-1537.
(480) Personal cooling system by Unico swiss tex GmbH (in German), http://www.unico-swiss tex.ch/personalcoolingsystem/medizin/index.html. (accessed June 2015).
(481) Hoffmann, E.; Pfenning, D. M.; Philippsen, E.; Schwahn, P.; Sieber, M.; Wehn, R.; Woermann, D. Evaporation of Alcohol-Water Mixtures through Hydrophobic Porous Membranes. *J. Membr. Sci.***1987**, *34*, 199-206.
(482) Tu, C.-Y.; Liu, Y.-L.; Lee, K.-R.; Lai, J.-Y. Hydrophilic surface-grafted poly(tetrafluoroethylene) membranes using in pervaporation dehydration processes. *J. Membr. Sci.* **2006**, *274*, 47-55.
(483) Curcio, E.; Drioli, E. Membrane distillation and related operations - A review. *Sep. Purif. Rev.* **2005**, *34*, 35-86.
(484) Huizing, R.; Merida, W.; Ko, F. Impregnated electrospun nanofibrous membranes for water vapour transport applications. *J. Membr. Sci.* **2014**, *461*, 146-160.
(485) Dobrusskin, S.; Singer, H.; Banik, G. Humidification with moisture permeable materials. *7. Internationaler Graphischer Restauratorentag, 26.-30. August 1991, Uppsala : IADA Preprints* **1991**, 68-70.
(486) Weder, M.; Hegemann, D.; Amberg, M.; Hess, M.; Boesel, L.; Abächerli, R.; Meyer, V.; Rossi, R. Embroidered Electrode with Silver/Titanium Coating for Long-Term ECG Monitoring. *Sensors-Basel* **2015**, *15*, 1750-1759.
(487) Amberg, M.; Rupper, P.; Storchenegger, R.; Weder, M.; Hegemann, D. Controlling the release from silver electrodes by titanium adlayers for health monitoring. *Nanomedicine: Nanotechnology, Biology and Medicine* **2015**.
(488) Blaiszik, B. J.; Kramer, S. L. B.; Olugebefola, S. C.; Moore, J. S.; Sottos, N. R.; White, S. R. Self-Healing Polymers and Composites. *Annu. Rev. Mater. Res.* **2010**, *40*, 179-211.
(489) Ponto, J. A. Self-sealing capacity of vial stoppers after multiple needle punctures. *J. Am. Pharm. Ass.* **2013**, *53*, 58-60.
(490) Simpson, R. S.; Wright, M. L.; Croft, W. J. Flashing and waterproofing membrane US20110091675A1.
(491) Shepherd, R. F.; Stokes, A. A.; Nunes, R. M. D.; Whitesides, G. M. Soft Machines That are Resistant to Puncture and That Self Seal. *Adv. Mater.* **2013**, *25*, 6709-6713.
(492) Spenadel, L.; Good, R. Synthetic Rubber for Self-Sealing Fuel Tanks. *Industr. Eng. Chem.* **1959**, *51*, 935-936.
(493) Nagaya, K.; Ikai, S.; Chiba, M.; Chao, X. Tire with Self-Repairing Mechanism. *JSME* **2006**, *49*, 379-384.
(494) Busch, S.; Seidel, R.; Speck, O.; Speck, T. Morphological aspects of self-repair of lesions caused by internal growth stresses in stems of Aristolochia macrophylla and Aristolochia ringens. *Proc. R. Soc. B* **2010**, *277*, 2113-2120.
(495) Rampf, M.; Speck, O.; Speck, T.; Luchsinger, R. H. Self-Repairing Membranes for Inflatable Structures Inspired by a Rapid Wound Sealing Process of Climbing Plants. *J. Bionic Eng.* **2011**, *8*, 242-250.
(496) Vrouenraets, C. M. F.; Sikkema, D. J. Flexible layered product EP111360A1.
(497) Erdodi, G.; Kennedy, J. P. Amphiphilic conetworks: Definition, synthesis, applications. *Prog. Polym. Sci.* **2006**, *31*, 1-18.
(498) Patrickios, C. S.; Georgiou, T. K. Covalent amphiphilic polymer networks. *Current Op. Coll. Interf. Sci.* **2003**, *8*, 76-85.
(499) Mespouille, L.; Hedrick, J. L.; Dubois, P. Expanding the role of chemistry to produce new amphiphilic polymer (co)networks. *Soft Matter* **2009**, *5*, 4878-4892.
(500) Béla, I.; Joseph, P. K.; Paul, W. M.: Amphiphilic Networks. In *Polymeric Drugs and Drug Delivery Systems*; ACS Symposium Series 469; American Chemical Society, 1991; Vol. 469; pp 194-202.
(501) Lequieu, W.; Du Prez, F. E. Segmented polymer networks based on poly(N-isopropyl acrylamide) and poly(tetrahydrofuran) as polymer membranes with thermo-responsive permeability. *Polymer* **2004**, *45*, 749-757.

(502) Hu, Z. K.; Chen, L.; Betts, D. E.; Pandya, A.; Hillmyer, M. A.; DeSimone, J. M. Optically Transparent, Amphiphilic Networks Based on Blends of Perfluoropolyethers and Poly(ethylene glycol). *J. Am. Chem. Soc.* **2008**, *130*, 14244-14252.
(503) Lin, C. P.; Gitsov, I. Preparation and Characterization of Novel Amphiphilic Hydrogels with Covalently Attached Drugs and Fluorescent Markers. *Macromolecules* **2010**, *43*, 10017-10030.
(504) Fodor, C.; Kali, G.; Ivan, B. Poly(N-vinylimidazole)-l-Poly(tetrahydrofuran) Amphiphilic Conetworks and Gels: Synthesis, Characterization, Thermal and Swelling Behavior. *Macromolecules* **2011**, *44*, 4496-4502.
(505) Rikkou-Kalourkoti, M.; Patrickios, C. S. Synthesis and Characterization of End-Linked Amphiphilic Copolymer Conetworks Based on a Novel Bifunctional Cleavable Chain Transfer Agent. *Macromolecules* **2012**, *45*, 7890-7899.
(506) Kali, G.; Vavra, S.; László, K.; Iván, B. Thermally Responsive Amphiphilic Conetworks and Gels Based on Poly(N-isopropylacrylamide) and Polyisobutylene. *Macromolecules* **2013**, *46*, 5337-5344.
(507) Xu, J.; Qiu, M.; Ma, B.; He, C. "Near Perfect" Amphiphilic Conetwork Based on End-Group Cross-Linking of Polydimethylsiloxane Triblock Copolymer via Atom Transfer Radical Polymerization. *ACS Appl. Mater. Interf.* **2014**, *6*, 15283-15290.
(508) Walker, C. N.; Bryson, K. C.; Hayward, R. C.; Tew, G. N. Wide Bicontinuous Compositional Windows from Co-Networks Made with Telechelic Macromonomers. *ACS Nano* **2014**, *8*, 12376-12385.
(509) Liu, D. E.; Dursch, T. J.; Oh, Y.; Bregante, D. T.; Chan, S. Y.; Radke, C. J. Equilibrium water and solute uptake in silicone hydrogels. *Acta biomater.* **2015**, *18*, 112-117.
(510) Qiu, M.; Zhao, X.-Z.; Liu, D.-P.; He, C.-J. pH sensitive amphiphilic conetworks based on end-group cross-linking of polydimethylsiloxane pentablock copolymer and polymethylhydrosiloxane. *RSC Advances* **2015**, *5*, 17851-17861.
(511) Kang, J.; Erdodi, G.; Kennedy, J. P. Third-generation amphiphilic conetworks. III. Permeabilities and mechanical properties. *J. Polym. Sci. A* **2007**, *45*, 4276-4283.
(512) Cui, J.; Lackey, M. A.; Madkour, A. E.; Saffer, E. M.; Griffin, D. M.; Bhatia, S. R.; Crosby, A. J.; Tew, G. N. Synthetically Simple, Highly Resilient Hydrogels. *Biomacromolecules* **2012**, *13*, 584-588.
(513) Xu, J.; Bohnsack, D. A.; Mackay, M. E.; Wooley, K. L. Unusual Mechanical Performance of Amphiphilic Crosslinked Polymer Networks. *J. Am. Chem. Soc.* **2007**, *129*, 506-507.
(514) Du Prez, F. E.; Goethals, E. J.; Schue, R.; Qariouh, H.; Schue, F. Segmented network structures for the separation of water/ethanol mixtures by pervaporation. *Polymer Int.* **1998**, *46*, 117-125.
(515) Li, X.; Basko, M.; Du Prez, F.; Vankelecom, I. F. J. Multifunctional Membranes for Solvent Resistant Nanofiltration and Pervaporation Applications Based on Segmented Polymer Networks. *J. Phys. Chem. B* **2008**, *112*, 16539-16545.
(516) Zhang, H.; Zhang, Y.; Li, L.; Zhao, S.; Ni, H.; Cao, S.; Wang, J. Cross-linked polyacrylonitrile/polyethyleneimine–polydimethylsiloxane composite membrane for solvent resistant nanofiltration. *Chem. Eng. Sci.* **2014**, *106*, 157-166.
(517) Tobis, J.; Boch, L.; Thomann, Y.; Tiller, J. C. Amphiphilic polymer conetworks as chiral separation membranes. *J. Membr. Sci.* **2011**, *372*, 219-227.
(518) Guiseppi-Elie, A.; Brahim, S. I.; Narinesingh, D. A chemically synthesized artificial pancreas: Release of insulin from glucose-responsive hydrogels. *Adv. Mater.* **2002**, *14*, 743-746.
(519) Schöller, K.; Küpfer, S.; Baumann, L.; Hoyer, P. M.; de Courten, D.; Rossi, R. M.; Vetushka, A.; Wolf, M.; Bruns, N.; Scherer, L. J. From Membrane to Skin: Aqueous Permeation Control Through Light-Responsive Amphiphilic Polymer Co-Networks. *Adv. Funct. Mater.* **2014**, *24*, 5194-5201.
(520) Scherble, J.; Ivan, B.; Mulhaupt, R. Online monitoring of silicone network formation by means of in-situ mid-infrared spectroscopy. *Macromol. Chem. Phys.* **2002**, *203*, 1866-1871.
(521) Bruns, N.; Scherble, J.; Hartmann, L.; Thomann, R.; Ivan, B.; Mulhaupt, R.; Tiller, J. C. Nanophase separated amphiphilic conetwork coatings and membranes. *Macromolecules* **2005**, *38*, 2431-2438.
(522) Dech, S.; Cramer, T.; Ladisch, R.; Bruns, N.; Tiller, J. C. Solid-solid interface adsorption of proteins and enzymes in nanophase-separated amphiphilic conetworks. *Biomacromolecules* **2011**, *12*, 1594-1601.
(523) Mauritz, K. A. Organic-inorganic hybrid materials: perfluorinated ionomers as sol-gel polymerization templates for inorganic alkoxides. *Mater. Sci. Eng. C* **1998**, *6*, 121-133.

(524) Mauritz, K. A.; Storey, R. F.; Jones, C. K.: Perfluorinated-Ionomer-Membrane-Based Microcomposites. In *ACS Symp. Ser. Vol. 395, Multiphase Polymers: Blends and Ionomers*; ACS Symposium Series 395; American Chemical Society, 1989; pp 401-417.
(525) Bruns, N. Design von amphiphilen Conetzwerken zur Generierung von nanoskaligen Reaktionsräumen für Biotransformationen in nichtwässrigen Medien. University of Freiburg, 2007.
(526) Performance of Sympatex Membrane, http://sympatex.com/en/membrane/213/performance. (accessed June 2015).
(527) Ramanathan, N. L. A new weighting system for mean surface temperature of the human body. *J. Appl. Physiol.* **1964**, *19*, 531-533.
(528) Farris, S.; Pozzoli, S.; Biagioni, P.; Duo, L.; Mancinelli, S.; Piergiovanni, L. The fundamentals of flame treatment for the surface activation of polyolefin polymers - A review. *Polymer* **2010**, *51*, 3591-3605.
(529) Wang, Y. X.; Jacob, J.; Wingfield, P. T.; Palmer, I.; Stahl, S. J.; Kaufman, J. D.; Huang, P. L.; Huang, P. L.; Lee-Huang, S.; Torchia, D. A. Anti-HIV and anti-tumor protein MAP30, a 30 kDa single-strand type-I RIP, shares similar secondary structure and beta-sheet topology with the A chain of ricin, a type-II RIP. *Protein Sci.* **2000**, *9*, 138-144.
(530) Meng, Y.; Lin, S.; Liu, S. F.; Fan, X.; Li, G. R.; Meng, Y. F. A Novel Method for Simultaneous Production of Two Ribosome-Inactivating Proteins, alpha-MMC and MAP30, from Momordica charantia L. *PloS one* **2014**, *9*.
(531) Wang, Y. X.; Neamati, N.; Jacob, J.; Palmer, I.; Stahl, S. J.; Kaufman, J. D.; Huang, P. L.; Huang, P. L.; Winslow, H. E.; Pommier, Y.; Wingfield, P. T.; Lee-Huang, S.; Bax, A.; Torchia, D. A. Solution structure of anti-HIV-1 and anti-tumor protein MAP30: structural insights into its multiple functions. *Cell* **1999**, *99*, 433-442.
(532) Toohey, K. S.; Sottos, N. R.; Lewis, J. A.; Moore, J. S.; White, S. R. Self-healing materials with microvascular networks. *Nat. Mater.* **2007**, *6*, 581-585.
(533) He, L.; Fullenkamp, D. E.; Rivera, J. G.; Messersmith, P. B. pH responsive self-healing hydrogels formed by boronate-catechol complexation. *Chem. Commun.* **2011**, *47*, 7497-7499.
(534) Tzlil, S.; Kindt, J. T.; Gelbart, W. M.; Ben-Shaul, A. Forces and pressures in DNA packaging and release from viral capsids. *Biophys. J.* **2003**, *84*, 1616-1627.

Chapter 5

Acknowledgments

The work for this thesis would not be possible without the support of many people whom I would like to express my sincere thanks.

First of all, I would like to deeply thank my parents Ursula and Norbert without whom I would not be in the place I am today. Thank you very much for your support, love and motivation throughout the years and your believing in me.

I would especially like to thank my supervisor Prof. Dr. Nico Bruns for the very inspiring and wonderful research topics and for his advices, enthusiastic guidance, his patience and support in all stages of my PhD work. I really appreciated the freedom he has given me for my research and how he let me evolve as a researcher.

Further, I would kindly like to thank my second supervisor Prof. Dr. Wolfgang Meier for hosting me in his group, for his support and for the excellent research environment. I also want to thank Prof. Dr. Marcus Textor for showing interest in my research and being coexaminer of my thesis. Prof. Dr. J. P. Maier is kindly acknowledged for being the chair.

The NanoArgovia-project would not be possible without the collaboration with external partners in Switzerland (Prof. Dr. Uwe Pieles, Dr. Olfa Glaied, Christian Rytka (FHNW, Muttenz and Brugg-Windisch), Dr. Jose V. Aurajo (AMI, Fribourg) and Markus Hess (Unico swiss-tex, Alpnachstad), the helping support of students (Sara Freund, Jonas Barmettler and Andreas Reichmuth) as well as the help of people from the University of Basel who did an excellent job with the SEM and cryo-SEM analysis (Giovanni Morson, Evi Bieler, Carola Alampi) and the AFM measurements (Dr. Justyna Kowal). Thank you very much.

Like other projects, the thermosome-project would not be possible without the help of many people. Thank you very much to Vesna Olivieri, Ursula Sauder and Gabriele Persy for the beautiful TEM-images of the thermosome and the conjugates. Thank you very much to Adrian Najer for help with the FCS measurements and Drs.

Jason Duskey and Viktoriia Postupalenko for their enormous help with the biological applications of the conjugates.

A big thanks to the "Thermosome-Team" Drs. Kasper Renggli and Martin Nussbaumer. It was a great time with you in a scientific and non-scientific aspect.

Thank you to the students I was supervising and advising in a project that is not part of this thesis (Kathrin Höhnerlage, Svetlana Stolarov, Sagana Thamboo and Claudio von Planta).

I would like to thank the people who read in parts through my manuscript and helped in improving it (Drs. Gesine Gunkel-Grabole, Martin Nussbaumer, Jason Duskey, Kasper Renggli, Jens Gaitzsch).

Further, thanks go to Grischa Martin, Philipp Knöpfel and Georg Holderied from the mechanical and electrical workshop and Jean-Pierre Ramseyer. Thank you to Maya Greuter and Danni Tischhauser for the administrative support.

I am also thankful to my colleagues and friends in the Meier and Bruns research groups for their support, their friendship and the time outside the university: Severin Sigg, Sven Kasper, Samuel Lörcher, Adrian Najer, Pascal Richard, Bernadetta Gajewska, Evgeniia Konishcheva and Drs. Fabian Itel, Farzad Seidi, Dalin Wu, Juan Liu, Jason Duskey, Jens Gaitzsch, Viktoriia Postupalenko, Justyna Kowal, Adrian Dinu, Gergely Kali, Agnieszka Tajchert, Thomas Schuster and all other people.

Thanks to all people who are involved in the ScienceSlam.

I would like to acknowledge the University of Basel for the travel grant I received.

Special thanks go to my family and friends in Germany and Poland. Further special thanks go to Michi, Max, Sarah, Artur (Archie), Jens Martin (Madt), Ami and Hannes. Besides my parents I am most thankful to my girlfriend Magda for being supportive and the time we are spending together.